

INFORMATION TO USERS

This manuscript has been reproduced from the microfilm master. UMI films the text directly from the original or copy submitted. Thus, some thesis and dissertation copies are in typewriter face, while others may be from any type of computer printer.

The quality of this reproduction is dependent upon the quality of the copy submitted. Broken or indistinct print, colored or poor quality illustrations and photographs, print bleedthrough, substandard margins, and improper alignment can adversely affect reproduction.

In the unlikely event that the author did not send UMI a complete manuscript and there are missing pages, these will be noted. Also, if unauthorized copyright material had to be removed, a note will indicate the deletion.

Oversize materials (e.g., maps, drawings, charts) are reproduced by sectioning the original, beginning at the upper left-hand corner and continuing from left to right in equal sections with small overlaps.

Photographs included in the original manuscript have been reproduced xerographically in this copy. Higher quality 6" x 9" black and white photographic prints are available for any photographs or illustrations appearing in this copy for an additional charge. Contact UMI directly to order.

ProQuest Information and Learning
300 North Zeeb Road, Ann Arbor, MI 48106-1346 USA
800-521-0600

UMI[®]

TITAN, TRITON, PLUTO, AND KUIPER BELT OBJECTS:
A STUDY OF PAST AND PRESENT ATMOSPHERES WITH
GREY AND NONGREY MODELS

by
Anupama M. N. Rao

Copyright © Anupama M. N. Rao 2001

A Dissertation Submitted to the Faculty of the
GRADUATE INTERDISCIPLINARY PROGRAM
IN APPLIED MATHEMATICS

In Partial Fulfillment of the Requirements
For the Degree of

DOCTOR OF PHILOSOPHY

In the Graduate College

THE UNIVERSITY OF ARIZONA

2001

UMI Number: 3010190

Copyright 2001 by
Rao, Anupama M. N.

All rights reserved.

UMI[®]

UMI Microform 3010190

Copyright 2001 by Bell & Howell Information and Learning Company.
All rights reserved. This microform edition is protected against
unauthorized copying under Title 17, United States Code.

Bell & Howell Information and Learning Company
300 North Zeeb Road
P.O. Box 1346
Ann Arbor, MI 48106-1346

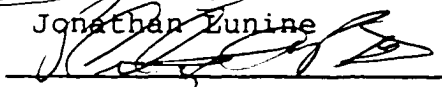
THE UNIVERSITY OF ARIZONA ©
GRADUATE COLLEGE

As members of the Final Examination Committee, we certify that we have read the dissertation prepared by Anupama M. N. Rao entitled Titan, Triton, Pluto, and Kuiper belt objects: a Study of Past and Present Atmospheres with Grey and Nongrey Models

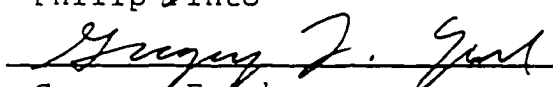
and recommend that it be accepted as fulfilling the dissertation requirement for the Degree of Doctor of Philosophy


Jonathan Lunine

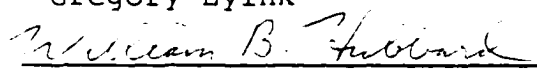
4/13/01
Date


Philip Pinto

4/13/01
Date


Gregory Eyink

4/13/01
Date


William Hubbard

4/13/01
Date

Date

Final approval and acceptance of this dissertation is contingent upon the candidate's submission of the final copy of the dissertation to the Graduate College.

I hereby certify that I have read this dissertation prepared under my direction and recommend that it be accepted as fulfilling the dissertation requirement.


Dissertation Director Jonathan Lunine

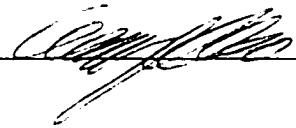
4/13/01
Date

STATEMENT BY AUTHOR

This dissertation has been submitted in partial fulfillment of requirements for an advanced degree at The University of Arizona and is deposited in the University Library to be made available to borrowers under rules of the Library.

Brief quotations from this dissertation are allowable without special permission, provided that accurate acknowledgment of source is made. Requests for permission for extended quotation from or reproduction of this manuscript in whole or in part may be granted by the copyright holder.

SIGNED: _____

A handwritten signature in black ink, written over a horizontal line. The signature is cursive and appears to be "C. J. ...".

ACKNOWLEDGMENTS

I would like to thank:

My advisor, Dr. Jonathan Lunine (Planetary Sciences Department, University of Arizona) for his guidance, patience, and support.

My co-advisor, Dr. Philip Pinto (Astronomy Department, University of Arizona), without whom our nongrey atmosphere model would not have happened.

NASA Grant NAG5-4051: Planetary Geosciences and Planetary Atmospheres, for funding this research.

My committee members, Dr. Gregory Eyink (Mathematics Department, University of Arizona) and Dr. William Hubbard (Planetary Sciences Department, University of Arizona), and my outside reviewer, Dr. Roger Yelle (Department of Physics and Astronomy, Northern Arizona University), for their helpful comments.

Dr. Regis Courtin (Observatoire de Paris - Section de Meudon), for his opacity code (which tremendously affected the types of models we developed) and for his observations/advice regarding *CO* contributions.

The Planetary Sciences Department, Mathematics Department, and Program in Applied Mathematics for the many resources provided to me.

The many friends who have come and gone.

My family, with whose help I never would have achieved my goal.

My significant other, Bob, for everything.

TABLE OF CONTENTS

LIST OF TABLES	7
LIST OF FIGURES	8
ABSTRACT	12
CHAPTER 1. INTRODUCTION	14
1.1. Trans-Neptunian Objects	18
1.1.1. Triton	18
1.1.2. Pluto	19
1.1.3. Kuiper Belt Objects	20
1.2. Titan	21
1.3. Comparisons	24
1.4. Previous Works in This Area	24
1.5. Energy Transport	27
1.5.1. Radiative Transfer	27
1.5.2. Convection	31
1.5.3. Opacity	33
1.5.4. Greenhouse and Antgreenhouse Effects	36
1.5.5. “Grey” Approximation	37
1.6. Equilibrium Conditions Used in Atmosphere Modelling	38
1.6.1. Hydrostatic Equilibrium	38
1.6.2. Local Thermodynamic Equilibrium	39
1.6.3. Radiative Equilibrium	39
CHAPTER 2. GREY ATMOSPHERES	41
2.1. The Model	41
2.1.1. Simplifying Assumptions	42
2.1.2. Derivation	42
2.2. Computational Results of the Grey Atmosphere Model	58
2.2.1. Model Implementation	58
2.2.2. Model Inputs	58
2.2.3. S-curves	60
2.2.4. Triton Results	67
2.2.5. Pluto (Tidal and Non-Tidal) Results	81
2.2.6. Kuiper Belt Object Results	84

TABLE OF CONTENTS—*Continued*

CHAPTER 3. NON-GREY ATMOSPHERES	93
3.1. The Model	94
3.1.1. Simplifying Assumptions	94
3.1.2. Solving the Equation of Radiative Transfer	95
3.1.3. Developing a Correction Scheme	106
3.1.4. Nongrey Model Outline	114
3.1.5. Initial Conditions/Grid Construction	116
3.2. Computational Results of the Nongrey Atmosphere Model	120
3.2.1. Model Implementation	120
3.2.2. Model Inputs	120
3.2.3. Model Results	121
CHAPTER 4. DISCUSSION, CONCLUSIONS, AND FUTURE DIRECTIONS	150
4.1. Grey Models of Past Triton, Pluto, and KBOs	150
4.1.1. Summary of Results	150
4.1.2. Discussion	152
4.1.3. Conclusions	156
4.1.4. Future Directions	157
4.2. Nongrey Model of Present Titan	158
4.2.1. Summary of Results	158
4.2.2. Discussion	166
4.2.3. Conclusions	167
4.2.4. Evolution of Titan	168
4.2.5. Future Directions	169
4.3. Comparison of Methods	169
APPENDIX A. TIMELINES	171
A.1. Triton	171
A.2. Pluto	171
A.3. Kuiper Belt	172
A.4. Titan	173
APPENDIX B. PHYSICAL CONSTANTS	174
REFERENCES	175

LIST OF TABLES

TABLE 1.1.	Physical quantities used for our models.	25
TABLE 2.1.	Pluto: Chandrasekhar Mean Opacity Results: $T_e = 44$ K.	81
TABLE 2.2.	Pluto: Planck Mean Opacity Results: $T_e = 44$ K.	81
TABLE 2.3.	Pluto: Rosseland Mean Opacity Results: $T_e = 44$ K.	84
TABLE 2.4.	KBO: Chandrasekhar Mean Opacity Results: $T_e = 49$ K.	85
TABLE 2.5.	KBO: Planck Mean Opacity Results: $T_e = 49$ K.	85
TABLE 2.6.	KBO: Rosseland Mean Opacity [cm^2/g].	91
TABLE 2.7.	KBO: Optical Depth calculated with Rosseland Mean Opacity. . .	91
TABLE 2.8.	KBO: Pressure [dyn/cm^2] calculated with Rosseland Mean Opacity. .	91
TABLE 3.1.	Code run labels with their corresponding volatile concentrations. . .	120
TABLE 4.1.	Titan 1-3: Comparison of convergence parameters.	158
TABLE 4.2.	Titan 1-3: Comparison of surface properties.	158
TABLE 4.3.	Titan 4: Comparison of convergence parameters.	168
TABLE 4.4.	Titan 4: Comparison of surface properties.	168

LIST OF FIGURES

FIGURE 1.1. Altitude versus Temperature for Titan. Data from [85] [170]. Concept from [14].	23
FIGURE 1.2. The physical picture. Redrawn and adapted from [15].	28
FIGURE 1.3. The transfer of energy via absorption and emission. Redrawn and adapted from [112].	30
FIGURE 1.4. Opacity [$1/\text{cm am}^2$] versus Frequency [Hz]. Redrawn and adapted from [106].	36
FIGURE 2.1. Energy dissipation as a function of time.	48
FIGURE 2.2. Temperature (Effective and Surface) versus Tidal Heat Flux (F_{tide}).	61
FIGURE 2.3. $P_v^2 - P(T)^2$ versus Surface Temperature.	62
FIGURE 2.4. Temperature (Effective and Surface) versus Tidal Heat Flux (F_{tide}).	63
FIGURE 2.5. $P_v(T)^2$ for $F_{tide} = \{120, 960, 1320, 1800, 3000\}$ dyn/cm s.	64
FIGURE 2.6. $P(T)^2$ for $F_{tide} = \{120, 960, 1320, 1800, 3000\}$ dyn/cm s.	65
FIGURE 2.7. $P_v(T)^2 - P(T, \tau)^2$ for $F_{tide} = \{120, 960, 1320, 1800, 3000\}$ dyn/cm s.	66
FIGURE 2.8. Triton: Temperature (Effective and Surface) versus Tidal Heat Flux (F_{tide}).	68
FIGURE 2.9. Triton: Chandrasekhar Mean Opacity versus Surface Temperature.	69
FIGURE 2.10. Triton: Planck Mean Opacity versus Surface Temperature.	70
FIGURE 2.11. Triton: Optical Depth versus Surface Temperature with Chan- drasekhar Mean Opacity.	71
FIGURE 2.12. Triton: Optical Depth versus Surface Temperature with Planck Mean Opacity.	72
FIGURE 2.13. Triton: Pressure versus Surface Temperature with Chandrasekhar Mean Opacity.	73
FIGURE 2.14. Triton: Pressure versus Surface Temperature with Planck Mean Opacity.	74
FIGURE 2.15. Triton: Altitude versus Temperature with Chandrasekhar Mean Opacity. $F_{tide}=3240$ dyn/cm s. $T_e = 99$ K. $T = 488$ K.	75
FIGURE 2.16. Triton: Altitude versus Temperature with Planck Mean Opacity. $F_{tide}=3240$ dyn/cm s. $T_e = 99$ K. $T = 601$ K.	76
FIGURE 2.17. Triton: Rosseland Mean Opacity versus Surface Temperature.	77
FIGURE 2.18. Triton: Optical Depth versus Surface Temperature with Rosse- land Mean Opacity.	78
FIGURE 2.19. Triton: Pressure versus Surface Temperature with Rosseland Mean Opacity.	79
FIGURE 2.20. Triton: Altitude versus Temperature with Rosseland Mean Opac- ity.	80

LIST OF FIGURES—*Continued*

FIGURE 2.21. Pluto: Altitude versus Temperature with Chandrasekhar Mean Opacity. $F_{tide}=3240$ dyn/cm s, $T_e = 44$ K. $T = 381$ K.	82
FIGURE 2.22. Pluto: Altitude versus Temperature with Planck Mean Opacity. $F_{tide}=3240$ dyn/cm s, $T_e = 44$ K. $T = 500$ K.	83
FIGURE 2.23. KBO: Altitude versus Temperature using the Chandrasekhar Mean Opacity.	86
FIGURE 2.24. KBO: Pressure versus Surface Temperature using the Chandrasekhar Mean Opacity.	87
FIGURE 2.25. KBO: Altitude versus Temperature using the Planck Mean Opacity.	88
FIGURE 2.26. KBO: Pressure versus Surface Temperature using the Planck Mean Opacity.	89
FIGURE 2.27. KBO: Temperature (Effective and Surface) versus Heat Flux with Rosseland Mean Opacity.	90
FIGURE 2.28. KBO: Altitude versus Surface Temperature. Pressure versus Surface Temperature, both with Rosseland Mean Opacity.	92
FIGURE 3.1. The Big Picture for our nongrey model of Titan's troposphere.	115
FIGURE 3.2. Titan 1: Altitude [km] versus Temperature [K]. The "Lindal/Yelle data" are from [85] [170].	122
FIGURE 3.3. Titan 1: Temperature [K] versus Pressure [dyn/cm ²]. The "Lindal/Yelle data" are from [85] [170].	123
FIGURE 3.4. Titan 1: Temperature [K] versus $\tau_{rosseland}$ [-].	124
FIGURE 3.5. Titan 1: Initial/Final Rosseland Mean Opacity [1/cm] versus Temperature [K].	125
FIGURE 3.6. Titan 1: Final Rosseland, Chandrasekhar, and Planck Mean Opacities[1/cm] versus Altitude [km].	126
FIGURE 3.7. Titan 1: Eddington flux [ergs/cm ² sec Hz sr] versus Altitude [km]. The flux is constant to within 1% ($(H_{max} - H_{min})/H_{max} < 0.01$). This yields an effective temperature of 67 K.	127
FIGURE 3.8. Titan 1: Flux [ergs/cm ² sec Hz sr] versus Frequency [Hz]. The "Data from Courtin paper" is taken from a brightness temperature graph [23] and converting it back to a flux value.	128
FIGURE 3.9. Titan 2: Altitude [km] versus Temperature [K]. The "Lindal/Yelle data" are from [85] [170].	129
FIGURE 3.10. Titan 2: Temperature [K] versus Pressure [dyn/cm ²]. The "Lindal/Yelle data" are from [85] [170].	130
FIGURE 3.11. Titan 2: Temperature [K] versus $\tau_{rosseland}$ [-].	131
FIGURE 3.12. Titan 2: Initial/Final Rosseland Mean Opacity [1/cm] versus Temperature [K].	132

LIST OF FIGURES—*Continued*

FIGURE 3.13. Titan 2: Final Rosseland, Chandrasekhar, and Planck Mean Opacities[1/cm] versus Altitude [km].	133
FIGURE 3.14. Titan 2: Eddington flux [ergs/cm ² sec Hz sr] versus Altitude [km]. The flux is constant to within 1% ($(H_{max} - H_{min})/H_{max} < 0.01$). This yields an effective temperature of 69 K.	134
FIGURE 3.15. Titan 2: Flux [ergs/cm ² sec Hz sr] versus Frequency [Hz]. The "Data from Courtin paper" is taken from a brightness temperature graph [23] and converting it back to a flux value.	135
FIGURE 3.16. Titan 3: Altitude [km] versus Temperature [K]. The "Lindal/Yelle data" are from [85] [170].	136
FIGURE 3.17. Titan 3: Temperature [K] versus Pressure [dyn/cm ²]. The "Lindal/Yelle data" are from [85] [170].	137
FIGURE 3.18. Titan 3: Temperature [K] versus $\tau_{rosseland}$ [-].	138
FIGURE 3.19. Titan 3: Initial/Final Rosseland Mean Opacity [1/cm] versus Temperature [K].	139
FIGURE 3.20. Titan 3: Final Rosseland, Chandrasekhar, and Planck Mean Opacities[1/cm] versus Altitude [km].	140
FIGURE 3.21. Titan 3: Eddington flux [ergs/cm ² sec Hz sr] versus Altitude [km]. The flux is constant to within 1% ($(H_{max} - H_{min})/H_{max} < 0.01$). This yields an effective temperature of 73 K.	141
FIGURE 3.22. Titan 3: Flux [ergs/cm ² sec Hz sr] versus Frequency [Hz]. The "Data from Courtin paper" is taken from a brightness temperature graph [23] and converting it back to a flux value.	142
FIGURE 3.23. Titan 4: Altitude [km] versus Temperature [K]. The "Lindal/Yelle data" are from [85] [170].	143
FIGURE 3.24. Titan 4: Temperature [K] versus Pressure [dyn/cm ²]. The "Lindal/Yelle data" are from [85] [170].	144
FIGURE 3.25. Titan 4: Temperature [K] versus $\tau_{rosseland}$ [-].	145
FIGURE 3.26. Titan 4: Initial/Final Rosseland Mean Opacity [1/cm] versus Temperature [K].	146
FIGURE 3.27. Titan 4: Final Rosseland, Chandrasekhar, and Planck Mean Opacities[1/cm] versus Altitude [km].	147
FIGURE 3.28. Titan 4: Eddington flux [ergs/cm ² sec Hz sr] versus Altitude [km]. The flux is constant to within 1% ($(H_{max} - H_{min})/H_{max} < 0.01$). This yields an effective temperature of 82 K.	148
FIGURE 3.29. Titan 4: Flux [ergs/cm ² sec Hz sr] versus Frequency [Hz]. The "Data from Courtin paper" is taken from a brightness temperature graph [23] and converting it back to a flux value.	149

LIST OF FIGURES—*Continued*

FIGURE 4.1. Pluto: Temperature (Effective and Surface) versus Heat Flux with Rosseland Mean Opacity and KBO Albedo.	153
FIGURE 4.2. Pluto: Temperature (Effective and Surface) versus Heat Flux with Rosseland Mean Opacity and KBO Gravity.	154
FIGURE 4.3. Sensitivity of mean opacities to percentage of H_2 by mass.	155
FIGURE 4.4. Altitude [km] versus Temperature [K].	159
FIGURE 4.5. Altitude [km] versus Relative Error in Temperature [K].	160
FIGURE 4.6. Temperature [K] versus Pressure [dyn/cm ²].	161
FIGURE 4.7. Rosseland Mean Opacity [1/cm] versus Temperature [K].	162
FIGURE 4.8. Temperature [K] versus $\tau_{\text{rosseland}}$ [-].	163
FIGURE 4.9. Eddington flux [ergs/cm ² sec Hz sr] versus Altitude [km].	164
FIGURE 4.10. Flux at top of the troposphere [ergs/cm ² sec Hz sr] versus Frequency [Hz]. The “Data from Courtin paper” is from taken from estimating the brightness temperature as a function of wavenumber from a graph [23] and converting it back to a flux versus frequency value.	165

ABSTRACT

This work is divided into two parts: a grey model for past Triton, Pluto, and Kuiper belt objects, and a nongrey model for current Titan's troposphere.

Steady-state, planar models of early atmospheres for Triton, Pluto, and Kuiper belt objects are computed using a grey approach that tracks the transfer/distribution of heat via radiative transport. These objects are treated here together because they resemble one another in size, surface chemical composition, and exist in the same cold portion of the outer solar system. Beginning with present-day volatiles observed on the surfaces of Triton and Pluto (methane and molecular nitrogen), a trace of molecular hydrogen (present in most primordial atmospheres) is added. It is assumed that as the object is heated by solar, tidal, accretional, or radiogenic methods (this varies between the objects treated here) these chemical species then evaporate from the surface to create an atmosphere. Binary collisions among the molecules account for the sources of opacity, and absorption coefficients are provided by [21]. The grey atmosphere calculations require a mean opacity, and its results are sensitive to the type of mean opacity used. Thus a variety of methods (Planck, Rosseland, and Chandrasekhar mean opacities) are used to accommodate this dependence and the variations in optical depth. Surface temperatures are then calculated as a function of the heating rate, molecular hydrogen abundance, and mean opacity type. As a result of these modelling experiments, tidal heating is found to be crucial to the formation of a thick atmosphere on Triton, and albedo and gravitational acceleration strongly affect the formation of atmospheres on less massive objects such as Pluto and Kuiper belt objects.

A nongrey, steady-state, planar model of Titan's current troposphere is developed to study the effect of varying methane mass fraction. Methods from stellar atmosphere modelling are used to solve the equation of transfer as a two-point boundary problem.

To additionally satisfy radiative, hydrostatic, and local thermodynamic equilibrium, an iterative correction procedure is utilized since the correct temperature and density profiles as a function of altitude are not known *a priori*. The volatile composition is taken from observation: molecular nitrogen, methane, and molecular hydrogen. Again, binary collisions among the molecules account for the sources of opacity, and absorption coefficients are provided by [21]. The heating source for Titan is solar radiation absorbed and reradiated by the planet's surface in the infrared region of the spectrum, with a small amount of heat emanating from the stratosphere. The chemical species evaporate from the surface to create an atmosphere. Models of Titan's troposphere are calculated using different amounts of methane (within observational constraints) since the presence of methane is evolving in Titan's atmosphere due to photolytic processes. From model results it is shown that that by solving the radiative transfer equation, subject to radiative, hydrostatic, and local thermodynamic equilibrium constraints, a model of Titan's troposphere with a maximum deviation of 8% from data [85] [170] can be obtained. The preliminary model of past Titan's troposphere is consistent with other analytic results [89].

CHAPTER 1

INTRODUCTION

The most fruitful areas for growth of the sciences are those between established fields. Science has been increasingly the task of specialists, in fields which show a tendency to grow progressively narrower. Important work is delayed by the unavailability in one field of results that may have already become classical in the next field. It is these boundary regions of science that offer the richest opportunities to the qualified investigator.

-- Norbert Wiener

In this work we model past atmospheres of the most distant planet Pluto, Neptune's moon Triton, and Kuiper belt objects (KBOs), and the present atmosphere of Titan. Our atmosphere models are in steady-state, utilize planar symmetry, and assume radiative, hydrostatic, and local thermodynamic equilibrium. Our analysis is divided into two parts: 1) we investigate the surface properties of early atmospheres on Triton, Pluto, and KBOs using a grey (frequency-independent opacity) model; 2) we model Titan's current atmospheric profile using a nongrey (frequency-dependent opacity) model.

Part I: Grey Models of Past Triton, Pluto, and KBOs Spacecraft and ground-based observations show that the surface ices on Triton and Pluto, both of which likely originated in solar orbit around 30-40 AU from the sun [12], differ in composition from that of the comets as inferred from observations of their gaseous comae [152]. It is believed that at least some comets, the ice-rich short-period comets, originated in the same part of space – the Kuiper Belt – as did Triton and Pluto [71]. It is also believed that these comets retained their primordial properties to an extent

greater than that of any other solar system objects [71]. How do we account for the differences in present-day surface ice composition?

It is possible that the discrepancies in volatile composition (meaning materials more easily vaporizable than water) between Triton/Pluto and the comets can be attributed to the formation of massive atmospheres on the former during their formation: atmospheres which led to early loss of volatiles to space [95]. As a start towards testing this hypothesis, we apply a grey atmosphere model to early Triton and Pluto to see if massive and optically thick atmospheres could have formed, given certain molecular hydrogen mass fractions and heating inputs. Also, it is not known *a priori* which mean opacity should be used given problems with self-consistency, so we apply the most widely used estimates (Chandrasekhar, Planck, and Rosseland). Our grey model calculates the surface temperature of the object for a given set of parameters. We also model an “averaged” KBO based on available data since.

Our model atmosphere can be described in the following heuristic way: start with a planar surface of ice in space and apply heating (solar, tidal, accretional, radiogenic) to the surface. This results in the outgassing of volatiles onto the surface and hence the development of an atmosphere.

For the surface ices on Triton, Pluto, and KBOs, we use present-day volatiles methane (CH_4) and molecular nitrogen (N_2), as determined by observation for Triton [26] [27] and Pluto [59] [125]. In addition, we add a trace amount of molecular hydrogen (which was probably present as a remnant of the solar nebula or as a photochemical by-product of the photolysis of methane [98]). The atmospheric sources of opacity are binary collisions among our volatile species [21].

Our model builds on work presented in [119] [98]. We present here new work on the problem: using a variety of mean opacities in our analysis, new mathematical approaches to calculating mean opacities, directly using detailed fits to laboratory opacity data instead of an interpolation table to calculate the mean opacities, adding radiogenic and accretional heating sources, searching for more than two roots, and

expanding the model to apply to Pluto and KBOs.

We find that molecular hydrogen plays a major role in the evolution of these atmospheres due to the “window effect” (see section 1.5.3). We also find temperature solutions undetected in previous works. For Triton, we discover that for concentrations of H_2 greater than 0.005% with the Rosseland mean opacity, greenhouse atmospheres develop. Models using the Chandrasekhar and Planck means yield hot and optically thick atmospheres for all concentrations of H_2 we tested. For Pluto, we find that hot optically thick atmospheres develop with the Chandrasekhar and Planck means only. For KBOs, we find that greenhouse atmospheres develop for H_2 greater than 1% with the Rosseland mean, and consistently arise using the Chandrasekhar and Planck means. The model results for Pluto and the averaged KBO were unexpectedly different. Further modelling indicates that this is due to the albedo and gravitational acceleration differences between the two objects.

Part II: Nongrey Model of Present Titan We wish to model current Titan’s troposphere with a nongrey atmosphere approach to study the effect of varying methane mass fraction. In a nongrey model, opacity is dependent on frequency. The inclusion of a spectral component (absent in a grey model) provides more flexibility and better accuracy. Methane plays an interesting role in Titan’s atmosphere: it is depleted via photolysis in the atmosphere, and the current inventory of methane will be depleted on a time scale of 10^7 to 10^8 years [171]. This indicates that either there is some replenishing interaction between the surface and the atmosphere [99] or that methane in Titan’s atmosphere does not exist in a long-term steady-state [89]. We wish to develop a model of Titan’s current troposphere, such that it can be easily modified to study Titan’s past and the effect of methane depletion. Any model of the past must first as a test be able to accurately reproduce the present atmosphere. This work is developed and present here.

The underlying physics of the nongrey model is similar to that of the grey model in

Part I. But instead of using the simplified grey approach, we utilize stellar atmosphere methods to develop a nongrey model of Titan's atmosphere. In particular, we use the Feautrier method [112] to solve the radiative transfer equation (RTE), then use correction methods [62] to satisfy radiative and hydrostatic equilibrium (RE and HE, respectively). We have adapted these methods to apply them for the first time to Titan atmosphere modelling.

For the atmospheric constituents on Titan, we use present-day volatiles molecular nitrogen (N_2), methane (CH_4), and molecular hydrogen (H_2), as determined by observation [85] [79] [164]). Again, the atmospheric sources of opacity are binary collisions among our volatile species [21]. Titan is also composed of rock and ice, and is heated primarily by solar radiation, thus causing the outgassing of volatiles.

Our model is an improvement over other nongrey models in the following areas: better spatial, spectral, and angular resolution (as compared to [106]), we put our model through a rigorous testing phase, and we include an initial damping phase to to the iterations to avoid initial overcorrections and reduce overall runtime.

We find that by solving the radiative transfer equation, subjecting the solution to radiative, hydrostatic, and local thermodynamic equilibrium constraints, and estimating the heat input from surface and the haze layer, we can model Titan's troposphere to a maximum deviation of 8% as compared to the data from [85] and [170]. Our preliminary model of past Titan's troposphere is in agreement with other analytic results [89].

In the rest of Chapter 1, we discuss in a little more detail the current knowledge of the objects in our study, as well as the underlying physics common to both problems. In Chapter 2 we develop the grey atmosphere model and report on the results. Similarly, in Chapter 3 we derive the nongrey model and present the results. In Chapter 4 we discuss the findings of this work and mention possible future directions.

1.1 Trans-Neptunian Objects

The small rock/ice system of Pluto-Charon differs significantly in size and composition from the giant planets of the outer Solar System (e.g., Uranus and Neptune) [108], but has much in common with Triton and Kuiper belt objects. Along with Centaurs (bodies with diameters less than 200 km whose eccentric orbits cross the paths of Saturn, Uranus, and Neptune [12]), Triton, Pluto-Charon, and KBOs inhabit an area known as the trans-Neptunian region, recently defined to be the region extending from the orbit of Neptune (30 AU) to just beyond the outer reaches of Pluto's orbit (50 AU) [166].

These trans-Neptunian objects (TNOs), the largest of which are Triton and Pluto, are primitive relative to the inner solar system, but do show varying degrees of evolution [12]. TNOs take about 160-800 years to orbit the sun, and about 1/2 the KBOs along with Triton and Pluto have stable dynamical relationships with Neptune (implying an origin from the solar nebula) [12]. The cold temperatures in the outer solar system allow for the existence of volatile ices on the surfaces of TNOs, perhaps leading to tenuous atmospheres [12]. A current list of TNOs is maintained online (see [114]).

1.1.1 Triton

Triton, the largest moon of Neptune, is theorized to be a former TNO that was captured by Neptune via collision with a regular satellite (due to its current inclined, retrograde orbit [109] [94]).

Though the bulk of our knowledge of Triton comes from the 1989 Voyager 2 flyby, Earth-based observations first detected gaseous methane in Triton's atmosphere in 1979 [30]. A few years later nitrogen ice was detected, and it was predicted that N_2 dominated Triton's atmosphere (rather than methane as previously thought) [26]. With the Voyager 2 flyby came a wealth of information and confirmation of ground-

based predictions: Triton's surface temperature was measured at ≈ 38 K, its surface pressure is ≈ 16 μ bar, and N_2 does indeed dominate Triton's atmosphere [156]. Subsequent spectroscopic observations indicate the presence of CO and CO_2 [27].

Arguments have been made that Triton's current atmosphere is in vapor equilibrium [165] [68]. Lightcurve models from the 1993 and 1995 occultations with Triton have refined the vital statistics measured by Voyager 2 [120] [37]. It is currently believed that the major constituents of Triton's atmosphere are N_2 , CH_4 , and CO [109].

1.1.2 Pluto

Pluto, the 9th planet in the Solar System, is known for its high obliquity and eccentric orbit. The small, rocky, and icy planet is very different from its outer solar system counterparts, which are very large and gaseous (e.g., Neptune, Uranus).

There are many theories on the origin of Pluto (summarized in this paragraph from [151]). It was believed that Pluto might have been a former satellite of Neptune, but this proved to be untenable when Pluto's 3:2 orbit resonance with Neptune was discovered (among other problems). Another theory hypothesized that Pluto was a giant planet core that somehow lost its gas, but this was shown to be invalid when Pluto's mass was determined - it was not massive enough. After the discovery of Charon, the origin of the binary system needed to be addressed. The idea of rotational fission was dismissed because the system has too much angular momentum. The currently accepted theory is that the Pluto-Charon binary system arose from a collision between Pluto and a Charon progenitor, both with heliocentric orbits.

In 1976 methane was first spectroscopically detected on Pluto [29]. A multitude of information, including verification of the presence of an atmosphere, was derived from Pluto's 1988 occultation with a bright star [59]. The lightcurve resulting from the 1988 occultation exhibits a curious "knee," a point at which the profile of a typical

isothermal atmosphere is interrupted by a steep descent [36]. Two major theories arose to explain the kink in the lightcurve. Some believe that the atmosphere of Pluto is isothermal, primarily composed of methane, and the steep extinction of the lightcurve can be explained by a low-lying haze layer of photochemical origin [36] [38]. Others examined the energy balance of the atmosphere and conclude that the temperature of the atmosphere is higher than the surface temperature, and hence a steep temperature gradient exists near the surface, which in turn implies that a molecule heavier than methane is present in the atmosphere [39] [169] [61] [148]. Currently the explanation involving a photochemical haze seems less probable [158].

Further spectroscopic observations indicate the presence of CO and N_2 ices on Pluto and establish N_2 (not CH_4) as the dominant ice on Pluto as well as the dominant atmospheric constituent [125] [94]. It is currently believed that the major constituents of Pluto's atmosphere are N_2 , CH_4 , and possibly CO [168]. It is believed that Pluto's atmosphere is in vapor-pressure equilibrium [150].

1.1.3 Kuiper Belt Objects

In 1949 Edgeworth [35] put forth the idea that a disk of unaccreted icy objects existed at a distance greater than 30 AU from the sun, leftover from the formation of the solar system. Kuiper elaborated on this idea in 1951 [80]. In 1980 it was suggested that such a disk (nicknamed the Kuiper belt) could be a source of low-inclination short-period comets [44], an idea strengthened by simulations [33]. In 1992 theory became fact when the first Kuiper belt object was observed [72]. It is estimated that there are at least 7×10^4 objects between 30-50 AU, with 50-200 km radius [71]. At the time of this writing, 366 TNOs have been discovered [114]. Very little is known about the composition or existence of atmospheres on KBOs, but spectroscopic studies show that the KBOs discovered thus far exhibit a range of colors, implying varied surface composition [102].

1.2 Titan

Titan is the largest moon of Saturn and the only solid body beyond Mars with a substantial atmosphere. It is believed to have formed from a proto-Saturn nebular disk at a time of swift contraction [129].

As with Triton, Titan's atmospheric discoveries can be divided into pre- and post-Voyager observations. The presence of an atmosphere was detected in 1908 by Comas Solas [94]. In 1944 Gerald Kuiper discovered methane on Titan via spectroscopic studies [79]. Unexpectedly high thermal brightness temperature measurements of Titan [90] [1] [116] spurred theories about Titan's atmospheric structure and composition. Soon followed the discovery of hydrogen in Titan's atmosphere [164]. Further spectroscopic studies between 1973 and 1975 revealed the following atmospheric constituents: C_2H_6 [51] [91], CH_3D , C_2H_4 , and C_2H_2 [50]. In 1975 limb darkening was observed, implying the existence of an optically thick atmosphere [159].

In late 1980 Voyager I made its rendezvous with Titan, and a wealth of information about its atmosphere was revealed. The cameras on Voyager I were not able to penetrate the orange haze to observe surface features [94]. Molecular nitrogen (N_2) was detected in data from the radio-occultation experiment (RSS) and the ultraviolet spectrometer (UVS), and was determined to be the most abundant atmospheric constituent [85]. Methane is next in abundance, constrained at 2-10% at the surface and 2-3% at the stratosphere's base [85]. In addition CO_2 was identified in the stratosphere from Voyager I infrared interferometer spectrometer (IRIS) data [141]. In 1983 CO was identified in Titan's troposphere via ground-based observations [101]. In 1993 CH_3CN was detected [8]. Further analysis of the IRIS data has detected C_4N_2 [142].

In summary, the major atmospheric constituents of Titan are N_2 , CH_4 , and H_2 . It is believed that there is yet another major component as yet undetected in Titan's atmosphere, based on atmospheric mean molecular mass measurements higher than

28 (that of nitrogen) [140]. Argon is considered a likely candidate based on its cosmic abundance and because it would not condense out under the atmospheric conditions present on Titan [124]. If argon is present, it would be constrained to a mole fraction of less than 6% [23].

The vertical temperature profile for altitudes below 200 km were also derived from the RSS: the temperature at the surface is about 95K, dropping to 71 K at the cold trap located at about 43 km altitude, and then increasing to the stratosphere to about 180 km [85] [82] [170] (see Figure 1.1). The latitudinal temperature structure was determined from infrared brightness temperatures as measured by IRIS, and showed a temperature contrast of about 20 K between equator and poles [45]. According to Voyager measurements Titan's atmosphere is close to radiative equilibrium, with convection dominating only in first 3-4 kilometers near the surface [85] [40] [46]. Stellar occultation light curves from ground-based observations have been inverted to yield temperature profiles between 300 and 500 km altitude at various locations [60].

Observations indicate that an obscuring high altitude haze [132] [131] is located in the stratosphere, optically thick, and composed of solid organic material [138] [75]. It is believed that the haze, composed of a several *H*, *C*, and *N* compounds, is produced from particle-induced and solar ultraviolet light dissociation of CH_4 and N_2 in Titan's atmosphere [171] [161]. Models indicate that Titan's atmosphere would be depleted of methane via photolysis on a timescale of 10 to 100 million years [171] (in comparison, the age of the solar system is estimated at 4.5 billion years). This indicates that either there is some replenishing interaction between the surface and the atmosphere [99] or that Titan's atmosphere does not contain large amounts of methane in a long-term steady-state [89].

In 1980 the possibility of methane oceans on Titan was hypothesized [70]. The theory of a global ocean was suggested [99], but was later proved to be inconsistent

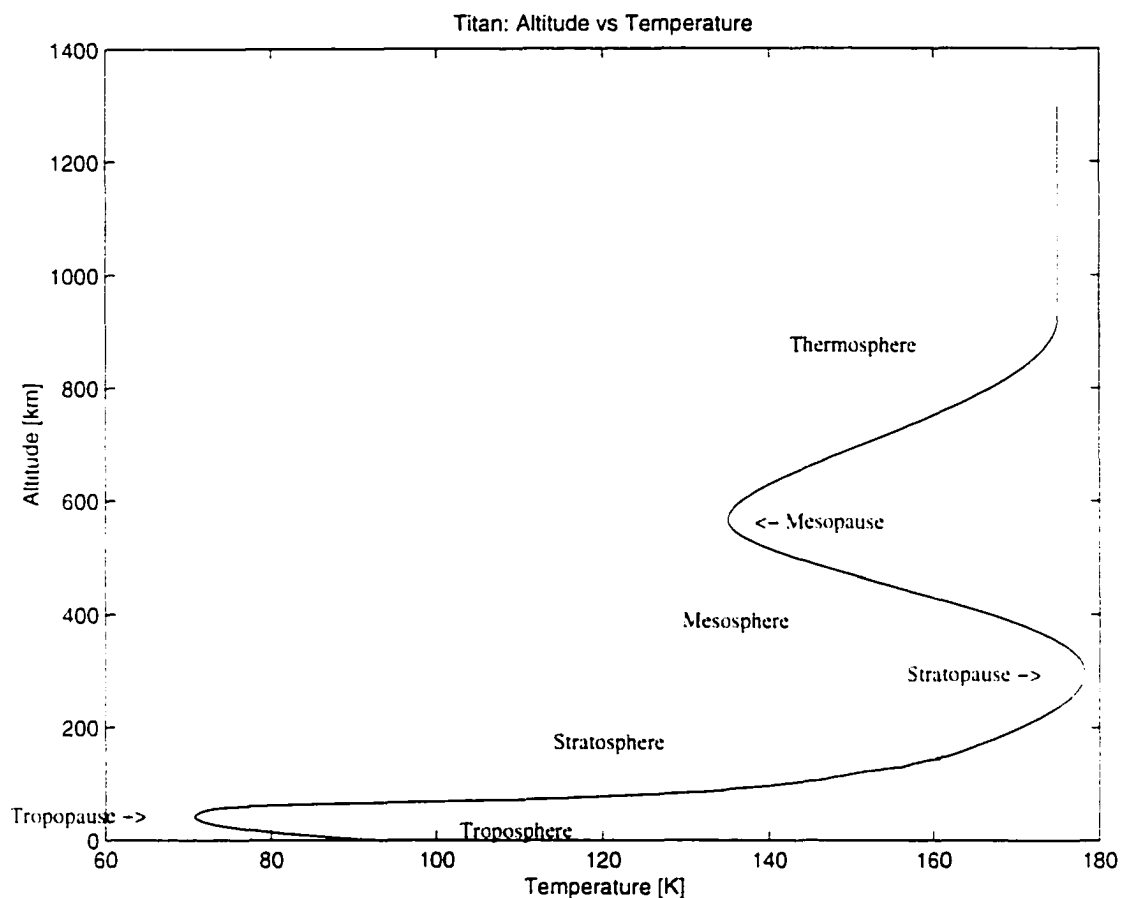


FIGURE 1.1. Altitude versus Temperature for Titan. Data from [85] [170]. Concept from [14].

with both theory and observation [145] [137]. Remote sensing data (for example, [117]) has not detected global oceans, but several times the atmospheric mass of Titan's methane could be present but out of sight in high-latitude crater lakes [88] or sub-surface reservoirs [154]. Observations in the radar [117] and near-infrared [83] [55] [84] part of the spectrum point to a heterogeneous surface. The first relative albedo maps were created using the Hubble Space Telescope's planetary camera, indicating the presence of a large bright area in Titan's surface (it had been anticipated that Titan's surface was completely coated with dark hydrocarbons) [146]. From observations of the geometric albedo over many years, Titan definitely seems to have seasons

[86] [67] [87]. Most recently, the detection of short-lived, sparse, daily clouds covering less than 1% of Titan's surface area has led to the suggestion that Titan's atmosphere is much like that of Earth's, "with clouds, rain, and an active weather cycle" [56].

The existence of a greenhouse effect on Titan was supported by many long before the Voyager observations [1] [116] [65] [136] [128]. Titan exhibits a greenhouse effect due to N_2 , CH_4 , and H_2 [139] [106] [107], and an antigreenhouse effect caused by the high-altitude organic haze layer discussed above [107]. We will discuss Titan's opacity further in section 1.5.3.

1.3 Comparisons

In Table 1.1 we list the physical quantities we use for our models. For modelling purposes, we list the properties for an "averaged" KBO, combining what little information is available over the various KBOs that have been observed. Note the similarities in size, mass, composition, and distance from the sun among Triton, Pluto, and KBOs. Also note that Titan, Triton, and Pluto all have N_2 dominant atmospheres, as does the Earth.

Reference [152], Table Ia contains some interesting surface composition comparisons between Pluto, Triton, and comets. Most notable: the strong presence of H_2O on comets and lack of same on Triton and Pluto; the presence of N_2 and CH_4 on Triton and Pluto and lack thereof on comets.

1.4 Previous Works in This Area

Our grey model is based on work developed to model past Triton atmospheres [119] [98]. We have expanded on this work by 1) using a variety of mean opacities; 2) developing new mathematical methods for evaluating the mean opacities; 3) using the real opacity instead of interpolated values to calculate the mean opacities; 4) adding radiogenic and accretional heat sources; 5) searching for more roots; 6) expanding

Quantity	Titan	Triton	Pluto	KBO	Units
radius	2.575×10^8 ²	1.352×10^8 ²	1.172×10^8 ⁷	1.2×10^7 ¹⁰	cm
semi-major axis of orbit	1.42×10^{14} ¹	4.503×10^{14} ¹	5.89×10^{14} ¹	5.98×10^{14} ¹⁰	cm
mass	1.345×10^{26} ²	2.147×10^{25} ²	1.27×10^{25} ⁸	7.24×10^{21} ⁵	g
surface temperature	95 ¹	38 ¹	40 ⁶	40 ¹¹	K
surface pressure	1.5×10^6 ¹	14 ¹	3 ¹	3 ¹¹	dyn/cm ²
mean molecular mass of atm.	4.648×10^{-23} ⁵	4.648×10^{-23} ⁵	4.648×10^{-23} ⁵	4.648×10^{-23} ⁵	g
gravitational accel.	135.0 ¹	78.0 ¹	66 ⁷	3 ⁵	cm/s ²
albedo	0.21 ²	0.85 ³	0.44-0.61 ⁷	0.04 ¹²	dimensionless
emissivity	≤ 1.0 ⁴	0.3-0.77, 0.4-0.85 ³	0.6 ⁶	0.6 ¹¹	dimensionless
sunlight redistribution factor	$> 4 \pi$ ⁴	2-4 ³	3 ¹³	3 ¹¹	dimensionless
solar flux received currently	1.516×10^4 ⁵	1.501×10^3 ⁵	8.812×10^2 ⁵	8.55×10^2 ⁵	dyn/cm s
solar flux received early in evolution	1.061×10^4 ⁵	1.051×10^3 ⁵	6.168×10^2 ⁵	5.98×10^2 ⁵	dyn/cm s
mixing ratio of N ₂	.90-.97 ¹	.99 ¹ .9975 ⁸	.90-.99 ¹ .98 ⁸	.98 ¹¹	dimensionless
mixing ratio of CH ₄	.02-.10 ¹	10 ⁻⁴ ¹ .0005 ⁸	10 ⁻⁴ ¹ .015 ⁸	.015 ¹¹	dimensionless
mixing ratio of H ₂	2 × 10 ⁻³ ¹	1	1	11	dimensionless

Table 1.1: Physical quantities used for our models.

¹J. Lunine, ERCA (1996)

²Horizons database, JPL (9/96)

³Lunine & Nolan (1992)

⁴Lunine pr. comm. (1997)

⁵calculation by author (1997)

⁶Stansberry, Pisano, Yelle. "The emissivity of volatile ices on Triton and Pluto (1996). Planetary Space Science, Vol 44, pp 945-955

⁷Tholen, D. J, and M. Buie. "Bulk Properties of Pluto and Charon," in **Pluto and Charon**, (eds. S. A. Stern and D. J. Tholen) University of Arizona Press (1997), pp. 193-219

⁸Cruikshank, D. P. *et al.* "The Surfaces of Pluto and Charon," in **Pluto and Charon**, (eds. S. A. Stern and D. J. Tholen) University of Arizona Press (1997), pp. 221-267

⁹Yelle, R. V. and J. Elliot. "Atmospheric Structure and Composition. Pluto and Charon," in **Pluto and Charon**, (eds. S. A. Stern and D. J. Tholen) University of Arizona Press (1997), pp. 347-390

¹⁰<http://www.ifa.hawaii.edu/faculty/jewitt/kb.html>

¹¹Taken to be the same as Pluto for modelling purposes

¹²Weissman, P. and H. Levinson. "The Population of the Trans Neptunian Region. The Pluto-Charon Environment," in **Pluto and Charon**, (eds. S. A. Stern and D. J. Tholen) University of Arizona Press (1997), pp. 559-601

¹³Taken to be the same as Triton for modelling purposes

the model to apply to Pluto and KBOs. As a result, we have obtained some new and interesting results.

In addition to the lightcurve models mentioned in section 1.1.1, others have modelled Triton's current atmosphere using Monin-Obukhov similarity theory [147] and conduction [76], to name a few. The papers described in section 1.1.2 model Pluto's *current* atmosphere, and use either inversion of the lightcurve or apply the heat equation (conduction) with a net radiative heating rate term.

The methods we utilize in our nongrey model to solve the radiative transfer equation and to solve for radiative and hydrostatic equilibrium have been used in modelling stellar atmospheres for some time (too many references to list here). Since the underlying physics is similar, we apply these methods for the first time to the nongrey modelling of Titan's atmosphere.

Several types of models for Titan have been developed over the years: based on Voyager radio occultation data [85], vertically homogeneous scattering radiative equilibrium [141], radiative-convective [106], spectrally-resolved radiative convective coupled atmosphere-ocean model [104], photochemical [171] [163], radiative-convective and radiative-saturated equilibrium [89], and greenhouse/antigreenhouse models [107] [105], to name a few.

Our model is an improvement over the McKay nongrey models (described in detail in [106]) in the following areas: we use more grid points to resolve the spatial and spectral regions (95 altitude layers as opposed to 30 in [106], 337 frequency grid points compared to 46 in [106]); we use the method of discrete ordinates as opposed to the two-stream approximation in [106] (which leads to better angular resolution); we put our model through rigorous testing procedures, and we include an initial damping phase to the iterations to avoid initial overcorrections and reduce overall runtime.

1.5 Energy Transport

The transport of energy, central to the study of atmospheres, is caused by a gradient in a temperature profile: heat is transferred from hotter regions to cooler regions. The three primary physical processes that transport energy are radiative transfer, conduction, and convection. There are no barriers that can completely contain photons: they travel from hotter to cooler regions of an atmosphere, impeded only by their interactions with the medium through which they are travelling [18]. This type of heat transport is called radiative transfer. Conduction occurs when the energy is carried by the particles themselves. Both radiative transfer and conduction are proportional to the temperature gradient, but in general radiative transfer is much more efficient than conduction in low density media [18]. There is, however, a limit to the rate of energy that can be transported via radiative transfer and conduction. If the temperature gradient becomes too large, an instability develops in the gas: bubbles of gas that are hotter than their surroundings rise until they re-equilibrate with a lower temperature environment [18].

In this study, we focus on radiative transfer as the primary mechanism of energy transport. Convection may play a role depending on the temperature gradient (see section 1.5.2).

1.5.1 Radiative Transfer

The equation of transfer, which describes the transfer of energy via radiation through a medium, is derived in detail in several references. In particular, in this section we will summarize the discussions presented in [15], [16], and [112].

We begin with the definition of specific intensity, I_ν . In the frequency range $(\nu, \nu + d\nu)$ the amount of radiant energy dE_ν moving across an element of area dS in the direction delineated by the solid angle $d\omega$ during time dt is defined to be

$$dE_\nu = I_\nu \cos(\theta) dS d\nu d\omega dt. \quad (1.1)$$

where θ is the angle the pencil of radiation makes with the outward normal to dS (see Figure 1.2). The units of I_ν are ergs/cm² sec Hz sr.

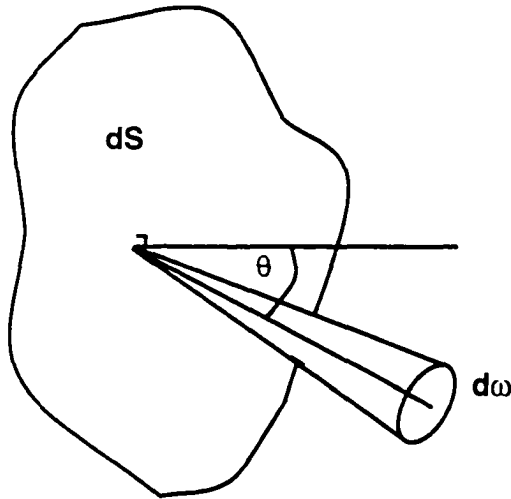


FIGURE 1.2. The physical picture. Redrawn and adapted from [15].

For a parallel plane atmosphere (in which all physical properties are constant over a plane)

$$I_\nu = I_\nu(\mathbf{r}, \theta, t).$$

The absorption of radiant energy by matter is described by the opacity, χ_ν , also called the extinction coefficient or total absorption coefficient. The opacity is defined so that a cross-section of material dS with length ds absorbs from a pencil of radiation with specific intensity $I_\nu(\mathbf{r}, \theta, t)$ travelling within the solid angle $d\omega$ and normal incidence to dS (i.e., $\theta = 0$) within the frequency range $(\nu, \nu + d\nu)$ and time dt , the following amount of energy:

$$\delta E = \chi_\nu(\mathbf{r}, t) I_\nu(\mathbf{r}, t) \rho dS ds d\nu d\omega dt, \quad (1.2)$$

where ρ , the density of the medium, is represented as dimensionless using "ama-gat" units (see section 1.5.3 for a detailed explanation). Thus the opacity has units 1/cm.

In general $\chi_\nu = \kappa_\nu + \sigma_\nu$, where κ_ν represents the "true absorption" contribution and σ_ν represents the scattering contribution to the total absorption. Examples of the scattering processes include Thomson scattering and Rayleigh scattering; examples of absorption processes include photoionization and photoexcitation [112].

The emission of radiation from matter can be described by the emission coefficient, j_ν , also known as the emissivity. We define the amount of energy released into a solid angle $d\omega$ from a cross-section of material dS that is ds in length, in the frequency range $d\nu$ and time dt , as

$$\delta E = j_\nu(\mathbf{r}, t) \rho dS ds d\nu d\omega dt. \quad (1.3)$$

The emission coefficient has units ergs/cm³ sec Hz sr.

Thus it is clear that an equation quantifying the changes in energy in a radiation field due to its interaction with matter will involve χ_ν and j_ν . In fact, the energy differences (and hence energy flow) result from the surplus of emission over absorption.

In particular, consider a cylindrical element of material with cross-section dS and length ds , where the specific intensity on the incident face is I_ν and the specific intensity leaving the second face is given by $I_\nu + dI_\nu$ (see Figure 1.3).

From equation 1.1 we see that the change in radiant energy crossing the faces with normal incidence (i.e., $\theta = 0$) in a time dt , in the frequency range $(\nu, \nu + d\nu)$, and solid angle $d\omega$, is given by

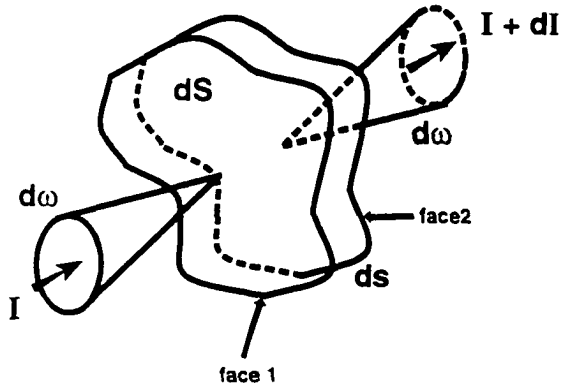


FIGURE 1.3. The transfer of energy via absorption and emission. Redrawn and adapted from [112].

$$\frac{dI_\nu}{ds} dS ds d\nu d\omega dt.$$

The amount of energy absorbed (equation 1.2) is given by

$$\chi_\nu I_\nu \rho dS ds d\nu d\omega dt$$

and the amount of energy emitted (equation 1.3) is given by

$$j_\nu \rho dS ds d\nu d\omega dt.$$

Combining the above three relations and integrating over S , ω , and t , we arrive at

$$\frac{dI_\nu}{ds} = -\chi_\nu \rho I_\nu + j_\nu \rho.$$

or rewritten in a more useful form,

$$-\frac{1}{\chi_\nu \rho} \frac{dI_\nu}{ds} = I_\nu - \frac{j_\nu}{\chi_\nu}. \quad (1.4)$$

The source function is defined to be $S_\nu \equiv j_\nu/\chi_\nu$, and the optical depth τ_ν is defined by the relation $d\tau_\nu = -\chi_\nu\rho ds$. Combining these two definitions with equation 1.4, we arrive at the “standard” form of the equation of transfer:

$$\frac{dI_\nu}{d\tau_\nu} = I_\nu - S_\nu. \quad (1.5)$$

The quantity τ_ν , known as the optical depth or optical thickness, is defined as

$$\tau_\nu(z) = \int_z^{z_{max}} \chi_\nu(z') dz'. \quad (1.6)$$

and physically is the number of photon mean-free paths at frequency ν along the path $z_{max} \rightarrow z$ [112]. Thus if a material is very opaque, or optically thick, it has several photon mean-free paths per unit length, i.e., τ_ν is large. An atmosphere that is optically thin has a small optical depth.

The moments of the radiation field:

$$J_\nu(\tau_\nu) = \int_{-1}^1 I_\nu(\tau_\nu, \mu) d\mu \quad (1.7)$$

$$H_\nu(\tau_\nu) = \int_{-1}^1 \mu I_\nu(\tau_\nu, \mu) d\mu \quad (1.8)$$

$$K_\nu(\tau_\nu) = \int_{-1}^1 \mu^2 I_\nu(\tau_\nu, \mu) d\mu \quad (1.9)$$

where $\mu = \cos(\theta)$. J_ν is the mean intensity of the radiation field. H_ν is the Eddington flux ($= \frac{\mathcal{F}}{4\pi} = \frac{F}{4}$: $\mathcal{F} \equiv$ the flux, $F \equiv$ astrophysical flux) [112].

1.5.2 Convection

In 1906, Karl Schwarzschild showed that in an astrophysical context, unstable motion occurs in a gas if the temperature gradient is too steep: this instability is known as convection [18].

The following characterization of convection is derived from [14] and [81]. The first law of thermodynamics states that for a gas element moving adiabatically in the model atmosphere.

$$C_V dT = -PdV.$$

where C_V is the specific heat constant at constant volume and V is the specific volume (volume of one gram of molecules).

Assuming the ideal gas law $PV = NkT$, via differentiation we obtain

$$dV = \frac{Nk}{P} dT - \frac{NkT}{P^2} dP.$$

Combining this with the first law of thermodynamics, we get the relation

$$C_V dT = -Nk dT + \frac{NkT}{P} dP.$$

Recall that the specific heat constant at constant pressure is given by $C_P = C_V + k/\bar{m}_A$, so we have

$$C_P dT = \frac{NkT}{P} dP = V dP = \frac{1}{\rho} dP.$$

Incorporating the hydrostatic equilibrium condition $dP/dz = -\rho g$, we arrive at

$$\frac{dT}{dz} = -\frac{g}{C_p}. \quad (1.10)$$

This relationship is called the dry adiabatic temperature gradient. If the temperature gradient of the atmosphere is greater than the dry adiabatic temperature gradient given above, i.e.,

$$\left| \left(\frac{dT}{dz} \right) \right|_{atm} > \left| \left(\frac{dT}{dz} \right) \right|_{adiab}. \quad (1.11)$$

then convection occurs [18] [98]. In principle this relationship allows us to construct a temperature profile with respect to altitude.

1.5.3 Opacity

TYPES OF OPACITY There is an excellent exposition on scattering and true absorption in [112]. Their discussion has been distilled in the next paragraph.

Absorption occurs when a photon's energy is partially or completely converted into the thermal energy of the medium it is travelling through: the photon is destroyed in the process. Scattering occurs when a photon, after interacting with a scattering center, departs in a different direction with a new energy state. Absorption is closely coupled to the local thermodynamic properties (such as temperature) of the medium because absorption processes directly contribute photon energy into the thermal kinetic energy of the gas. Scattering relies primarily on the radiation field and is weakly related to the local thermodynamic properties of the medium. Thermal absorption/emission tends to lead to local equilibrium between the radiation and the medium. Scattering, on the other hand, allows photons from one region of the atmosphere to travel to another region without directly affecting local thermodynamic properties.

We will denote the opacity in units of $1/\text{cm}$ with the symbol χ_ν , and in units of cm^2/g with κ_ν .

OPACITY SOURCE FOR OUR PROBLEM For our atmospheric models, we will assume that the opacity is from true absorption only (i.e., no scattering) since we are concerned with establishing local thermodynamic equilibrium. That is, $\chi_\nu \equiv \kappa_\nu$. We will also assume that our true absorption opacity source is produced by binary collisions between molecules (see [20] [21] for a detailed discussion).

In practice, the opacity represents complex interactions and is very difficult to calculate. To overcome this difficulty, we compute χ_ν from data generated by a FORTRAN computer program generously provided by R. Courtin (streamlined and rewritten in ANSI C by the author).

We denote χ_ν as the opacity as a function of frequency (units: 1/cm), and κ_{ctn} denote the opacity as calculated from Courtin's code. His code provides (κ_{XY}) , the absorption coefficients resulting from binary collisions between molecules X and Y at a particular temperature. We then combine with molar fractions f_X, f_Y to compute κ_{ctn} :

$$\kappa_{ctn} = \kappa_{CH_4CH_4} f_{CH_4}^2 + \kappa_{CH_4N_2} f_{CH_4} f_{N_2} + \kappa_{N_2N_2} f_{N_2}^2 + \kappa_{H_2N_2} f_{H_2} f_{N_2}.$$

Note κ_{ctn} has units of 1/(cm am²). An amagat is a dimensionless measure of density in terms of conditions at standard temperature and pressure ($\frac{\rho}{\rho_{STP}}$) [53]. The program uses these units since the absorption is proportional to the square density [22]). We must calculate the opacity χ_ν using the dimensionless amagat = ρ/ρ_{std} (where $\rho_{std} = m_A * n_L$), where n_L = Loschmidt's number = a reference particle density at Earth STP [64] [53]. Thus χ_ν is defined by

$$\begin{aligned} \chi_\nu &= \kappa_{ctn} \left(\frac{\rho}{\rho_{std}} \right)^2 \\ &\sim \frac{1}{(\text{cm am}^2)} \text{am}^2 = \frac{1}{\text{cm}} \end{aligned}$$

The mixing ratios (percentages by mass: $F_{HYD}, F_{MET}, F_{NIT}$) are more readily available in the literature than the mole fractions ($f_{CH_4}, f_{H_2}, f_{N_2}$). We calculate the mole fractions from the mixing ratios in the following manner:

1. determine the molecular weights for N_2, H_2, CH_4 : $MW_{N_2} = 28$ g/mol.
 $MW_{H_2} = 2$ g/mol. $MW_{CH_4} = 16$ g/mol
2. determine the total number of moles

$$tot = \frac{F_{HYD}}{MW_{H_2}} + \frac{F_{MET}}{MW_{CH_4}} + \frac{F_{NIT}}{MW_{N_2}}$$

3. calculate mole fractions

$$f_{CH_4} = \frac{FMET/MWCH4}{tot}$$

$$f_{H_2} = \frac{FHYD/MWH2}{tot}$$

$$f_{N_2} = \frac{FNIT/MWN2}{tot}$$

We take into account the opacity due to the presence of N_2 , CH_4 , and H_2 for Titan, Triton, Pluto, and KBOs. We note that CO has also been detected on Titan, Triton, Pluto. Since CO and N_2 are very similar from a molecular physics/chemistry viewpoint [98], and to our knowledge the contribution of CO to opacity at the temperatures we are investigating has not been well-studied [22], we assume that CO and N_2 are physically interchangeable [98].

Figure 1.4 is a sample infrared opacity calculated with data from Courtin's code at a temperature of $95K$, with $FHYD = 0.002$, $FMET = 0.1$, and $FNIT = 0.898$ (parameters at Titan's surface).

The contributions to opacity are in the frequency range $10^{10} - 10^{13}$ Hz, which is in the infrared part of the electromagnetic spectrum. Note the "window" effect (the low opacity dip seen Figure 1.4) caused by the presence of H_2 (the collision-induced opacity from $N_2 - H_2$ [141]; this is an important contributor to the greenhouse effect [89]). The spectral location of this window contains a noticeably large amount of radiation and thus contributes significantly to Titan's greenhouse effect [106]. Triton and Pluto have similar atmospheric compositions, and thus with molecular hydrogen most likely present in their past atmospheres the greenhouse effect possibly influenced their early atmospheres as well.

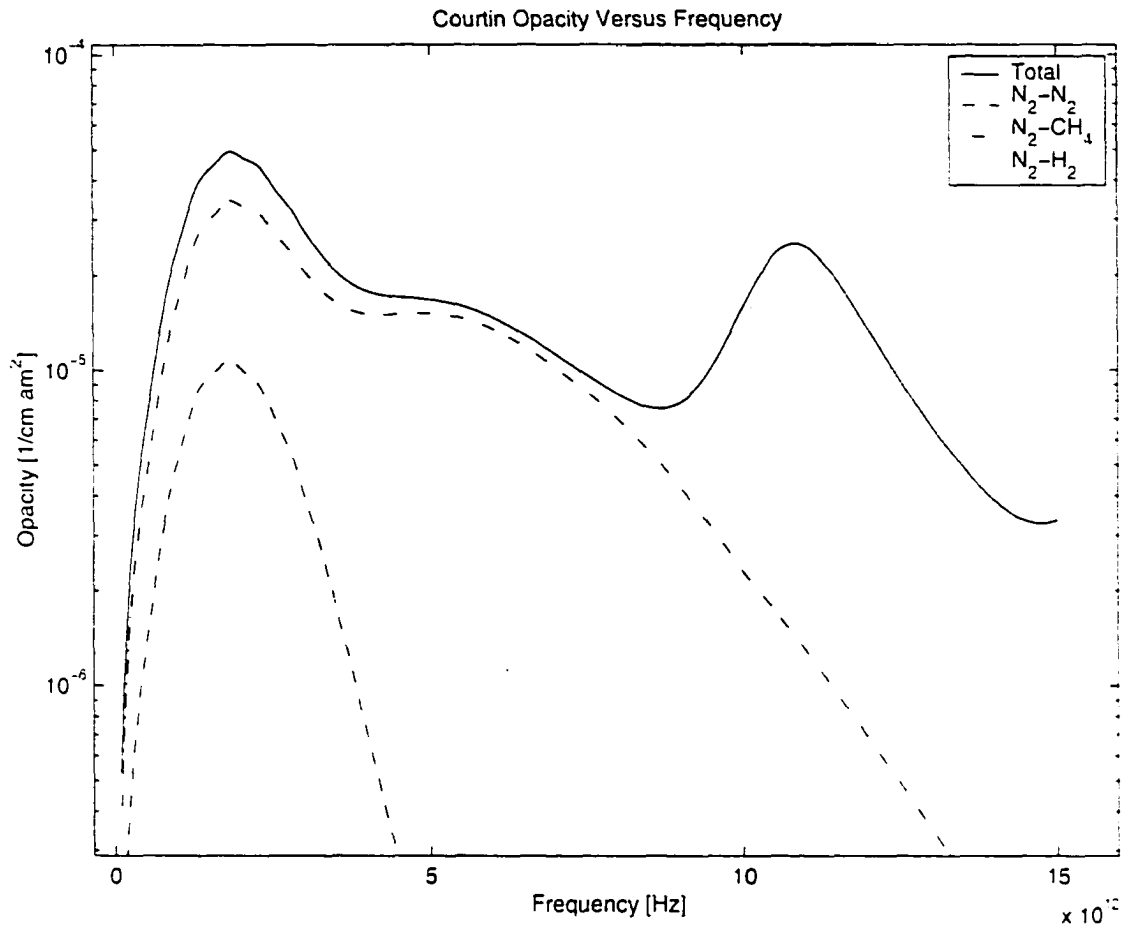


FIGURE 1.4. Opacity [1/cm am²] versus Frequency [Hz]. Redrawn and adapted from [106].

1.5.4 Greenhouse and Antigreenhouse Effects

The greenhouse effect occurs in planetary atmospheres when atmospheric gases are transparent to the visible portion of the electromagnetic radiation spectrum, hence allowing solar radiation to pass through to the planet surface, but are opaque to thermal infrared radiation and thus trap the infrared radiation emitted by the planet [107]. In such a situation, visible solar radiation from the Sun passes through the atmosphere and is absorbed by the planet and then reradiated in the thermal infrared part of the spectrum. An atmosphere under the greenhouse effect has a

surface temperature greater than the effective temperature (temperature if $\tau = 0$) [53]. The antigreenhouse effect, on the other hand, is exactly the reverse situation. It results from a high-altitude atmospheric layer that is strongly absorbing in the visible part of the spectrum but weakly absorbing in the infrared, and thus cools the planet [107].

1.5.5 “Grey” Approximation

A grey atmosphere model is one in which the opacity is independent of frequency. Typically one uses the grey approximation to simplify an atmosphere model by replacing the full, frequency-dependent opacity by some averaged value, a “mean” opacity. There are three standard types of mean opacity: Rosseland, Planck, and Chandrasekhar (Flux). Each one conserves a different physical quantity. The Rosseland mean is a harmonic mean and yields the correct total transport of radiant energy [113]. It is appropriate for large optical thicknesses ($\tau \gg 1$), gives the greatest weighting to the most transparent regions of the spectrum (i.e., smaller absorption coefficients), and thus is a conservative estimate for the total mass absorption coefficient [119]. The Chandrasekhar mean yields the correct radiation force on a material [113]. It has been suggested that for planetary atmospheres the Chandrasekhar mean works better than the Rosseland mean because in the LTE approximation, T and $B_\nu(T)$ vary with depth, and κ_x cannot be treated as constant with respect to depth [14]. The Planck mean opacity is a geometric mean of the mass absorption coefficient weighted by the Planck function [119], is good for optically thin material ($\tau \ll 1$), and yields the correct total emission [113].

The state of the atmosphere is very sensitive to opacity, and hence to the type of mean opacity and how accurately it is calculated. Often a grey model is a poor approximation, but serves to quantify the limiting cases of either a fully transparent (Planck mean opacity) or opaque (Rosseland mean opacity) atmosphere [53].

If in addition to the grey approximation one assumes LTE and radiative equilibrium, then the temperature profile can be written as [15]

$$T^4 = \frac{3}{4}T_e^4(\tau + q(\tau)) \quad (1.12)$$

where $q(\tau)$ is the Hopf function and the effective temperature is calculated from the relation $\sigma T_e^4 = \pi F$. For $\tau \gg 1$ (optically thick), the Eddington approximation states that $q(\tau) \equiv \frac{2}{3}$ [112].

Note that since the relation $T(\tau)$ is known for a grey atmosphere in LTE, the radiative transfer equation can be solved analytically in this case. For a nongrey atmosphere this is not necessarily true.

1.6 Equilibrium Conditions Used in Atmosphere Modelling

1.6.1 Hydrostatic Equilibrium

In general, hydrostatic equilibrium is the balance between gravity and atmospheric gas pressure and radiation pressure, but for these atmospheres we can neglect the latter and write:

$$\frac{dP_{tot}}{dz} = -\rho g \quad (1.13)$$

where $P_{tot} = P_{gas} + P_{radiation}$, z = altitude, ρ = density, and g is gravitational acceleration.

To quantify the assumption of hydrostatic equilibrium, calculate $\lambda = r/H$ where r is the radius of the object, $H = kT/\bar{m}_A g$ is the pressure scale height: if $\lambda \ll 1$ then the atmosphere is not tightly bound and hydrostatic equilibrium is not a reasonable assumption [95].

1.6.2 Local Thermodynamic Equilibrium

In general, the source function for true absorption (with no scattering) is given by $S_\nu = j_\nu/\kappa_\nu$. If we assume thermal equilibrium (TE), then the source function depends only on temperature, frequency, and the speed of light [53]. The intensity of the radiation field at temperature T is then given by the Planck function, i.e., $J_\nu = \kappa_\nu B_\nu(T)$. This condition holds for LTE also, since LTE means that all the local thermodynamic properties of the material are the same as their TE values throughout the atmosphere [112]. Thus assuming LTE, the source function is given by

$$S_\nu = \frac{j_\nu}{\kappa_\nu} = B_\nu(T) = \frac{2h\nu^3}{c^2} \frac{1}{e^{\frac{h\nu}{kT}} - 1}. \quad (1.14)$$

1.6.3 Radiative Equilibrium

We have a static medium in steady state (i.e., independent of time and no hydrodynamic movement), for which the only mode of energy transport is radiative transfer: the material must emit exactly as much energy as it absorbs [113]:

$$\int_0^\infty \kappa_\nu [S_\nu - J_\nu] d\nu = 0. \quad (1.15)$$

Another way of expressing radiative equilibrium is that since the medium must emit exactly as much energy as it absorbs,

$$\nabla \cdot \mathcal{F} = 0 \quad (1.16)$$

where \mathcal{F} is the flux, related to the astrophysical flux F by $\mathcal{F} = \pi F$ [112]. For a planar parallel atmosphere, this translates to $\frac{dF_z}{dz} = 0$, that is, F_z is constant with altitude, and the net flux out of the atmosphere must equal the net flux into the atmosphere.

As a photon travels from the planet surface to the top of the atmosphere, it loses energy to the atmosphere due to the opacity of the atmosphere and has thus its frequency becomes lower and lower as it reaches the top of the atmosphere. Thus a graph of of the flux as a function of frequency and altitude should show a gradual red-shifting of the flux as one moves from the bottom of the atmosphere to the top.

CHAPTER 2

GREY ATMOSPHERES

As far as the laws of mathematics refer to reality, they are not certain; and as far as they are certain, they do not refer to reality. — Albert Einstein

2.1 The Model

Our grey atmosphere model, based on models developed in [119] and [98], varies the following physical parameters:

- heat flux (heating comes from different sources) (Φ)
- fraction of total vapor (by mass) that is H_2 ($FHYD$)
- type of mean opacity ($\kappa_R, \kappa_c, \kappa_p$)

We wish to calculate values for the following physical variables (which indicate to us the state of the atmosphere):

- surface temperature T
- surface pressure P
- optical depth τ
- mean opacity κ_x
- volatile concentrations (N_2, CH_4, H_2)

We construct a set of 4 equations that relate the 4 unknowns (T, P, τ, κ_x) and involve our system parameters, based on the physics we believe is taking place.

2.1.1 Simplifying Assumptions

We use utilize some physical assumptions to 1) account for the we believe are present. 2) simplify the model to make it more tractable. They are all listed below with the corresponding section containing the explanation for their use.

Planar symmetry [Equation 1]: the thickness of our atmosphere is much smaller than the radius of our object, and thus we can approximate it as a series of planes.

Vapor pressure equilibrium [Solving the System]: the vapor and solid forms of a material are in equilibrium with each other.

Ideal gas law [Equation 1, Convection]: $PV = NkT$, where P = pressure, V = volume, N = number of molecules, k = Boltzmann's constant, T = temperature.

Hydrostatic equilibrium [Equation 1, Convection]: see definition in section 1.6.1.

Radiative equilibrium [Equation 2]: see definition in section 1.6.3.

Grey atmosphere [Equations 1, 2, and 4]: see definition in section 1.5.5.

Eddington Approximation [Equation 2]: see definition in section 1.5.5.

Local Thermodynamic Equilibrium/No Scattering [Equation 4]: see definition in section 1.6.2.

2.1.2 Derivation

EQUATION ONE: RELATING τ , P , T , AND κ_τ The optical depth, τ_ν , is defined as

$$\tau_\nu = \int_0^\infty \kappa_\nu \rho dz. \quad (2.1)$$

where κ_ν is the absorption coefficient, ρ is the density (we assume it is constant), and z is the altitude.

For pressure-induced/collision-induced opacity, one can approximate κ_ν [21] with

$$\kappa_\nu \approx \kappa_x \frac{\rho}{D}.$$

where κ_x is some type of mean opacity (Rosseland, Chandrasekhar, or Planck, to be defined in section 2.1.2), and D is as defined in section 1.5.3.

Hence we can express $\tau_\nu = \tau$ as

$$\tau = \frac{\kappa_x}{D} \int_0^\infty \rho^2 dz.$$

Assuming hydrostatic equilibrium,

$$\frac{dP}{dz} = -\rho g \implies dz = -\frac{1}{\rho g} dP.$$

where P is pressure and g is gravitational acceleration. Assuming g is independent of P (valid for a thin atmosphere), we can now write the optical depth as

$$\tau = -\frac{\kappa_x}{gD} \int_0^\infty \rho dP.$$

If we assume that the ideal gas law hold, then it follows that

$$\frac{PV}{kT} = N = \frac{M_{tot}}{\bar{m}_A},$$

where M_{tot} is the total mass of the atmosphere. So we can rewrite ρ as

$$\rho = \frac{M_{tot}}{V} = \frac{P\bar{m}_A}{kT}.$$

Substituting the above expression into the equation for τ and assuming T and \bar{m}_A are independent of P (this is not strictly true, but the dependence is weak [95]), we arrive at

$$\begin{aligned}
\tau &= -\frac{\kappa_x}{gD} \int_0^\infty \frac{P\bar{m}_A}{kT} dP \\
&= -\frac{\kappa_x\bar{m}_A}{kTgD} \int_0^\infty P dP \\
&= \frac{\kappa_x\bar{m}_A}{2kTgD} [P^2(z=0) - P^2(z=\infty)].
\end{aligned}$$

But $P(z=\infty) = 0$, and $P(z=0) = P_T =$ surface pressure, so we are left with

$$\tau = \frac{\kappa_x\bar{m}_A}{2kTgD} P_T^2 = \frac{\kappa_x P_T^2}{2kTgn_L}. \quad (2.2)$$

EQUATION TWO: RELATING τ AND T Recall from section 1.5.5 temperature structure for a grey atmosphere in the Eddington approximation is given by [113]

$$T^4 = T_e^4 \left[\frac{1}{2} + \frac{3}{4}\tau \right]. \quad (2.3)$$

where $T =$ surface temperature and $T_e =$ effective temperature = the temperature the atmosphere would radiate at if it were a perfect blackbody (a convenient mathematical definition).

Assuming radiative equilibrium, the effective temperature can be calculated using the Stefan-Boltzmann relation

$$\Phi_T = \varepsilon\sigma T_e^4.$$

where Φ_T is the total heat flux, ε is the emissivity, and σ is the Stefan-Boltzmann constant. The total heat flux is the sum of the heat fluxes (Φ_i) of the contributing heat sources. The individual heat fluxes are derived from the physical processes that heat the atmosphere via radiative transfer. We take into account the following types of heating: solar (Φ_s), tidal (Φ_t), accretional (Φ_a), and radiogenic (Φ_r).

Solar Heating The flux due to solar heating is given by [98]

$$\Phi_s = \frac{S(1 - A)}{\varepsilon f},$$

where S is the solar flux bombarding the surface, A is the albedo, f accounts for the redistribution of sunlight during reradiation, ε is the emissivity of the absorbing surface and atmosphere, and σ is the Stefan-Boltzmann constant [98]. Triton, Pluto, and Kuiper belt objects are all affected by solar heating.

Tidal Heating In the time frame we are modelling (early in the Solar System's history) Triton is undergoing tidal evolution: tidal heating is in effect as Triton's orbit about Neptune circularizes from its originally eccentric orbit [109]. We will use Triton's tidal heat flux $\Phi_t \equiv F_{tide}$ as a parameter for our system. Kuiper belt objects, however, experience no tidal heating.

Pluto may or may not be experiencing tidal heating in the time frame we are modelling ($\sim 10^8$ years after its formation: estimates for the end of Pluto's accretional phase range from $10^7 - 10^9$ [152]). For completeness we will investigate both possibilities.

The following derivations/equations are very approximate and attempt to obtain the order of magnitude of tidal heating only.

The tidal heating flux for Pluto is given by

$$\Phi_t = \frac{\Delta E}{2S_P \Delta t}, \quad (2.4)$$

where ΔE is the change in orbital energy due to tidal heating, Δt is the time over which this change occurs, and S_P is the surface area of Pluto. We multiply by a factor of $\frac{1}{2}$ to account for equally partitioning the tidal energy between Pluto and Charon.

The orbital energy of Charon in an elliptic orbit about Pluto is given by

$$E = -\frac{Gm_P m_C}{2a},$$

where a is the semi-major axis of Charon's orbit about Pluto and m_P and m_C are the masses of Pluto and Charon, respectively.

Thus the change in orbital energy as the Pluto-Charon system tidally evolves is given by

$$E = \frac{Gm_P m_C}{2} \left(\frac{1}{a_i} - \frac{1}{a_f} \right),$$

where a_i is the initial semi-major axis of Charon's orbit, and a_f is the final axis value. The unknown in the above relationship is a_i . The formula for a_i is given by $a_i = \sqrt{b_i^2 / (1 - e_i)}$, where b_i is the initial semi-minor axis and e_i is the initial eccentricity of Charon's orbit about Pluto. To estimate a_i we make the following assumptions:

- the initial eccentricity of Charon's orbit is 0.9 (highly elliptic - a worse-case scenario)
- the current semi-minor axis has remained relatively unchanged during tidal evolution (since the resulting orbit is virtually circular, we assume that most of the change has occurred in the semi-major axis direction).

Using these assumptions, we can calculate a_i and thus ΔE .

To calculate Δt , we use the average characteristic time for decay $\tau_t = 4.30 \times 10^4 Q$ years [32], where $1/Q$ is the dissipation function ($Q \sim 100$ for Pluto [108]). The characteristic time for decay satisfies the following relation:

$$e(t) = e_i \exp\left(-\frac{t}{\tau_t}\right).$$

To calculate the time it takes for Charon's orbit to tidally evolve from e_i to e_f , we solve the above expression for time:

$$\Delta t = \tau_t \ln \left(\frac{e_f}{e_i} \right).$$

The surface area for Pluto is $S_P = 4\pi R_P^2$ where R_P is the radius of Pluto.

Putting it all together, equation 2.4 becomes

$$\Phi_t = \frac{Gm_P m_C \left(\frac{1}{\sqrt{b_i^2/(1-e_i)}} - \frac{1}{a_f} \right)}{16\pi R_P^2 \tau_t \ln \left(\frac{e_f}{e_i} \right)}. \quad (2.5)$$

Since there are many details of tidal heating associated with orbital decay that remain unknown to us, we make the following assumptions about tidal heating in general: it is removed uniformly over the surface from the interior of the object; it occurs in a narrow region of the interior near the surface, and the effective temperature at the surface is a uniform and instantaneous function of the tidal heating rate (i.e., we assume that the surface and interior are in thermal equilibrium) [98].

Accretional Heating Pluto and Kuiper belt objects experience accretion (the process by which an astrophysical body increases in mass by the gravitational attraction of matter) in the time frame we are modelling. For Triton, the accretion contribution turns out to be negligible compared to solar and tidal heating fluxes and thus is not considered further here.

Denote the radius at time $t_0 = 0$ (e.g., about 4500 Myr ago for Pluto) by R_0 and the radius at some later time t_f by R_f . The gravitational energy at time t_0 is given by

$$E_0 = \frac{G(M_C)^2}{R_0}.$$

If we assume that the density remains constant during the accretion process, we can rewrite the above equation as

$$E_0 = G \left(\frac{4}{3} \pi \rho \right)^2 R_0^5.$$

Then the increase in energy due to accretional impacts at time t_f is given by

$$E = G \left(\frac{4}{3} \pi \rho \right)^2 (R_f^5 - R_0^5).$$

The amount of heat actually *absorbed* by the planet is given by hE , where h is the fraction of heat retained by the planet after the impact of the smaller bodies (taken to be about 0.5 for objects greater than 10 km in radius) [110].

The energy absorbed per unit area is then given by

$$E_{acc} = \frac{hE}{4\pi R_f} = \frac{4}{9} \pi h G \rho^2 \left(R_f^3 - \frac{R_0^5}{R_f^2} \right).$$

To calculate the energy flux, we need to know at what rate the accretional energy per area is dissipated as a function of time. We generate a dissipation function $F_{acc}(t)$ (based on exponential decay: see Figure 2.1) such that at time t_f , 0.1% of the maximum energy is left.

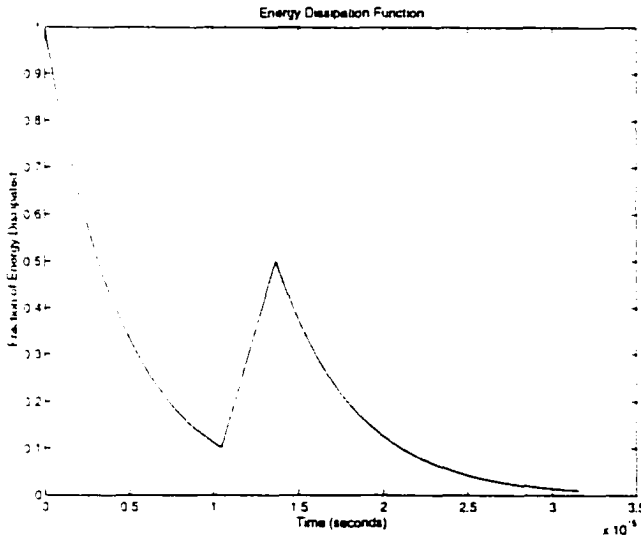


FIGURE 2.1. Energy dissipation as a function of time.

We assume that the accretion time is short compared to the time it takes for heat to leak out of the object. Thus at time t_0 we presume that accretion has ended and we begin the onset of accretional energy dissipation. For a homogeneous rock/ice object, there is a point in its thermal evolution at which mass differentiation occurs (i.e., ice melts and the rock sinks towards the center of the object) [95]. This process adds additional heat, as represented by the second peak, and we continue energy dissipation from that point.

Our accretional energy flux is thus given by

$$\Phi_a = E_{acc} \times F_{acc}(t).$$

Radiogenic Heating Pluto and Kuiper belt objects experience radiogenic heating in the time frame we are modelling. The heating arises from the radioactive decay of U, Th, and ^{40}K [108]. For Triton, we assume the radiogenic contribution is negligible compared to solar and tidal heating fluxes (as with the accretion contribution).

We can estimate the maximum amount of flux arising from radiogenic heating by knowing $H(0)$ = the rate of radiogenic heating per unit volume at time t_0 (e.g., 1.7×10^{-6} dyn/cm² for Pluto [108]) and f_R = the rock volume fraction (the fraction of the object's volume that generates radiogenic heating) (e.g., ≈ 0.4 for Pluto [108]). In theory, radiogenic flux = energy/(time*area) = [rock volume fraction] * [maximum radiogenic heating/ (volume*time)] * [volume of object] / [surface area of object] [95].

Thus at some time t_f we have

$$\begin{aligned} \Phi_r &= \frac{f_R H(0) (\frac{4}{3} \pi R_p^3)}{4 \pi R_f^2} \\ &= \frac{1}{3} f_R H(0) R_f. \end{aligned}$$

EQUATION THREE: RELATING P AND T For the empirical definitions of the vapor pressures, we follow the prescription provided in [98].

For H_2 : $P_{H_2} = 1$ mbar to 4.4 mbar; H_2 is above its critical point for all cases considered here.

For N_2 ,

$$P_{N_2} = \begin{cases} e^{(-791.8/T+10.475)} & T < 63 \text{ K} \\ 10^{(-339.8/T+4.836-0.0056286 T)} & T \geq 63 \text{ K} \end{cases}$$

We impose the additional assumptions:

- the relative humidity of N_2 is 50%
- if $P_{N_2} > 34$ bars (the critical point for nitrogen) then $P_{N_2} = 34$ bars.

For CH_4

$$P_{CH_4} = \begin{cases} 10^{(-532.2/(T+1.842)+4.820)} & T < 91 \text{ K} \\ e^{(-1023.1/T+9.135)} & T \geq 91 \text{ K} \end{cases}$$

Again, we impose the additional assumptions that:

- the relative humidity of CH_4 is 50%
- if $P_{CH_4} > 45$ bars (the critical point for methane) then $P_{CH_4} = 45$ bars.

A relative humidity of 50% for our primary volatiles is a standard assumption [53] which is conservative and allows for: 1) incomplete liquid or frost coverage on the surface; 2) a discontinuity in temperature at the surface [98].

The H_2 partial pressure is $P_{H_2} = FH_2 * (P_{CH_4} + P_{N_2})$ where $FHYD$ is fixed.

The total pressure is simply the sum of the partial pressures

$$P_v(T) = P_{N_2} + P_{CH_4} + P_{H_2}. \quad (2.6)$$

EQUATION FOUR: RELATING κ_x AND T There are three types of mean opacity that are discussed in the grey atmosphere modelling literature (such as [112], [113], and [14]): Rosseland, Chandrasekhar, and Planck. By using a mean opacity we lose some information about the total mass absorption coefficient, but each type of mean opacity attempts to conserve some physical property of the system. We choose to utilize all three types of mean opacities since our model atmospheres are neither exclusively optically thick or thin, and therefore correspond to no one type of mean opacity.

In general, we denote

$$\kappa_x = \kappa_x(\kappa_\nu, T), \quad (2.7)$$

where κ_ν is calculated as described in section 1.5.3.

We now describe the different mean opacities ($\kappa_R, \kappa_c, \kappa_p$) and the methods we have developed to calculate them.

The Rosseland Mean Opacity The formula for the Rosseland mean opacity is

$$\kappa_R = \left[\frac{\pi h^2}{2kT^5 \sigma c^2} \int_0^\infty \frac{\nu^4 e^{\frac{h\nu}{kT}}}{\left(e^{\frac{h\nu}{kT}} - 1\right)^2 \kappa_\nu} d\nu \right]^{-1}.$$

With a little mathematical manipulation we can rewrite the above expression for κ_R as

$$\kappa_R = \left[B \int_0^\infty \frac{\nu^4}{\kappa_\nu \sinh^2(a\nu)} d\nu \right]^{-1}, \quad (2.8)$$

where $B = \frac{\pi h^2}{8kT^5 \sigma c^2}$ and $a = \frac{h}{2kT}$.

Using Courtin's code to provide us with values for κ_ν , we use three different methods to comparatively evaluate equation (2.8):

1. assume κ_ν is some constant value (say, the arithmetic average) over the entire frequency domain
2. numerical integration (using Simpson's 3/8 Rule)

Method 1 If we assume that we can substitute κ_ν by its average value $\bar{\kappa}_\nu$ then we can rewrite equation (2.8) κ_R as

$$\kappa_R = \left[\frac{B}{\bar{\kappa}_\nu} \int_0^\infty \frac{\nu^4}{\sinh^2(a\nu)} d\nu \right]^{-1}.$$

From [54] we find that the above definite integral has the analytic solution:

$$\int_0^\infty \frac{x^4}{\sinh^2(ax)} dx = \frac{\pi^4}{30a^5}.$$

So κ_R becomes

$$\begin{aligned} \kappa_R &= \left[\frac{B}{\bar{\kappa}_\nu} \frac{\pi^4}{30a^5} \right]^{-1} \\ &= \frac{15\sigma c^2 h^3}{2\pi^5 k^4} \bar{\kappa}_\nu. \end{aligned}$$

The arithmetic average of $\bar{\kappa}_\nu(\nu)$ is easily computed from Courtin's data and is the only numerical calculation used in this method. This method provides a very rough estimate for κ_R and does not take into account the harmonic weighting.

Method 2 We can numerically evaluate the integral in equation 2.8 over the domain of the data we have available for κ_ν from Courtin's code. A simple and reasonably approximate method for numerical integration is Simpson's 3/8 Rule:

$$\text{Area}_s = \int_a^b f(x) dx = \frac{h}{3} \left[f_0 + \left(\sum_{i=1, i+=2}^{N-2} (4f_i + 2f_{i+1}) \right) + 4f_{N-1} + f_N \right].$$

where N is the number of points, $h = (b - a)/N$ is the step size, $f_i = f(a + ih)$, and the error is bounded by $|f_{max}^{(iv)}h^5/180N^2|$.

So in our case, where $f(x) = x^4/(\sinh^2(ax)\kappa_\nu(x))$, we find that

$$\kappa_R = \frac{1}{B \text{ Area}_s}.$$

The Chandrasekhar Mean Opacity The Chandrasekhar mean is yet another way of estimating an averaged version of the the mass absorption coefficient:

$$\kappa_c = \frac{\int_0^\infty \kappa_\nu F_\nu d\nu}{\int_0^\infty F_\nu d\nu}. \quad (2.9)$$

where F_ν is the net flux. The Chandrasekhar mean, as with the Rosseland mean, can be difficult to compute. In this case, the F_ν is not known in advance and thus we must use some sort of iterative method.

We will discuss two methods of computing κ_c below. Note that in both methods we will be integrating numerically over a grid of frequency values ν .

Method 1 The first method involves the moment equation is given by:

$$\frac{d^2 F_\nu}{d\tau_\nu^2} - 3F_\nu = -4 \frac{dB_\nu}{d\tau_\nu}.$$

1. For each grid point ν , we calculate F_ν by solving the moment equation

This inhomogeneous ODE can be solved using the method of parameters [77].

Applying this method to our ODE, we find we must solve for

$$F_\nu = \frac{e^{\sqrt{3}\tau}}{2\sqrt{3}} \int_0^\tau \frac{c_1 e^{-\sqrt{3}\tau' - c_2(\frac{1}{2} + \frac{3}{4}\tau')^{-1/4}}}{(e^{c_2(\frac{1}{2} + \frac{3}{4}\tau')^{-1/4}} - 1)^2 (\frac{1}{2} + \frac{3}{4}\tau')^{5/4}} d\tau' - \frac{e^{-\sqrt{3}\tau}}{2\sqrt{3}} \int_0^\tau \frac{c_1 e^{\sqrt{3}\tau' + c_2(\frac{1}{2} + \frac{3}{4}\tau')^{-1/4}}}{(e^{c_2(\frac{1}{2} + \frac{3}{4}\tau')^{-1/4}} - 1)^2 (\frac{1}{2} + \frac{3}{4}\tau')^{5/4}} d\tau'.$$

where $c_1 = \frac{3}{4} \frac{h^2 \nu^4}{c^2 k T_e}$ and $c_2 = \frac{h \nu}{k T_e}$.

2. Now that we have calculated F_ν at each grid point ν , we can evaluate the integral in equation 2.9, and thus we have the Chandrasekhar mean κ_c .

Method 2 This method involves successive iterations which converge to a value of F_ν [95].

1. First we start with an estimate value for F_ν . For the initial iteration we will start with radiation flux from a black body, which is $F_\nu = \pi B_\nu(T)$. This calculation is independent of altitude.
2. Next, we calculate κ_c using the above estimate for F_ν and equation 2.9.
3. Knowing κ_c we can theoretically calculate the intensity I_ν . Combining the formal solution of the transfer equation with the fact that for LTE the source function $S_\nu = B_\nu(T)$, we get

$$I_\nu(z) = I_\nu(0)e^{-\tau} + \int_0^s B_\nu e^{-\tau} \kappa_c \rho dz.$$

In order to calculate the intensity we need to know τ . Recall that τ is defined by $\tau = \int_0^\infty \kappa \rho dz$. Also recall that $\kappa \approx \kappa_c \frac{\rho}{D}$. So

$$\tau = \frac{\kappa_c}{D} \int_0^\infty \rho^2(z) dz.$$

To calculate τ we need to know the density ρ as a function of z . We will use a simple exponential decay/isothermal density profile (not exact, but a good first approximation as T varies slowly with P compared to $\rho(P)$).

$$\rho(z) = \rho(0) \left(\frac{\rho(z_f)}{\rho(0)} \right)^{z/z_f}.$$

where $\rho(0) = \rho_{surf} = \frac{P_T \bar{m}_A}{kT} \approx \frac{P_T \bar{m}_A}{k \cdot 0.8T_e}$, and z_f is the elevation at which the density becomes 10^{-5} its value at the surface.

4. The net flux F_ν is defined as

$$\pi F_\nu = 2\pi \int_{-1}^1 I_\nu(\mu) \mu d\mu.$$

where $\mu = \cos\theta$ (θ being the angle from the vertical).

Now in our case, θ is fixed, namely zero (since we are dealing with a plane-parallel atmosphere that is laterally homogeneous: the vectors corresponding to $\pm\theta$ cancel each other out). Now we can pull I_ν out of the above integral. Also, $\mu = \cos\theta = 1 = \text{constant}$, so that leaves us with

$$F_\nu = 2I_\nu \int_{-1}^1 d\mu.$$

Integrating, we obtain $F_\nu = 4I_\nu$.

5. We now use F_ν as calculated above for our new estimate in step 1, and repeat until we converge on the function F_ν .

Now we can calculate κ_c in formula 2.9.

The Planck Mean Opacity The Planck mean is defined as

$$\kappa_p = \frac{2hc^2\pi}{\sigma T^4} \int_0^\infty \frac{\nu^3 \kappa_\nu}{e^{\frac{hc}{kT}\nu} - 1} d\nu.$$

We can use the same type of methods described in the Rosseland mean section to evaluate this integral. In particular, if we apply *Method 1* from Section 2.1.2, then with a change of variable we can rewrite the above integral as

$$\kappa_p = \frac{2hc^2\pi\bar{\kappa}_\nu}{\sigma T^4} \left(\frac{kT}{hc}\right)^4 \int_0^\infty \frac{u^3}{e^u - 1} du.$$

From [54] we find a closed solution to the integral and end up with

$$\kappa_p = \frac{2\pi^5 k^4 \bar{\kappa}_v}{15\sigma h^3 c^2}.$$

Applying *Method 2* is straightforward.

SIMULTANEOUSLY SOLVING FOR τ , T , P , AND κ_x Equations 2.2, 2.3, 2.6, and 2.7 yield a system of four equations and four unknowns. Assuming vapor pressure equilibrium, the pressure in equations 2.2 and 2.6 must be the same, i.e.,

$$P_v(T)^2 - P(T)^2 = 0. \quad (2.10)$$

Filling in the details,

$$P_v(T)^2 - \frac{T^5 - B_1 T}{A_1 B_2} = 0. \quad (2.11)$$

where $B_1 = 1/2 T_e^4$, $B_2 = 3/4 T_e^4$, and $A_1 = \kappa_x/2kgn_L$. We solve the above equation for T using the bisection method, then backsolve for P and τ . We shall use bracketing with the bisection method to ensure we catch all the roots (i.e., to 1 degree Kelvin accuracy). Bracketing is more computationally intensive but is worth the extra time to make sure we catch as many roots as possible. Other methods (Newton, Secant, etc.) were tried but none were as successful and consistent as the bisection method, given the nonlinear nature of the equation.

Note that we assume P is a real (not complex) quantity, so P^2 is therefore a real and positive number. This imposes the constraint on equation 2.10.

$$T^5 - B_1 T > 0 \implies T \geq 2^{-\frac{1}{4}} T_e.$$

In practice we solve for P^2 rather than P so that we may computationally bracket the root from the positive P^2 (positive P) side and negative P^2 (imaginary P) side.

We impose an additional constraint to ensure that we do not exceed the supply of ice available [95]. The mass available for creating the atmosphere is Mf_i , where M is the total mass of the object and f_i is the ice fraction (by mass) of the rock/ice object (35% ice for Triton [109], 35% ice for Pluto [108], and we'll assume 35% ice for KBO since they are presumed to be the building blocks for Triton and Pluto).

Of the mass available, the resulting atmospheric pressure should yield atmospheres no more massive than 28% [96] of the total ice mass of the object. This constraint corresponds to the chemically/experimentally determined amount of gases that can be trapped/freed in the ice and the amount of ice in the bodies based on the measured bulk densities. Thus we require that $M_A < .28 Mf_i$.

Combining the above relation with $F = M_A g$ and $P = F/A = F/4\pi R^2$, we estimate the maximum pressure of the atmosphere [95]:

$$P_{max} = \frac{0.28 Mf_i g}{4\pi R^2}. \quad (2.12)$$

From the formula above, the limiting pressures for Triton, Pluto, and the averaged KBO are $\{ 1.02 \times 10^9, 6.71 \times 10^8, 1.68 \times 10^6 \}$ g/(cm s²), respectively.

CONVECTION The system described above assumes radiative equilibrium, which may not be an adequate approximation for optically thick planetary atmospheres that are primarily heated from below. When the optical depth increases above ≈ 1 , convection may exceed radiative transfer as the main method of energy transport in the atmosphere. But computing a combined convective/radiative (mixing length theory) atmosphere would be very computationally intensive. Instead we choose a more heuristic approach: we construct radiative profiles as described in the previous sections, then evaluate where the profiles are superadiabatic [98]. The procedure is outlined in detail in [14] [53].

In such regions, the simplest model of convection yields a temperature gradient given by the equation 1.10:

$$\frac{dT}{dz} = -\frac{gf}{C_p}. \quad (2.13)$$

This relationship is called the dry adiabatic temperature gradient, and allows us to construct a temperature profile with respect to altitude. The factor f is typically set to 0.8 for a profile that is intermediate to the full dry and wet adiabats [98].

As described in [14] [53] [98], the temperature profile resulting from equation 2.13 is below the fully radiative profile, and thus cannot supply the radiant flux necessary for radiative equilibrium above the radiative-convective boundary. To compensate, we adjust the height of the radiative-convective boundary until the convective profile provides the same radiative flux to the radiative region as did the fully radiative profile.

2.2 Computational Results of the Grey Atmosphere Model

2.2.1 Model Implementation

To solve the system described in section 2.1, we have written a 3000-line C program that takes approximately one to eight hours to run (depending on opacity type/method chosen). These code runs were performed on PCs running Linux with 200 MHz CPUs.

2.2.2 Model Inputs

To solve equation 2.10 (the culmination of our physical conditions/four equations: hydrostatic and radiative equilibrium, grey atmosphere, Eddington approximation) we look for roots of that equation, i.e., value(s) of T that satisfy vapor pressure equilibrium and equations 2.2, 2.3, 2.6, and 2.7. We perform our bisection method on the region $T \in [2^{-\frac{1}{4}}T_e, 1000]$ Kelvin.

For each Triton model run we choose:

- a value for the H_2 concentration, $FHYD$
- one of the 3 mean opacity types ($\kappa_R, \kappa_p, \kappa_c$)
- for each value of F_{tide} (ranging from 0 to 6000 at increments of 1.0) we check to see if there is a root for our system of 4 equations

For each Pluto model run we choose:

- a value for the H_2 concentration, $FHYD$
- one of the 3 mean opacity types ($\kappa_R, \kappa_p, \kappa_c$)
- whether to include tidal heating or not
- what fraction of accretional heating is absorbed by the planet (the h factor)
- at what point in its accretional dissipation evolution we are looking at

For each Kuiper-belt object model run choose:

- a value for the H_2 concentration, $FHYD$
- one of the 3 mean opacity types ($\kappa_R, \kappa_p, \kappa_c$)
- what fraction of accretional heating is absorbed by the planet (the h factor)
- at what point in its accretional dissipation evolution we are looking at

In our model runs for Triton, Pluto, and Kuiper-belt objects, we have found that certain parameter values yield multiple solutions to equation 2.10, i.e., that one, two, and three surface temperature values may exist for a single tidal heat flux value. When this occurs, a plot of surface temperature T versus the input tidal heating flux F_{tide} yields an “S-shaped” curve. Before presenting the full model results, we shall discuss this S-curve phenomenon and its origin.

2.2.3 S-curves

The S-curves are caused by our choice of vapor pressure representation. We will dissect a constant pressure case and our varying pressure S-curve case to verify this assertion. In particular, we choose as our base a Triton model run with $H_2 = 0.1\%$ that uses the Rosseland mean opacity. We shall examine the pressure values at $F_{tide} = \{120, 960, 1320, 1800, 3000\}$ dyn/(cm s).

CONSTANT PRESSURE First let us examine a control case where the vapor pressure is a constant: $P_v = 14$ dyn/cm² (Triton's present-day surface pressure). For each value of the parameter F_{tide} we apply the bisection method to equation 2.10, which in this case reduces to the simple form $T^5 - B_1 T - P_v^2 / (A_1 B_2) = 0$. We obtain the following results (see Figure 2.2) from our control case:

From Figure 2.2 we see that for each value of F_{tide} we have one surface temperature that satisfies equation 2.10. This equation is a 5th order polynomial and thus potentially has 5 distinct roots. Recall that we are looking for roots where $T > 2^{-1} T_c$; Figure 2.3 shows $P_v^2 - P(T)^2$ at $F_{tide} = \{120, 960, 1320, 1800, 3000\}$ dyn/(cm s), where we see that there is but one intersection with the zero line, i.e., a single root, in this temperature domain.

It can also be shown analytically that the constant pressure case has exactly one positive root using Descartes' Rule of Signs [41], which states that a polynomial with real coefficients has n positive roots (where n equals the number of sign changes in the coefficient list) or is less than n by a multiple of 2 [10] [31]. Since all the constants in equation 2.11 are real and positive, the quintic polynomial has one sign variation and thus has exactly one positive root [41].

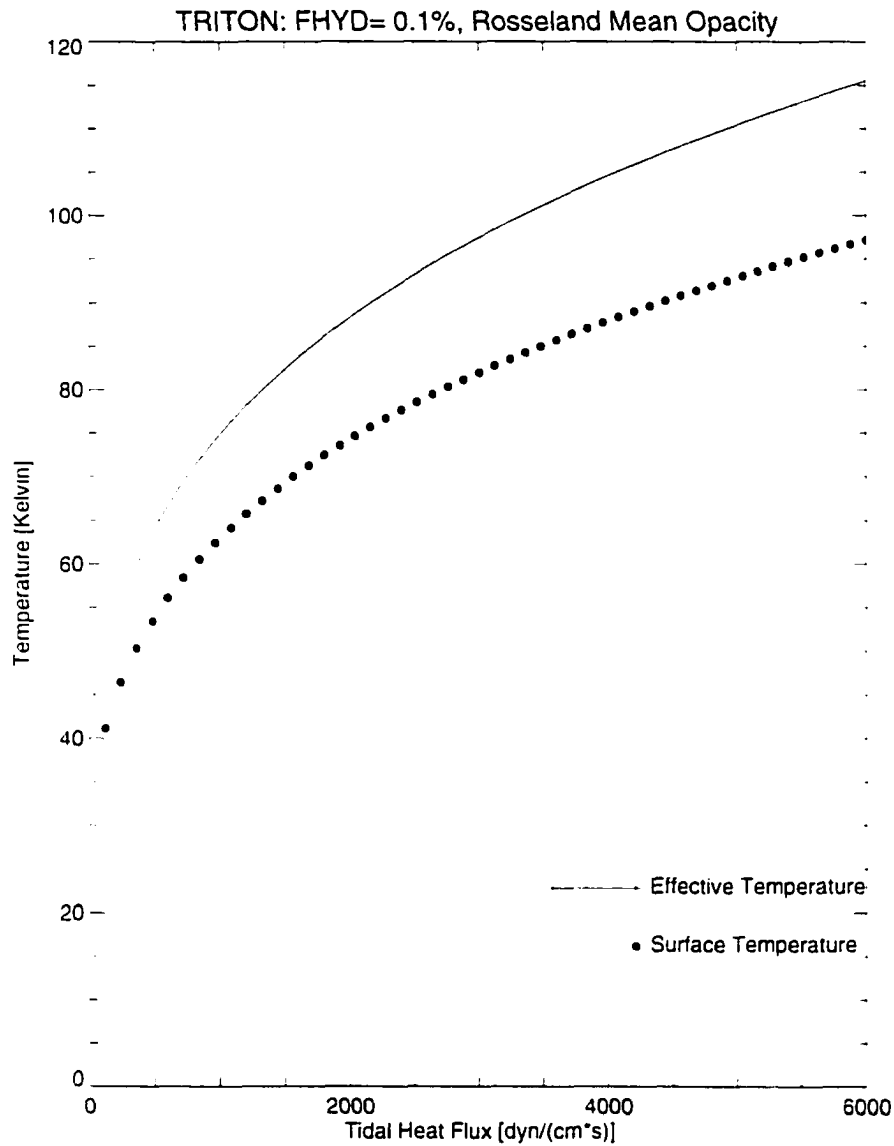


FIGURE 2.2. Temperature (Effective and Surface) versus Tidal Heat Flux (F_{tide}).

VARYING PRESSURE The values for F_{tide} are carefully chosen for this examination so that in this varying pressure case, a broad cross-section of solutions to $P_r(T)^2 - P(T, \tau)^2 = 0$ (i.e., one, two, and three roots) can be examined (see Figure 2.4).

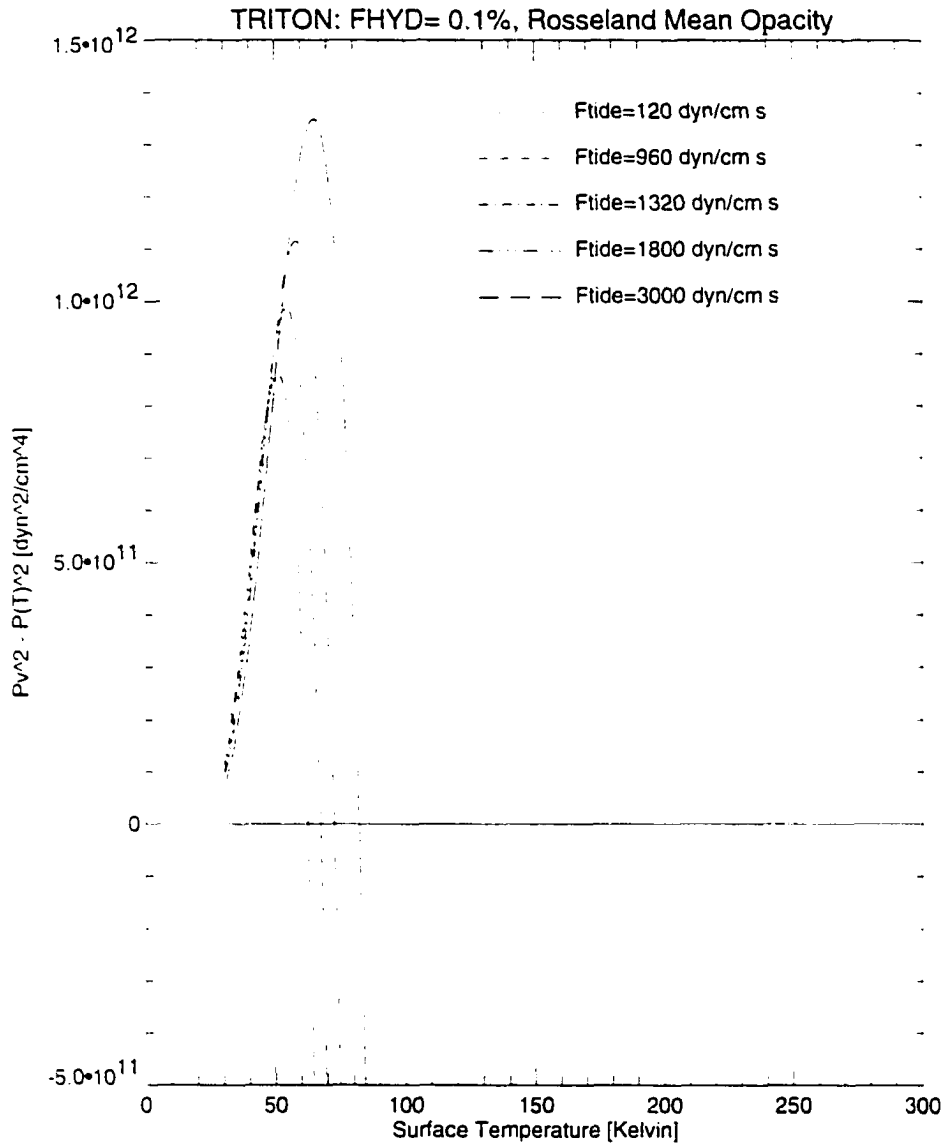


FIGURE 2.3. $P_v^2 - P(T)^2$ versus Surface Temperature.

We see that $F_{tide} = 120$ dyn/(cm s) and $F_{tide} = 3000$ dyn/(cm s) each yield one root. $F_{tide} = 960$ dyn/(cm s) and $F_{tide} = 1800$ dyn/(cm s) each have two roots, and $F_{tide} = 1320$ dyn/(cm s) yields 3 roots.

For these five cases we have plotted $P_v(T)^2$ and $P(T, \tau)^2$ for $T : 30 \rightarrow 300$ K to see what these functions look like.

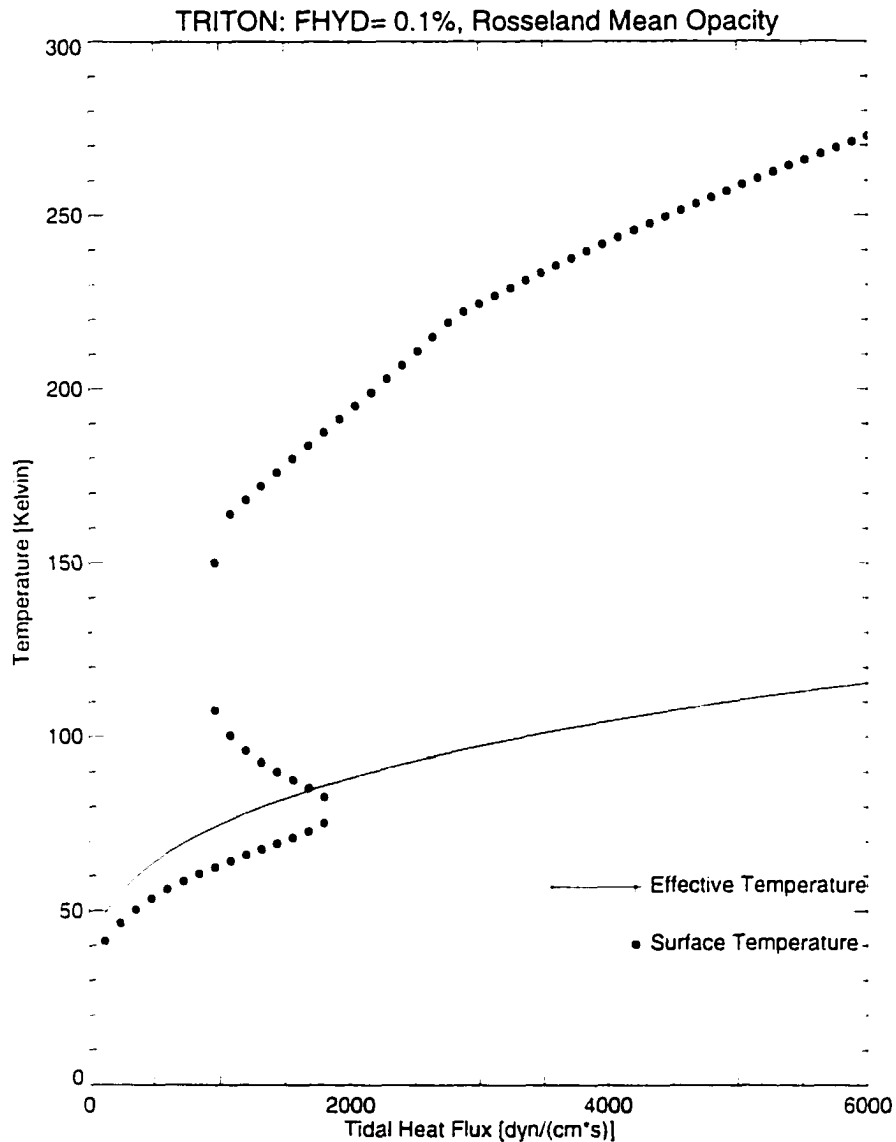


FIGURE 2.4. Temperature (Effective and Surface) versus Tidal Heat Flux (F_{tide}).

Note that $P_v(T)^2$ versus T (shown in Figure 2.5) is independent of F_{tide} and thus remains the same in all five cases. There are two very noticeable “kinks” in the curve $P_v(T)^2$ versus T . The first “knee” is caused by the cap of 34 bars on the N_2 partial pressure (P_{N_2} reaches this limit around 163 K). The second kink (which leads to the plateau) is caused by the additional cap of 45 bars on the CH_4 partial pressure (P_{CH_4}

attains this limit around 215 K). After 215 K both partial pressures are a constant, and thus $P_v(T)$ becomes constant.

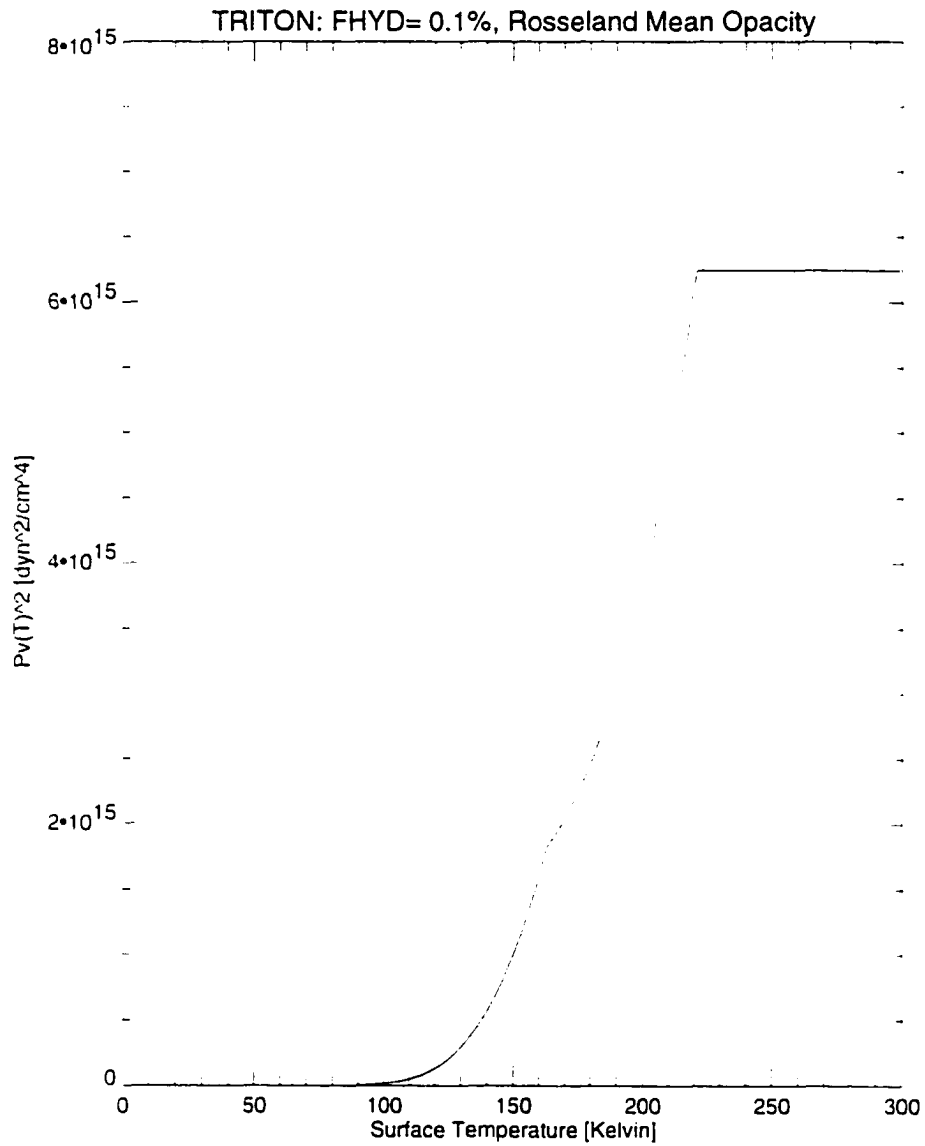


FIGURE 2.5. $P_v(T)^2$ for $F_{\text{tide}} = \{120, 960, 1320, 1800, 3000\}$ dyn/cm s.

On the other hand $P(T)^2$ does depend on F_{tide} (see Figure 2.6):

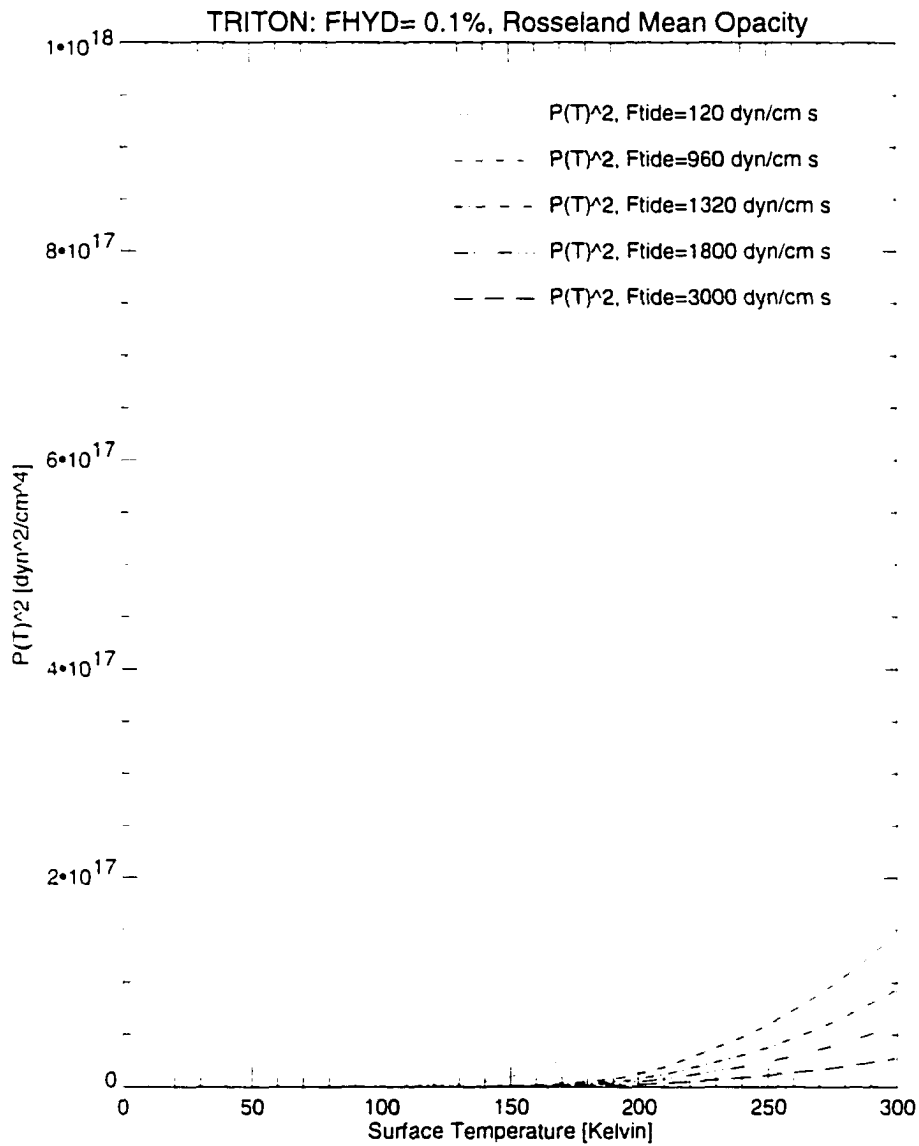


FIGURE 2.6. $P(T)^2$ for $F_{tide} = \{120, 960, 1320, 1800, 3000\}$ dyn/cm s.

As we increase F_{tide} , the $P_v(T)^2$ curve remains fixed, but the $P(T)^2$ curve sweeps from left to right. Thus if we follow the intersections of these curves for increasing

values of F_{tide} , we see that first there is one intersection, then two, three, two, then one intersection again.

Below is a plot of $P_v(T)^2 - P(T, \tau)^2$ for $T : 2^{-\frac{1}{4}}T_e(F_{tide}) \rightarrow 300$ K (see Figure 2.7), where we can more easily observe the intersections (i.e., the temperature values for which $P_v(T)^2 - P(T, \tau)^2 = 0$).

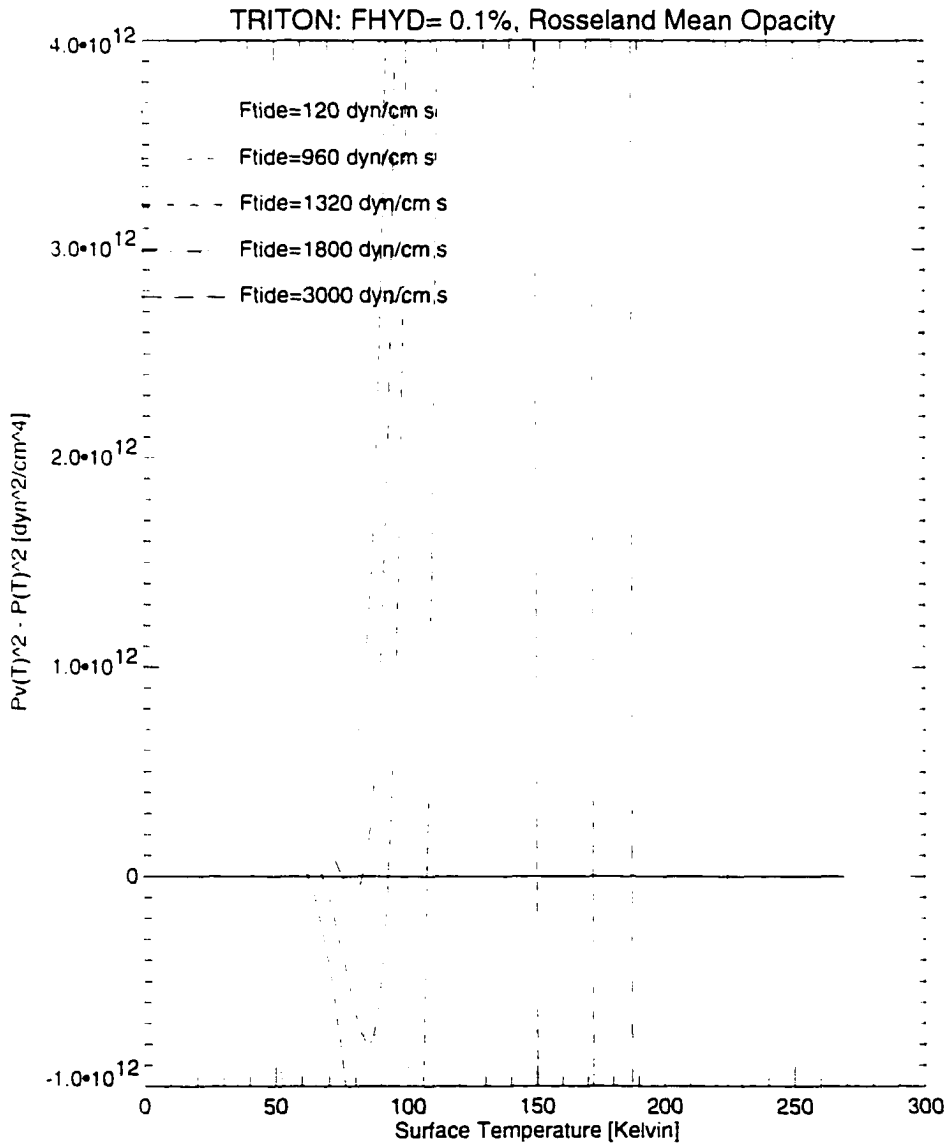


FIGURE 2.7. $P_v(T)^2 - P(T, \tau)^2$ for $F_{tide} = \{120, 960, 1320, 1800, 3000\}$ dyn/cm s.

We now see how the triple roots evolve: as F_{tide} increases, the $P(T)^2$ curve moves from left to right: it sweeps across the fixed vapor pressure curve and intersects $P_r(T)^2$ first singly, then multiply, then singly again. With two monotonic increasing curves we might expect one or two intersections, but three roots seem to arise in this case because of the vapor pressure kinks and eventual pressure ceiling imposed by criticality and the mass limit (see Figure 2.5) that occur above $T \approx 215$ K. Detailed analysis looking for additional roots in the area around the “knee” resulted in no more than a total of three roots.

2.2.4 Triton Results

As seen in Figure 2.8, the Chandrasekhar and Planck mean opacities yield surprisingly hot atmospheres. Their solutions behave similarly: they both display S-curves truncated at the left (their lower branches are indistinguishable from the cold Rosseland mean solution), and their hot atmospheres seem to rise together as we increase the tidal heat flux. Note also that these solutions are independent of the H_2 concentration.

The Rosseland mean opacity atmospheres, on the other hand, remain cold until we reach about $FHYD = 0.01\%H_2$, where we start to see an atmosphere develop with increasing H_2 fraction. As we increase $FHYD$, we obtain hotter and hotter atmospheres with S-curves developing and moving towards the left.

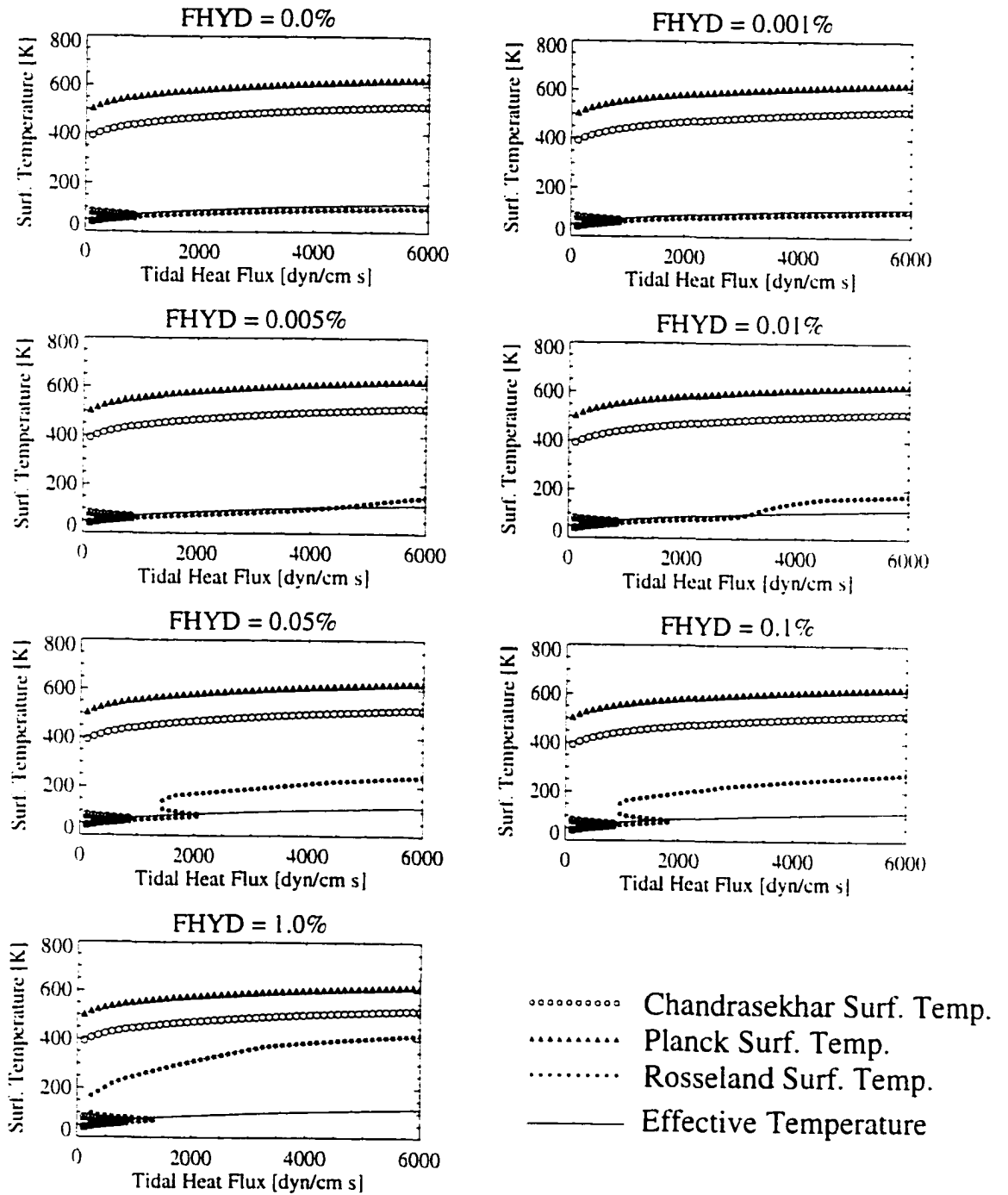


FIGURE 2.8. Triton: Temperature (Effective and Surface) versus Tidal Heat Flux (F_{tide}).

CHANDRASEKHAR AND PLANCK MEAN OPACITY RESULTS In Figures 2.9 and 2.10 we see that the Chandrasekhar and Planck mean opacities are insensitive to changes in the H_2 concentration. Also, there is a distinct gap between the cold S-curve branch and the hot atmosphere values, but overall the Chandrasekhar and Planck mean opacities are on the order of $10^{-7} - 10^{-6} \text{cm}^2/\text{g}$. The U-shape in both figures is due to the low-temperature kink we see in Figure 2.8.

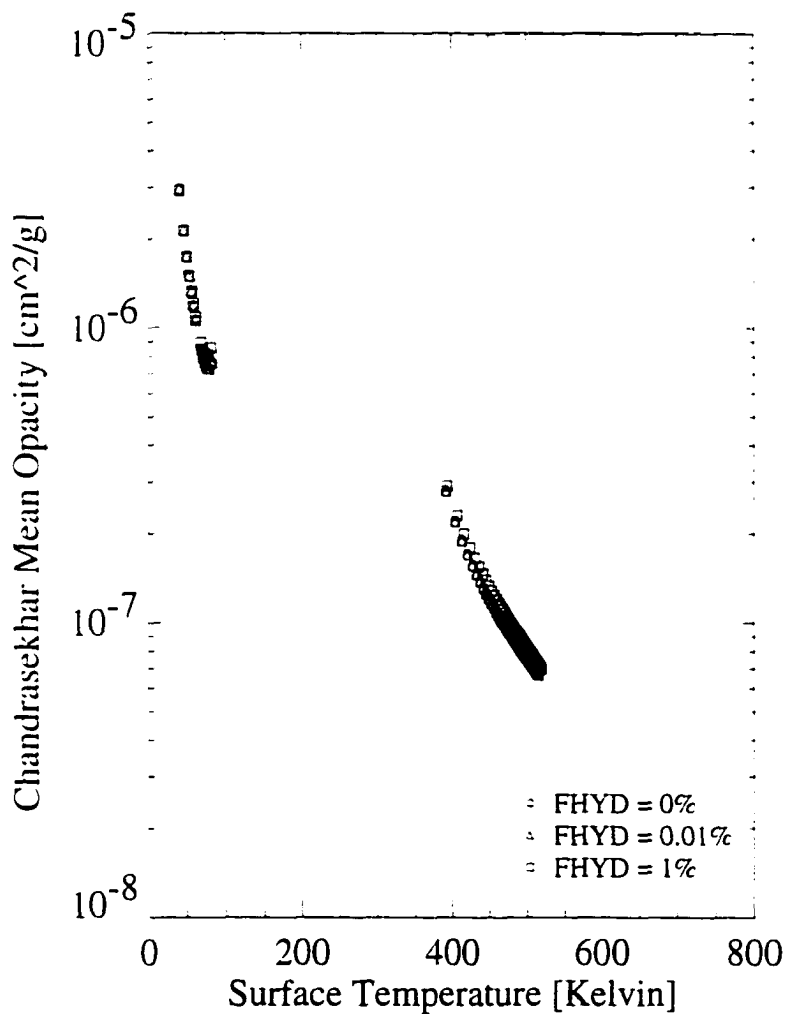


FIGURE 2.9. Triton: Chandrasekhar Mean Opacity versus Surface Temperature.

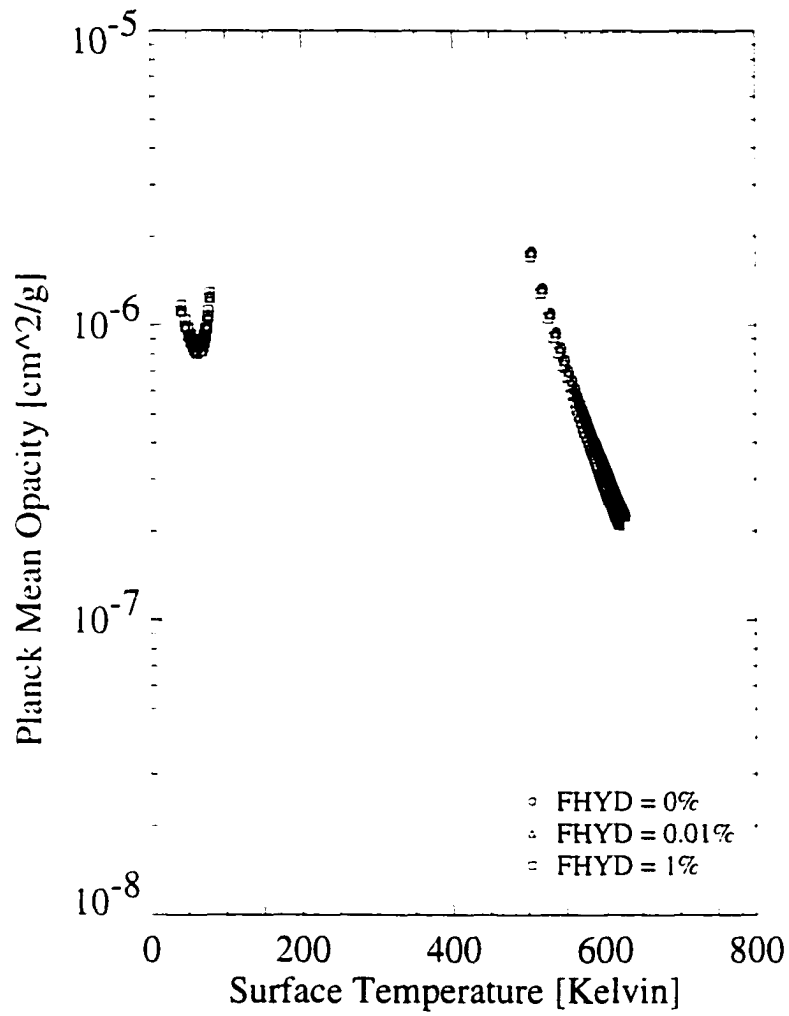


FIGURE 2.10. Triton: Planck Mean Opacity versus Surface Temperature.

In Figures 2.11 and 2.12 we see that the optical depths calculated with the Chandrasekhar and Planck means behave similarly. At low temperatures, the optical depth rises steeply as we increase the temperature. Again there is a chasm between the cold branch of the S-curves and the hot atmosphere. At high temperatures the optical depth falls off slowly.

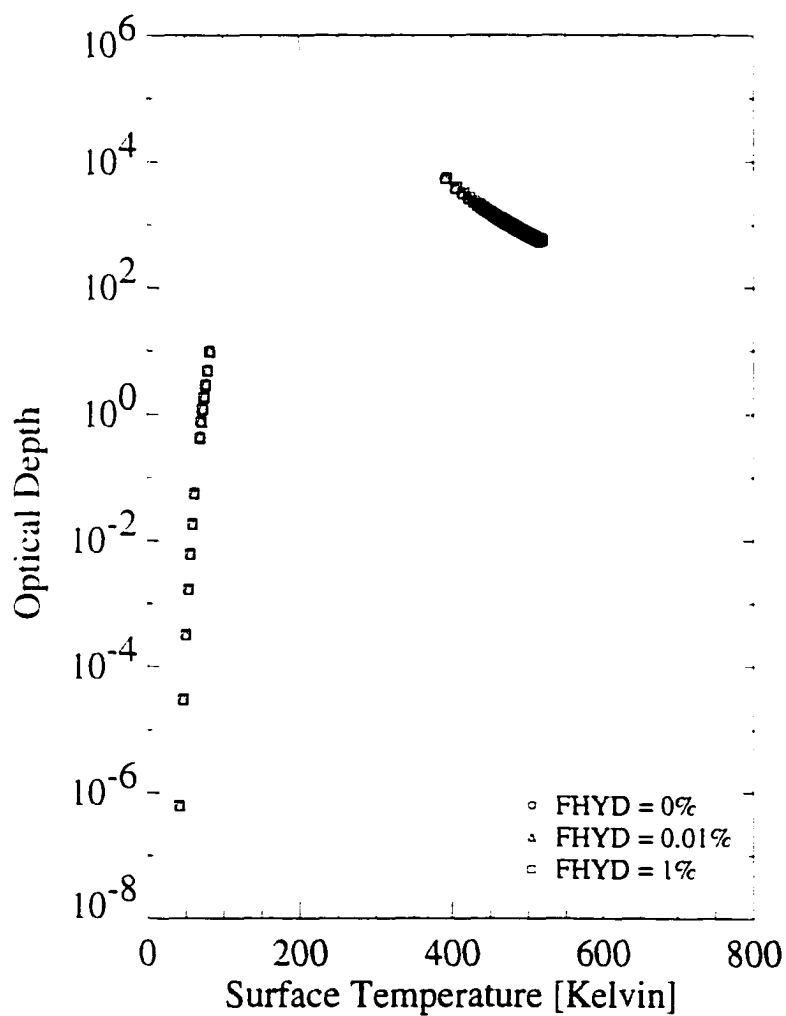


FIGURE 2.11. Triton: Optical Depth versus Surface Temperature with Chandrasekhar Mean Opacity.

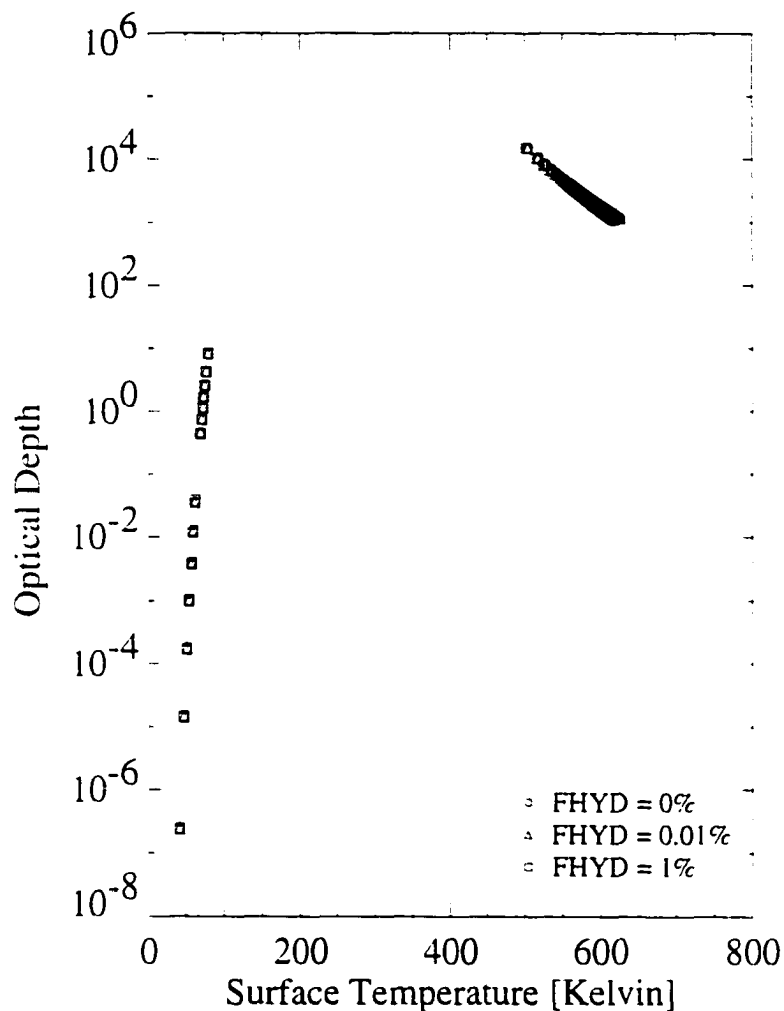


FIGURE 2.12. Triton: Optical Depth versus Surface Temperature with Planck Mean Opacity.

From Figures 2.13 and 2.14 we find that the pressure increases as we increase the temperature at low temperatures, but eventually levels out at $\approx 10^8 \text{ dyn/cm}^2$. Note that the pressure cap (critical pressure) for N_2 is $3.4 \times 10^7 \text{ dyn/cm}^2$ and the pressure cap for CH_4 is $4.5 \times 10^7 \text{ dyn/cm}^2$, so the total pressure limit is at $7.9 \times 10^7 \text{ dyn/cm}^2$. Thus the atmospheric pressure is leveling out not too far from the pressure cap we

have imposed.

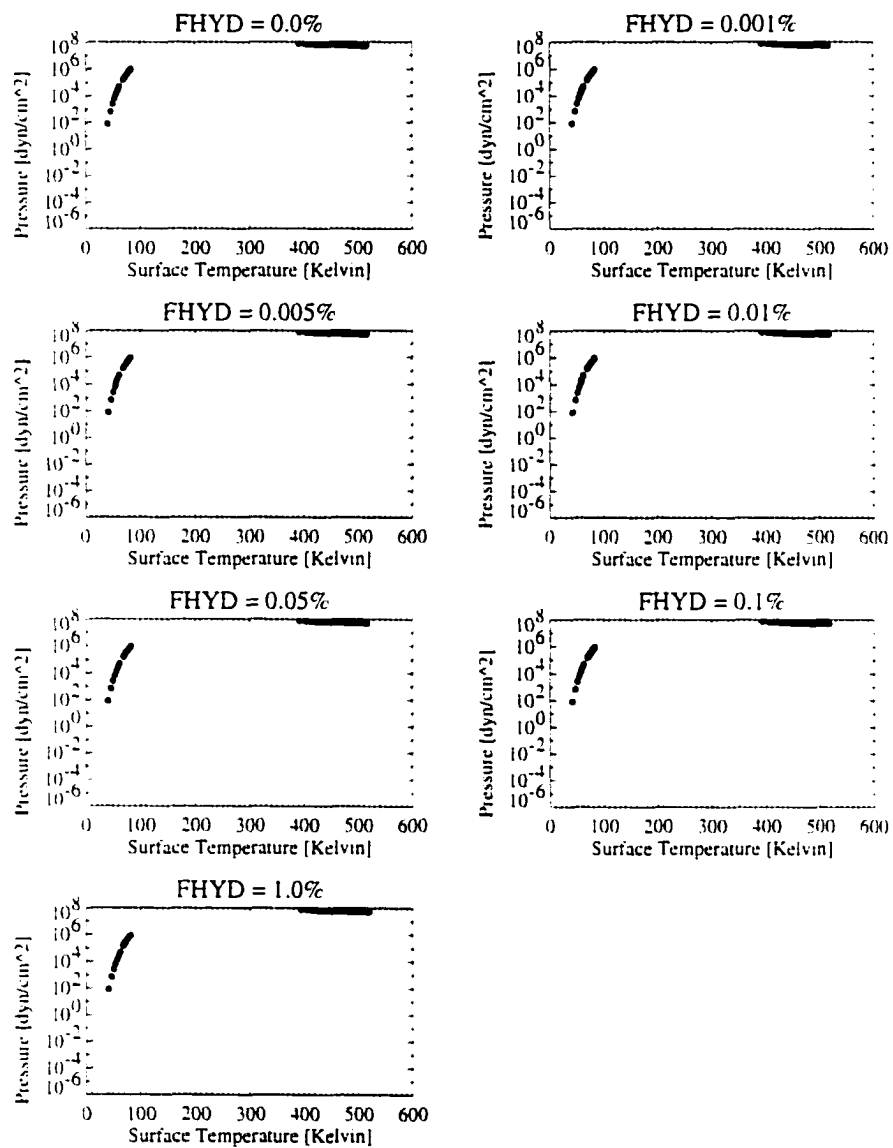


FIGURE 2.13. Triton: Pressure versus Surface Temperature with Chandrasekhar Mean Opacity.

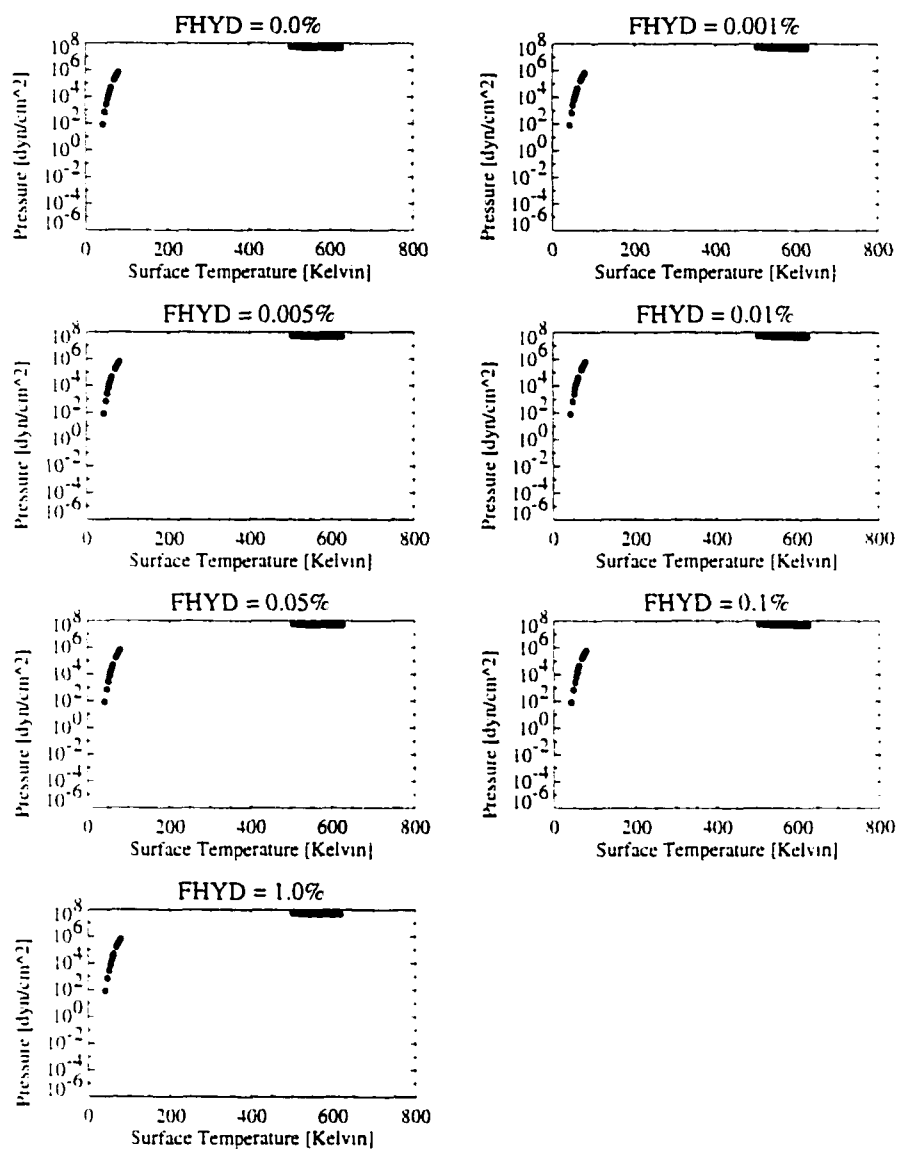


FIGURE 2.14. Triton: Pressure versus Surface Temperature with Planck Mean Opacity.

In Figures 2.15 and 2.16 the first real difference between the Chandrasekhar and Planck mean opacity calculations, most probably due to the difference in surface temperatures at the chosen point of reference. $F_{tide}=3240$ dyn/cm s.

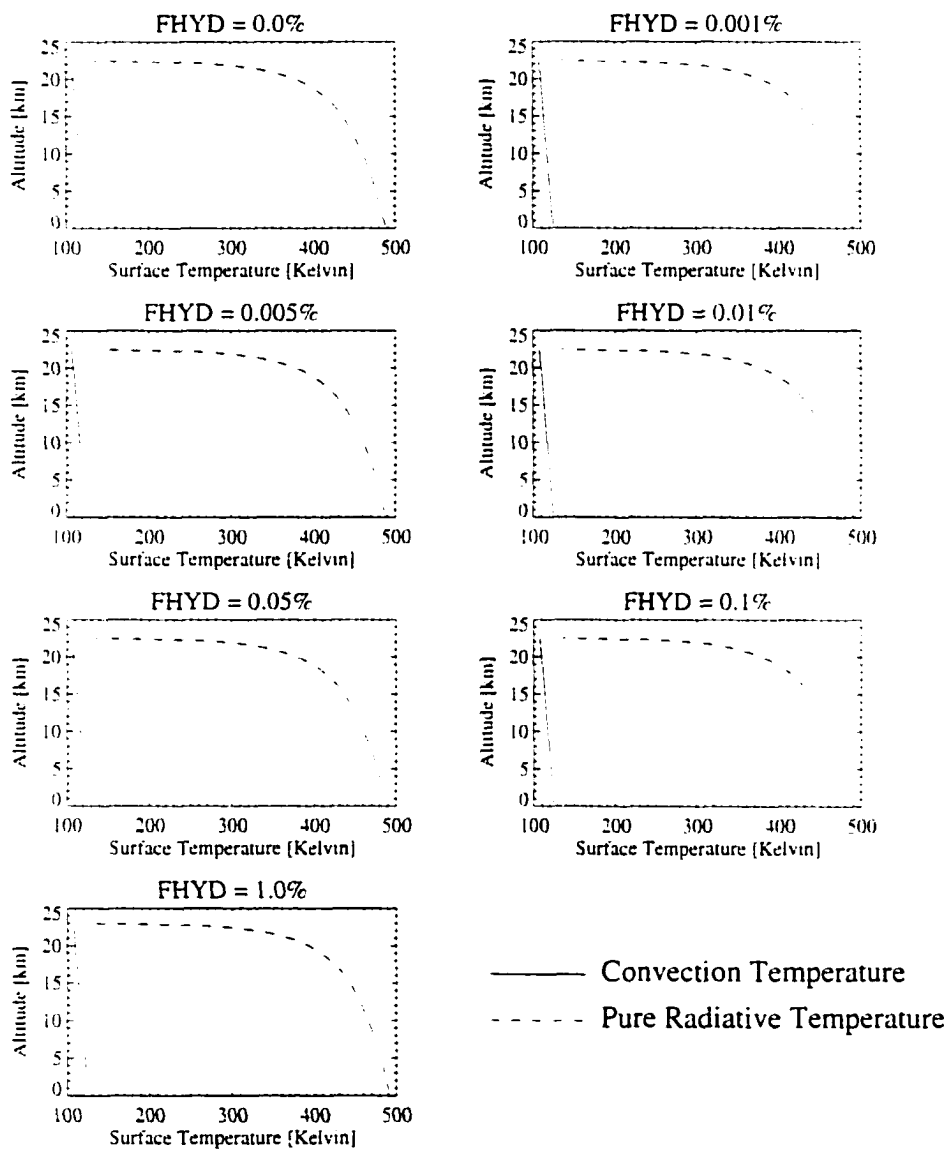


FIGURE 2.15. Triton: Altitude versus Temperature with Chandrasekhar Mean Opacity. $F_{tide}=3240$ dyn/cm s, $T_e = 99$ K. $T = 488$ K.

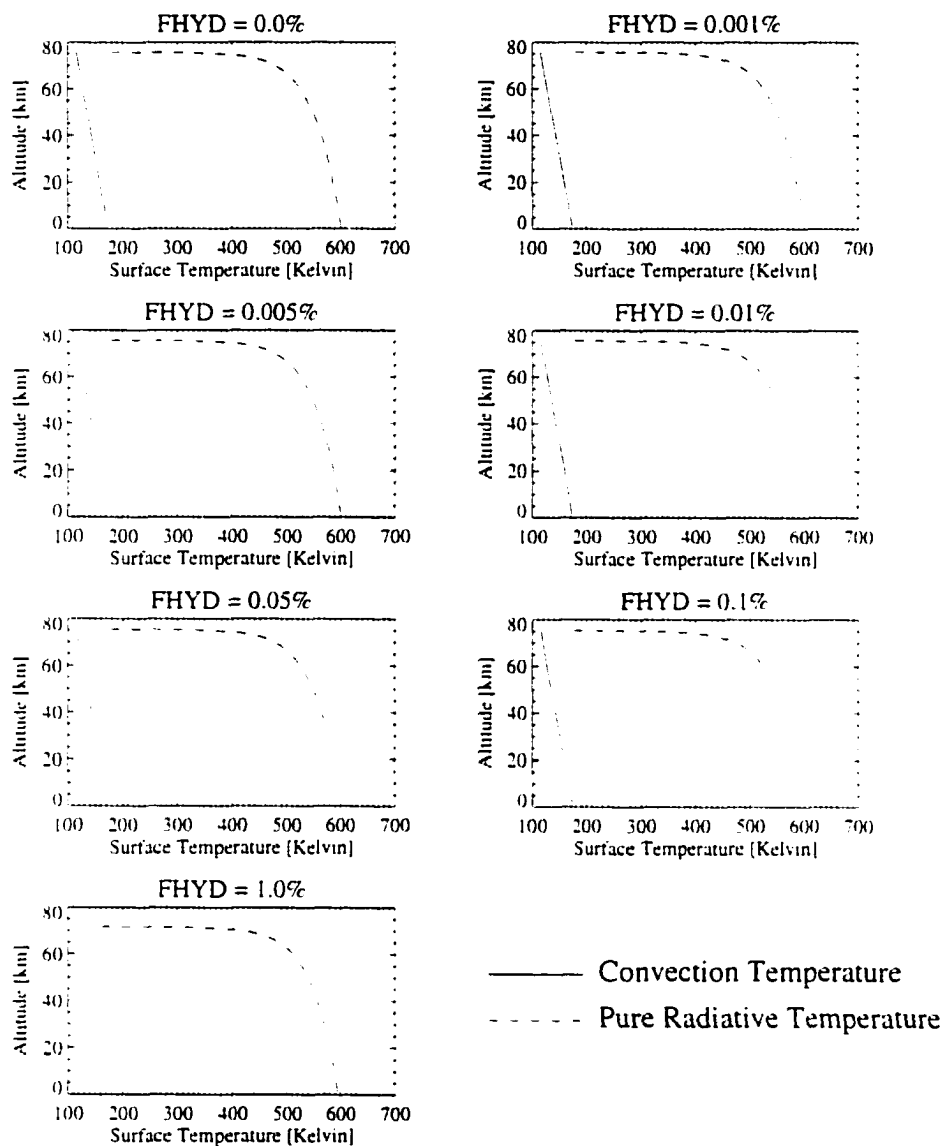


FIGURE 2.16. Triton: Altitude versus Temperature with Planck Mean Opacity. $F_{tide} = 3240$ dyn/cm s. $T_e = 99$ K. $T = 601$ K.

ROSSELAND MEAN RESULTS In contrast to the Chandrasekhar and Planck mean opacity calculations, we see from Figures 2.17 and 2.18 that the Rosseland mean opacity and the optical depth both increase as we increase the H_2 concentration in the atmosphere. Also, there are discontinuities between the hot and cold solutions in the 1% $H - 2$ case (see Figure 2.8) so we see rifts in the mean opacity and optical depth values. Note that the Rosseland mean opacities are of the order $10^{-10} - 10^{-7}$.

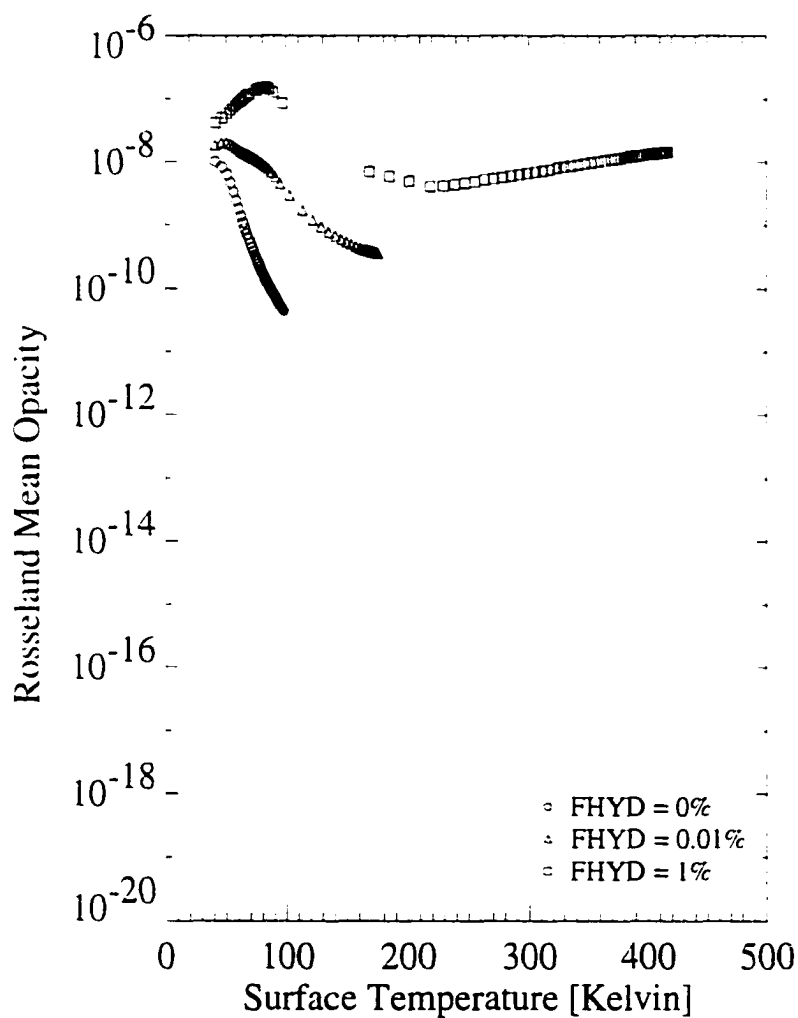


FIGURE 2.17. Triton: Rosseland Mean Opacity versus Surface Temperature.

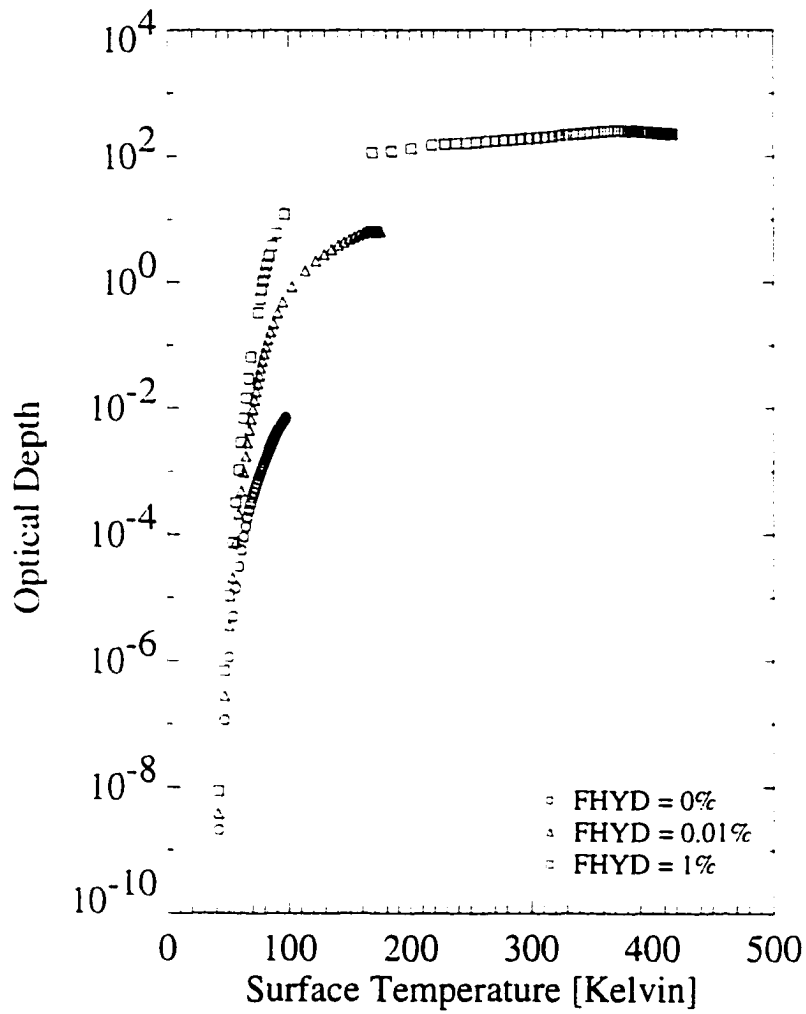


FIGURE 2.18. Triton: Optical Depth versus Surface Temperature with Rosseland Mean Opacity.

From Figure 2.19 we find that the pressures calculated using the Rosseland mean opacity behave similarly to the Chandrasekhar and Planck mean opacity cases, with a leveling off at $\approx 10^8$ dyn/cm². Recall that the total pressure cap is at 7.9×10^7 dyn/cm².

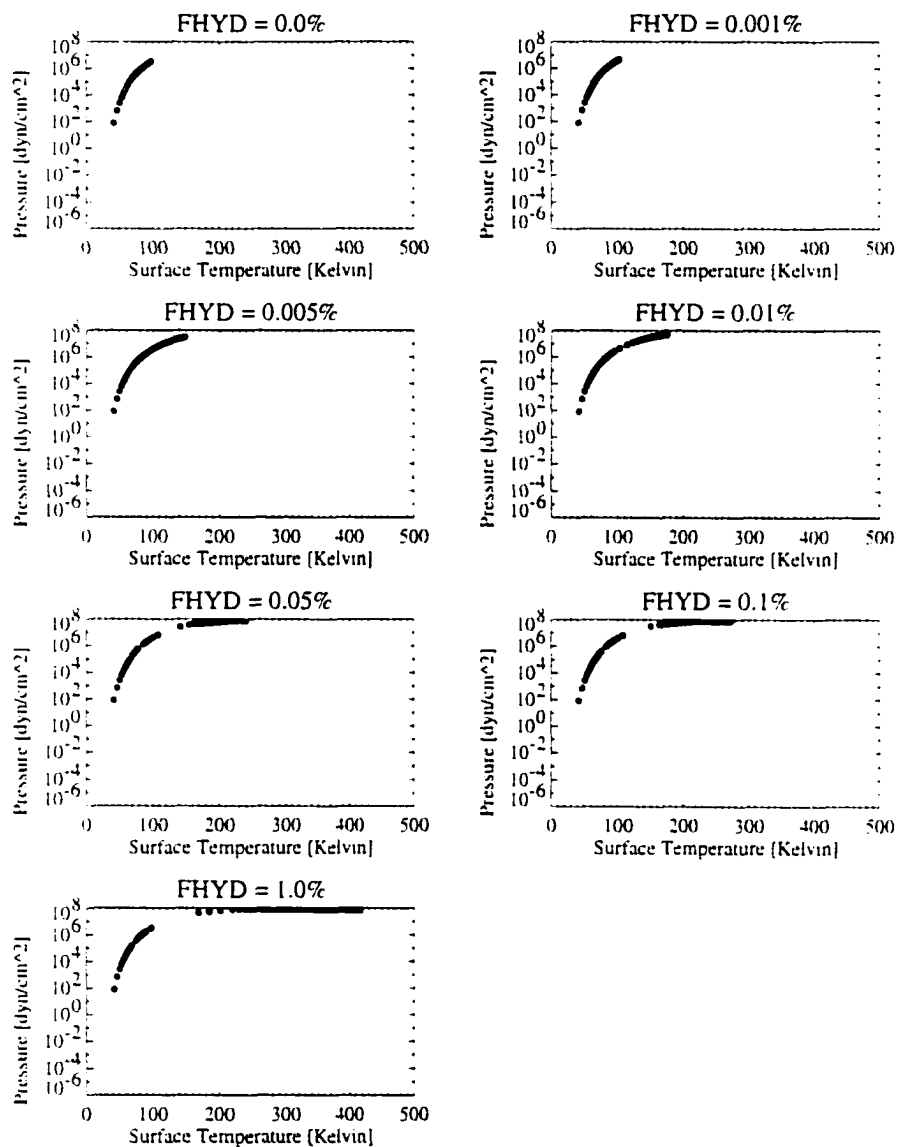


FIGURE 2.19. Triton: Pressure versus Surface Temperature with Rosseland Mean Opacity.

In Figure 2.20 the convection profile deviates from the radiative profile only for H_2 greater than 0.05%.

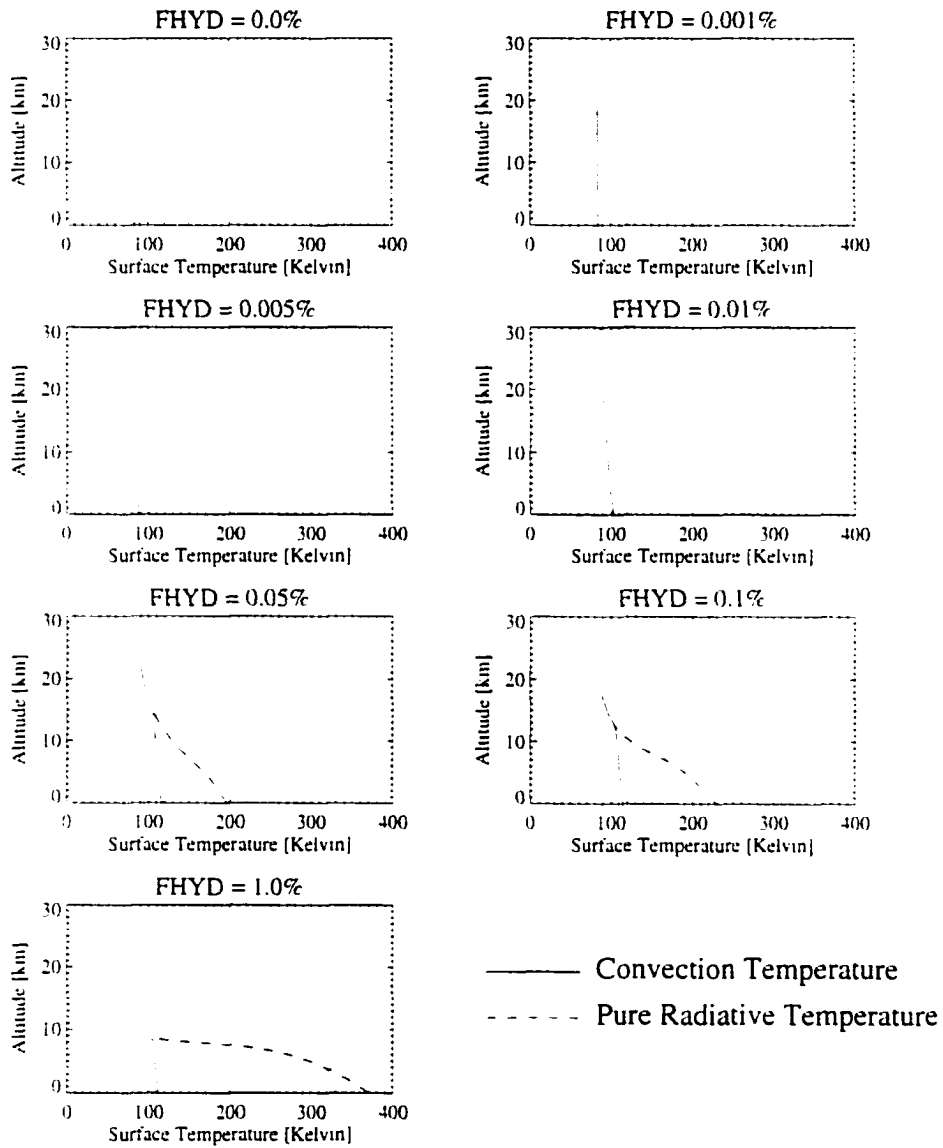


FIGURE 2.20. Triton: Altitude versus Temperature with Rosseland Mean Opacity.

2.2.5 Pluto (Tidal and Non-Tidal) Results

For Pluto, we found that the tidal heating results were indistinguishable from the non-tidal heating results since tidal heating is small compared to other heat sources. Hence we present the non-tidal heating results only (see below).

We use h , the fraction of accretional heating absorbed by the object, as a parameter for the system. Accretional heating is orders of magnitudes smaller than solar heating and thus it makes little difference what h is. The effective temperature used in this calculation is 44 K.

The solutions obtained by using the Chandrasekhar and Planck mean opacities were very similar (see Tables 2.1 and 2.2). Both were independent of varying H_2 concentrations, and both produced 3 solutions each, with two of the three having surface temperatures higher than the effective temperature and high optical depths. The multiple solutions are explained by the S-curve phenomenon described in Section 2.2.3.

Quantity	Solution 1	Solution 2	Solution 3	Units
Surface Temp.	36.9	86.4	382	Kelvin
Pressure	8.50	1.35×10^6	7.63×10^7	dyn/cm ²
Mean Opacity	2.42×10^{-6}	5.74×10^{-7}	3.08×10^{-7}	cm ² /g
Optical Depth	7.73×10^{-9}	19.4	7668	none

TABLE 2.1. Pluto: Chandrasekhar Mean Opacity Results: $T_e = 44$ K.

Quantity	Solution 1	Solution 2	Solution 3	Units
Surface Temp.	36.9	79.9	500	Kelvin
Pressure	8.5	6.87×10^5	5.61×10^7	dyn/cm ²
Mean Opacity	1.28×10^{-6}	1.44×10^{-6}	2.17×10^{-6}	cm ² /g
Optical Depth	4.09×10^{-9}	14.0	2.23×10^4	none

TABLE 2.2. Pluto: Planck Mean Opacity Results: $T_e = 44$ K.

In Figures 2.21 and 2.22 we see that the convective profile differs significantly from the radiative profiles for all H_2 concentrations.

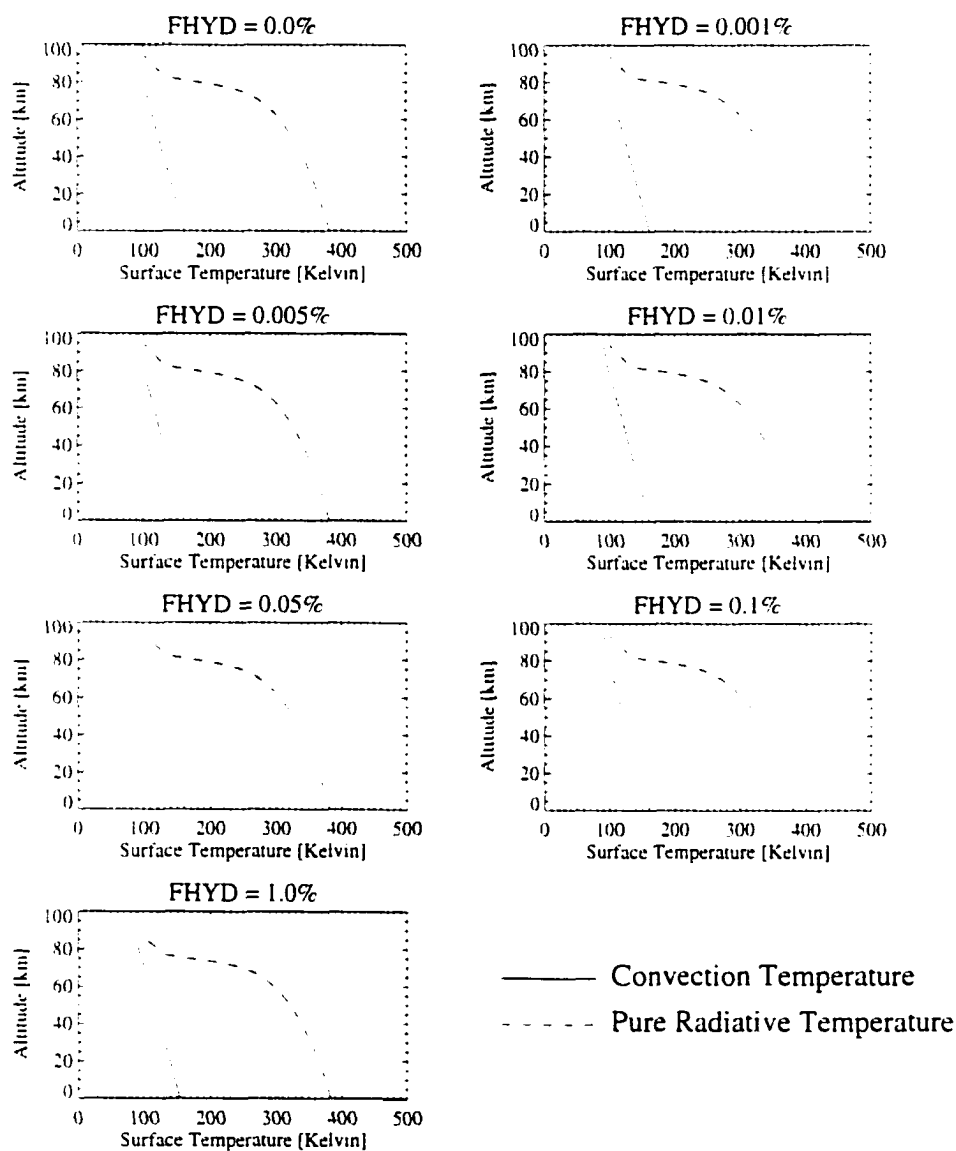


FIGURE 2.21. Pluto: Altitude versus Temperature with Chandrasekhar Mean Opacity. $F_{tide}=3240$ dyn/cm s. $T_e = 44$ K, $T = 381$ K.

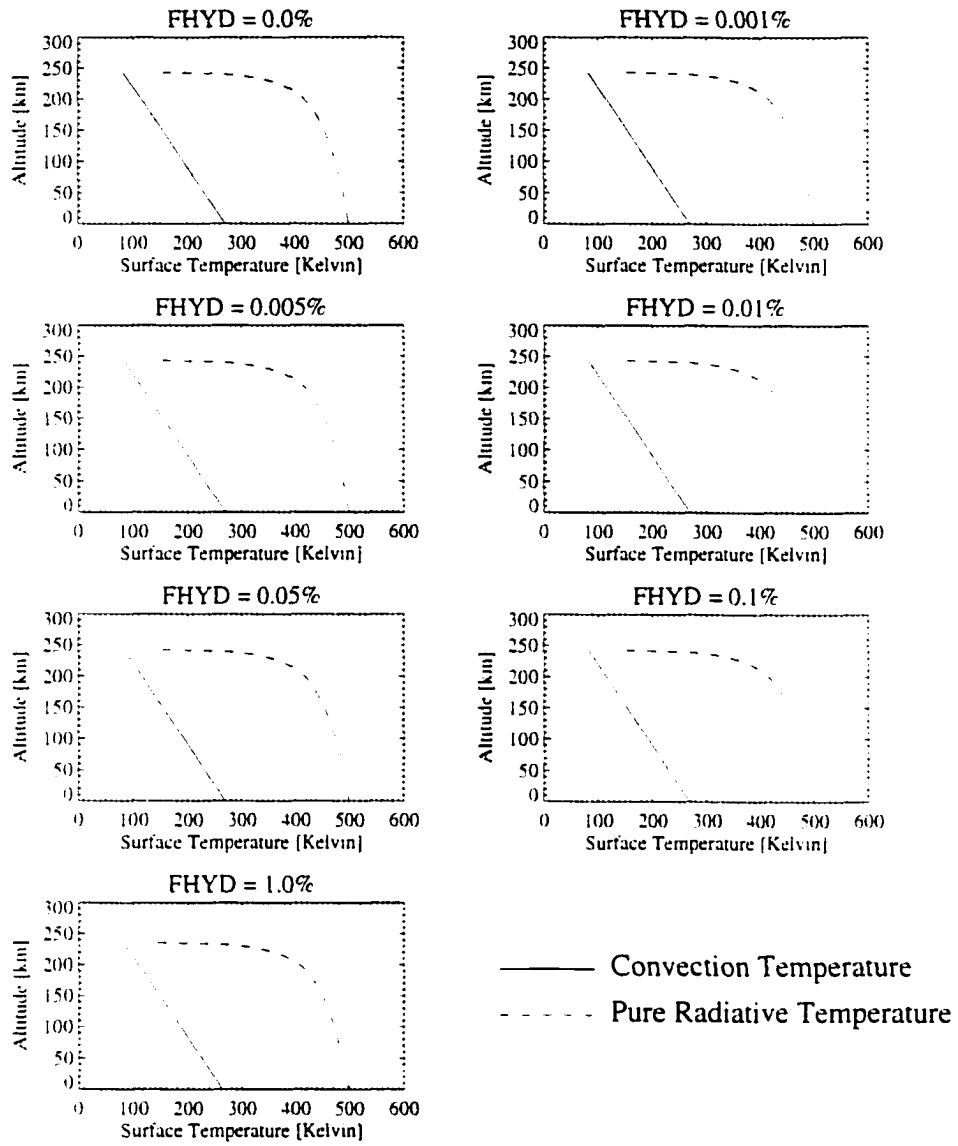


FIGURE 2.22. Pluto: Altitude versus Temperature with Planck Mean Opacity. $F_{\text{tide}}=3240 \text{ dyn/cm s}$, $T_e = 44 \text{ K}$, $T = 500 \text{ K}$.

From Table 2.3 we see that the Rosseland mean opacity run yields one cold solution.

Quantity	Solution	Units
Surface Temp.	36.9	Kelvin
Pressure	8.5	dyn/cm ²
Mean Opacity	2.45×10^{-8}	cm ² /g
Optical Depth	7.96×10^{-11}	none

TABLE 2.3. Pluto: Rosseland Mean Opacity Results: $T_e = 44$ K.

2.2.6 Kuiper Belt Object Results

For KBOs we use h , the fraction of accretional heating absorbed by the object, as a parameter for the system. The contribution from accretional heating is orders of magnitudes smaller than that of solar heating and thus it makes little difference what h is. The effective temperature used in this calculation is 49 K.

The solutions obtained by using the Chandrasekhar and Planck mean opacities were very similar (see Tables 2.4 and 2.5). Both were independent of varying H_2 concentrations, and both produced 2 solutions each, with one of the two having surface temperatures higher than the effective temperature and high optical depths. The multiple solutions are explained by the S-curve phenomenon described in Section 2.2.3.

Quantity	Solution 1	Solution 2	Units
Surface Temp.	41.1	66.1	Kelvin
Pressure	75.7	1.10×10^5	dyn/cm ²
Mean Opacity	1.79×10^{-6}	6.20×10^{-7}	cm ² /g
Optical Depth	8.96×10^{-6}	3.81	none

TABLE 2.4. KBO: Chandrasekhar Mean Opacity Results: $T_e = 49$ K.

Quantity	Solution 1	Solution 2	Units
Surface Temp.	41.1	63.6	Kelvin
Pressure	75.7	6.91×10^4	dyn/cm ²
Mean Opacity	1.14×10^{-6}	1.17×10^{-6}	cm ² /g
Optical Depth	5.73×10^{-6}	3.17	none

TABLE 2.5. KBO: Planck Mean Opacity Results: $T_e = 49$ K.

From Figures 2.23 and 2.25 we see that the convective and radiative profiles coincide for all H_2 concentrations.

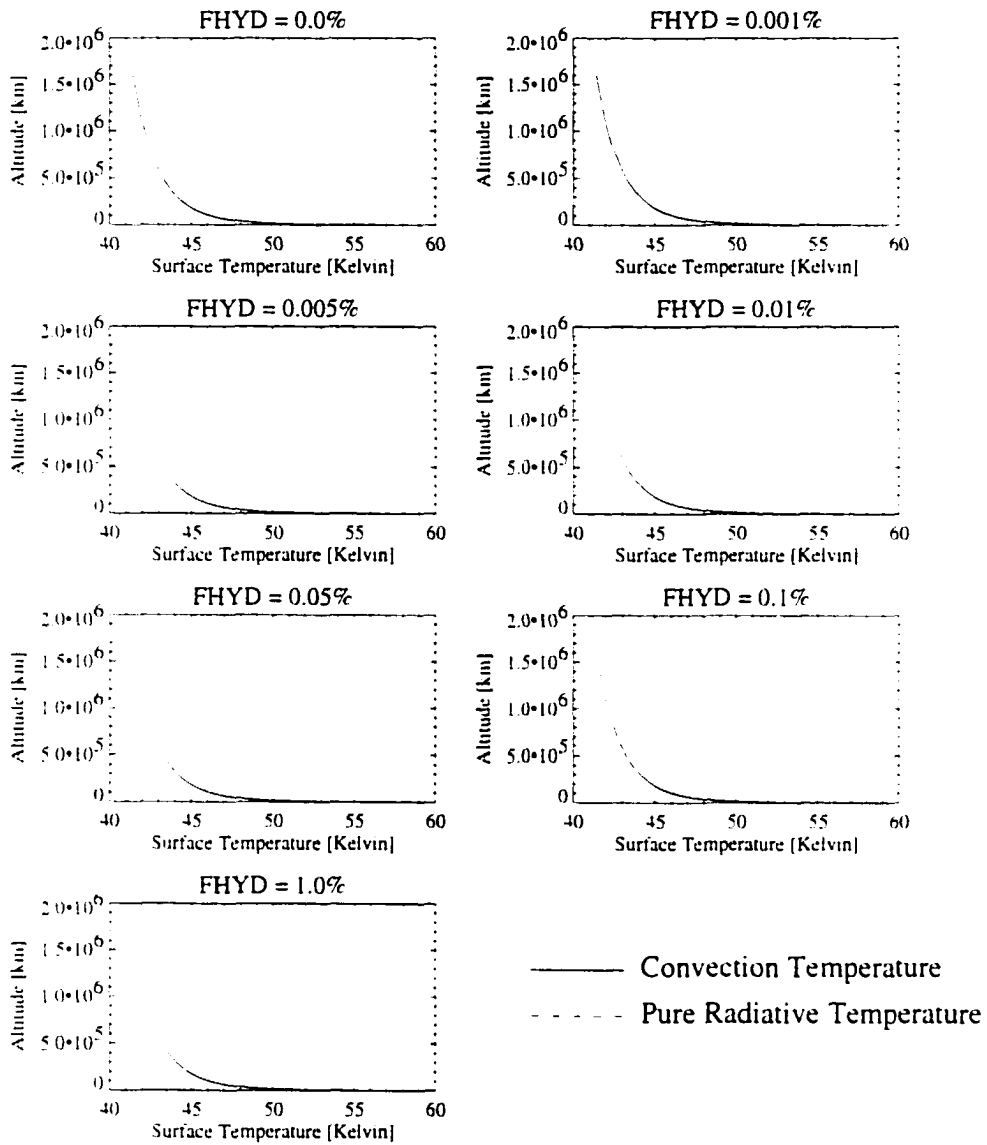


FIGURE 2.23. KBO: Altitude versus Temperature using the Chandrasekhar Mean Opacity.

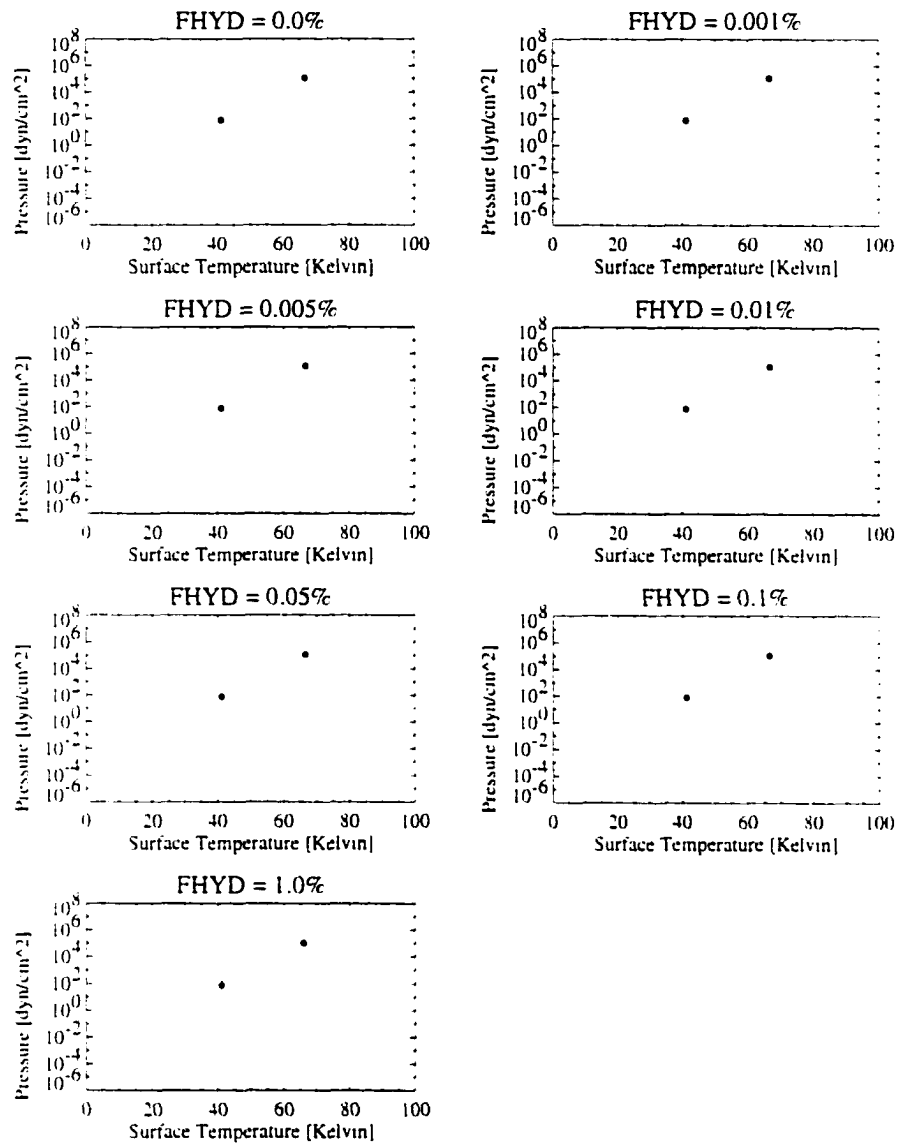


FIGURE 2.24. KBO: Pressure versus Surface Temperature using the Chandrasekhar Mean Opacity.

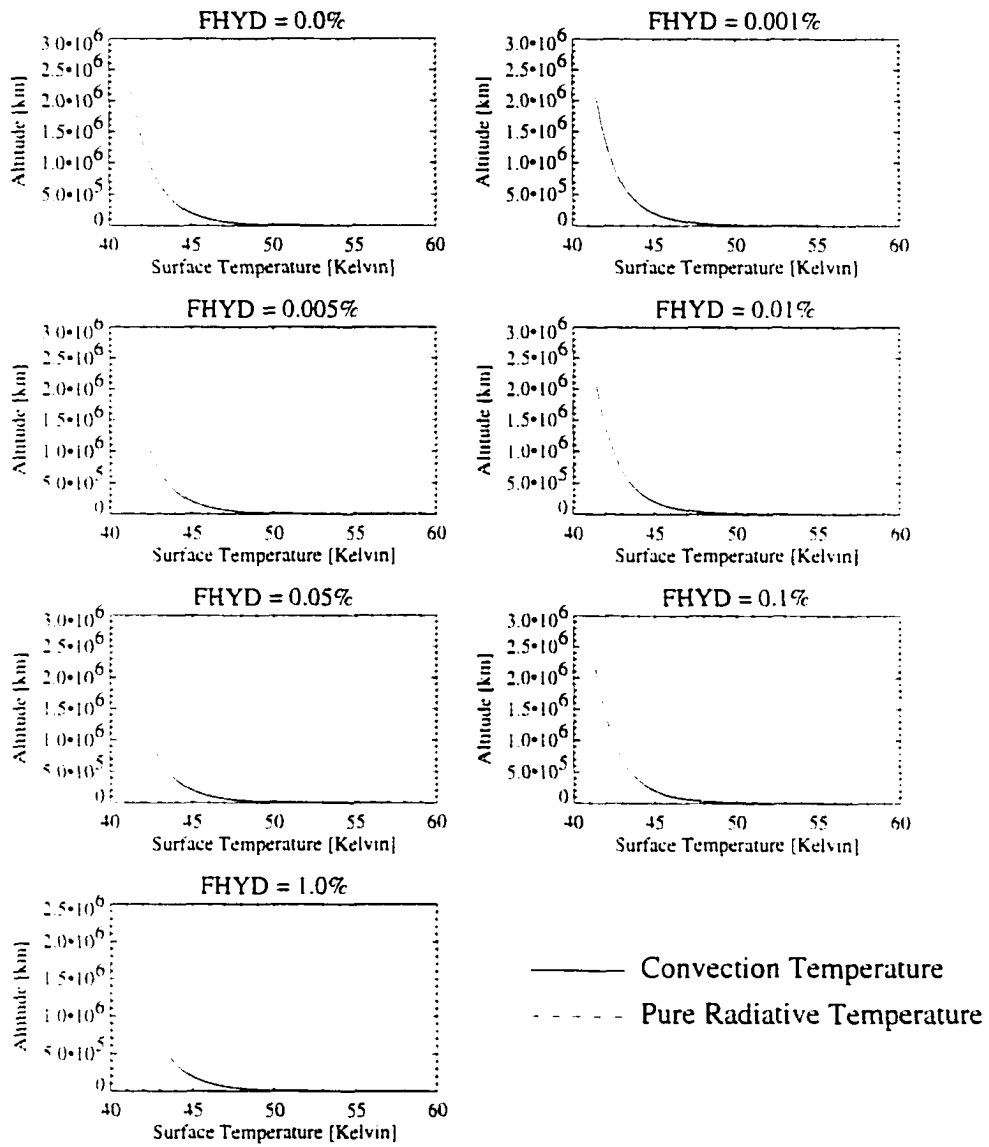


FIGURE 2.25. KBO: Altitude versus Temperature using the Planck Mean Opacity.

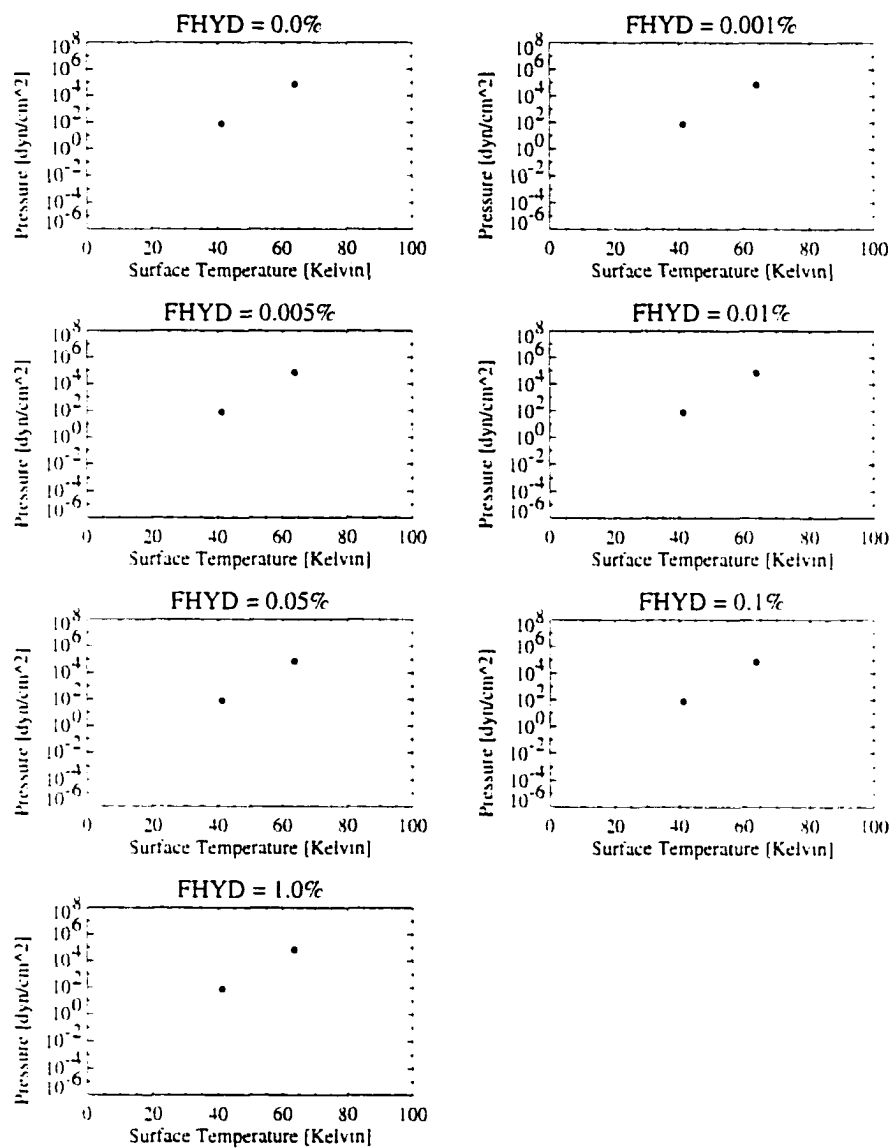


FIGURE 2.26. KBO: Pressure versus Surface Temperature using the Planck Mean Opacity.

With the Rosseland mean opacity we see that there is only one, cold solution until the H_2 concentration is around 1.0%, at which point the cold solution is joined by a hotter, more optically thick solution (see Figure 2.27).

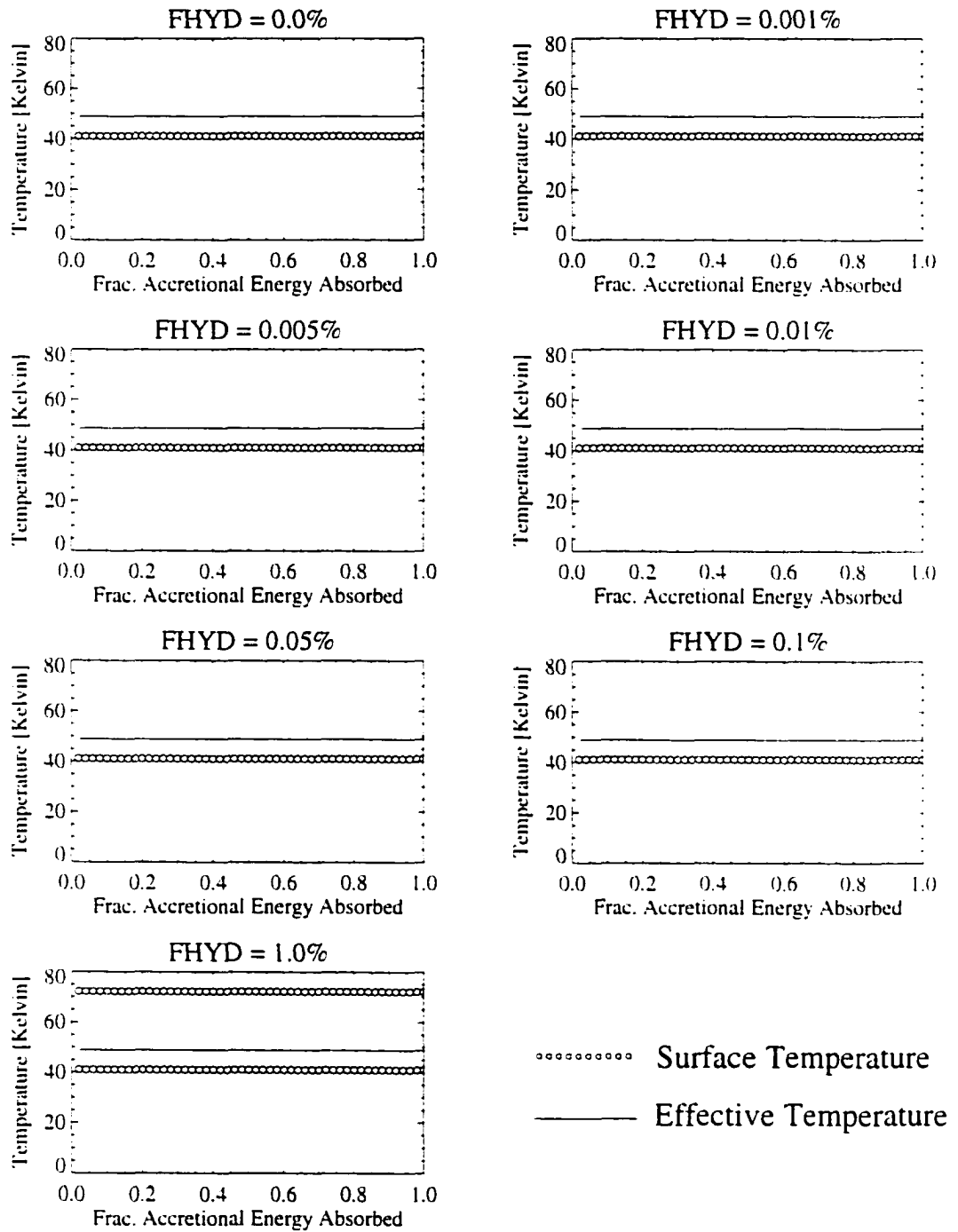


FIGURE 2.27. KBO: Temperature (Effective and Surface) versus Heat Flux with Rosseland Mean Opacity.

From Tables 2.6 and 2.7 we observe that the Rosseland mean opacity and optical depth do vary as we increase the H_2 concentration.

H_2 Conc. (%)	Solution 1	Solution 2
0.0	1.00×10^{-8}	no soln
0.001	1.34×10^{-8}	no soln
0.005	1.67×10^{-8}	no soln
0.01	1.82×10^{-8}	no soln
0.05	2.20×10^{-8}	no soln
0.1	2.42×10^{-8}	no soln
1.0	4.15×10^{-8}	1.61×10^{-7}

TABLE 2.6. KBO: Rosseland Mean Opacity [cm^2/g].

H_2 Conc. (%)	Solution 1	Solution 2
0.0	5.02×10^{-8}	no soln
0.001	6.73×10^{-8}	no soln
0.005	8.40×10^{-8}	no soln
0.01	9.13×10^{-8}	no soln
0.05	1.10×10^{-7}	no soln
0.1	1.22×10^{-7}	no soln
1.0	2.08×10^{-7}	5.68

TABLE 2.7. KBO: Optical Depth calculated with Rosseland Mean Opacity.

H_2 Conc. (%)	Solution 1	Solution 2
0.0	75.7	no soln
0.001	75.7	no soln
0.005	75.7	no soln
0.01	75.7	no soln
0.05	75.7	no soln
0.1	75.7	no soln
1.0	75.7	2.66×10^5

TABLE 2.8. KBO: Pressure [dyn/cm^2] calculated with Rosseland Mean Opacity.

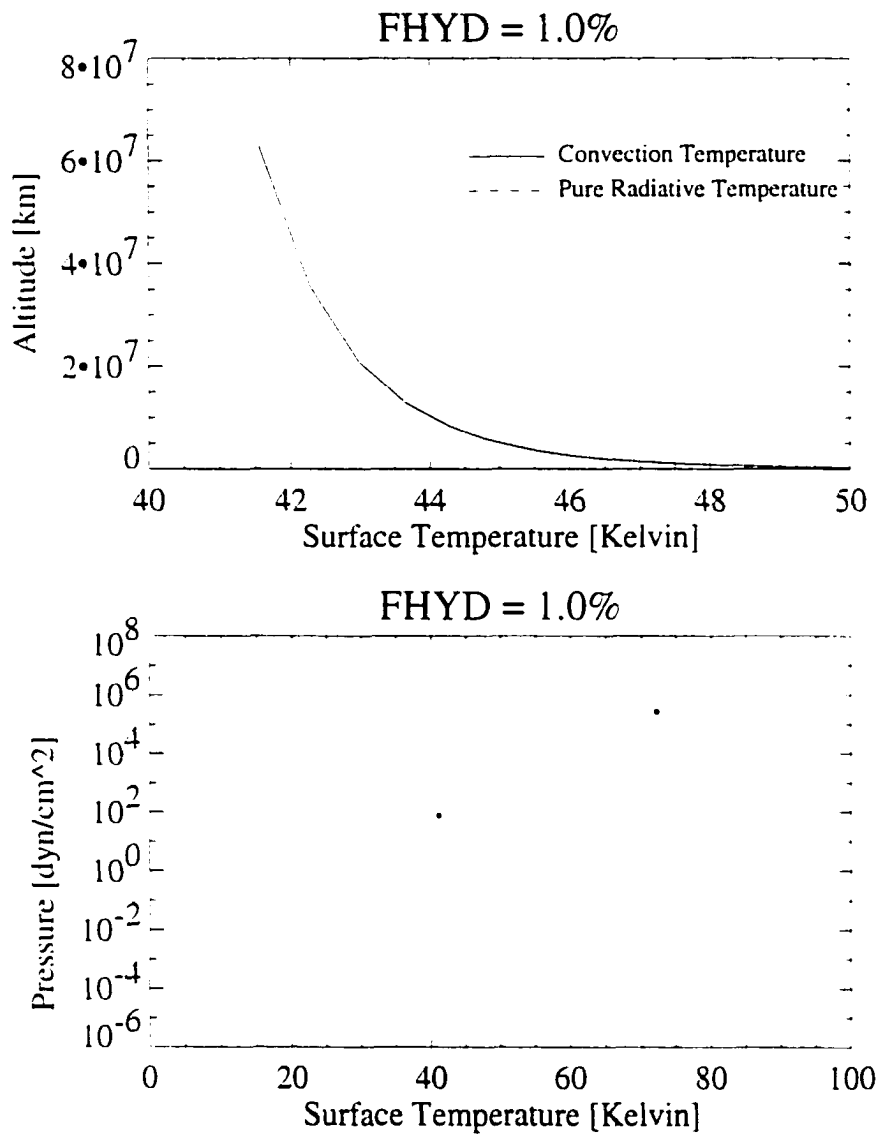


FIGURE 2.28. KBO: Altitude versus Surface Temperature. Pressure versus Surface Temperature, both with Rosseland Mean Opacity.

CHAPTER 3

NON-GREY ATMOSPHERES

To a pure mathematician, the methods described here [non-gray problem] may seem to be a “brute force” approach to the problem. In a sense, they are: certainly they lack the mathematical elegance of the solution to the gray problem. The trouble is that astronomers are trying to build models that help in the interpretation of real stars. — L. Auer

In the last chapter, we simplified the problem of atmosphere modelling by assuming a grey atmosphere. In this chapter, we develop a model for a full nongrey atmosphere. In particular, we wish to develop a frequency-dependent model of Titan’s troposphere to investigate the effect of diminishing methane on Titan’s vertical temperature profile. To this end we solve the radiative transfer equation such that the resulting temperature and density profiles satisfy radiative equilibrium (RE), hydrostatic equilibrium (HE), and local thermodynamic equilibrium (LTE) (see section 1.6 for definitions). To develop our nongrey model, we utilize some techniques found in the field of stellar atmospheres.

Our model is akin to a multi-dimensional Newton-Raphson system [126]. Here is a brief outline:

1. We make an initial estimate of the temperature and density profiles of Titan’s troposphere.
2. Using temperature and density profiles, solve the radiative transfer equation using the Ray/Moment equation approach developed by Feautrier [42] and described by Mihalas [112] [113].

3. Within a desired tolerance, check to see if the radiative transfer solution (from step 2) is in radiative and hydrostatic equilibrium.
 - (a) If true, we are done.
 - (b) Else compute a correction [63] [127] to the T and ρ profiles based on the deviation from RE and HE. Goto 2.

3.1 The Model

3.1.1 Simplifying Assumptions

IDEAL GAS See section 2.1.1.

PLANE PARALLEL ATMOSPHERE If we assume that the atmosphere can be represented by a series of parallel planes, then the geometry of the equation of transfer is simplified. We replace the distance variable s with the height variable z , where $s = z/\cos(\theta)$ (recall θ is the angle of the pencil of radiation with respect to the normal of the object surface). Thus we redefine τ_ν as the the normal optical depth $\tau_\nu = \int_z^\infty \chi_\nu \rho dz$. Then equation 1.5 becomes

$$\mu \frac{dI_\nu(\mu, \tau_\nu)}{d\tau_\nu} = I_\nu(\mu, \tau_\nu) - S_\nu. \quad (3.1)$$

where $\mu = \cos(\theta)$.

LOCAL THERMODYNAMIC EQUILIBRIUM/NO SCATTERING See section 1.6.2.

RADIATIVE EQUILIBRIUM See section 1.6.3.

METHOD OF DISCRETE ORDINATES Recall the equation of transfer:

$$\mu \frac{dI_\nu(\mu, \tau_\nu)}{d\tau_\nu} = I_\nu(\mu, \tau_\nu) - S_\nu. \quad (3.2)$$

The method of discrete ordinates rewrites $I_\nu(\mu, \tau_\nu) \equiv I_\nu^+(\tau_\nu)$ for $0 \leq \mu \leq 1$, and $I_\nu(\mu, \tau_\nu) \equiv I_\nu^-(\tau_\nu)$ for $-1 \leq \mu \leq 0$ [113]. Thus the angular variation in $I_\nu(\mu, \tau_\nu)$ is represented by pencils of radiation $I_{\nu_i} = I_\nu(\mu_i, \tau_\nu)$ and equation 3.2 can then be written as a set of coupled ODEs [113]:

$$\mu_i \frac{dI_{\nu_i}(\tau)}{d\tau_\nu} = I_{\nu_i}(\tau) - S_\nu \quad (3.3)$$

for $i = \pm 1, \pm 2, \dots, \pm M$. We can now separate the boundary conditions for transferred and reflected radiation.

Next we describe how to solve this set of differential equations.

3.1.2 Solving the Equation of Radiative Transfer

THE RAY EQUATIONS

Development of Second-Order Form We follow the framework developed by P. Feautrier [42] and described in English in [112] and [113]. As described in the previous section, the first order form of the equation of transfer (see equation 3.2) is converted to a set of coupled second-order ordinary differential equations (see equation 3.3) via the method of discrete ordinates.

$$-\mu \frac{dI_\nu^-}{d\tau_\nu} = I_\nu^- - S_\nu \quad (3.4)$$

$$+\mu \frac{dI_\nu^+}{d\tau_\nu} = I_\nu^+ - S_\nu. \quad (3.5)$$

Define a mean-intensity-like variable

$$j_{\mu\nu} \equiv \frac{1}{2} [I_\nu^+ + I_\nu^-] \quad (0 \leq \mu \leq 1) \quad (3.6)$$

and a flux-like variable

$$h_{\mu\nu} \equiv \frac{1}{2} [I_{\nu}^{+} - I_{\nu}^{-}] \quad (0 \leq \mu \leq 1) \quad (3.7)$$

Adding equations 3.4 and 3.5 results in

$$\mu \frac{d}{d\tau_{\nu}} [h_{\mu\nu}] = j_{\mu\nu} - S_{\nu}. \quad (3.8)$$

Subtracting equations 3.4 and 3.5 results in

$$\mu \frac{d}{d\tau_{\nu}} [j_{\mu\nu}] = h_{\mu\nu}. \quad (3.9)$$

Using equation 3.8 to eliminate $h_{\mu\nu}$ in equation 3.9 we get

$$\mu^2 \frac{d}{d\tau_{\nu}^2} [j_{\mu\nu}] = j_{\mu\nu} - S_{\nu}.$$

With our assumption of LTE (see equation 1.14), the above equation becomes

$$\mu^2 \frac{d^2}{d\tau_{\nu}^2} [j_{\mu\nu}] = j_{\mu\nu} - B_{\nu}(T). \quad (3.10)$$

This is known as the “ray equation” since there is a dependence on the angle μ . Though $j_{\mu\nu}$ and $h_{\mu\nu}$ are similar to the zeroth and first moments of the transfer equation, this system is closed [113]. Augmented with boundary conditions, this system solves the original radiative transfer equation.

Boundary Conditions For the typical stellar atmosphere, a diffusion boundary condition is used at the bottom of the star’s atmosphere, and a Schuster boundary condition is used at the top [112]. This is appropriate for stellar atmosphere problems where radiation is input from the center of the star and the surface optical depth is sufficiently large to satisfy the diffusion approximation ($\tau \gg 1$). Titan’s small surface optical depth (τ on the order of 3-5) suggests that instead we must use Schuster boundary conditions both at the top and the bottom of Titan’s atmosphere [126] [112] [113].

We describe the Schuster boundary conditions for the top and bottom of the atmosphere. As derived in [4] [112] [113], from equations 3.6 and 3.7 we obtain the identity $j_{\mu\nu} + h_{\mu\nu} \equiv I_{\mu\nu}$. Combining this with equation 3.9, at the upper boundary ($\tau = \tau_{min}$) we obtain

$$\mu \frac{d}{d\tau_\nu} [j_{\mu\nu}]_{\tau_{min}} = j_{\mu\nu}(\tau_{min}) - I_{\mu\nu}^- \quad (3.11)$$

and similarly for the lower boundary ($\tau = \tau_{max}$).

$$\mu \frac{d}{d\tau_\nu} [j_{\mu\nu}]_{\tau_{max}} = I_{\mu\nu}^- - j_{\mu\nu}(\tau_{max}). \quad (3.12)$$

where $I_{\mu\nu}^- \equiv I_\nu(-\mu, \tau_{min})$ and $I_{\mu\nu}^+ \equiv I(+\mu, \tau_{max})$.

We determine $I_{\mu\nu}^-$ and $I_{\mu\nu}^+$ from information known about Titan. We know that the primary source of heating for Titan comes from solar radiation absorbed and reradiated by Titan's surface in the infrared portion of the spectrum. We assume that Titan's surface and the haze layer above the radiative equilibrium region of Titan's atmosphere 1) radiate as blackbodies, 2) radiate equally over all μ [95]. With these two assumptions, we can define

$$I_{\mu\nu}^- = I_\nu^- = \epsilon^- B_\nu(T^-) \quad (3.13)$$

$$I_{\mu\nu}^+ = I_\nu^+ = \epsilon^+ B_\nu(T^+) \quad (3.14)$$

where ϵ^- , ϵ^+ are the respective emissivities, and T^- , T^+ are the corresponding blackbody temperatures. Integrating over frequency, we obtain

$$I^- = \epsilon^- \sigma (T^-)^4 / \pi$$

$$I^+ = \epsilon^+ \sigma (T^+)^4 / \pi$$

There are physical constraints on the values of I^- and I^+ . By figuring out from haze scattering how much sunlight actually gets to the surface to heat the ground

and generate the upward infrared flux, we know that the ratio of I^- to the incident sunlight on Titan is between 8 - 10% [103]. The sunlight incident on Titan (S_T) can be calculated knowing the solar constant (S_\odot) and the distance from the sun to Titan (R_T):

$$\begin{aligned} S_T &= S_\odot * \left(\frac{1AU}{R_T} \right)^2 \\ &\approx 1.52 \times 10^4 \text{ergs/cm}^2\text{s} \end{aligned}$$

The constraints on I^- are not so well-defined. We know that there is a small amount of infrared radiation emanating from the stratosphere boundary. We also know that I^- must be smaller than I^+ , otherwise Titan's atmosphere would be dominated by the infrared source from the haze, leading to a temperature inversion of what is observed. We estimate that $I^-/I^+ < 10\%$ [95].

Given the constraints above, we use the estimated values $\epsilon^+ = 0.7$, $T^+ = 105K$, $\epsilon^- = 1.0$, $T^- = 67.5K$. Now we can calculate I_ν^+ and I_ν^- from equations 3.13 and 3.14 and use them in the Schuster boundary conditions in equations 3.11 and 3.12.

Discretizing the System We follow the discretization framework described in [112]. The variables μ and ν are discretized as follows:

$$\begin{aligned} \mu \in [-1, 1] &\longrightarrow \{\mu_m : m = 1, \dots, M\} \\ \nu \in [\nu_{\min}, \nu_{\max}] &\longrightarrow \{\nu_n : n = 1, \dots, N\}. \end{aligned}$$

We use Gaussian quadrature to integrate over μ , so we choose M to be the number of Gaussian quadrature points we wish to integrate over for μ [112] [113]. Thus the spacing between the $\{\mu_m\}$ are determined by the Gaussian quadrature formula (see [130] for details on the algorithm). For integration over ν we use Weddle's rule (similar to Simpson's rule in that it is derived from the Newton-Cotes formula, but is 9th order

[155]). According to the number of terms used for Weddle's rule integration, we must choose N such that $(N \bmod 6) + 1 = 0$. The $\{\nu_n\}$ are equally spaced.

We divide the medium over a grid with D points, where $d = 1$ corresponds to $\tau = \tau_{min}$ and $d = D$ corresponds to $\tau = \tau_{max}$. The rest of the variables then follow as:

$$\begin{array}{ll} m_d, \rho_d, T_d & \{1, 2, \dots, D\} \\ \chi_{d,n}, B_{d,n} = B_n(T_d) & \{1, 2, \dots, D\}, \{1, 2, \dots, N\} \\ \Delta\tau_{d+\frac{1}{2},n} & \{1, 2, \dots, D-1\}, \{1, 2, \dots, N\} \\ J_{d,k} & \{1, 2, \dots, D\}, \{1, 2, \dots, K\} \\ h_{d-\frac{1}{2},k} & \{1, 2, \dots, D-1\}, \{1, 2, \dots, K\} \end{array}$$

where $k = m + (n-1)M$ with $K = MN$ represents the joint dependence on both μ_m and ν_n . See section 3.1.5 for a discussion of the initial values of the $m_d, \rho_d, \chi_{d,n}$ and T_d .

We use the forward Euler scheme for discretization for $d = 1, \dots, D-1$, and backward Euler for $d = D$. In this system, the general derivative formulas then become:

$$\begin{aligned} \left(\frac{dx}{d\tau}\right)_{d+\frac{1}{2}} &= \frac{[x_{d+1} - x_d]}{\Delta\tau_{d+\frac{1}{2},n}} \\ \left(\frac{d^2x}{d\tau^2}\right)_d &= \frac{\left[\left(\frac{dx}{d\tau}\right)_{d+\frac{1}{2}} - \left(\frac{dx}{d\tau}\right)_{d-\frac{1}{2}}\right]}{\Delta\tau_{d,n}} \end{aligned}$$

where

$$\begin{aligned} \Delta\tau_{d+\frac{1}{2},n} &\equiv \frac{(\chi_{d+1,n} + \chi_{d,n})(m_{d+1} - m_d)}{(\rho_{d+1} + \rho_d)} \\ \Delta\tau_{d,n} &\equiv \frac{1}{2} \left[\Delta\tau_{d+\frac{1}{2},n} + \Delta\tau_{d-\frac{1}{2},n} \right]. \end{aligned}$$

Using the above discretizations and a little algebraic manipulation, equation 3.10 becomes

$$\begin{aligned}
j_{d-1,k} \left[\frac{\mu_m^2}{\Delta\tau_{d-\frac{1}{2},n}\Delta\tau_{d,n}} \right] &+ j_{d,k} \left[\frac{-\mu_m^2}{\Delta\tau_{d,n}} \left(\frac{1}{\Delta\tau_{d-\frac{1}{2},n}} + \frac{1}{\Delta\tau_{d+\frac{1}{2},n}} \right) - 1 \right] \\
&+ j_{d+1,k} \left[\frac{\mu_m^2}{\Delta\tau_{d,n}\Delta\tau_{d+\frac{1}{2},n}} \right] = -B_{d,n}. \tag{3.15}
\end{aligned}$$

for unknowns $\{j_{d,k}\}$, with $d = 2, \dots, D-1$, $k = m + (n-1)M$, $m = 1, \dots, M$, $n = 1, \dots, N$.

To obtain a second-order boundary condition, we follow the procedure outlined in [112]: Taylor expand the outer boundary points about the points just inside the boundaries, then replace the derivatives in the Taylor expansion with the difference approximation, the boundary conditions, and the radiative transfer equation.

First we Taylor-expand:

$$j_{2,k} = j_{1,k} + \Delta\tau_{\frac{1}{2},n} \left(\frac{dj}{d\tau} \right)_1 + \frac{1}{2} \Delta\tau_{\frac{1}{2},n}^2 \left(\frac{d^2j}{d\tau^2} \right)_1 \tag{3.16}$$

$$j_{D-1,k} = j_{D,k} - \Delta\tau_{D-\frac{1}{2},n} \left(\frac{dj}{d\tau} \right)_D + \frac{1}{2} \Delta\tau_{D-\frac{1}{2},n}^2 \left(\frac{d^2j}{d\tau^2} \right)_D. \tag{3.17}$$

Then we replace the first-order derivatives with their forward/backward difference representations:

$$\begin{aligned}
\left(\frac{dj}{d\tau} \right)_1 &\equiv \frac{j_{2,k} - j_{1,k}}{\Delta\tau_{\frac{1}{2},n}} \\
\left(\frac{dj}{d\tau} \right)_D &\equiv \frac{j_{D,k} - j_{D-1,k}}{\Delta\tau_{D-\frac{1}{2},n}}.
\end{aligned}$$

Incorporating the boundary conditions from equations 3.11 and 3.12 into the above definitions we arrive at

$$\begin{aligned}
\left(\frac{dj}{d\tau} \right)_1 &= \frac{1}{\mu} (j_{1,k} - I_\nu^-) \\
\left(\frac{dj}{d\tau} \right)_D &= \frac{1}{\mu} (I_\nu^+ - j_{D,k}).
\end{aligned}$$

If we substitute the above relations in for $(\frac{dj}{d\tau})_1$ and $(\frac{dj}{d\tau})_D$, and the radiative transfer expression from equation 3.10 for $(\frac{d^2j}{d\tau^2})_1$ and $(\frac{d^2j}{d\tau^2})_D$, then we obtain

$$j_{1,k} \left[-\frac{\mu_m}{\Delta\tau_{\frac{3}{2},n}} - 1 - \frac{\Delta\tau_{\frac{3}{2},n}}{2\mu_m} \right] + j_{2,k} \left[\frac{\mu_m}{\Delta\tau_{\frac{3}{2},n}} \right] = -I_{\mu\nu}^- - \frac{\Delta\tau_{\frac{3}{2},n}}{2\mu_m} B_{1,n} \quad (3.18)$$

$$j_{D-1,k} \left[\frac{\mu_m}{\Delta\tau_{D-\frac{1}{2},n}} \right] + j_{D,k} \left[-\frac{\mu_m}{\Delta\tau_{D-\frac{1}{2},n}} - 1 - \frac{\Delta\tau_{D-\frac{1}{2},n}}{\mu_m} \right] = -I_{\mu\nu}^+ - \frac{\Delta\tau_{D-\frac{1}{2},n}}{2\mu_m} B_{D,n}. \quad (3.19)$$

For each μ_m and ν_n we have a system of D equations and D unknowns. We solve each $D \times D$ matrix using LU decomposition ([112] and [113] use Gaussian elimination). Thus for each value of μ_m and ν_n we end up with a series of solution vectors $(j_{1,k}, j_{2,k}, \dots, j_{D,k})$, where k is as previously defined. From the vectors $J_{d,k}$ we calculate the mean intensity $J_{d,\nu}$ for each frequency and depth grid point by integrating over μ [113] [4] [126]:

$$\begin{aligned} J_{d,\nu} &\equiv \frac{1}{2} \int_{-1}^1 I(\mu) d\mu = \frac{1}{2} \int_{-1}^0 I(\mu) d\mu + \frac{1}{2} \int_0^1 I(\mu) d\mu \\ &= \frac{1}{2} \int_1^0 I(-\mu)(-d\mu) + \frac{1}{2} \int_0^1 I(\mu) d\mu = \frac{1}{2} \int_0^1 I(-\mu) d\mu + \frac{1}{2} \int_0^1 I(\mu) d\mu \\ &= \frac{1}{2} \int_0^1 [I(-\mu) + I(\mu)] d\mu = \int_0^1 j_{d\mu\nu} d\mu. \end{aligned}$$

Note that we drop the d and ν subscripts for clarity. Evaluating the above integral using Gaussian quadrature, we get

$$J_{d,\nu} = \int_0^1 j_{d\mu\nu} d\mu = \sum_{m=\frac{M}{2}+1}^M w_m j_{d,m,n} \quad (3.20)$$

where $\{w_m\}$ are the Gaussian quadrature weights. We sum over $m = \frac{M}{2} + 1, \dots, M$ because range of integration is $[0, 1]$ instead of $[-1, 1]$.

Similarly,

$$\begin{aligned} H_{d,\nu} &\equiv \frac{1}{2} \int_{-1}^1 \mu I(\mu) d\mu = \int_0^1 \mu h_{d\mu\nu} d\mu \\ &= \sum_{m=\frac{M}{2}+1}^M w_m \mu_m h_{d,m,n} \end{aligned}$$

and

$$\begin{aligned} K_{d,\nu} &\equiv \frac{1}{2} \int_{-1}^1 \mu^2 I(\mu) d\mu = \int_0^1 \mu^2 j_{d\mu\nu} d\mu \\ &= \sum_{m=\frac{M}{2}+1}^M w_m \mu_m^2 j_{d,m,n}. \end{aligned}$$

We then calculate the Eddington factor

$$f_{d,\nu} \equiv \frac{K_{d,\nu}}{J_{d,\nu}}. \quad (3.21)$$

and define boundary quantities

$$h_{1,\nu} \equiv \frac{\int_0^1 j_{1\mu\nu} d\mu}{J_{1,\nu}} \quad (3.22)$$

$$h_{D,\nu} \equiv \frac{\int_0^1 j_{D\mu\nu} d\mu}{J_{D,\nu}}. \quad (3.23)$$

all of which we will require to solve the Moment equations.

THE MOMENT EQUATIONS In the method described in the previous section, we are solving a $D \times D$ linear system for every frequency and angle point, which is computationally intensive. If the material is isotropic (as it is in our case), then it

would be advantageous to eliminate repetitious angle information. One way to do this in a computationally swift manner is to use the moments of the transfer equation and close the system using the variable Eddington factors [113]. Variable Eddington factors are more accurate because they depend on the ratio of radiation moments only and thus eliminate systematic/round-off errors [113] [4]. This method, known as the variable Eddington factors method, is described in the following sections, following the framework presented in [4] and [113].

Derivation Recall the second-order form of the transfer equation (3.10):

$$\mu^2 \left(\frac{d^2 j_{\mu\nu}}{d\tau_\nu^2} \right) = j_{\mu\nu} - B_\nu(T).$$

As described in [112], if we integrate the above equation over angle variable μ , we obtain

$$\left(\frac{d^2 K_\nu}{d\tau_\nu^2} \right) = J_\nu - B_\nu(T). \quad (3.24)$$

Recalling the definition of the Eddington factor from equation 3.21, equation 3.24 becomes

$$\left(\frac{d^2 (f_\nu J_\nu)}{d\tau_\nu^2} \right) = J_\nu - B_\nu(T). \quad (3.25)$$

This is known as the “moment equation” form of the transfer equation [126].

Boundary Conditions Integration over μ transforms the boundary conditions from equations 3.18 and 3.19 to [112] [4]

$$\begin{aligned} \frac{d}{d\tau_\nu} (f_\nu J_\nu) \Big|_0 &= \int_0^1 \mu j_{\mu\nu}(0) d\mu - \int_0^1 \mu I_{\mu\nu}^- d\mu \\ \frac{d}{d\tau_\nu} (f_\nu J_\nu) \Big|_{\tau_{max}} &= \int_0^1 \mu I_{\mu\nu}^+ d\mu - \int_0^1 \mu j_{\mu\nu}(\tau_{max}) d\mu. \end{aligned}$$

For brevity, we define $II_\nu^- = \int_0^1 \mu I_{\mu\nu}^- d\mu$ and $II_\nu^+ = \int_0^1 \mu I_{\mu\nu}^+ d\mu$. Combining this notation with the equations 3.22 and 3.23, the boundary conditions above may be rewritten as

$$\begin{aligned} \frac{d}{d\tau_\nu} (f_\nu J_\nu) \Big|_0 &= h_{1,\nu} J_{1,\nu} - II_\nu^- \\ \frac{d}{d\tau_\nu} (f_\nu J_\nu) \Big|_{\tau_{max}} &= II_\nu^- - h_{D,\nu} J_{D,\nu}. \end{aligned}$$

Discretization Using the prescription for discretization from section 3.1.2 we get a scheme similar to that of equation 3.15:

$$\begin{aligned} J_{d-1,n} \left[\frac{f_{d-1,n}}{\Delta\tau_{d,n} \Delta\tau_{d-\frac{1}{2},n}} \right] &+ J_{d,n} \left[-\frac{f_{d,n}}{\Delta\tau_{d,n}} \left(\frac{1}{\Delta\tau_{d-\frac{1}{2},n}} + \frac{1}{\Delta\tau_{d+\frac{1}{2},n}} \right) - 1 \right] \\ &+ J_{d+1,n} \left[\frac{f_{d+1,n}}{\Delta\tau_{d,n} \Delta\tau_{d+\frac{1}{2},n}} \right] = -B_{d,n} \end{aligned} \quad (3.26)$$

for $d = 2, \dots, D-1$.

As in section 3.1.2 we discretize the boundary condition and use a Taylor expansion to obtain second-order accurate formulas:

$$\begin{aligned} J_{1,n} \left[f_{1,n} + \Delta\tau_{\frac{3}{2},n} h_{1,n} + \frac{1}{2} \Delta\tau_{\frac{3}{2},n}^2 \right] &+ J_{2,n} [-f_{2,n}] \\ &= \frac{1}{2} \Delta\tau_{\frac{3}{2},n}^2 B_{1,n} + \Delta\tau_{\frac{3}{2},n} II_\nu^- \end{aligned} \quad (3.27)$$

$$\begin{aligned} J_{D-1,n} [-f_{D-1,n}] &+ J_{D,n} \left[f_{D,n} + \Delta\tau_{D-\frac{1}{2},n} h_{D,n} + \frac{1}{2} \Delta\tau_{D-\frac{1}{2},n}^2 \right] \\ &= \frac{1}{2} \Delta\tau_{D-\frac{1}{2},n}^2 B_{D,n} + \Delta\tau_{D-\frac{1}{2},n} II_\nu^- \end{aligned} \quad (3.28)$$

Solving the System In the last section (3.1.2) we were able to solve each system of $D \times D$ equations for each μ_m and ν_n separately because there were no cross terms. But such is not the case for the variable Eddington factors method (equations 3.26, 3.27, 3.28): our differential equations include integrals over ν . This requires us to solve over both the n and d indices *simultaneously*. This process can be simplified by the fact that we can write our system as a block tridiagonal system (suggested by [42], described in [112] and [113]). The algorithms for solving such systems are widely known in mathematics (see [52] [155] for more details). We follow the procedure described in [112] [113] by defining

$$-\mathbf{A}_d \mathbf{J}_{d-1} + \mathbf{B}_d \mathbf{J}_d - \mathbf{C}_d \mathbf{J}_{d+1} = \mathbf{L}_d \quad (3.29)$$

for $d = 1, \dots, D$, where \mathbf{A} , \mathbf{B} , and \mathbf{C} are $N \times N$ matrices, and \mathbf{J} and \mathbf{L} are $N \times 1$ vectors

$$\begin{aligned} \mathbf{J}_d &= \{J_{d,1}, J_{d,2}, \dots, J_{d,N}\} \\ \mathbf{L}_d &= \{L_{d,1}, L_{d,2}, \dots, L_{d,N}\} \end{aligned}$$

for $d = 1, \dots, D$.

The full system looks like

$$\begin{pmatrix} \mathbf{B}_1 & -\mathbf{C}_1 & 0 & \dots & \dots & \dots & 0 \\ -\mathbf{A}_2 & \mathbf{B}_2 & -\mathbf{C}_2 & 0 & \dots & \dots & 0 \\ 0 & -\mathbf{A}_3 & \mathbf{B}_3 & -\mathbf{C}_3 & 0 & \dots & 0 \\ \vdots & \vdots & \vdots & \vdots & \vdots & \vdots & \vdots \\ 0 & \dots & \dots & 0 & -\mathbf{A}_{D-1} & \mathbf{B}_{D-1} & -\mathbf{C}_{D-1} \\ 0 & \dots & \dots & \dots & 0 & -\mathbf{A}_D & \mathbf{B}_D \end{pmatrix} \begin{pmatrix} \mathbf{J}_1 \\ \mathbf{J}_2 \\ \mathbf{J}_3 \\ \vdots \\ \mathbf{J}_{D-1} \\ \mathbf{J}_D \end{pmatrix} = \begin{pmatrix} \mathbf{L}_1 \\ \mathbf{L}_2 \\ \mathbf{L}_3 \\ \vdots \\ \mathbf{L}_{D-1} \\ \mathbf{L}_D \end{pmatrix}$$

Note that the boundary conditions imply that $\mathbf{A}_1 \equiv 0$ and $\mathbf{C}_D \equiv 0$.

As detailed in [112] and [113], an algorithm may be developed which enables us to solve the above system using Gaussian elimination.

To solve the system:

- (1) Determine the **A**, **B**, **C** matrices and the **L** vectors from equations 3.26, 3.27, and 3.28.
- (2) From the information in step (1), calculate

$$\mathbf{D}_1 \equiv \mathbf{B}_1^{-1} \mathbf{C}_1$$

$$\mathbf{v}_2 \equiv \mathbf{B}_1^{-1} \mathbf{L}_1$$

- (3) Using the information from step(2), calculate the rest of the **D**'s and **v**'s for $d = 2, D - 1$ using

$$\mathbf{D}_d \equiv [\mathbf{B}_d - \mathbf{A}_d \mathbf{D}_{d-1}]^{-1} \mathbf{C}_d$$

$$\mathbf{v}_d \equiv [\mathbf{B}_d - \mathbf{A}_d \mathbf{D}_{d-1}]^{-1} (\mathbf{A}_d \mathbf{v}_{d-1} + \mathbf{L}_d)$$

- (4) For $d = D$, recall that $\mathbf{C}_D \equiv 0$, so $\mathbf{J}_D \equiv \mathbf{v}_D$. Use \mathbf{J}_D to calculate the rest of the **J**'s using

$$\mathbf{J}_d = \mathbf{D}_d \mathbf{J}_{d+1} + \mathbf{v}_d$$

3.1.3 Developing a Correction Scheme

SATISFYING RADIATIVE EQUILIBRIUM

General Discussion Recall the condition of radiative equilibrium:

$$\int_0^\infty \chi_\nu^i (J_\nu^i - S_\nu^i) d\nu = 0 \quad (3.30)$$

where “ i ” denotes the current iteration step. If our current state of the atmosphere does not satisfy RE, then we wish to compute a correction such that

$$\int_0^\infty \chi_\nu^{i+1} (J_\nu^{i+1} - S_\nu^{i+1}) d\nu = 0 \quad (3.31)$$

where “ $i + 1$ ” denotes the next (future) step.

There are two broad approaches for proceeding from this point: complete linearization (first developed by [6]) and accelerated lambda iteration (ALI) (first conceived in [13]; various approaches are described in [112], and progressive improvements are developed in [143] [144] [121]). Complete linearization involves linearizing all variables in terms of all the other variables [4]. Though this is a powerful and easily programmable method, it is very expensive computationally since it scales as the cube of the number of unknowns [63].

The lambda operator is defined from the moment form of the radiative transfer equation, where we write J_ν in terms of a linear integral operator acting on S_ν [112] [34]:

$$J_\nu = \Lambda_\nu [S_\nu]. \quad (3.32)$$

where for each ν , if D is the number of depth points, J_ν and S_ν are $D \times 1$ vectors and Λ_ν is a $D \times D$ matrix.

Lambda iteration is then defined as [34]

$$J_\nu^{i+1} = \Lambda_\nu [S_\nu^i (J_\nu^i)]. \quad (3.33)$$

where i denotes the iteration step, and the relationship S_ν^i is often defined by $S_\nu^i (J_\nu) = (1 - \varepsilon) J_\nu^i + \varepsilon B_\nu^i$ with ε as the thermalization constant ($\varepsilon = 1$ is LTE) [113]. Lambda iteration has its disadvantages. The convergence rate is very slow for large optical depths because the eigenvalues of Λ_ν approach 1 quickly as $J_\nu \approx B_\nu$ simply because of the large optical depth, regardless of how close we actually are to radiative equilibrium [112]. Thus applying Λ_ν over successive iterations is like multiplying by

the unit matrix, and the iterations lead to a stable solution instead of converging to the real solution [127]

Accelerated lambda iteration, a.k.a. “Cannon’s method.” is known in mathematics jargon as “splitting” and is used to iteratively solve linear systems (see [157] [52] for further details). To speed up convergence of lambda iteration, employ operator splitting/lambda iteration by rewriting equation 3.33 as

$$\begin{aligned} J_\nu^{i+1} &= \Lambda_\nu^*[S_\nu^{i+1}] + (\Lambda_\nu - \Lambda_\nu^*)[S_\nu^i] \\ &= \Lambda_\nu^*[S_\nu^{i+1}] + J_\nu^i - \Lambda_\nu^*[S_\nu^i], \end{aligned} \quad (3.34)$$

where Λ_ν^* is a reduced version of Λ_ν [13]. Note that in the above equation, we do not require the full Λ_ν matrix in our computations [126].

The convergence rate for ALI can be greatly enhanced based on the choice of Λ_ν^* . In [121] it was shown that choosing Λ_ν^* equal to the diagonal of Λ_ν is “nearly optimal” [121] because of Gershgorin’s theorem, which states that for matrix A , every eigenvalue of A is contained in at least one of the circles C_i defined with centers a_{ii} (the diagonal entries of A) and radii $r_i = \sum_{j \neq i} |a_{ij}|$ [157]. Since all the elements of the Λ matrix are positive and the sum of any row is less than magnitude one, subtraction of the diagonal of the Λ matrix bounds the eigenvalues away from one [122]. Improved convergence rates can be achieved by defining Λ^* to be the tridiagonal or pentadiagonal of Λ [122].

Our Approach We combine the ideas of linearization and ALI (also called “preconditioning”), following some of the ideas and procedures employed in [34], [62], and [127].

In practice, we define the matrix \mathbf{M} from the discretized differential version of the moment equation (equation 3.26) and its boundary conditions (equations 3.27 and 3.28) to obtain $\mathbf{M}J_\nu = S_\nu$, and then define $\Lambda = \mathbf{M}^{-1}$ [126]. We also choose Λ_ν^* to be

the tridiagonal band of Λ_ν^* since this has been shown to be an optimal choice [122].

If we substitute equation 3.34 back into 3.31, and replace S_ν with $B_\nu(T)$ given that we assume LTE, we get

$$\int_0^\infty \chi_\nu^{i+1} (\Lambda_\nu^*[B_\nu^{i+1}] + J_\nu^i \Lambda_\nu^*[B_\nu^i] - B_\nu^{i+1}) d\nu = 0 \quad (3.35)$$

We use the idea of linearization, but simplify over the complete version [6] by limiting linearization to those variables we judge are necessary, and keeping the other variables fixed with respect to linearization and updating them at the next formal solution [62]. We Taylor expand equation 3.35 to first order with respect to T and ρ [126]. In addition, we do not linearize Λ^* ; instead we leave it fixed and recalculate it by resolving the radiative transfer equation with the corrected quantities in the next iteration [62]. We assume that Λ^* is not changing rapidly as T and ρ change.

The Taylor expansion of a variable, say X , is written as

$$X_d^{i+1} = X_d^i + \left(\frac{\partial X^i}{\partial T} \right)_d \Delta T_d + \left(\frac{\partial X^i}{\partial \rho} \right)_d \Delta \rho_d \quad (3.36)$$

where i indicates information from the current iteration, and d indicates the depth index. If we apply this expansion formula to equation 3.35 and discretize the integral to a sum:

$$\begin{aligned}
& \sum_{n=1}^N b_n \begin{bmatrix} \chi_{1n} + \frac{\partial \chi_{1n}}{\partial T_1} \Delta T_1 + \frac{\partial \chi_{1n}}{\partial \rho_1} \Delta \rho_1 \\ \vdots \\ \chi_{Dn} + \frac{\partial \chi_{Dn}}{\partial T_D} \Delta T_D + \frac{\partial \chi_{Dn}}{\partial \rho_D} \Delta \rho_D \end{bmatrix} \\
& + \left\{ \Lambda_n^* \begin{bmatrix} B_{1n} + \frac{\partial B_{1n}}{\partial T_1} \Delta T_1 + \frac{\partial B_{1n}}{\partial \rho_1} \Delta \rho_1 \\ \vdots \\ B_{Dn} + \frac{\partial B_{Dn}}{\partial T_D} \Delta T_D + \frac{\partial B_{Dn}}{\partial \rho_D} \Delta \rho_D \end{bmatrix} \right. \\
& + \begin{bmatrix} J_{1n} \\ \vdots \\ J_{Dn} \end{bmatrix} - \Lambda_n^* \begin{bmatrix} B_{1n} \\ \vdots \\ B_{Dn} \end{bmatrix} \\
& \left. - \begin{bmatrix} B_{1n} + \frac{\partial B_{1n}}{\partial T_1} \Delta T_1 + \frac{\partial B_{1n}}{\partial \rho_1} \Delta \rho_1 \\ \vdots \\ B_{Dn} + \frac{\partial B_{Dn}}{\partial T_D} \Delta T_D + \frac{\partial B_{Dn}}{\partial \rho_D} \Delta \rho_D \end{bmatrix} \right\} = 0 \quad (3.37)
\end{aligned}$$

where $\{b_n\}$ are the numerical integration coefficients (in our case, for Weddle's rule as mentioned in section 3.1.2). Keeping only terms to first order, we collect terms for ΔT and $\Delta \rho$ to arrive at

$$\begin{aligned}
& \sum_{j=1}^D \Delta T_j \left\{ \sum_{n=1}^N b_n \left(\Lambda_{djn}^* \chi_{dn} \frac{\partial B_{jn}}{\partial T_j} - \delta_{dj} \chi_{dn} \frac{\partial B_{dn}}{\partial T_d} + \delta_{dj} (J_{dn} - B_{dn}) \frac{\partial \chi_{dn}}{\partial T_d} \right) \right\} \\
& + \sum_{j=1}^D \Delta \rho_j \left\{ \sum_{n=1}^N b_n \left(\Lambda_{djn}^* \chi_{dn} \frac{\partial B_{jn}}{\partial \rho_j} - \delta_{dj} \chi_{dn} \frac{\partial B_{dn}}{\partial \rho_d} + \delta_{dj} (J_{dn} - B_{dn}) \frac{\partial \chi_{dn}}{\partial \rho_d} \right) \right\} \\
& = \sum_{n=1}^N b_n \chi_{dn} \{B_{dn} - J_{dn}\} \quad (3.38)
\end{aligned}$$

where we have dropped the superscript i since all terms are of the current iteration.

SATISFYING HYDROSTATIC EQUILIBRIUM If HE is not satisfied by our current iteration, we wish to calculate a correction such that HE is satisfied in the next iteration

$$\frac{dP^{i+1}}{dm^{i+1}} = g. \quad (3.39)$$

If we discretize the above equation using a simple forward difference, we get

$$\frac{P_{d+1}^{i+1} - P_d^{i+1}}{m_{d+1}^{i+1} - m_d^{i+1}} = g. \quad (3.40)$$

Using our linearization scheme from equation 3.36 and then collecting terms, our scheme from above becomes [127]

$$\begin{aligned} & \Delta T_{d-1} \left[\frac{\partial P_{d+1}}{\partial T_{d+1}} - g \frac{\partial m_{d+1}}{\partial T_{d+1}} \right] + \Delta T_d \left[-\frac{\partial P_d}{\partial T_d} + g \frac{\partial m_d}{\partial T_d} \right] + \Delta \rho_{d-1} \left[\frac{\partial P_{d+1}}{\partial \rho_{d+1}} - g \frac{\partial m_{d+1}}{\partial \rho_{d+1}} \right] \\ & - \Delta \rho_d \left[-\frac{\partial P_d}{\partial \rho_d} + g \frac{\partial m_d}{\partial \rho_d} \right] = -P_{d-1} + P_d + gm_{d+1} - gm_d \end{aligned} \quad (3.41)$$

At the upper boundary, we assume that $P_1 = gm_1$. Applying the discretization formula and collecting terms, we get [127]

$$\Delta T_1 \left[\frac{\partial P_1}{\partial T_1} - g \frac{\partial m_1}{\partial T_1} \right] + \Delta \rho_1 \left[\frac{\partial P_1}{\partial \rho_1} - g \frac{\partial m_1}{\partial \rho_1} \right] = gm_1 - P_1 \quad (3.42)$$

THE FULL CORRECTION SCHEME Now we combine the radiative and hydrostatic equilibrium correction schemes from equations 3.38, 3.41, and 3.42. This results in $2D$ equations to solve for $2D$ unknowns, namely $\{\Delta T_d, \Delta \rho_d : d = 1, D\}$. We construct the $2D \times 2D$ matrix \mathbf{P} composed of the left-hand sides of the above equations:

row 1: columns 1, . . . , D : LHS of RE equation 3.38 with $d = 1$

row 2: columns 1, . . . , D : LHS of HE equation 3.42 with $d = 1$

row 3: columns 1, . . . , D : LHS of RE equation 3.38 with $d = 2$

row 4: columns 1, . . . , D : LHS of HE equation 3.41 with $d = 2$

⋮

row $D - 3$: columns $1, \dots, D$: LHS of RE equation 3.38 with $d = D - 1$

row $D - 2$: columns $1, \dots, D$: LHS of HE equation 3.41 with $d = D - 1$

row $D - 1$: columns $1, \dots, D$: LHS of RE equation 3.38 with $d = D$

row D : columns $1, \dots, D$: LHS of HE equation 3.41 with $d = D$

We similarly construct the $2D$ vector \mathbf{b} composed of the right-hand sides of the equations 3.38 3.41 3.42. Our $2D$ vector of unknowns looks like

$$\mathbf{x} = \begin{pmatrix} \Delta T_1 \\ \Delta \rho_1 \\ \Delta T_2 \\ \Delta \rho_2 \\ \vdots \\ \Delta T_{D-1} \\ \Delta \rho_{D-1} \\ \Delta T_D \\ \Delta \rho_D \end{pmatrix}$$

Thus we solve the system $\mathbf{P}\mathbf{x} = \mathbf{b}$. Numerically we solve this system using LU decomposition.

Once the system has been solved, we add the corrections to the current temperature and density profiles. These new profiles are then used in the next iteration. When T and ρ change, however, we must recalculate several variables that depend on them:

- Recalculate P
- Recalculate $FHYD, FMET, FNIT$
- Recalculate $\chi_\nu, \bar{\chi}$

- Recalculate B_ν
- Recalculate z

TESTING FOR CONVERGENCE We measure the relative error ϵ in vector x with respect to vector y with

$$\epsilon = \frac{\|x - y\|_\infty}{\|y\|_\infty}$$

where $\|\cdot\|_\infty$ denotes the ∞ -norm.

Any norm may be used, but by using the ∞ -norm the number of correct significant digits can be obtained from above equation through the following relationship:

$$\epsilon \approx 10^{-p} \quad (3.43)$$

where p is the approximate number of significant digits for the largest component of x [52].

To test for convergence of our iterative method, we check the relative error for both radiative and hydrostatic equilibrium. For radiative equilibrium, we know that the total flux must be constant at every level of the atmosphere. Our code calculates the Eddington flux as a function of depth and frequency, $H_\nu(\tau)$; we integrate this quantity over frequency (using Weddle's rule) to obtain the total flux at each depth level τ_d , $H(\tau_d) = H_d$. Unfortunately we do not know *a priori* what this flux value should converge to, so we perform the following tests:

$$\frac{|\max_d H_{\text{current_iter}} - \min_d H_{\text{current_iter}}|}{|\min_d H_{\text{current_iter}}|} < \epsilon_{RE1} \quad (3.44)$$

to make sure that the maximum and minimum values are within our desired tolerance, i.e., the flux is constant to within our desired tolerance:

$$\frac{\|H_{\text{current_iter}} - H_{\text{previous_iter}}\|_\infty}{\|H_{\text{previous_iter}}\|_\infty} < \epsilon_{RE2} \quad (3.45)$$

to make sure the iterations are actually converging.

We perform a similar check for hydrostatic equilibrium:

$$\frac{\left\| \frac{dP}{dz} - (-\rho g) \right\|_{\infty}}{\|\rho g\|_{\infty}} < \epsilon_{HE} \quad (3.46)$$

We choose ϵ_{RE1} to be 1%: this is the standard value used in the literature [126]. We also choose ϵ_{RE2} and ϵ_{HE} to be 1% since that would imply from equation 3.43 an accuracy of 2 significant digits, which is plenty given the estimates being made in this model.

3.1.4 Nongrey Model Outline

Figure 3.1 is a flowchart of the nongrey model with all its major components.

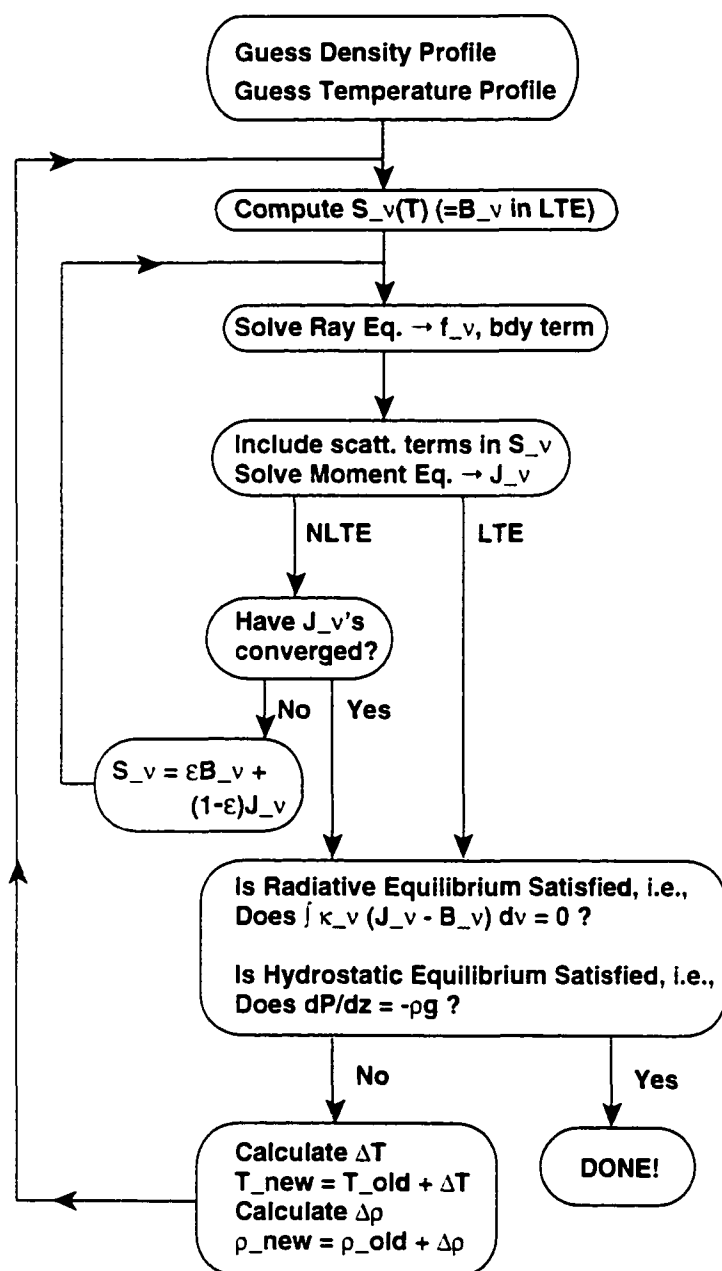


FIGURE 3.1. The Big Picture for our nongrey model of Titan's troposphere.

3.1.5 Initial Conditions/Grid Construction

Choosing the initial conditions can be a tricky process. As with Newton-Raphson iteration, we want our initial condition to lie in the basin of attraction, otherwise our iterations will diverge. Given the multi-dimension aspect of our iterative process, choosing appropriate initial conditions often involves brute-force trial and error.

Define the following Titan parameters:

- g = Titan's gravity = 135 cm/s^2 .
- T^+ , ϵ^+ = a guess for Titan's surface temperature and emissivity to estimate to what extent Titan's surface approaches a blackbody radiator in the relation $I_\nu^+ = \epsilon^+ B_\nu(T^+)$; $T^+ = 105 \text{ K}$, $\epsilon^+ = 0.7$.
- T^- , ϵ^- = a guess for Titan's upper boundary temperature and emissivity to estimate to what extent Titan's haze approaches a blackbody radiator in the relation $I_\nu^- = \epsilon^- B_\nu(T^-)$; $T^- = 67.5 \text{ K}$, $\epsilon^- = 1.0$.
- ν_{min} , ν_{max} = the maximum and minimum values of the frequency grid: this is determined by the frequency ranges of the the Planck function in the two items above and by the active frequency range of the infrared opacity: based on graphs of the Planck function and the opacity for Titan, we define $\nu_{min} = 1.0\text{e}11 \text{ Hz}$, $\nu_{max} = 3.0\text{e}14 \text{ Hz}$.
- τ_{min} = the minimum value of the optical depth grid = 10^{-3} : we need to choose a value of $\tau_{min} \ll 1$ so that the grid extent is good for numerical purposes and so we can calculate a good estimate for m_{min} : Titan's troposphere actually only extends to about $\tau = 0.02$.

- z_{max} = the maximum altitude ≈ 70 km; this value corresponds to $\tau_{min} = 10^{-3}$; Titan's troposphere actually only extends to about 42 km.
- $[CH_4]$, $[H_2]$, $[N_2]$ = the mass fractions of methane, molecular hydrogen, and molecular nitrogen at the lower boundary (set $[CH_4]$ and $[H_2]$, then $[N_2] = 1 - [CH_4] - [H_2]$).
- T_e Titan's effective temperature = 85 K; used only for the initial Titan temperature profile guess since we do not know the resulting effective temperature or net flux *a priori*.
- Initial temperature guess: using our τ grid and the guess for T_e , we use the grey approximation (see section 1.5.5).
- Equation of state: we use the ideal gas law $P = \rho k T / \bar{m}_A$.

Note that though we wish to model the troposphere, which extends to 42 km, our model extends to 70 km. This is for numerical purposes only. Our model should be compared to data [85] [170] in the 0 to 42 km range.

Define the following code parameters:

- M = number of angle grid points = 4 points: this is a typical value used in the literature for the angle quadrature.
- N = number of frequency grid points = 337 points: must be chosen to be large enough to obtain accurate integrals over frequency using Weddle's rule: as a measure of this accuracy we integrate $B_\nu(T)$ over frequency and compare this to the analytical result $\sigma T^4/\pi$...if their ratio ever goes beyond a specified tolerance the code exits with an error.
- D = number of depth grid points = 95 points: if too few points are used then numerical instabilities develop.

- *NDIAG* = number of diagonals we use from Λ to construct $\Lambda^* = 3$.
- *DAMP_ITER*. d_ρ , = the number of iterations to initially apply damping to and the density damping factor: we use *DAMP_ITER* = 5 and $d_\rho = 0.05$ to damp out some initial transient overcorrections...the code iterates nicely after such damping is applied to the first few iterations.

We now describe the steps involved in generating our initial grid. The depth grids range from $1, \dots, D$ where grid points at $d = D$ correspond to Titan surface values, and grid points at $d = 1$ correspond to values at the “top” of the atmosphere at τ_{min} , z_{max} . This is a bootstrapping method, since the value of the next grid point invariable depends on the previous grid point value [95]. Because of the way the optical depth is defined, we start at the top of the atmosphere ($d = 1$) and construct inward [126].

1. Define logarithmically-spaced $\{\tau_d : d = 1, \dots, D\}$ grid using τ_{min} and τ_{max} , where we estimate a value for τ_{max} and find-tune the value to match the choice of z_{max} .
2. Define linearly-spaced $\{\nu_n : n = 1, \dots, N\}$ grid using ν_{min} and ν_{max} .
3. Define $\{\mu_m : m = 1, \dots, M\}$ grid based on the Gaussian quadrature scheme for range $[-1, 1]$.
4. Define initial guess at temperature profile $\{T_d : d = 1, \dots, D\}$ using the Edington approximation $T_d = T_e \left(\frac{3}{4}(\tau_d + q(\tau_d))\right)^{\frac{1}{4}}$, where $q(\tau)$ is the Hopf function [112]: we calculate the Hopf function by numerically evaluating its integral form given in [112].
5. Define the source function $\{B_{\nu_n}(T_d) : d = 1, \dots, D\}$ (= Planck function = source function in LTE; see section 1.6.2).

6. Define $z_d = z_{max}$ for $d = 1$. z_{max} must be chosen to be consistent with τ_{min} : we do this by integrating atmosphere model data from [170] from the top of the atmosphere to estimate the relationship between τ and z .
7. Define $\rho_d = \rho(z_d)$ for $d = 1$ using the Titan data from [170], from which we get our initial estimate of ρ as a function of z .
8. Calculate $P_d = P(\rho_d, T_d)$ for $d = 1$ using the ideal gas law
9. Calculate $FHYD_d, FMET_d, FNIT_d$ for $d = 1$ as a function of T_d .
10. Calculate $\chi_{dn} = \chi(\rho_d, T_d, FHYD_d, FMET_d, FNIT_d)$ for $d = 1$ as described in section 1.5.3.
11. Calculate $\bar{\chi}_d = \bar{\chi}_{rosseland}$ for $d = 1$ as described in section 2.1.2: we use the Rosseland mean opacity here because empirically it gives our data the best fit to the Titan data from [85] [170]: the irony here is that if we use the Planck mean opacity, which is most appropriate for small optical depth, then our grid calculation yields an optical depth on the order of 20, which is much too high for Titan: if we use the Rosseland mean opacity, which is most appropriate for large optical depth, then our grid calculation yields an infrared optical depth on the order of 1-3, which is more in line with accepted values (2-5 [95]).
12. Calculate z_d for $d = 2$ by solving the ODE $\Delta\tau = -\bar{\chi}\Delta z$ using 4th order Runge-Kutta. we know z_1 from step 6.
13. Calculate m_d for $d = 2$ by solving the ODE. $\Delta m = -\rho\Delta z$ using 4th order Runge-Kutta. we estimate m_1 from the following formula: $m_1 \approx \tau_{min}\rho_1/\bar{\chi}_1$ [127].
14. repeat steps 7 - 13 for $d = 2, \dots, D$.

3.2 Computational Results of the Nongrey Atmosphere Model

3.2.1 Model Implementation

To solve the system described in section 3.1, we have written a 10,000-line C program that takes approximately 5 to 10 days to run, depending on the CPU speed and number of iterations required to reach convergence. These code runs were performed on PCs running Linux with either dual-466 MHz CPUs (10 days), a single 800 MHz CPU (7 days), or a single 1.2 GHz CPU (5 days). Routines from Numerical Recipes in C are used to calculate Gaussian quadrature weights and to perform matrix inversions/solve linear systems via LU decomposition and Gaussian elimination.

3.2.2 Model Inputs

We vary the mass fraction of methane and label the corresponding code runs as follows:

Run Label	CH_4 %	H_2 %
Titan 1	10	0.2
Titan 2	5	0.2
Titan 3	1	0.2
Titan 4	0.1	0.04

TABLE 3.1. Code run labels with their corresponding volatile concentrations.

Note that code runs Titan 1-3 are modelling current Titan with varying amounts of methane. The Titan 4 code run is intended as a preliminary code run of past Titan, where we maintain the current solar radiation levels but reduce the amount of methane well below the currently accepted range of 2-10% (thus we must also reduce the amount of molecular hydrogen since methane is its source via photolysis).

3.2.3 Model Results

Note that in the following figures, the term “Lindal/Yelle data” shall refer to output from a data analysis model based on Voyager I data [85], and then rescaled to correspond to a volatile inventory of N_2 : 95%, CH_4 : 3%, Ar : 2% [170]. The labels “Titan 1”, “Titan 2”, “Titan 3”, and “Titan 4” correspond to the descriptions in Table 3.1.

The Lindal/Yelle data specifies the following error deviations: the surface temperature is 94.0 ± 0.7 K, the temperature at the top of the troposphere is 71.4 ± 0.5 K, and the pressure at the surface is $1.496 \times 10^6 \pm 2.0 \times 10^4$ dyn/cm² [85]. To estimate the error bars for the entire troposphere temperature profile from Lindal/Yelle, we use the average value, ± 0.6 K. For the pressure profile, we use the error ratio from the surface, i.e., at z the error in $P(z)$ is given by $\pm(2.0 \times 10^4 / 1.496 \times 10^6) \times P(z)$ dyn/cm².

TITAN 1

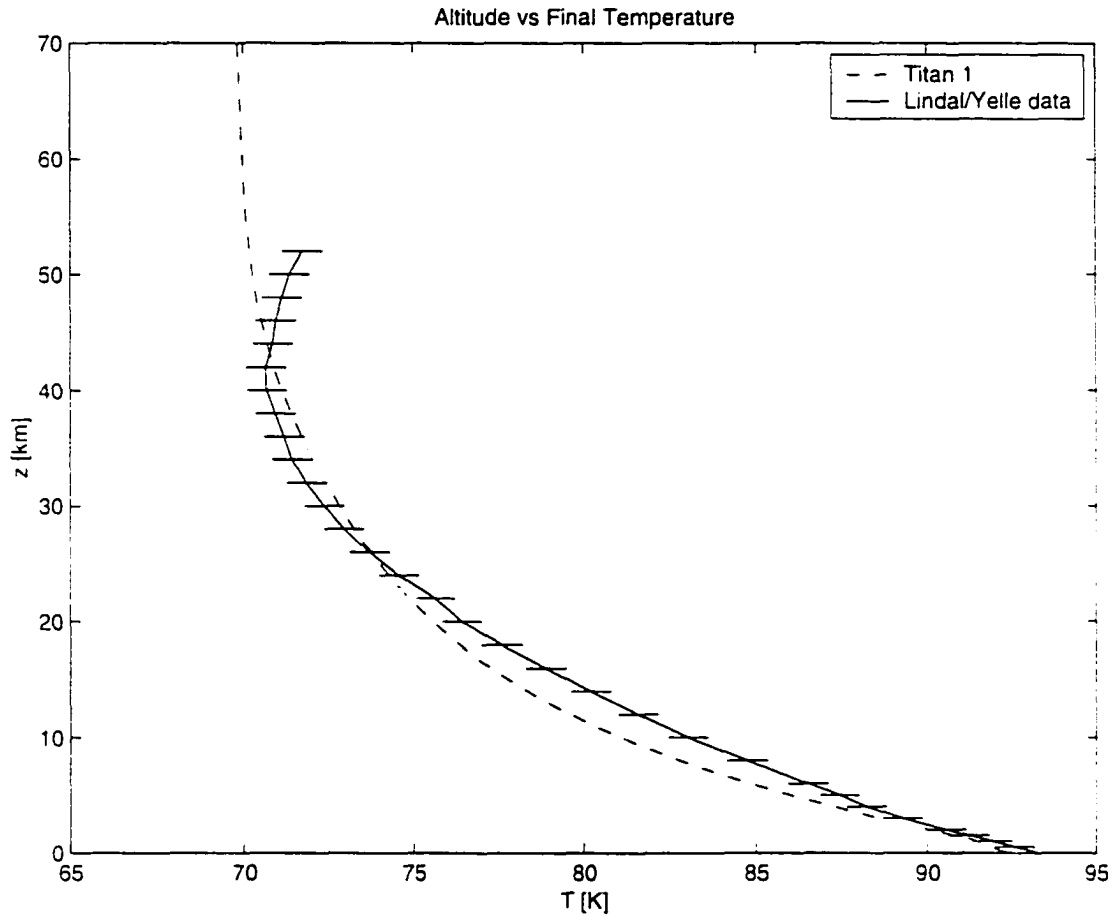


FIGURE 3.2. Titan 1: Altitude [km] versus Temperature [K]. The "Lindal/Yelle data" are from [85] [170].

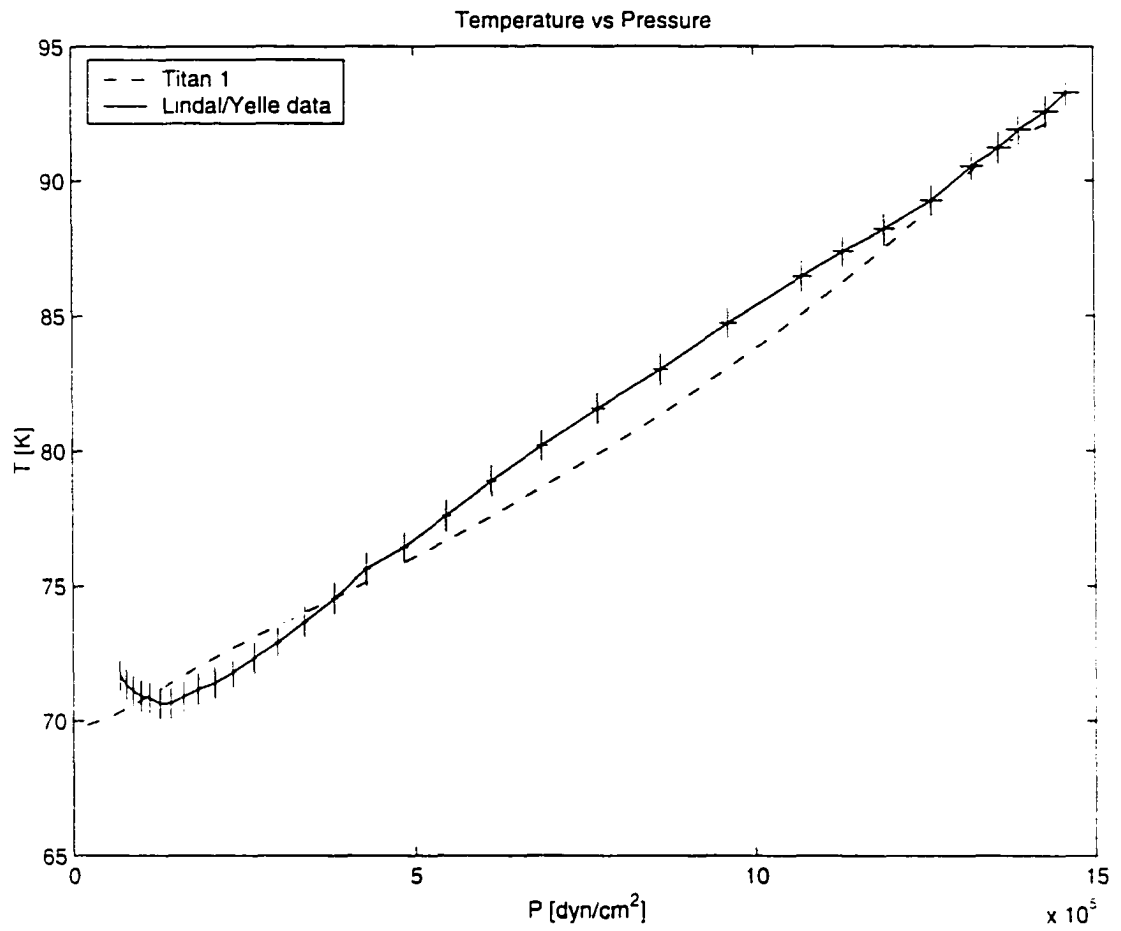


FIGURE 3.3. Titan 1: Temperature [K] versus Pressure [dyn/cm²]. The "Lindal/Yelle data" are from [85] [170].

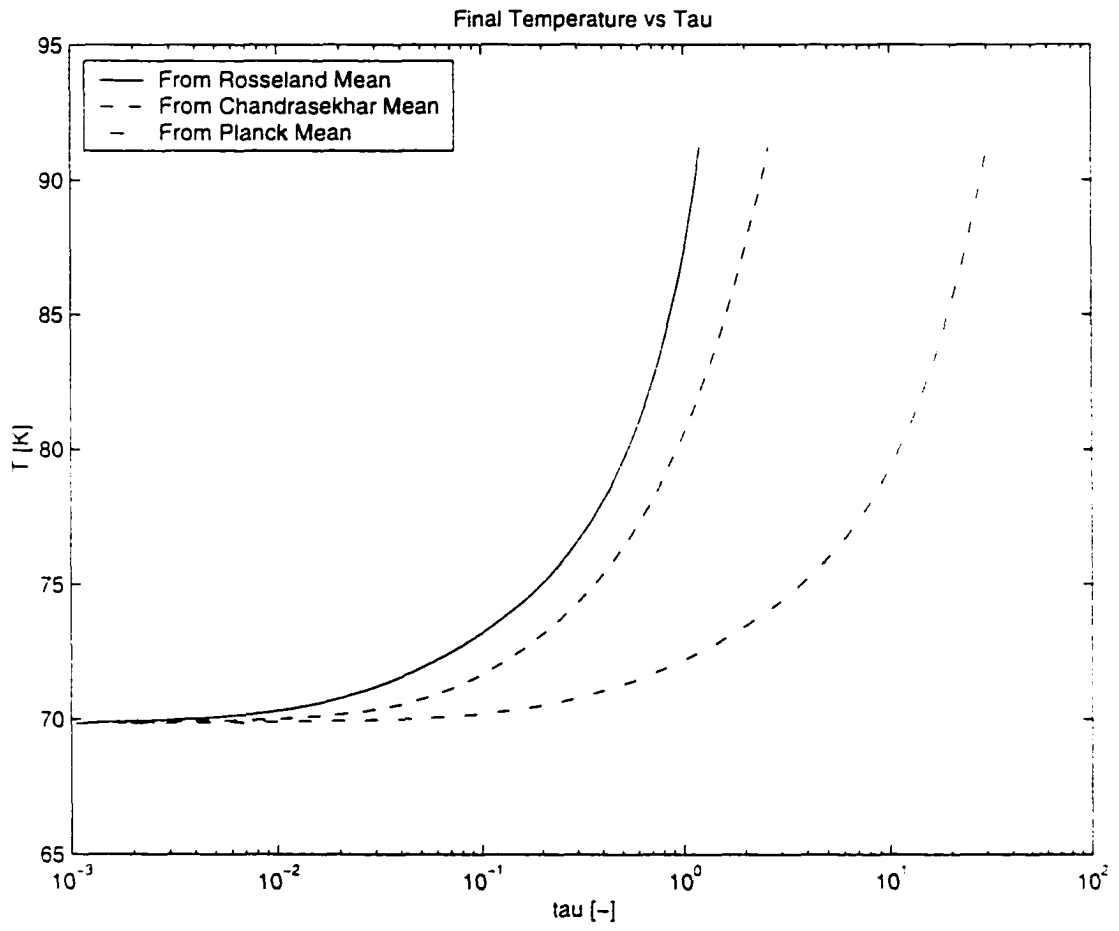


FIGURE 3.4. Titan 1: Temperature [K] versus $\tau_{\text{Rosseland}}$ [-].

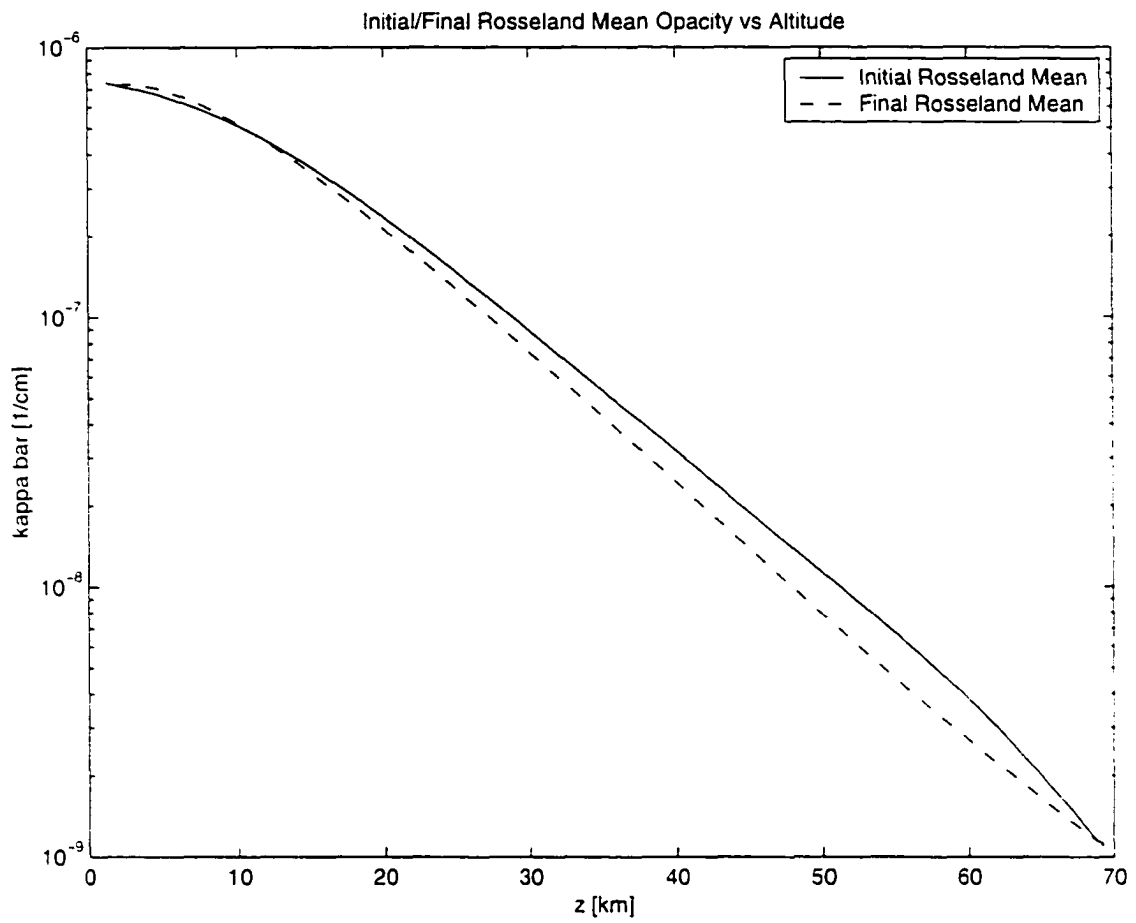


FIGURE 3.5. Titan 1: Initial/Final Rosseland Mean Opacity [$1/\text{cm}$] versus Temperature [K].

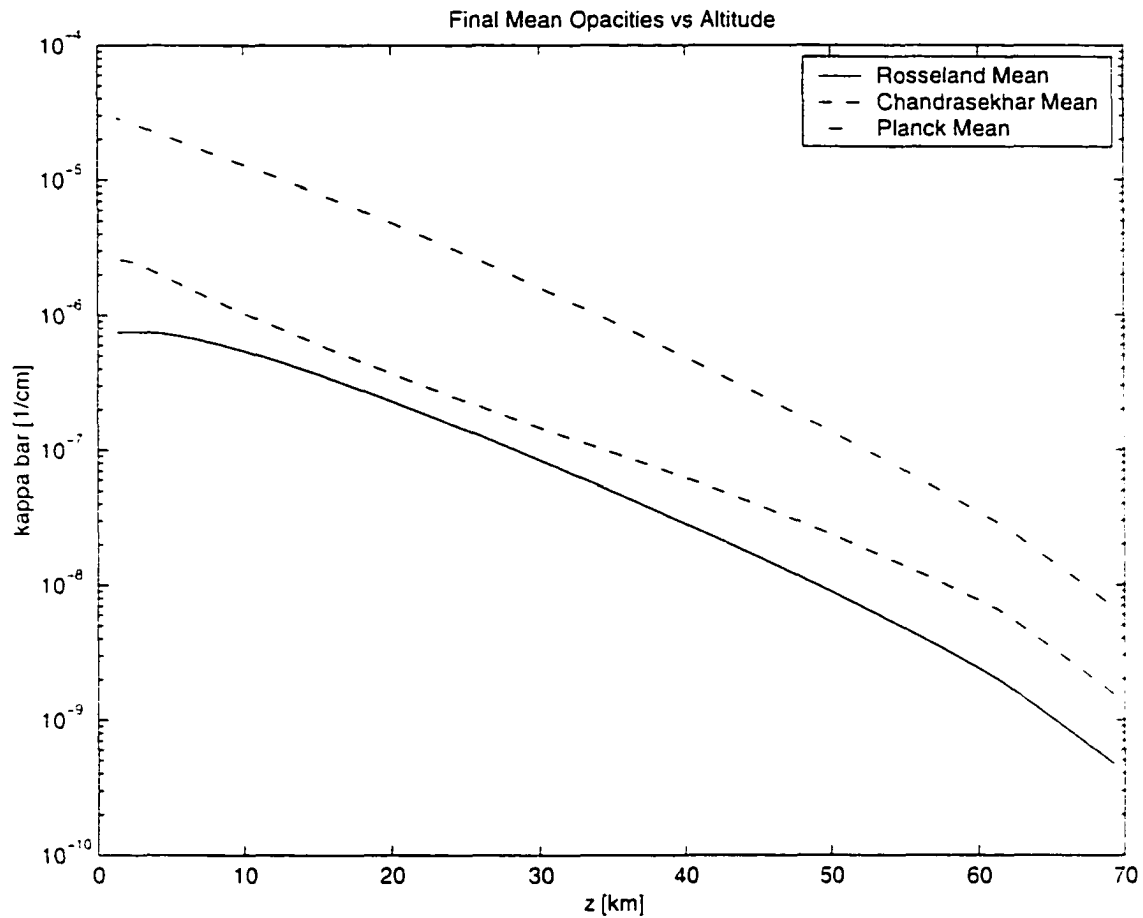


FIGURE 3.6. Titan 1: Final Rosseland, Chandrasekhar, and Planck Mean Opacities [1/cm] versus Altitude [km].

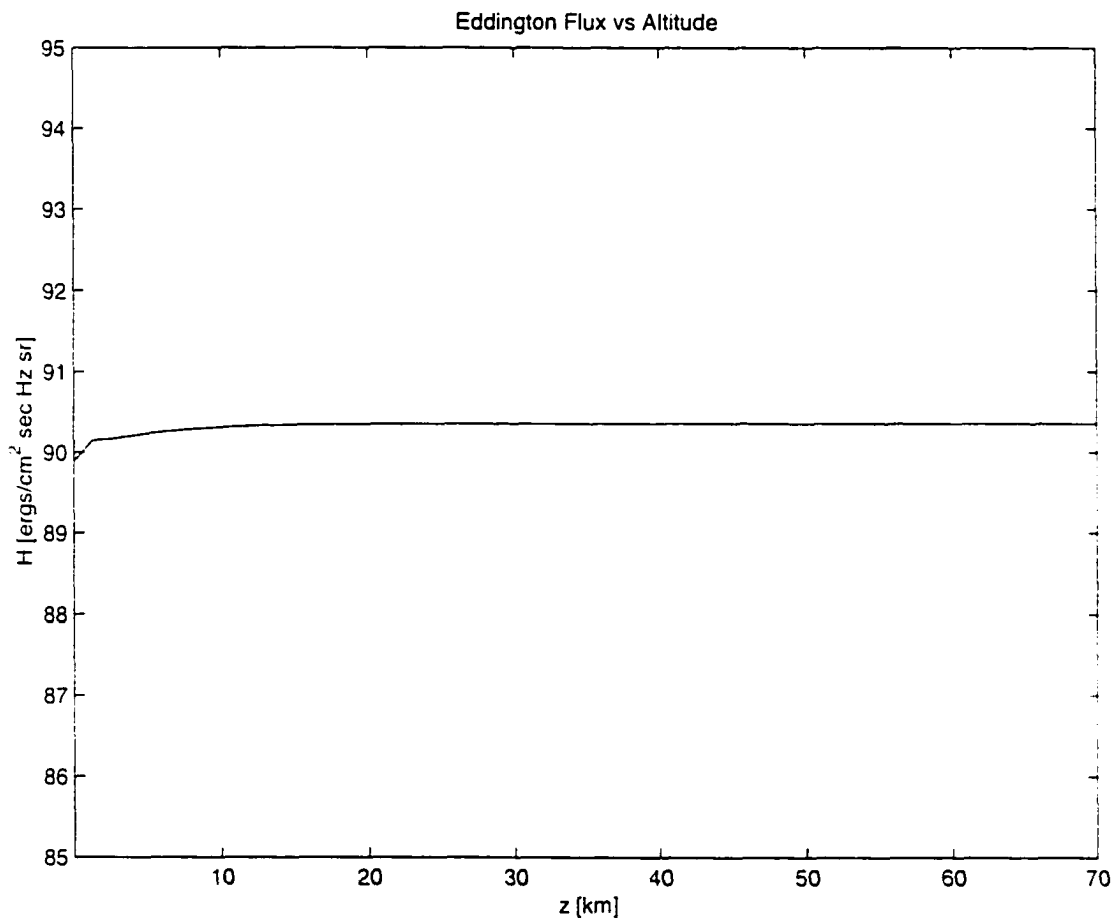


FIGURE 3.7. Titan 1: Eddington flux [ergs/cm² sec Hz sr] versus Altitude [km]. The flux is constant to within 1% ($(H_{max} - H_{min})/H_{max} < 0.01$). This yields an effective temperature of 67 K.

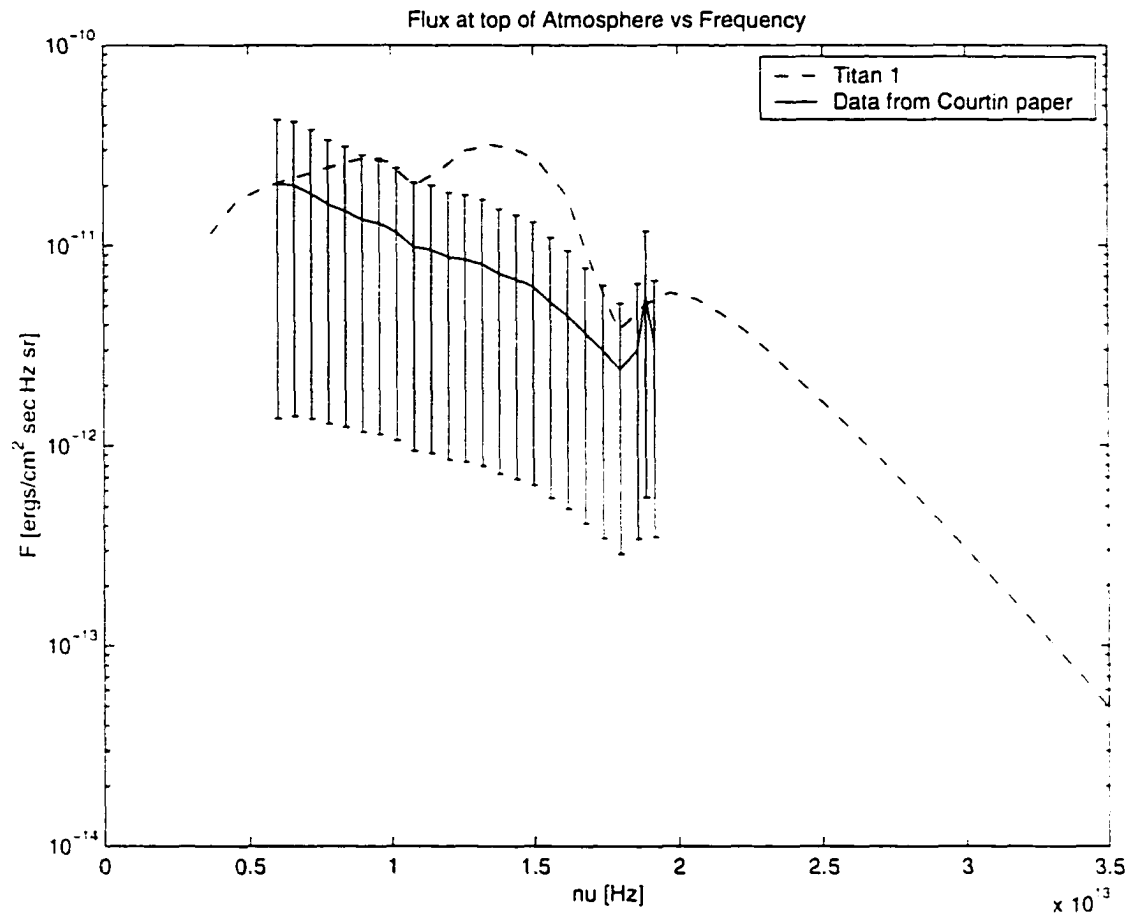


FIGURE 3.8. Titan 1: Flux [ergs/cm² sec Hz sr] versus Frequency [Hz]. The "Data from Courtin paper" is taken from a brightness temperature graph [23] and converting it back to a flux value.

TITAN 2

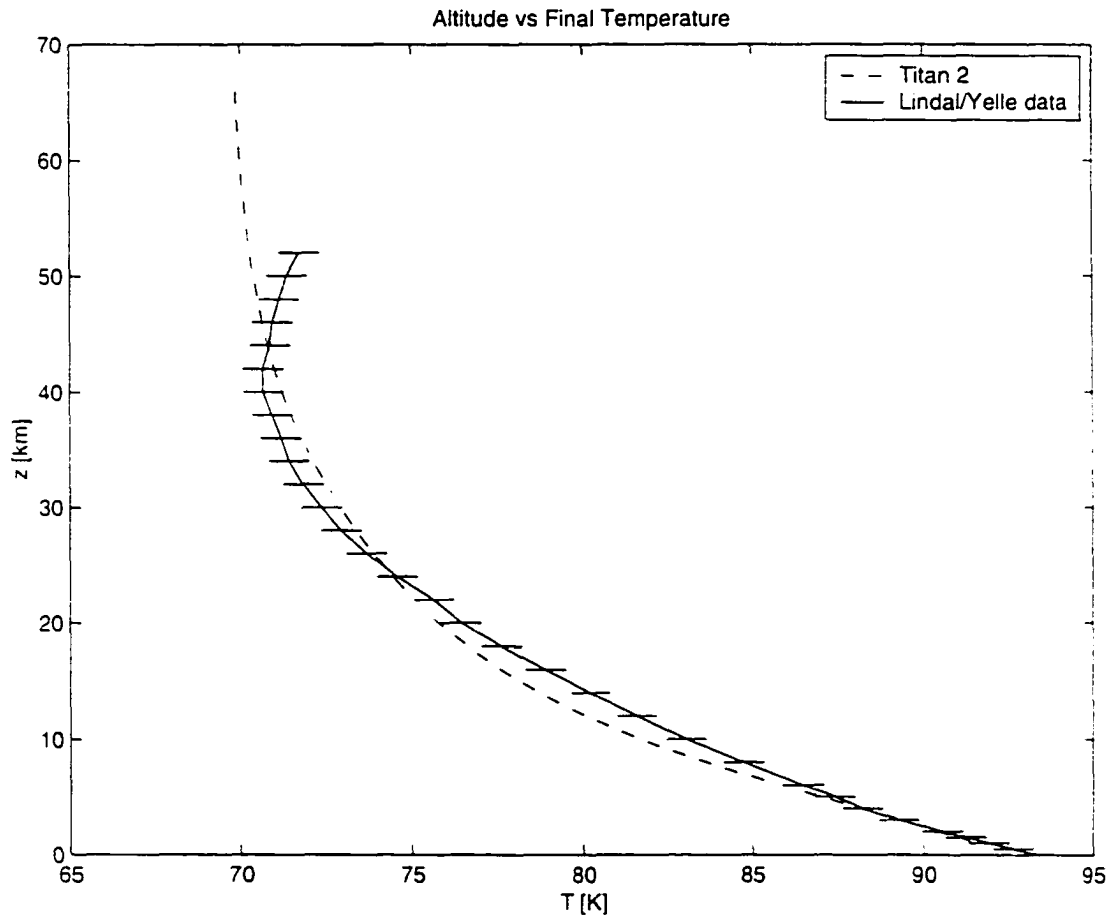


FIGURE 3.9. Titan 2: Altitude [km] versus Temperature [K]. The "Lindal/Yelle data" are from [85] [170].

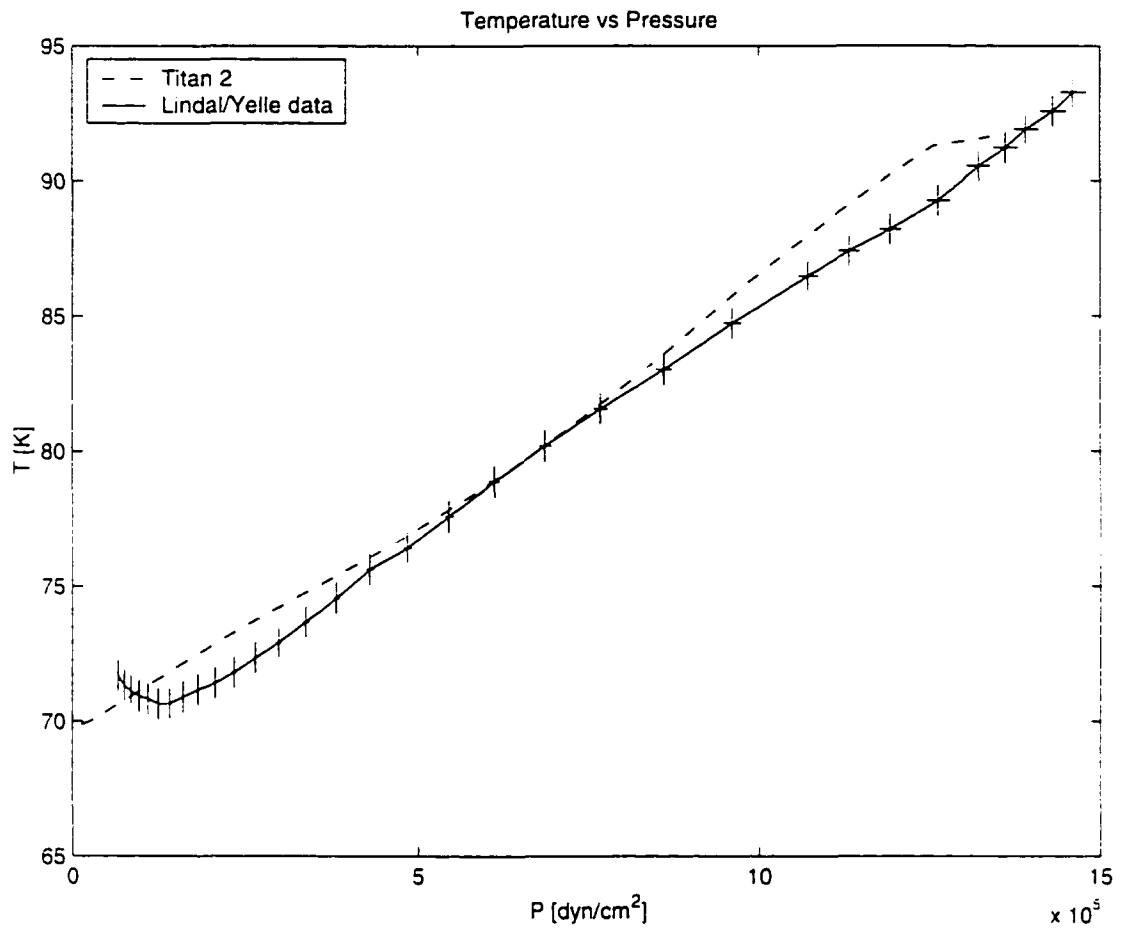


FIGURE 3.10. Titan 2: Temperature [K] versus Pressure [dyn/cm²]. The "Lindal/Yelle data" are from [85] [170].

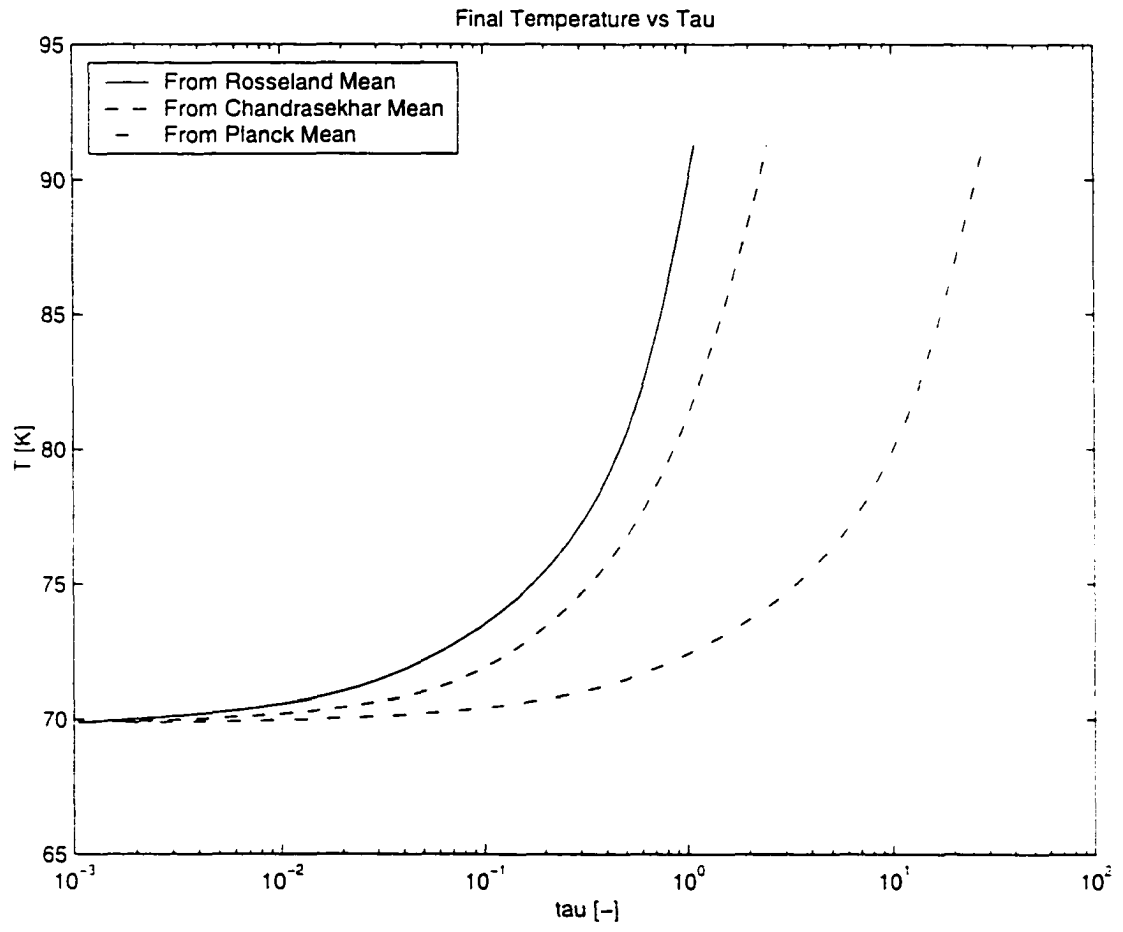


FIGURE 3.11. Titan 2: Temperature [K] versus $\tau_{\text{rosseland}}$ [-].

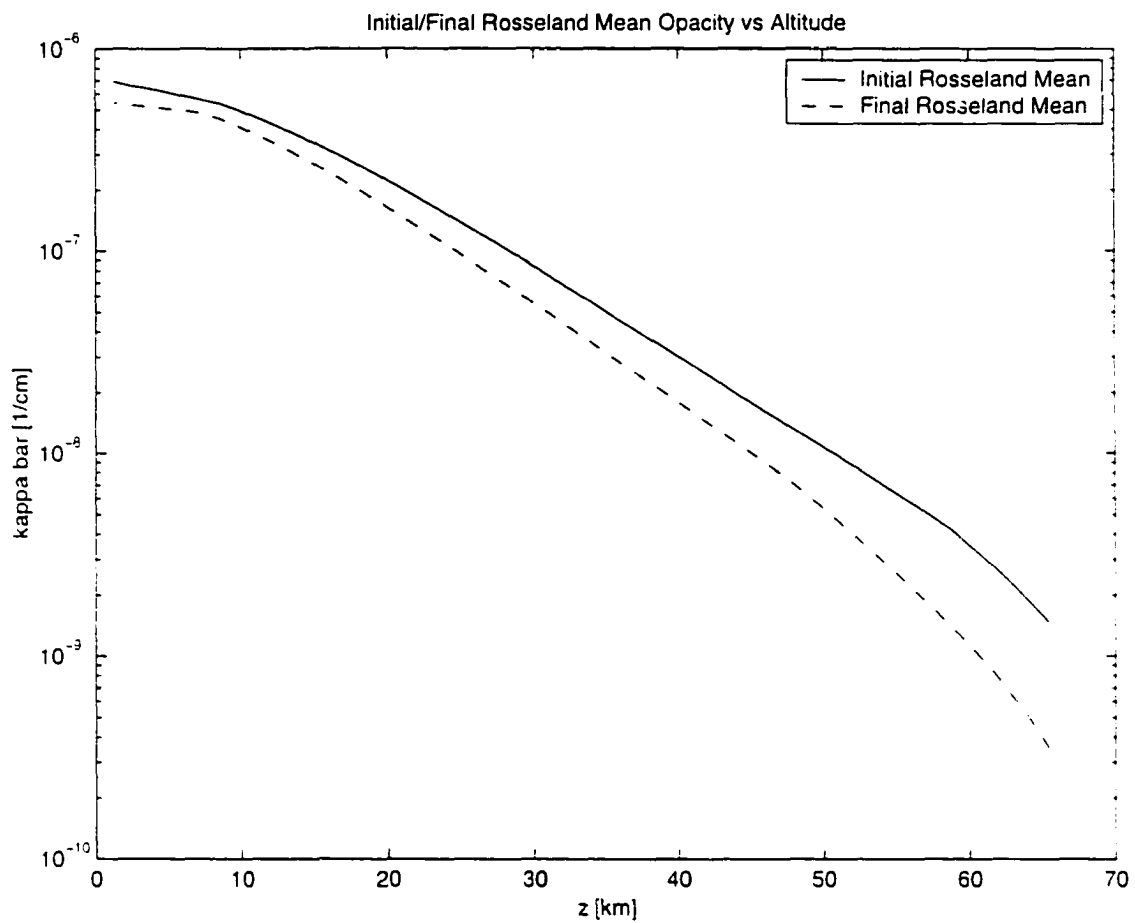


FIGURE 3.12. Titan 2: Initial/Final Rosseland Mean Opacity [1/cm] versus Temperature [K].

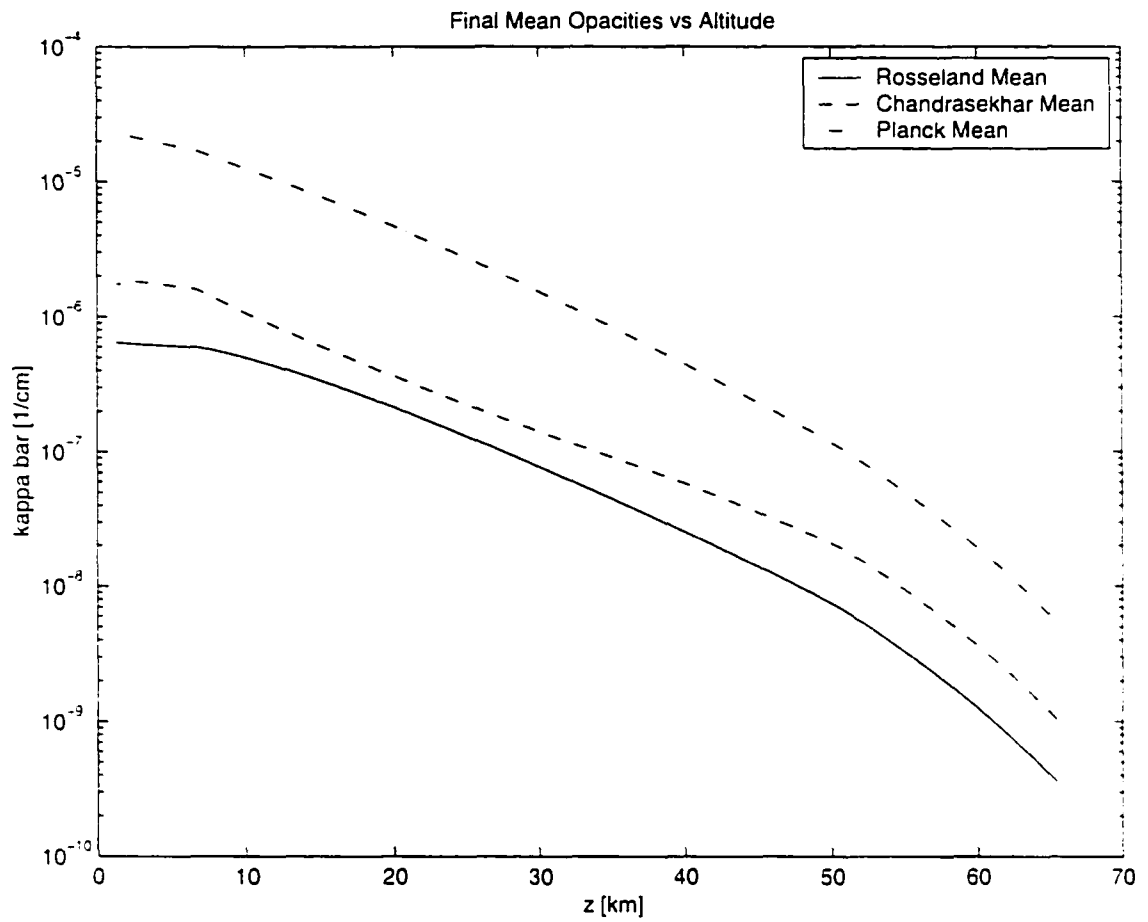


FIGURE 3.13. Titan 2: Final Rosseland, Chandrasekhar, and Planck Mean Opacities [1/cm] versus Altitude [km].

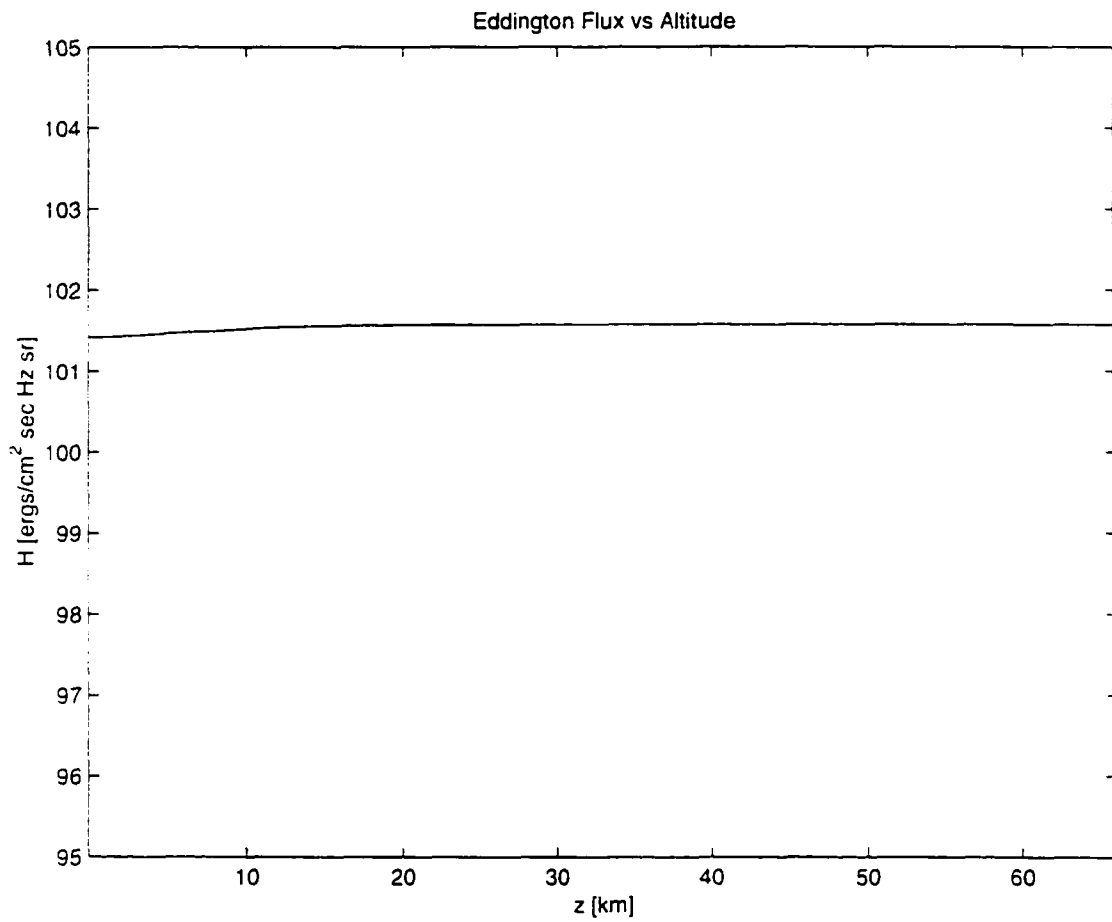


FIGURE 3.14. Titan 2: Eddington flux [ergs/cm² sec Hz sr] versus Altitude [km]. The flux is constant to within 1% ($(H_{max} - H_{min})/H_{max} < 0.01$). This yields an effective temperature of 69 K.

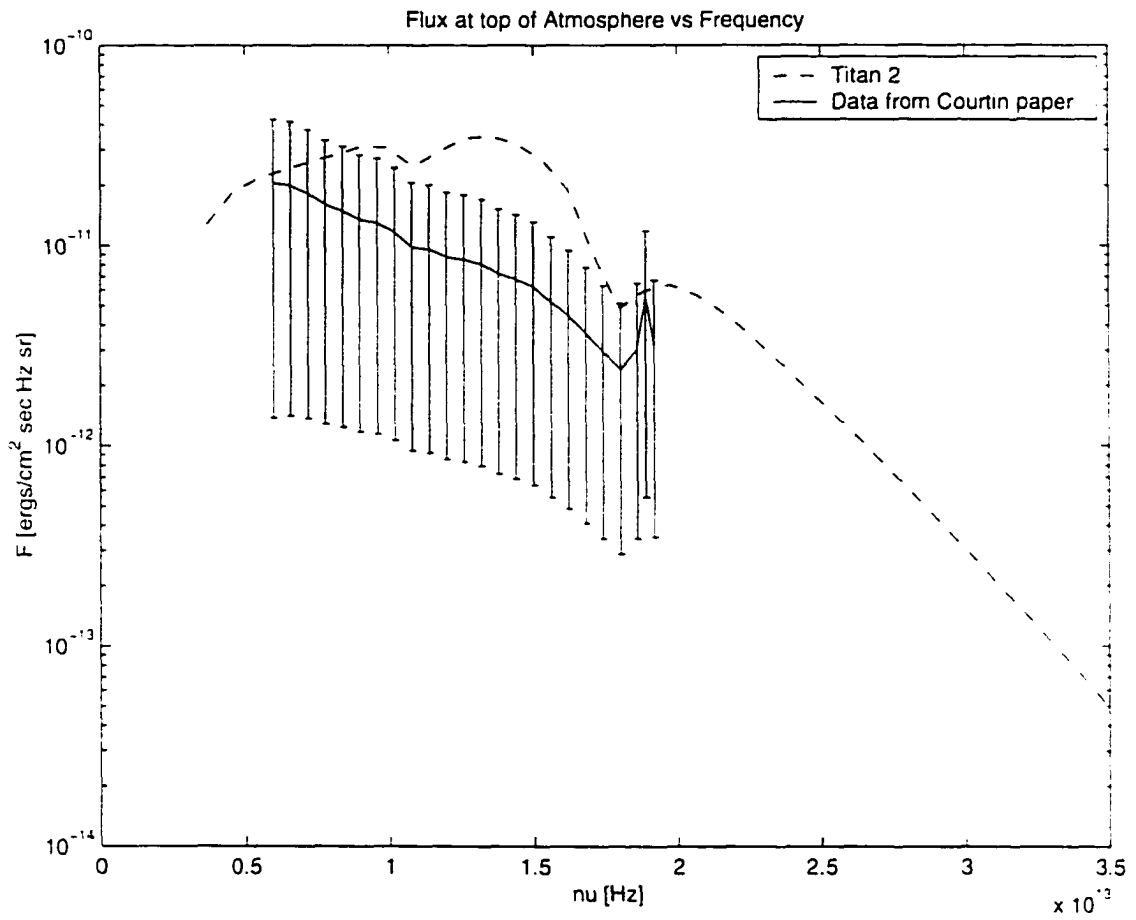


FIGURE 3.15. Titan 2: Flux [ergs/cm² sec Hz sr] versus Frequency [Hz]. The "Data from Courtin paper" is taken from a brightness temperature graph [23] and converting it back to a flux value.

TITAN 3

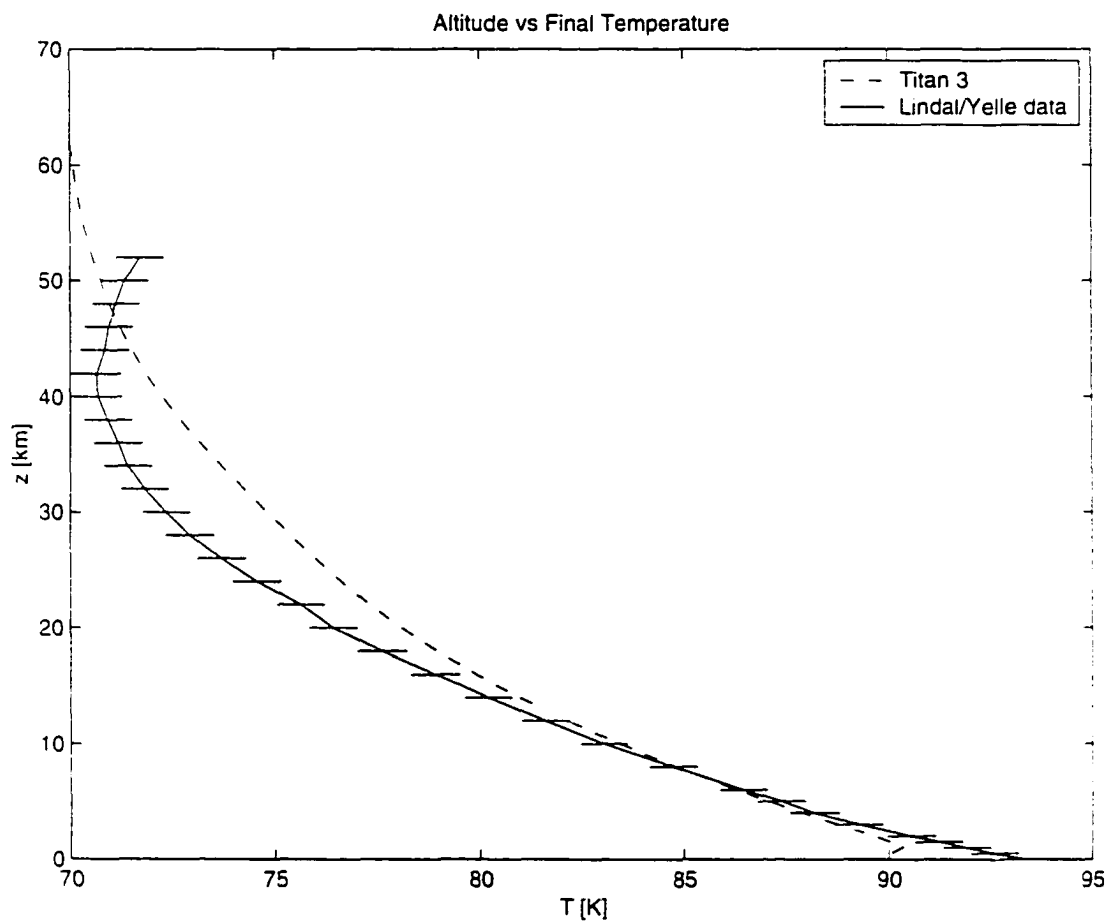


FIGURE 3.16. Titan 3: Altitude [km] versus Temperature [K]. The “Lindal/Yelle data” are from [85] [170].

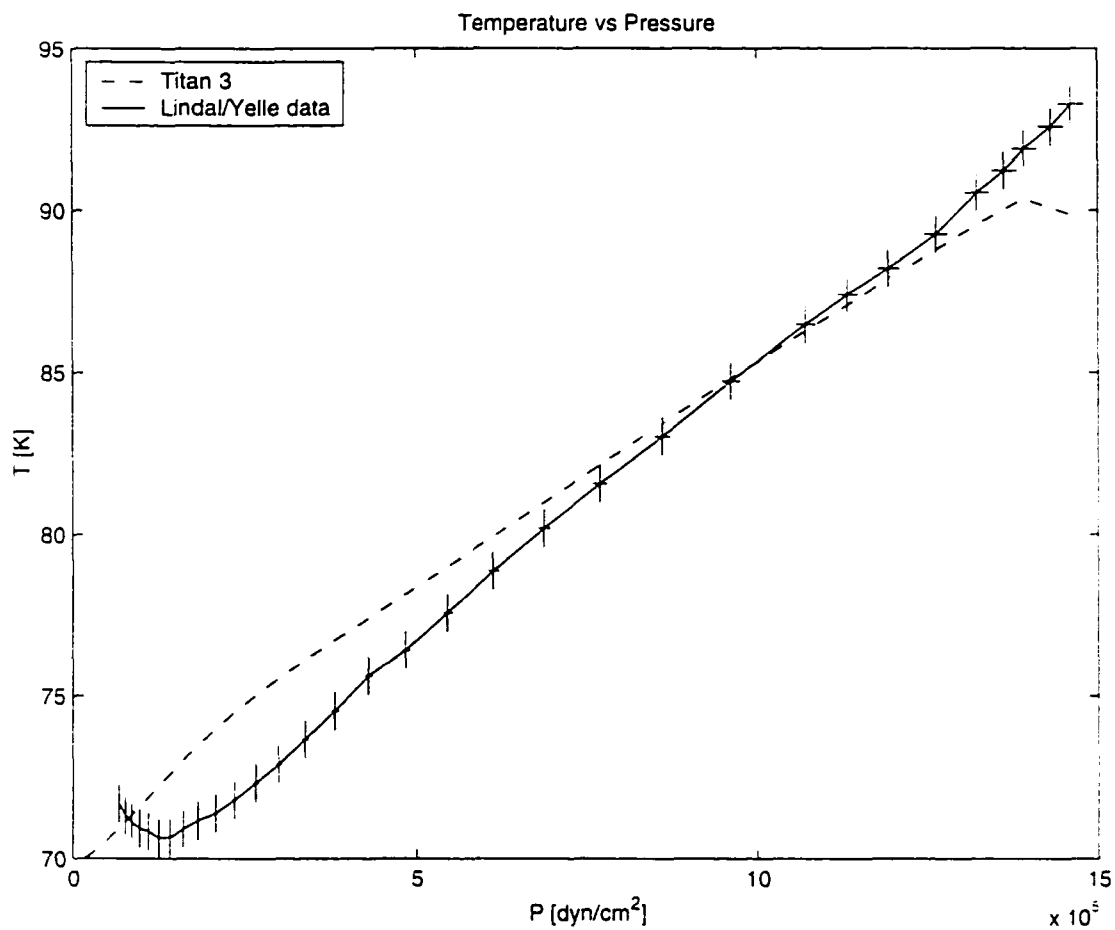


FIGURE 3.17. Titan 3: Temperature [K] versus Pressure [dyn/cm²]. The "Lindal/Yelle data" are from [85] [170].

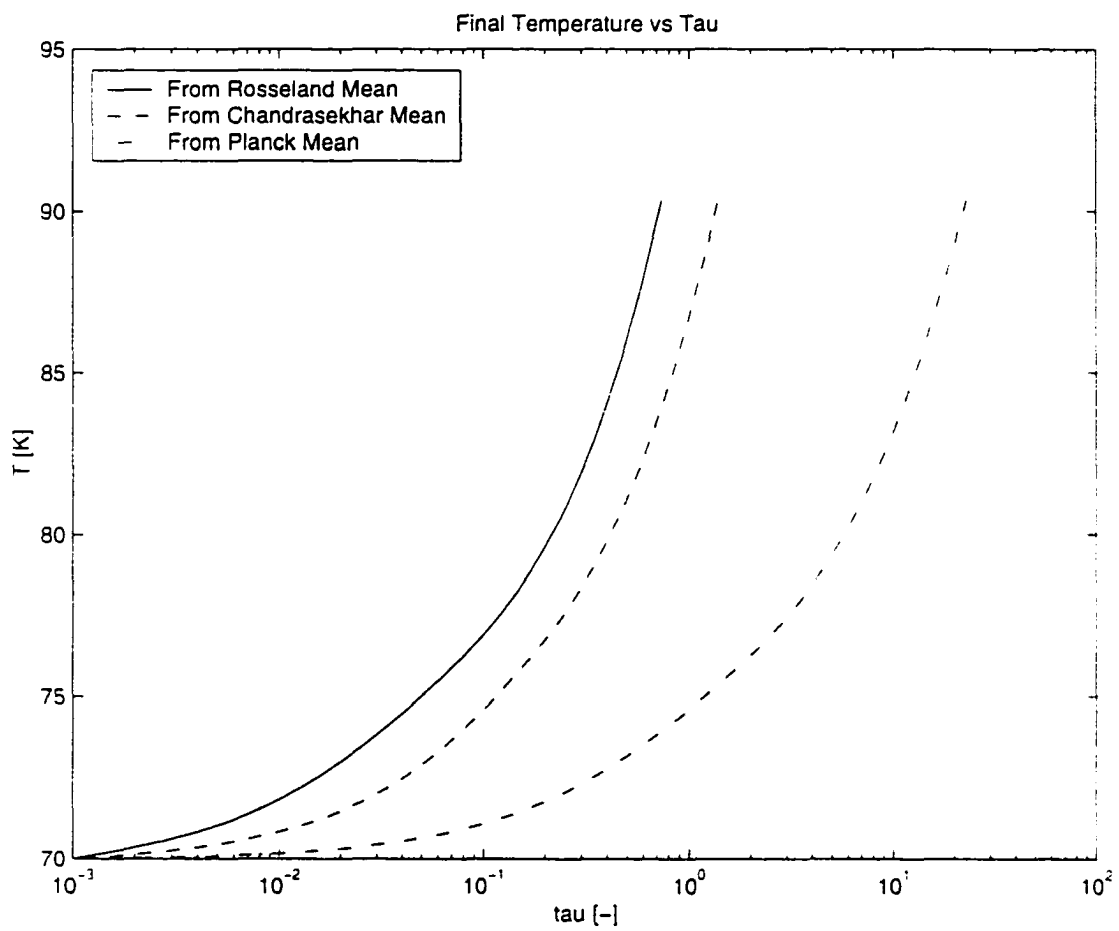


FIGURE 3.18. Titan 3: Temperature [K] versus $\tau_{\text{rosseland}}$ [-].

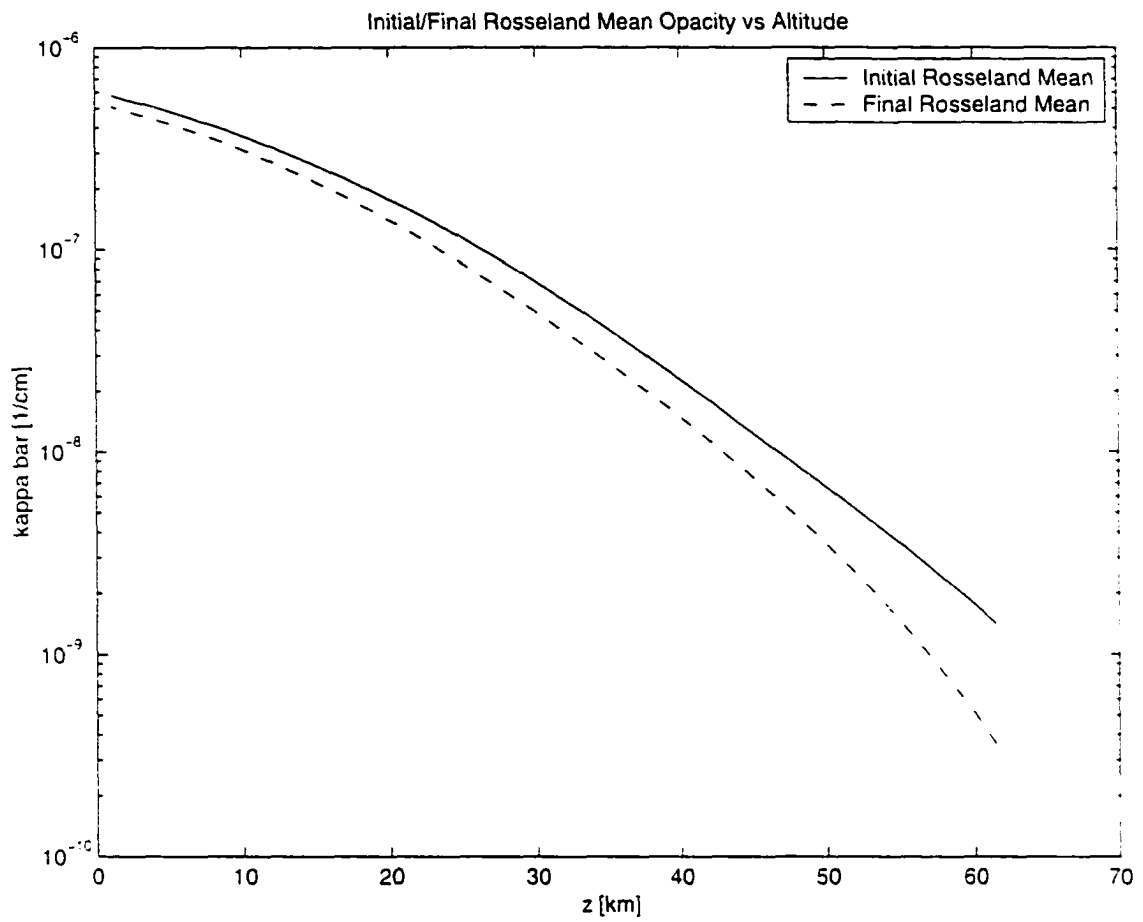


FIGURE 3.19. Titan 3: Initial/Final Rosseland Mean Opacity [1/cm] versus Temperature [K].

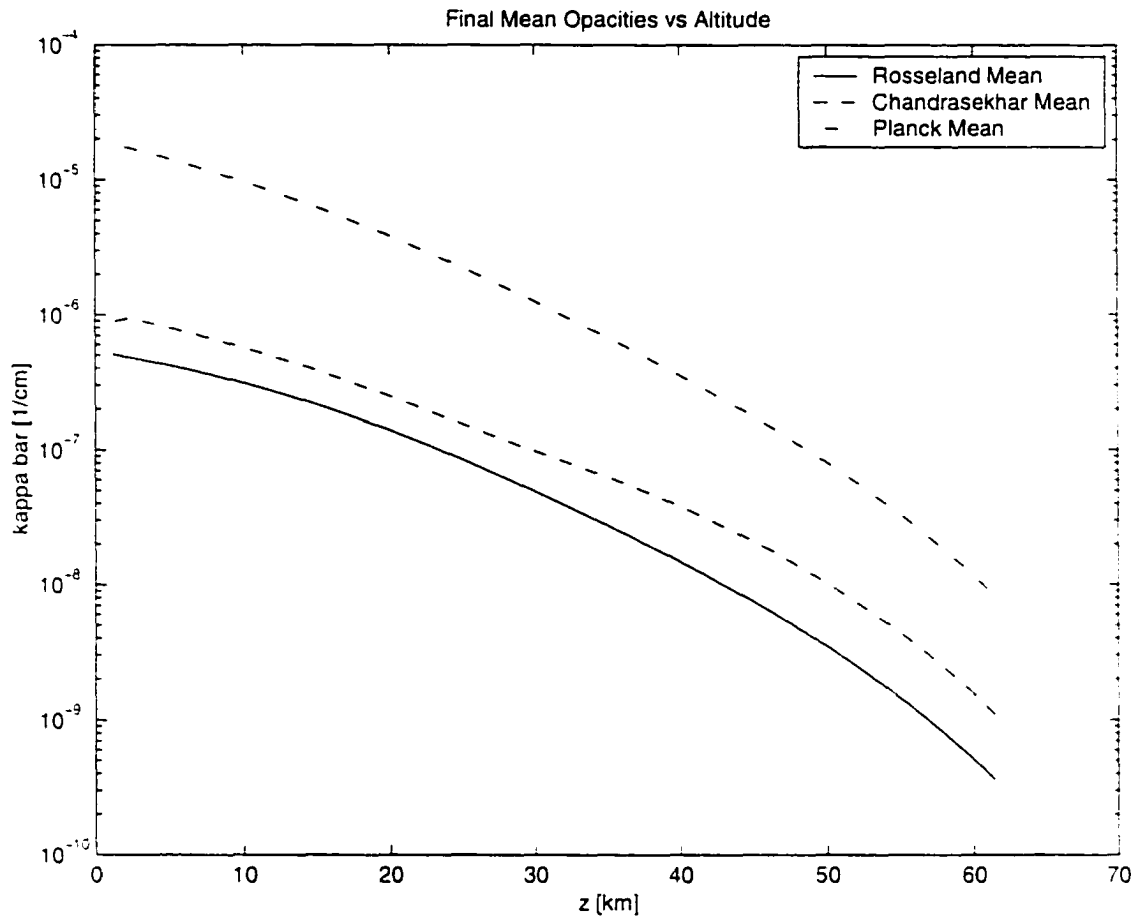


FIGURE 3.20. Titan 3: Final Rosseland, Chandrasekhar, and Planck Mean Opacities [1/cm] versus Altitude [km].

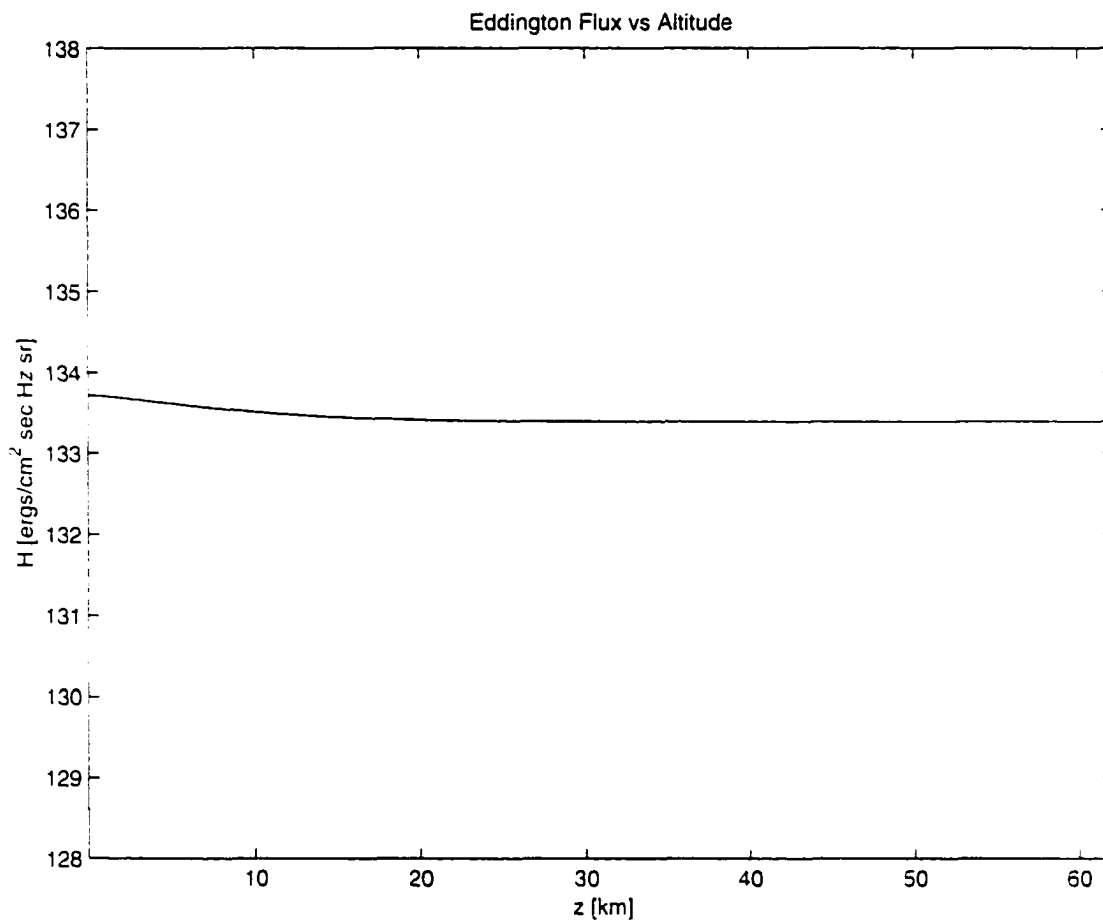


FIGURE 3.21. Titan 3: Eddington flux [ergs/cm² sec Hz sr] versus Altitude [km]. The flux is constant to within 1% ($(H_{max} - H_{min})/H_{max} < 0.01$). This yields an effective temperature of 73 K.

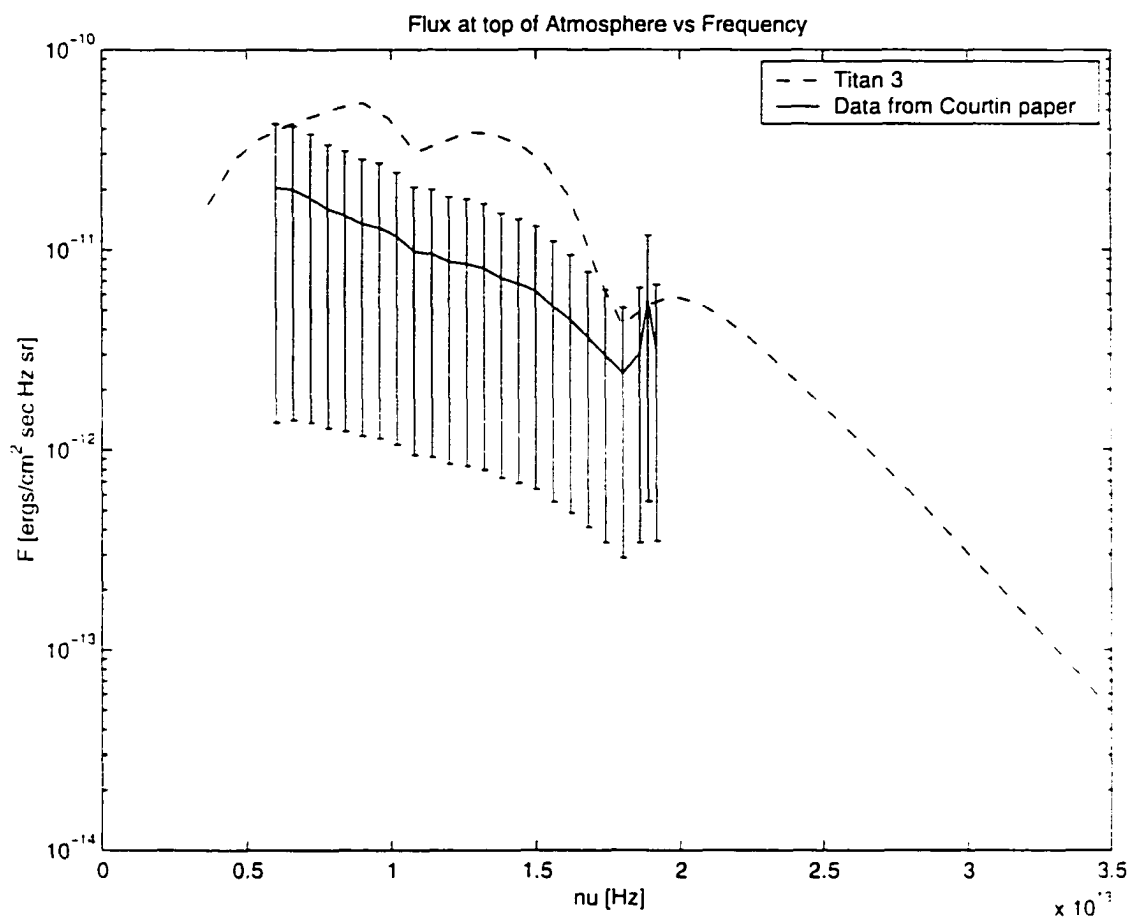


FIGURE 3.22. Titan 3: Flux [ergs/cm² sec Hz sr] versus Frequency [Hz]. The "Data from Courtin paper" is taken from a brightness temperature graph [23] and converting it back to a flux value.

TITAN 4

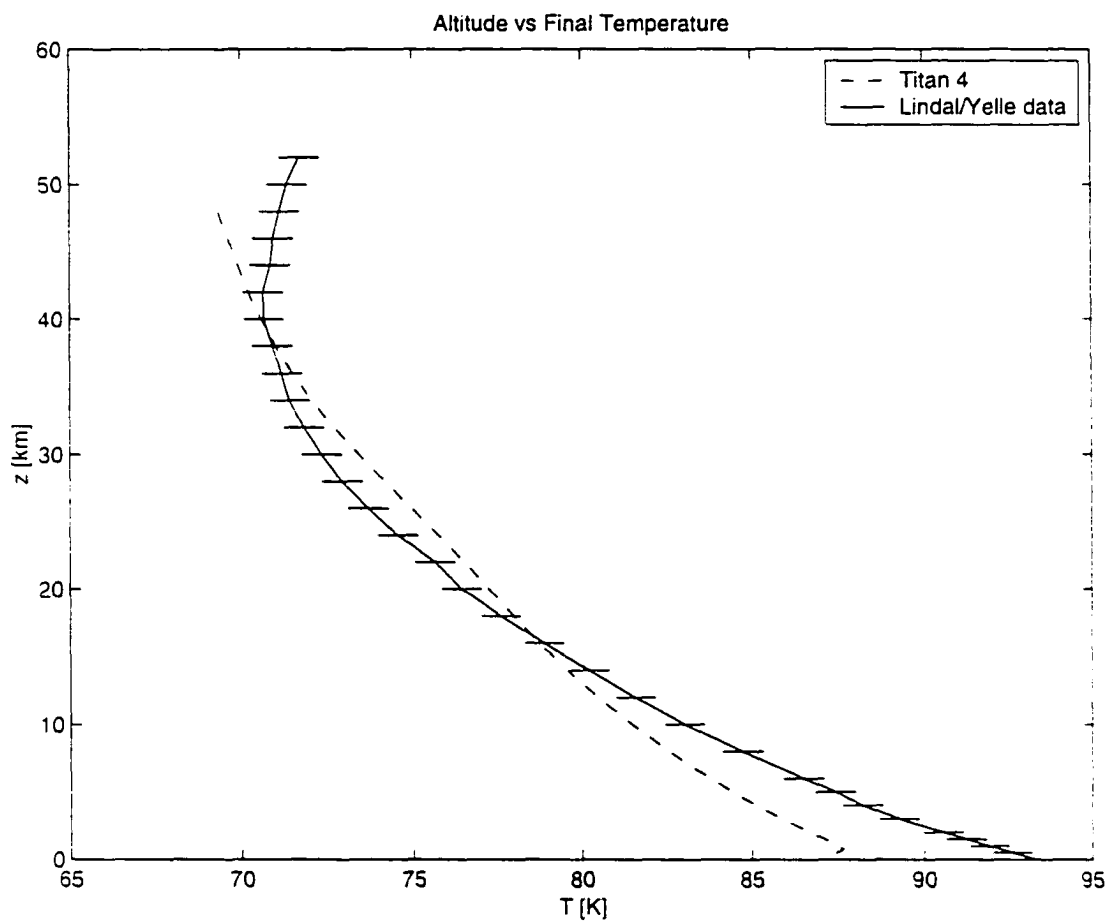


FIGURE 3.23. Titan 4: Altitude [km] versus Temperature [K]. The “Lindal/Yelle data” are from [85] [170].

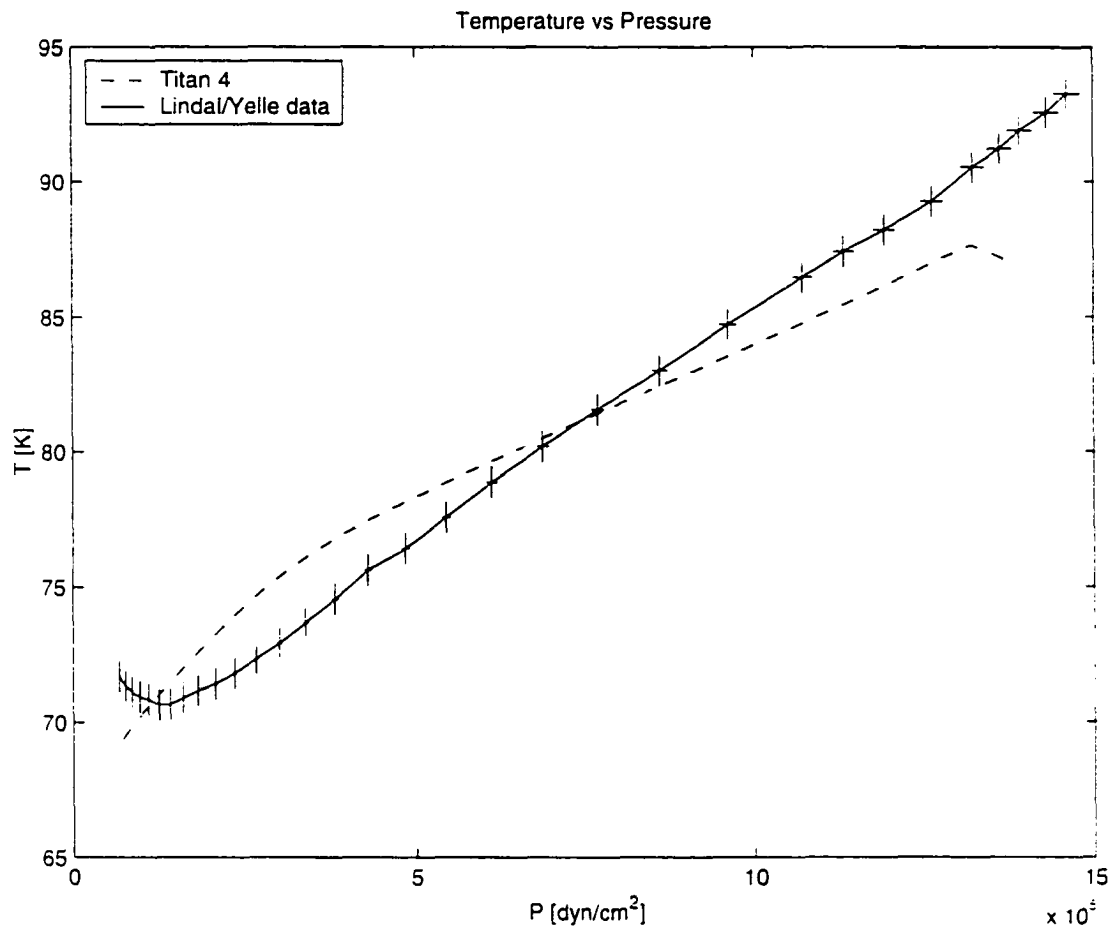


FIGURE 3.24. Titan 4: Temperature [K] versus Pressure [dyn/cm^2]. The "Lindal/Yelle data" are from [85] [170].

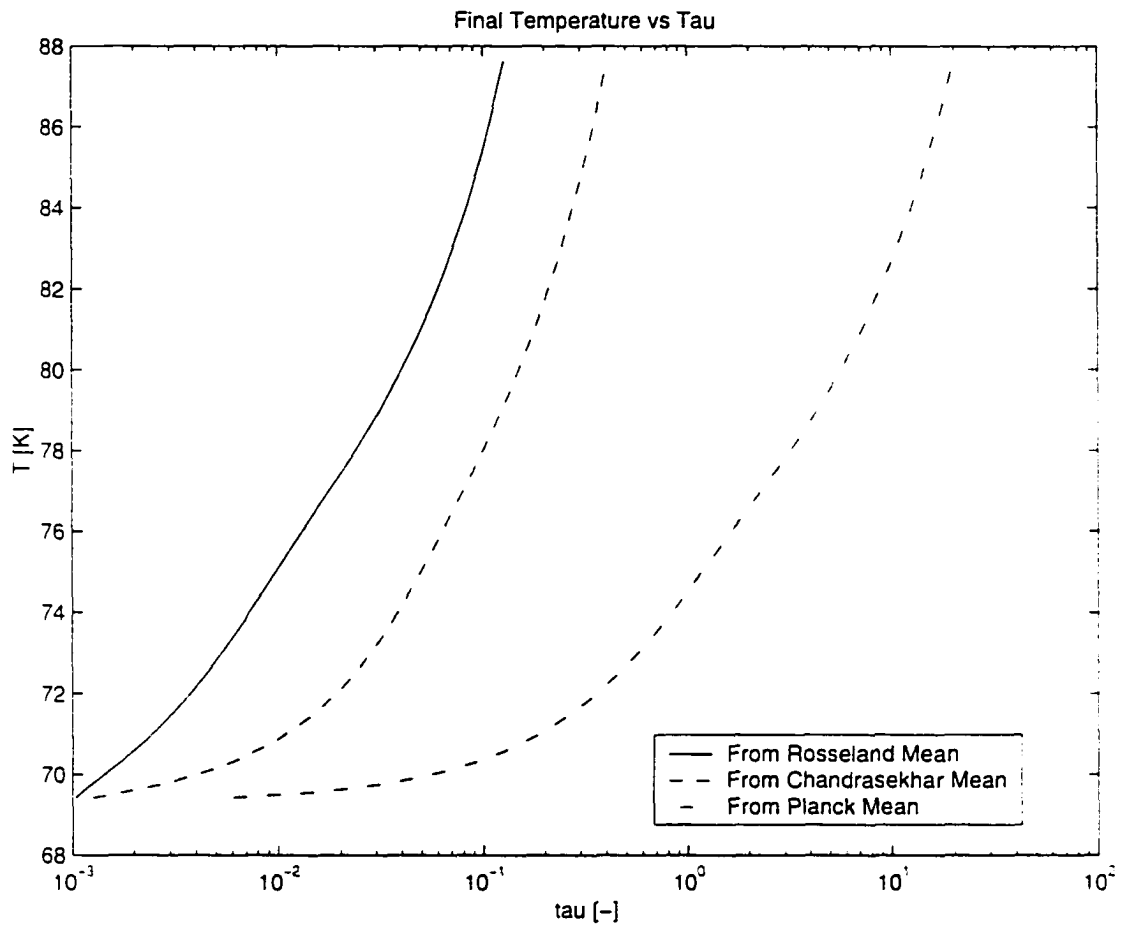


FIGURE 3.25. Titan 4: Temperature [K] versus $\tau_{\text{Rosseland}}$ [-].

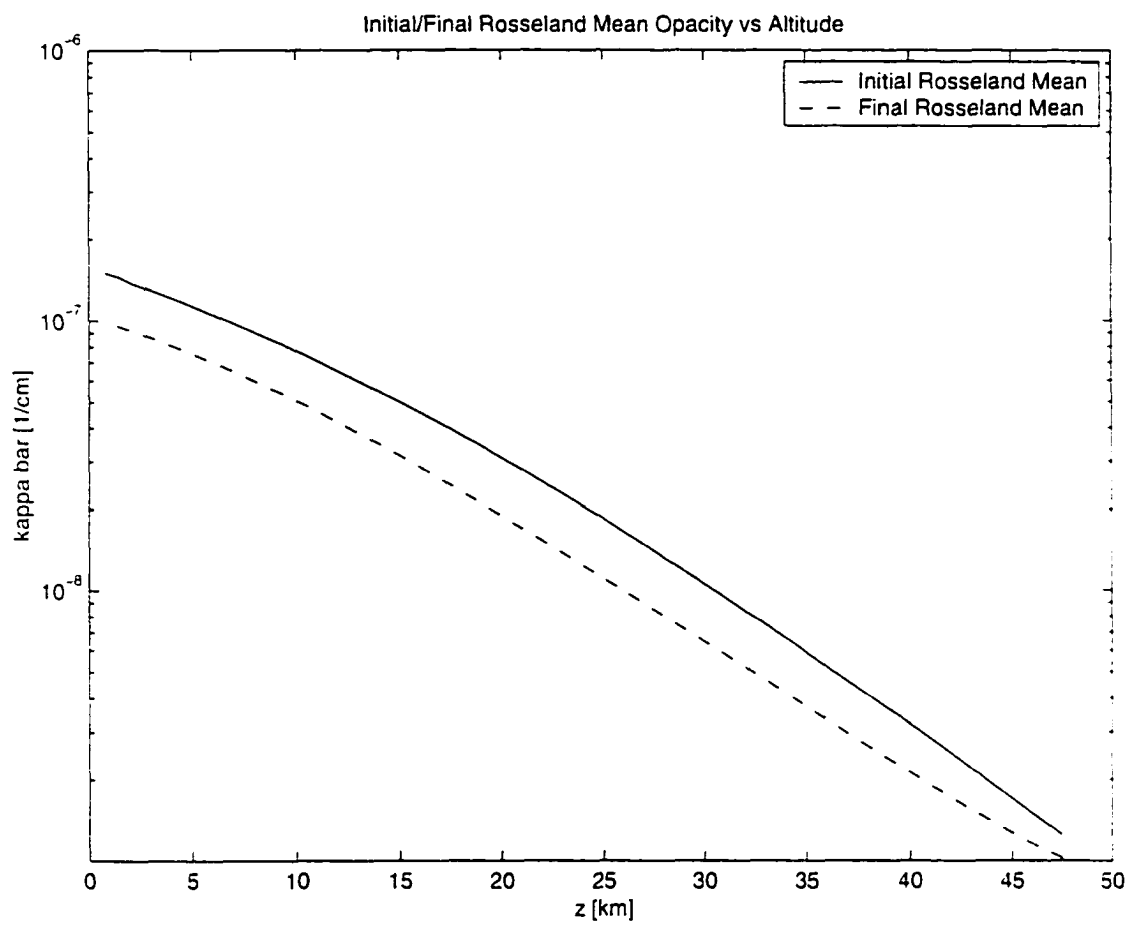


FIGURE 3.26. Titan 4: Initial/Final Rosseland Mean Opacity [1/cm] versus Temperature [K].

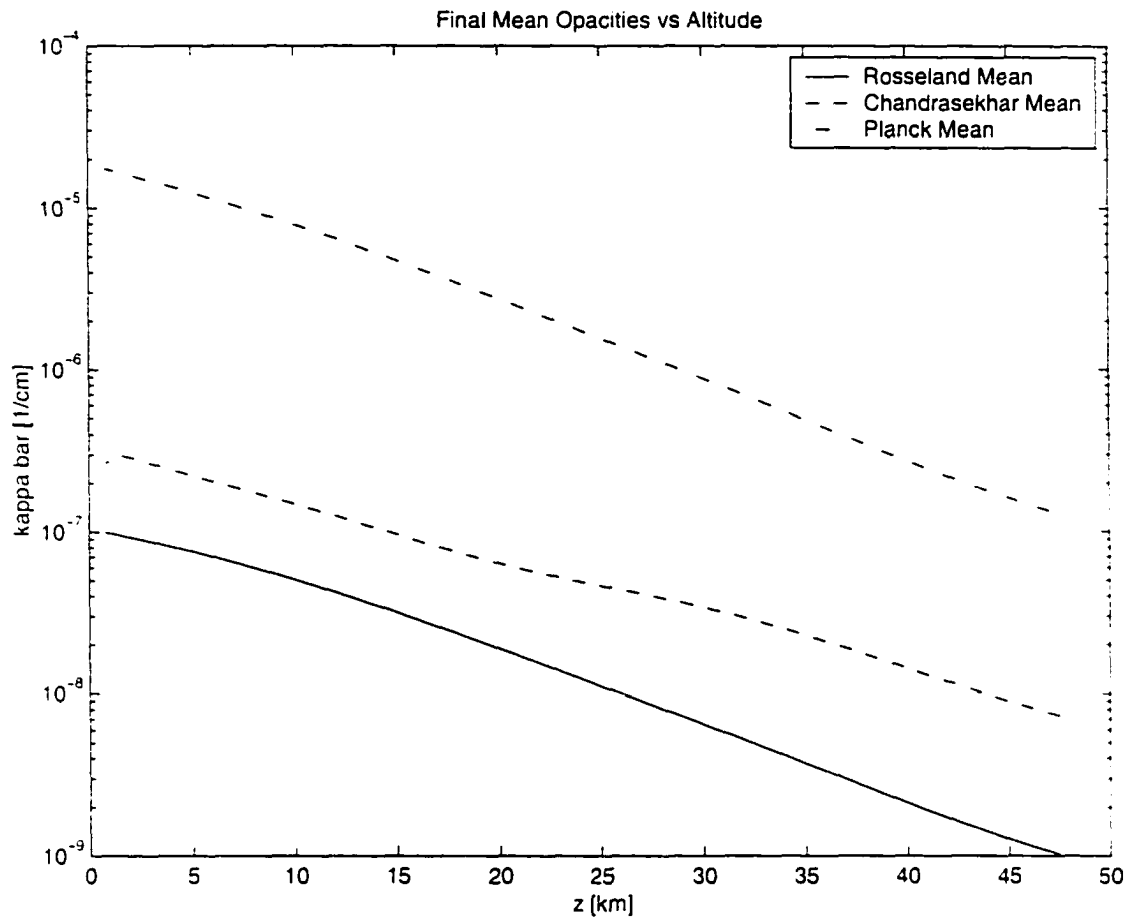


FIGURE 3.27. Titan 4: Final Rosseland, Chandrasekhar, and Planck Mean Opacities [1/cm] versus Altitude [km].

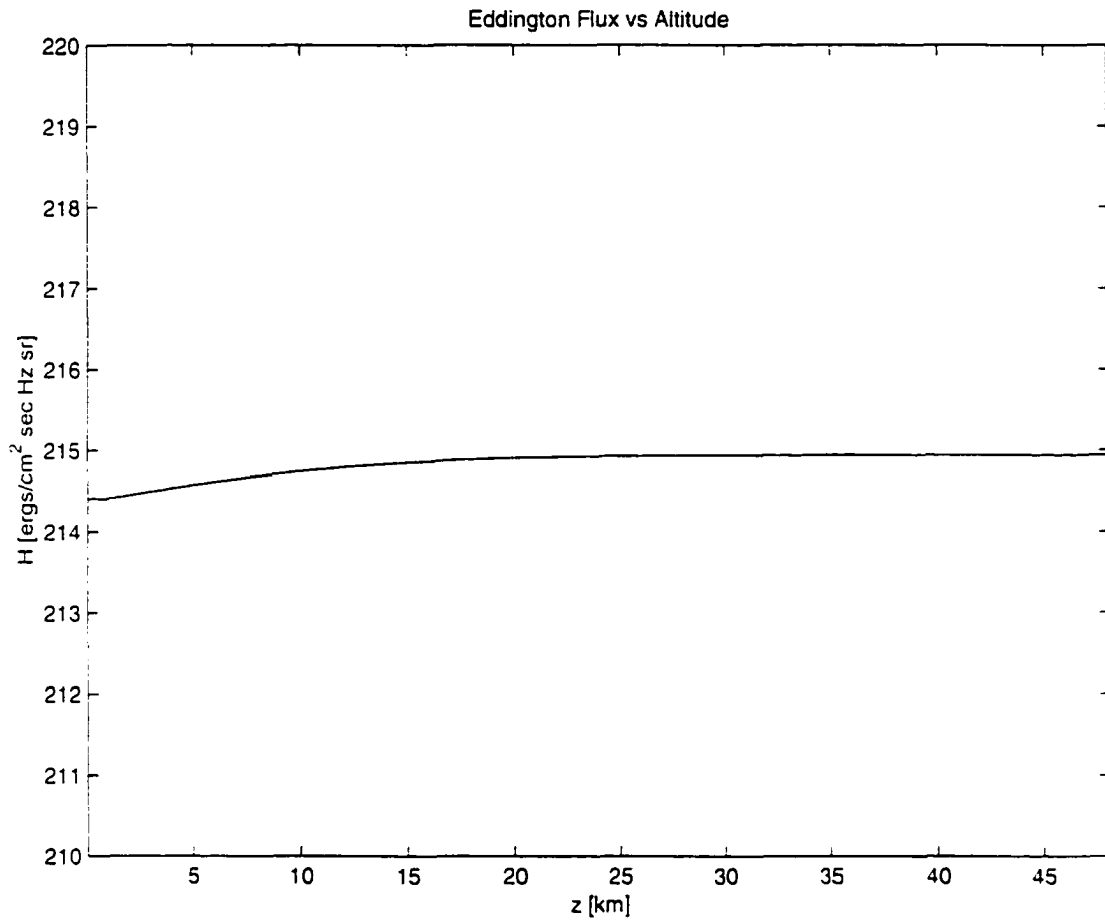


FIGURE 3.28. Titan 4: Eddington flux [ergs/cm² sec Hz sr] versus Altitude [km]. The flux is constant to within 1% ($(H_{max} - H_{min})/H_{max} < 0.01$). This yields an effective temperature of 82 K.

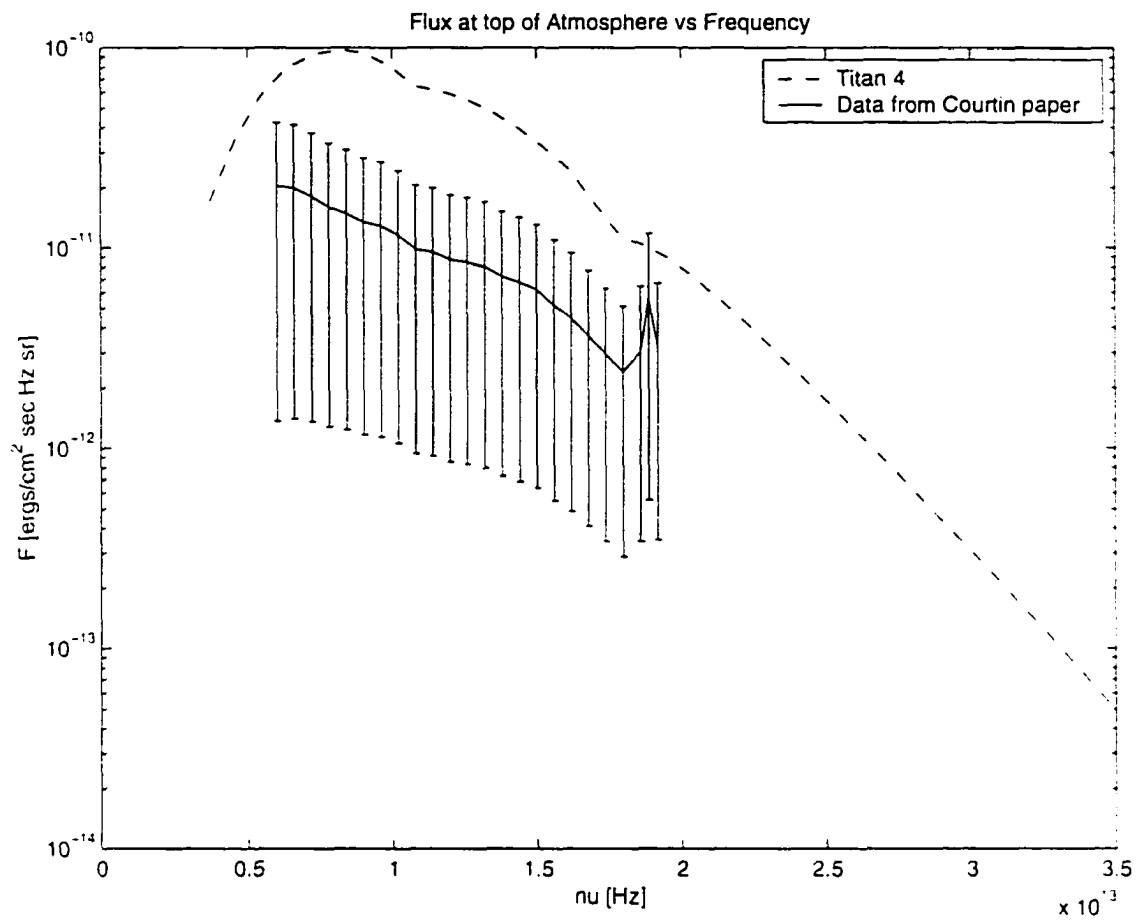


FIGURE 3.29. Titan 4: Flux [$\text{ergs/cm}^2 \text{ sec Hz sr}$] versus Frequency [Hz]. The "Data from Courtin paper" is taken from a brightness temperature graph [23] and converting it back to a flux value.

CHAPTER 4

DISCUSSION, CONCLUSIONS, AND FUTURE DIRECTIONS

To laugh often and much; to win the respect of intelligent people and the affection of children; to earn the appreciation of honest critics and endure the betrayal of false friends; to appreciate beauty; to find the best in others; to leave the world a bit better, whether by a healthy child or a garden patch or a redeemed social condition; to know even one life has breathed easier because you lived. This is to have succeeded. — Ralph Waldo Emerson

4.1 Grey Models of Past Triton, Pluto, and KBOs

4.1.1 Summary of Results

TRITON For Triton, we see that the Chandrasekhar and Planck estimates of the opacity yield high temperature, optically thick atmospheres. The properties of these atmospheres are unaffected by small changes in the H_2 concentrations. All solutions exhibit the S-curve phenomenon discussed in section 2.2.3. The atmospheres generated with these two mean opacities are colder with convection, but still yield a surface temperatures greater than the effective temperature.

The more conservative Rosseland mean opacity results yield hot atmospheres for H_2 concentrations above 0.005%. These results exhibit the S-curve characteristics for H_2 concentrations of 0.05% and above. We observe that the convective profile is coincident with the radiative profile up until F_{HYD} reaches 0.05%.

If we compute λ (from section 1.6.1) for Triton for the hot atmosphere results, the extreme case results are $\lambda_{Chandrasekhar} \approx 6$ and $\lambda_{Rosseland} \approx 9$. Thus an assumption of hydrostatic equilibrium for Triton is reasonable.

PLUTO For Pluto we find that the results with tidal heating and without were virtually identical. We also find that our results did not vary appreciably with the fraction of accretional heating absorbed. Solar heating is the dominant heat source for past Pluto in this work.

Our model generates two hot and optically thick solutions and one cold, optically thin atmosphere using the Chandrasekhar and Planck mean opacities. Again, the results using these two opacities are also insensitive to variations in H_2 concentration. Including the effects of convection for the hottest solution, the atmospheres generated with these two mean opacities cool down considerably, but still yield surface temperatures greater than the effective temperature.

In contrast to the Triton results, the Rosseland mean opacity solution yields one cold, optically thin solution for all values of $FHYD$.

If we compute λ (from section 1.6.1) for Pluto for the hot atmosphere results, the extreme case result is $\lambda_{Planck} \approx 5$. Thus an assumption of hydrostatic equilibrium for Pluto is reasonable.

KBOS The Chandrasekhar and Planck mean opacities yielded similar results: one hot optically thick solution and one cold optically thin solution. The results did not change as the H_2 concentration and fraction of accretional heating absorbed are varied. The check for superadiabaticity yields nothing, so convection does not dominate in either of these mean opacity results.

The conservative Rosseland mean opacity solution yields one cold, optically thin solution until the H_2 concentration reaches 1.0%. At this point we obtain both a cold solution and a hot, optically thick solution. Again a check for convection yields a negative result.

If we compute λ (from section 1.6.1) for our hypothetical KBO for the hot atmosphere results, the extreme case result is $\lambda_{Chandrasekhar} \approx 0.2$. Thus an assumption of hydrostatic equilibrium for the KBO is not reasonable, but we do not know this until

after the fact, that is, until we formulate the model with hydrostatic equilibrium and calculate a surface temperature.

4.1.2 Discussion

It is curious that the Rosseland mean opacity solution for Pluto should yield a cold optically thin atmosphere for all values of $FHYD$, whereas the KBO model (with a lower heating flux) should result in a hot atmosphere for certain values of $FHYD$. There are two major differences in the characteristics of Pluto and our averaged KBO: albedo and gravitational acceleration.

The albedo for the KBO is 0.04, whereas the albedo for Pluto is 0.52. We run the model for Pluto with a KBO's albedo, and find results (see Figure 4.1) comparable to those for KBOs (see Figure 2.27).

Pluto's gravitational acceleration is $g_{Pluto} \approx 66 \text{ cm/s}^2$, whereas $g_{KBO} \approx 3 \text{ cm/s}^2$. We again run a modified Pluto model, this time with a KBO's gravitational acceleration. We again find results comparable to the KBO model (Figure 2.27).

We note that the independence of the Planck mean and the dependence of the Rosseland mean on the hydrogen concentration observed in this work is echoed in [119]. We illustrate these sensitivities, as well as that of the Chandrasekhar mean opacity, in Figure 4.3.

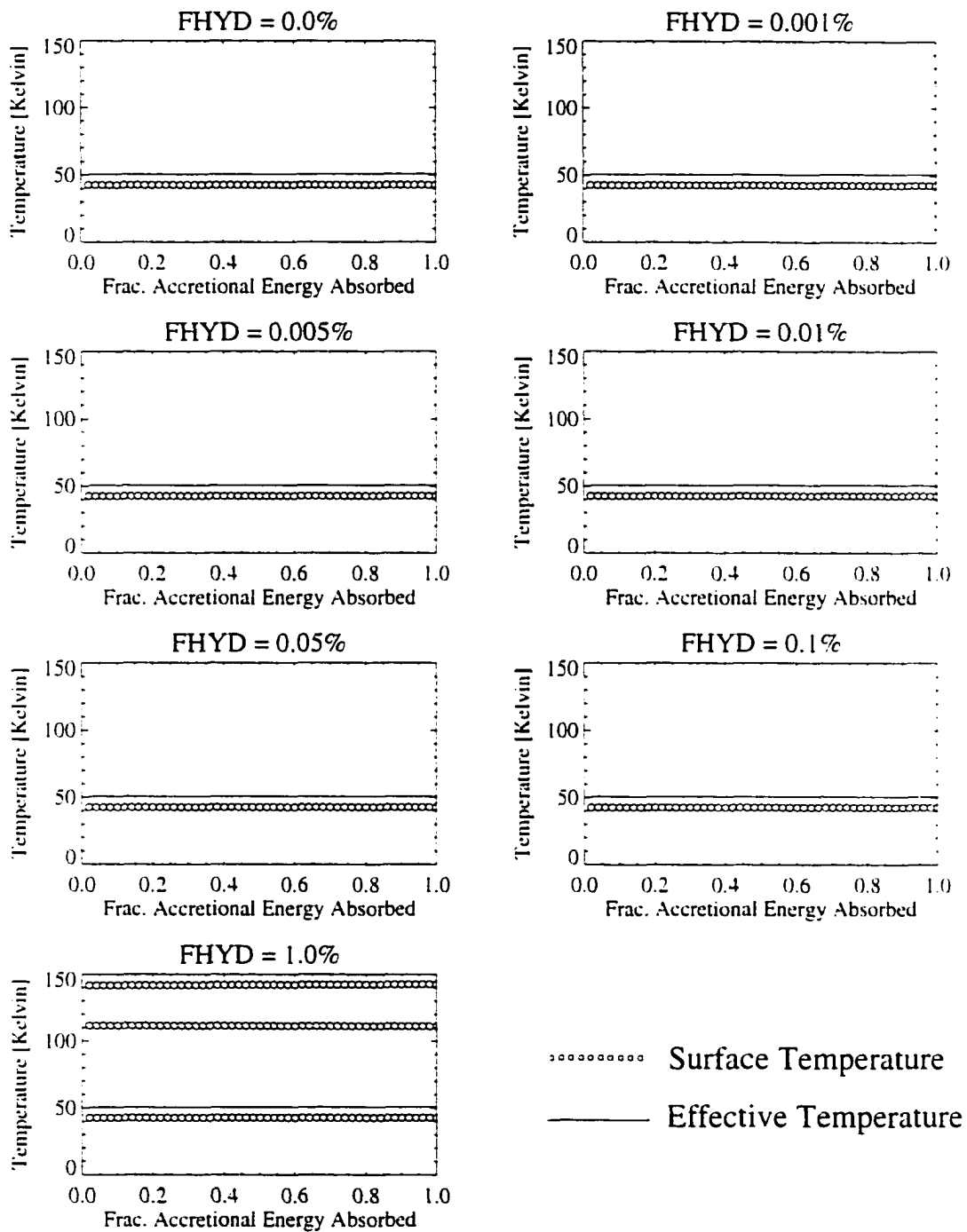


FIGURE 4.1. Pluto: Temperature (Effective and Surface) versus Heat Flux with Rosseland Mean Opacity and KBO Albedo.

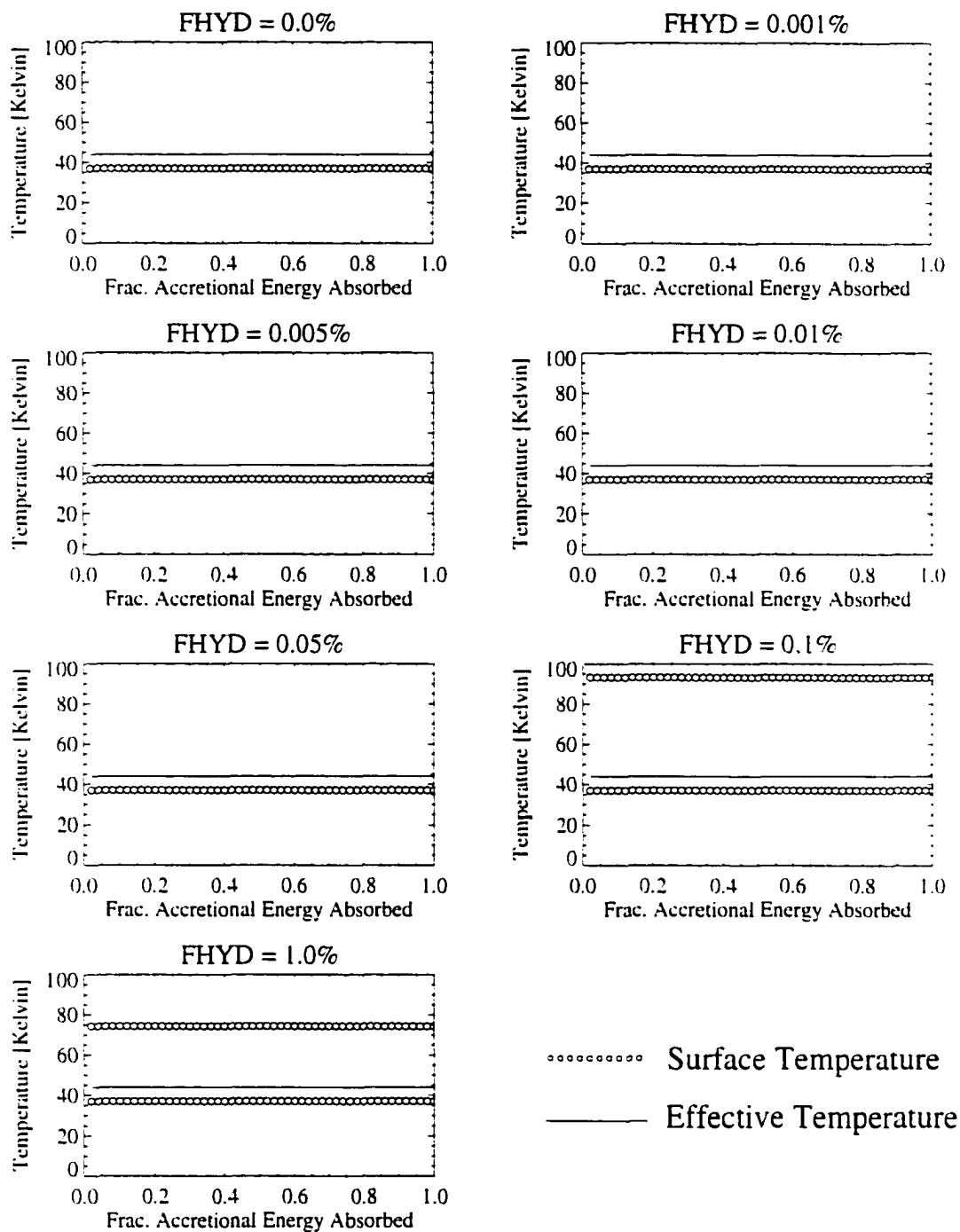


FIGURE 4.2. Pluto: Temperature (Effective and Surface) versus Heat Flux with Rosseland Mean Opacity and KBO Gravity.

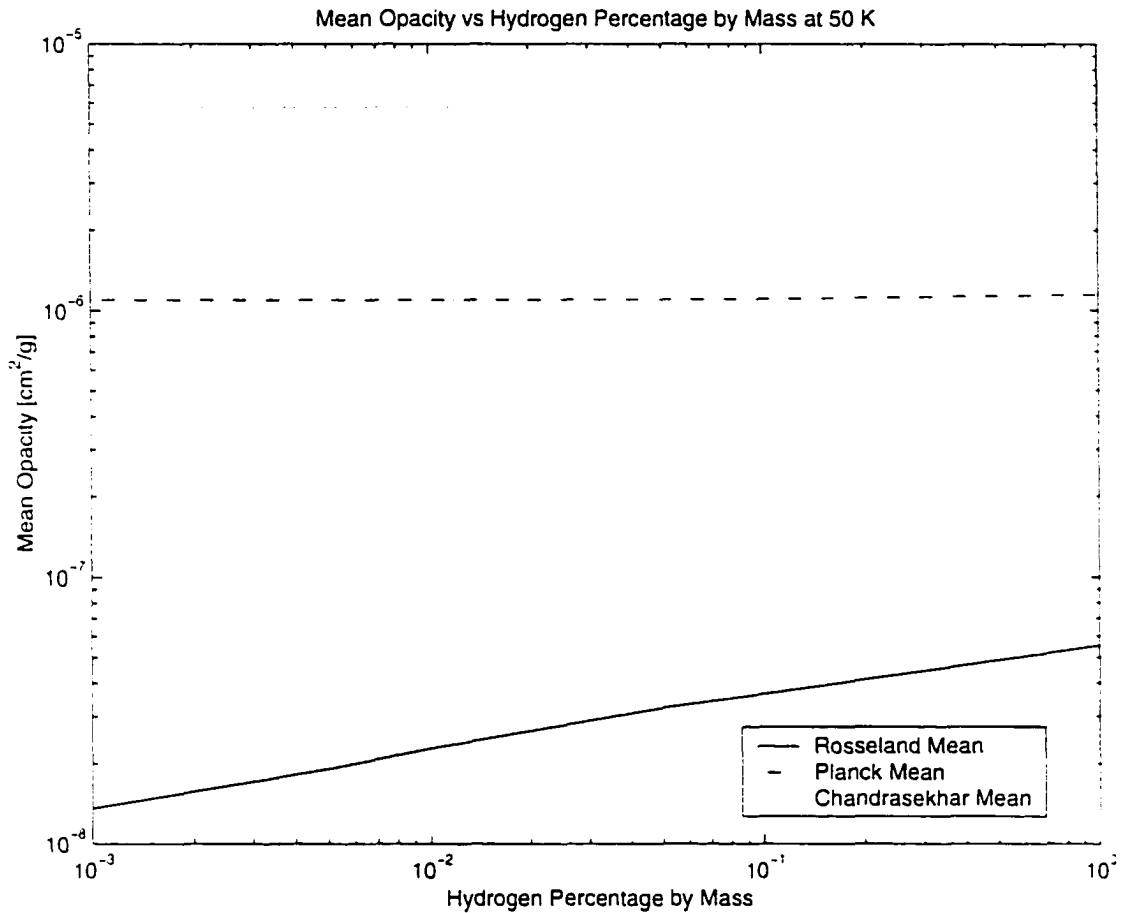


FIGURE 4.3. Sensitivity of mean opacities to percentage of H_2 by mass.

The S-curve results obtained in this work are not an isolated phenomena. Such curves have been obtained by other atmosphere models (generic atmosphere model [133]; Titan [105]). S-curves are seen in a range of problems [73] [78] for similar situations. We interpret regions where the temperature decreases as the heating increases as true mathematical solutions but physically unstable situations [111], and the regions above and below (higher or lower temperature) are the physical solutions. Thus the physical state of the atmosphere in this “backwards” region is either at the higher or lower temperature. To determine which state the system is in (the higher or the lower temperature) requires some sort of hysteresis analysis that depends on initial

conditions and perturbations that could push the system from the lower temperature curve to the higher temperature curve or vice versa (a catastrophic event such as a major meteor impact).

4.1.3 Conclusions

We apply a grey atmosphere model to early Triton and Pluto to see if massive and optically thick atmospheres could have formed, given certain molecular hydrogen mass fractions and heating inputs. Also, it is not known in advance which mean opacity estimate should be used given self-consistency problems, so we apply the most commonly used mean opacity estimates (Chandrasekhar, Planck, and Rosseland). Our grey model calculates the surface temperature of an object a given set of parameters.

Our model builds on work presented in [119] [98]. We present here new work on the problem: using a variety of mean opacities in our analysis, new mathematical approaches to calculating mean opacities, directly using detailed fits to laboratory opacity data instead of an interpolation table to calculate the mean opacities, adding radiogenic and accretional heating sources, searching for more than two roots, and expanding the model to apply to Pluto and KBOs.

From our grey model results we observe:

- On Triton, tidal heating through radiative transfer led to an optically thick atmosphere: for the Rosseland mean opacity a high H_2 concentration was necessary.
- Depending on mean opacity type and H_2 concentration, an optically thick atmosphere may have formed on our hypothetical KBO: for the Rosseland mean opacity a high H_2 concentration was necessary.
- On Pluto, an optically atmosphere did for for the Chandrasekhar and Planck mean cases: for the Rosseland mean opacity no optically thick atmosphere

formed (unless our standard albedo and gravity were changed).

We find, as previous works with similar atmosphere compositions [141] [106] [89] that molecular hydrogen plays a major role in the evolution of these atmospheres due to the “window effect” (see section 1.5.3). We also find multiple temperature solutions undetected in previous works, with physically stable and unstable solutions.

4.1.4 Future Directions

We have shown that under certain circumstances hot optically thick atmospheres form on these objects. The next logical step would be to apply atmospheric escape mechanisms to the results of the hot optically thick solutions to see if they evolve to something resembling the current atmospheres. One possible improvement to the grey model would be to take into account the opacity contribution of *CO* on Triton (when such data are available to us). Also, change albedo and gravity to become formal parameters of the model. It is hoped that more information on Pluto will be collected by a future robot mission to visit no earlier than 2016, with an excursion to a Kuiper belt object after the Pluto flyby [95].

As for the grey model itself, the run-time can be greatly accelerated by using an interpolation table (calculated just once: method used in [119] [98]) instead of calculating the opacity on the fly. But an interpolation table may miss key features of the opacity, and should only be used when the opacity is slowly varying with frequency and does not contain sharp lines. Also, if the vapor pressure P_v is a simple nonlinear function of T , then a faster root-finding (such as Newton-Raphson, Secant, Regula-Falsi) may be employed instead of the slow but dependable Bisection method.

4.2 Nongrey Model of Present Titan

4.2.1 Summary of Results

Note in Table 4.1 that we run beyond the $\epsilon_{RE1} = 1\%$ radiative equilibrium convergence tolerance that we had decided upon earlier. We find that for all code runs, the grid point at the surface is converging but not as quickly as the rest of the grid, which produces a little bump between the grid point at the the surface and the one just above it. To smooth this bump we run to either 0.5% or 0.25% instead, depending on the magnitude of the bump. For some code runs, this is still not enough, and further iteration is necessary to completely smooth the bump. But given that these bumps are only of order 1 degree K, we decide not to iterate beyond $\epsilon_{RE1} = 0.25\%$ just for further smoothing.

Run Label	# Iterations	R.E. % Accuracy.	H.E. % Accuracy
Titan 1	759	0.5	4e-9
Titan 2	619	0.25	5e-9
Titan 3	311	0.25	1e-8

TABLE 4.1. Titan 1-3: Comparison of convergence parameters.

The surface temperature and density values for Titan runs 1-3 in Table 4.2 are close to the accepted value of 95 K and 0.005 g/cm³.

Run Label	T [K]	ρ [g/cm ³]	P [dyn/cm ²]	$\bar{\chi}_{rossetland}$ [1/cm]	$\tau_{rossetland}$ [-]
Titan 1	92	0.0053	1.44e+6	7.7e-07	1.3
Titan 2	92	0.0049	1.34e+6	7.1e-07	1.2
Titan 3	90	0.0055	1.47e+6	5.9e-07	0.8

TABLE 4.2. Titan 1-3: Comparison of surface properties.

Note that in the following figures, as in section 3.2.3, the term “Lindal/Yelle data” shall refer to output from a data analysis model based on Voyager I data [85], and then rescaled to correspond to a volatile inventory of N_2 : 95%, CH_4 : 3%, Ar : 2% [170]. The labels “Titan 1”, “Titan 2”, and “Titan 3” correspond to the descriptions in Table 3.1.

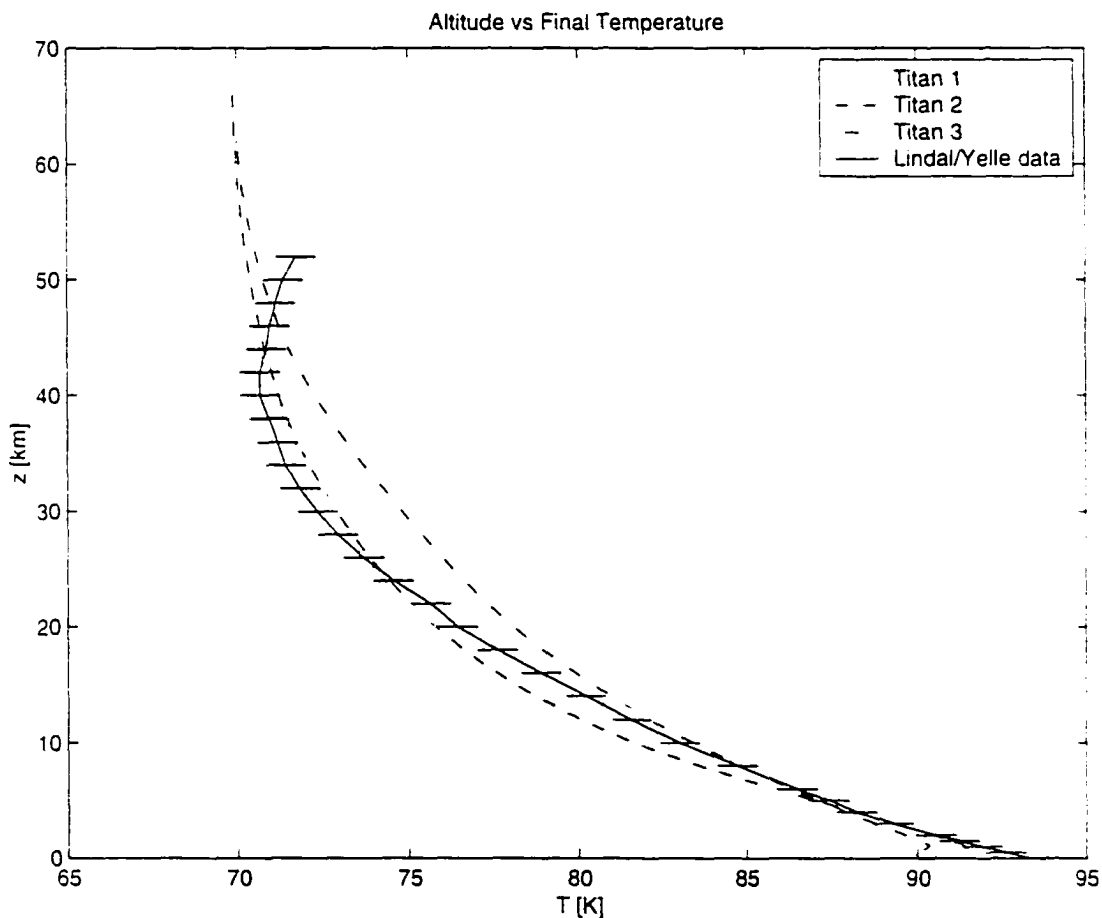


FIGURE 4.4. Altitude [km] versus Temperature [K].

From Figure 4.4 we see that all three models of current Titan are of the correct order of magnitude. To determine which code run (Titan 1, 2, or 3) provides the best

fit to the tropospheric temperature from the Lindal/Yelle data in Figure 4.4. we plot the relative error of each run with respect to the Lindal/Yelle data.

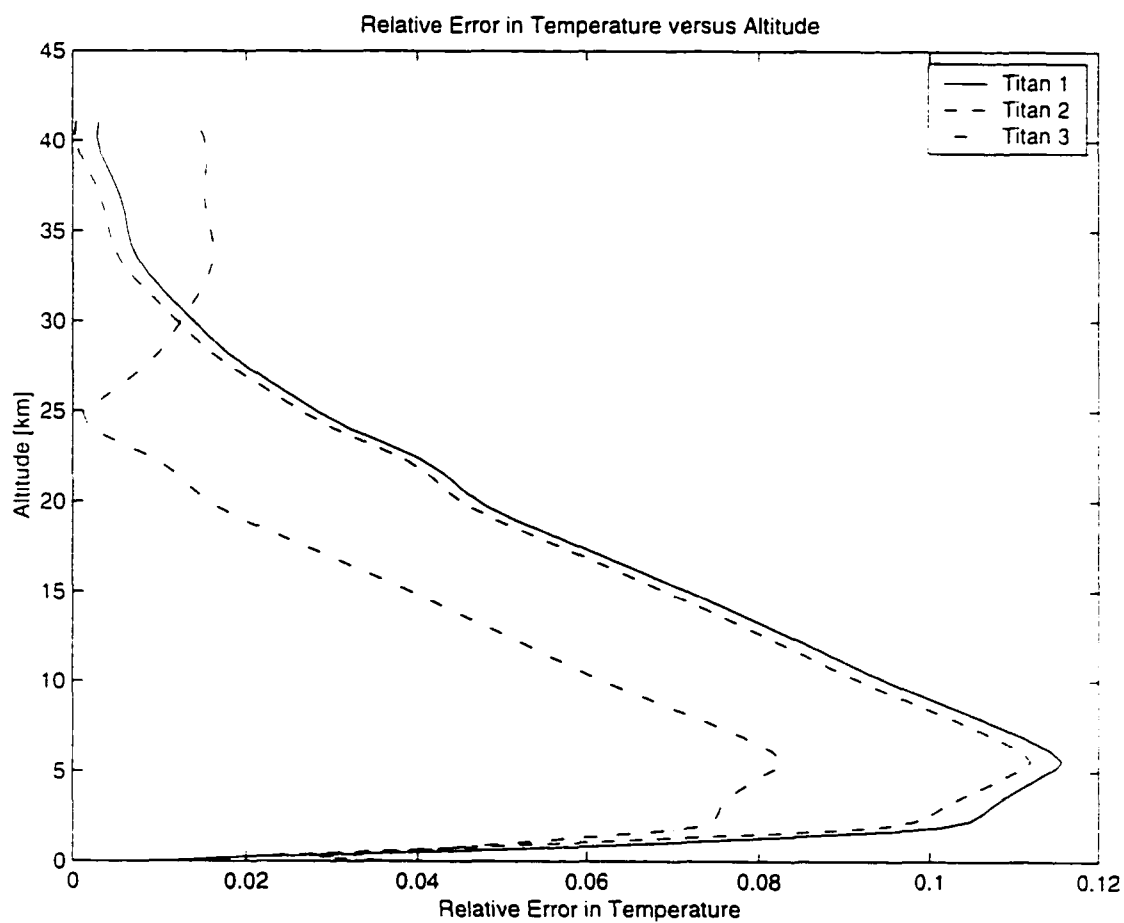


FIGURE 4.5. Altitude [km] versus Relative Error in Temperature [K].

From Figure 4.5 we see that from 0 to 30 km Titan 3 provides the better fit, and from 30 to 40 km Titan 2 is the better model. Overall, the maximum relative error from Titan 1 is 12%, from Titan 2 we get 11%, and from Titan 3 the maximum relative error is 8%.

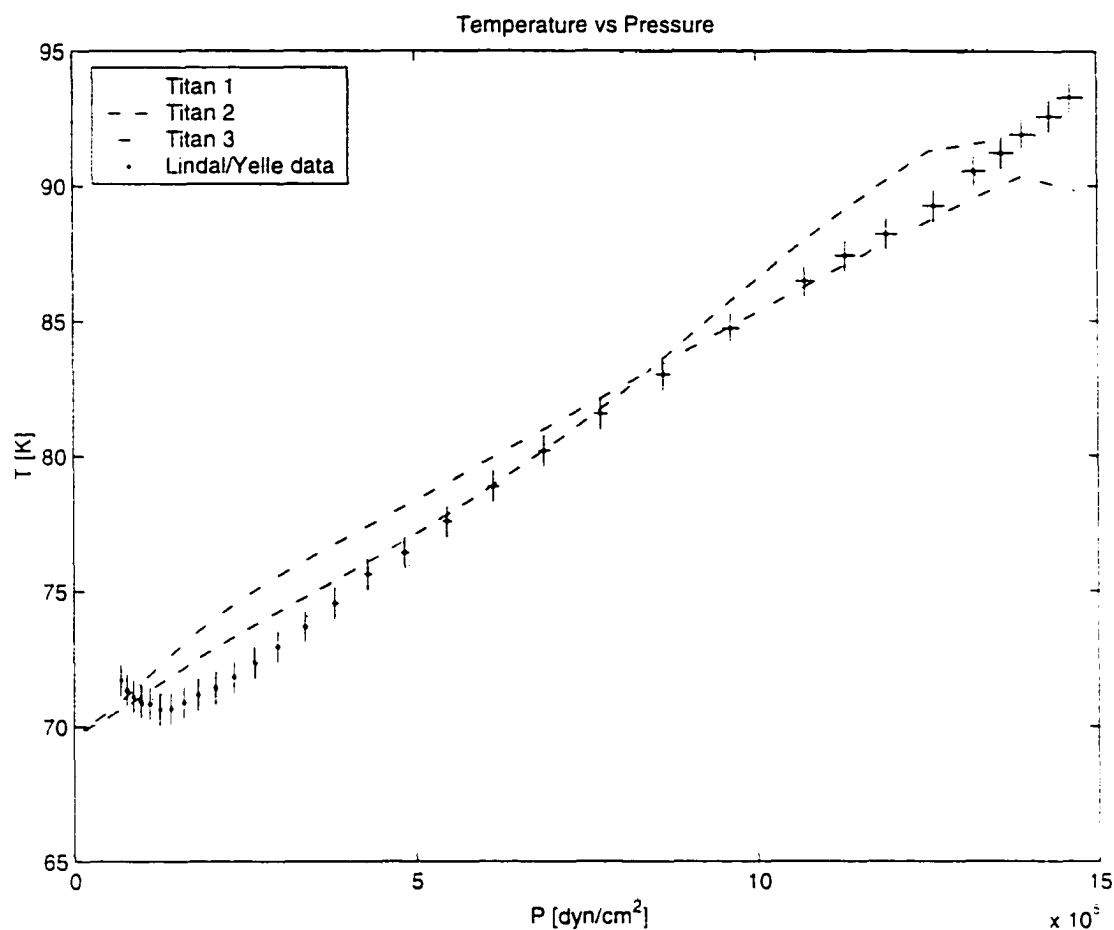


FIGURE 4.6. Temperature [K] versus Pressure [dyn/cm²].

In Figure 4.6 we see the same result: Titan 1 and 2 are the better models for the low temperature/low pressure regime, and Titan 3 is the better estimate for high temperature/high pressure.

For the next four figures, we take the altitude, temperature, density, and pressure profiles from the Lindal/Yelle data for the troposphere (0 to 42 km) and run them through one iteration of our radiative transfer equation solver (with no correction procedure) to see the resulting opacities and flux [126]. Note that the Lindal/Yelle data composition is N_2 : 95%, CH_4 : 3%, Ar : 2%. We approximate this in our model

with N_2 : 96.8%, CH_4 : 3%, H_2 : 0.2% [95].

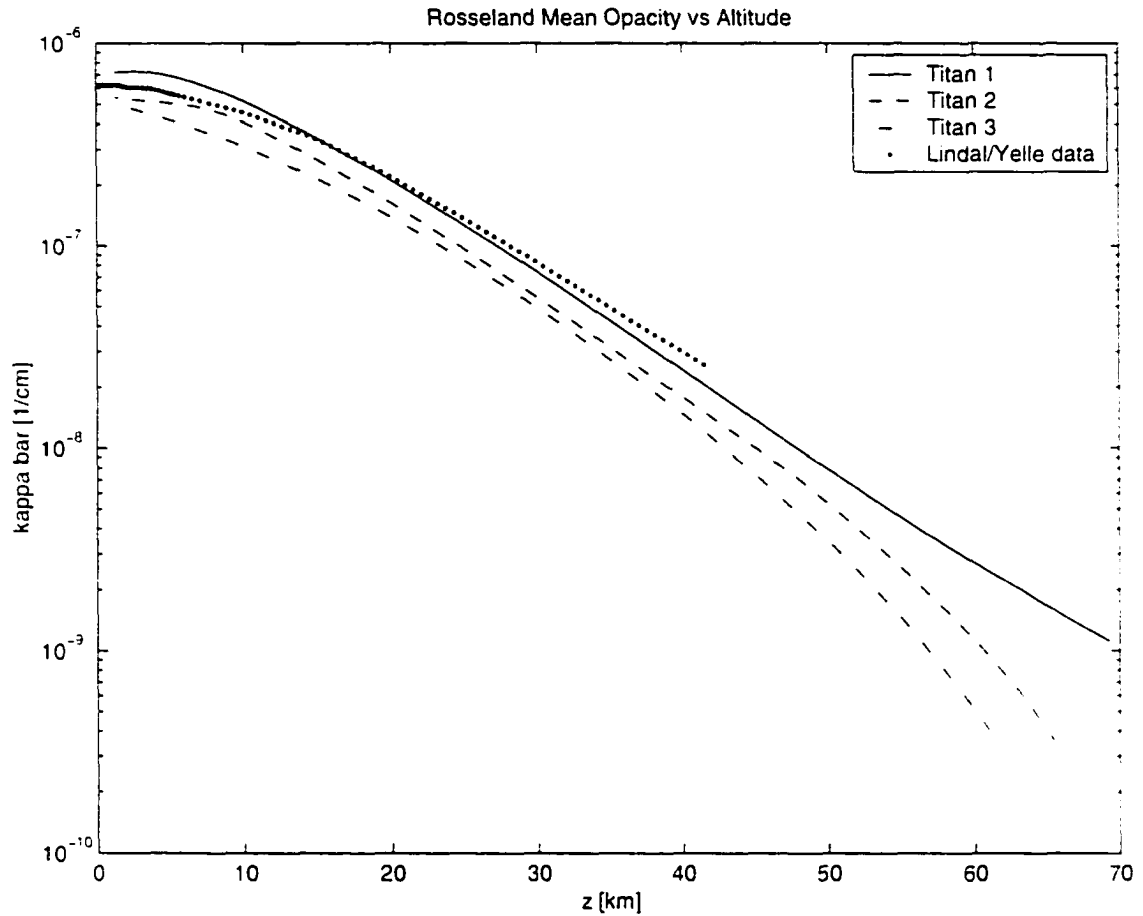


FIGURE 4.7. Rosseland Mean Opacity [1/cm] versus Temperature [K].

In Figure 4.7 we see that the Rosseland mean opacity decreases from Titan1 to Titan 3. i.e., as we decrease the amount of methane. Titan 1 and 2 seem to best estimate the Rosseland mean opacity.

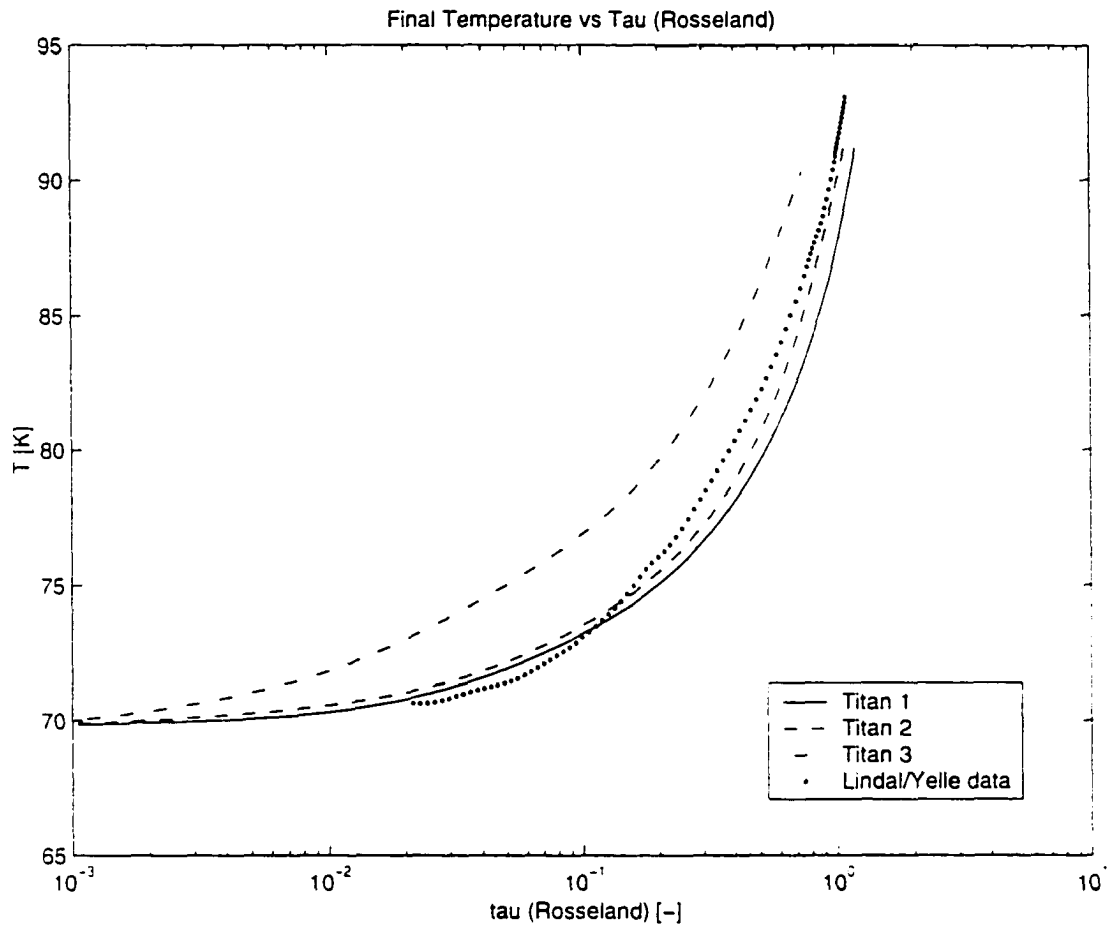


FIGURE 4.8. Temperature [K] versus $\tau_{rosseland}$ [-].

In Figure 4.8 the optical depth calculated from the Rosseland mean opacity also decreases at the surface from Titan 1 to Titan 3, i.e., as the amount of methane is decreased. Predictably, Titan 1 and 2 provide the best fit.

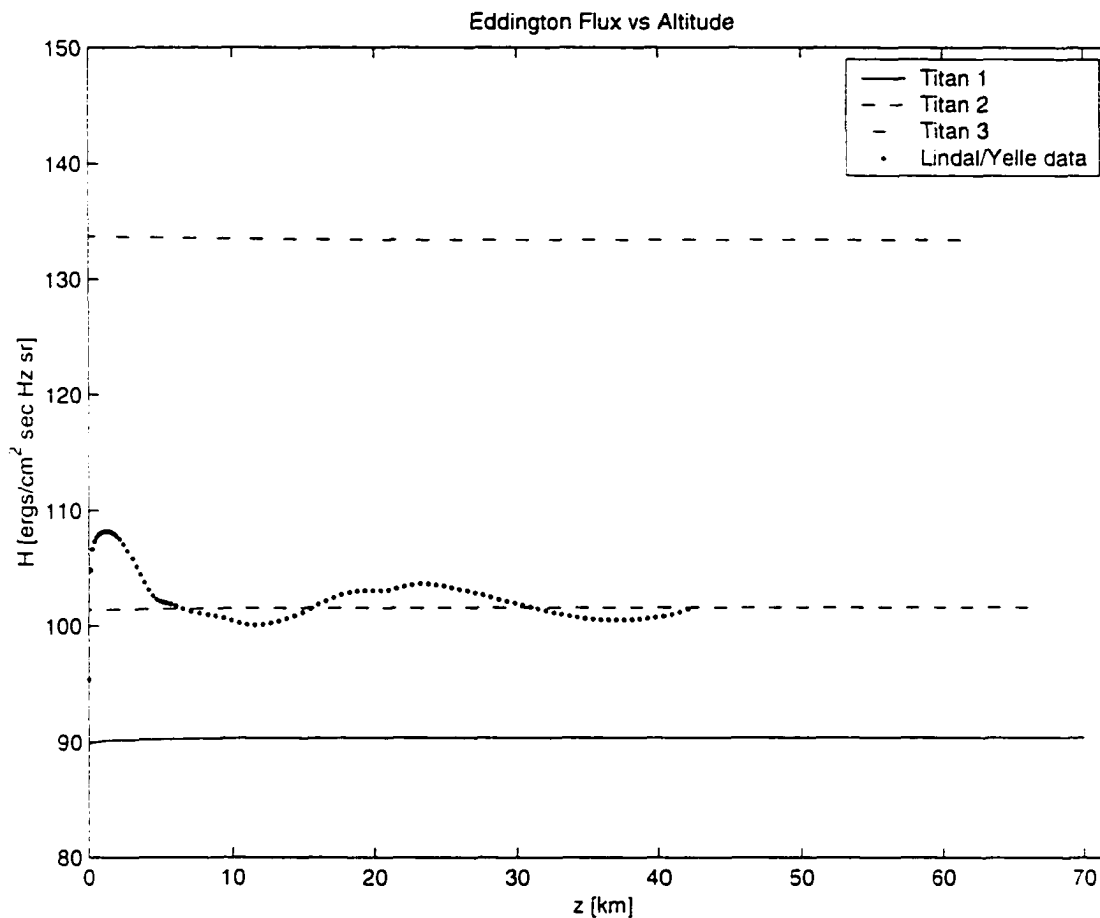


FIGURE 4.9. Eddington flux [$\text{ergs/cm}^2 \text{ sec Hz sr}$] versus Altitude [km].

Figure 4.9 reaffirms that our model results are in radiative equilibrium. We also graph the resulting total flux from running the Lindal/Yelle data through our radiative transfer equation solver as a comparison. Note that from Figure 4.7 the Rosseland mean opacity decreases as we decrease the methane mass fraction. This implies that we should also see a corresponding increase in the total flux at each level, since the smaller opacities will absorb less energy at each level. This is confirmed by Figure 4.9. The Lindal/Yelle data result closely bounds the Titan 2 total flux.

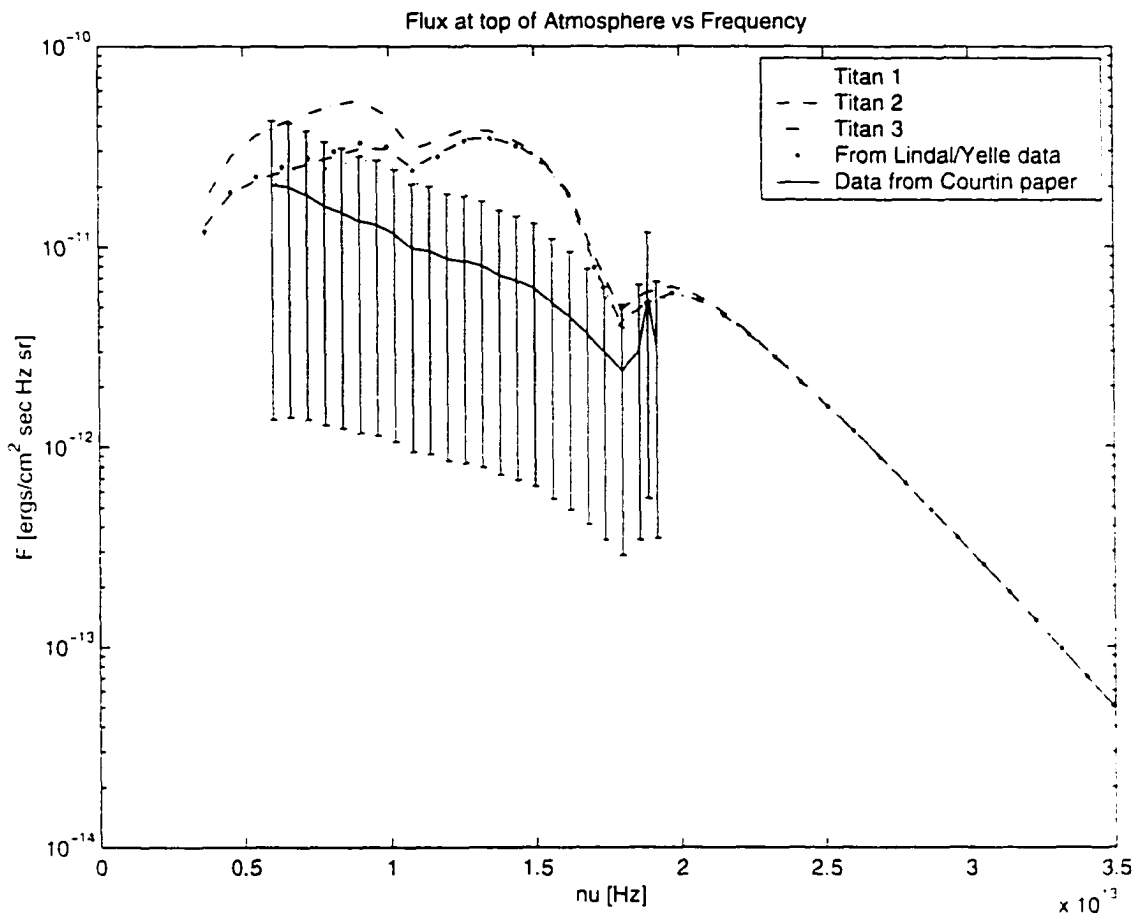


FIGURE 4.10. Flux at top of the troposphere [ergs/cm² sec Hz sr] versus Frequency [Hz]. The "Data from Courtin paper" is from taken from estimating the brightness temperature as a function of wavenumber from a graph [23] and converting it back to a flux versus frequency value.

In Figure 4.10 we plot the flux coming out the top of the troposphere to compare with brightness temperature values found in the literature [23]. From a graph of brightness temperature versus wavenumber, we estimated the values and converted them to flux versus frequency values. The error bars on the graph correspond to a 0.25 K degree error from instrumental noise in measuring the brightness temperature [23] plus 1 K degree error in our estimation from the original graph. We convert the

total temperature error of ± 1.25 K degree to flux values and plot as error bars on the “Data from Courtin paper” curve. We also plot the resulting flux output from the Lindal/Yelle data (obtained by running the Lindal/Yelle data through our radiative transfer equation solver); it is a close match to Titan 2. The differences between our model output and the Courtin et al. paper [23] results are due to the fact that we are looking at the flux at the top of the troposphere, whereas the Courtin et al. paper [23] examines the brightness temperature for Titan’s entire atmosphere.

4.2.2 Discussion

In terms of temperature, Titan 3 appears to be the overall best model of current Titan, with the lowest relative error and best match from 0 to 30 km. But in terms of flux Titan 2 looks to be the most appropriate model. Given that Titan 3 is better in relative error of temperature by such a small margin, and that Titan 2 seems to hit close in terms of the flux, we think Titan 2 best represents Titan’s current troposphere. Our current Titan models estimate the effective temperature in the range of 67 to 73 K. The global effective temperature for Titan is 85 K, which is calculated assuming that all the solar radiation incident on the top of the atmosphere makes it down to Titan’s surface. This is not the case, given the antigreenhouse effect present in the stratospheric haze. Thus our effective temperature is lower than the global value of 85 K. about It should be noted that other models exhibit an approximately 10% maximum deviation from troposphere temperature data [105] and deviate from radiative equilibrium by about 5% [106].

As we noted in our grid generation description, the Rosseland mean opacity empirically provides the best fit to current Titan troposphere data: this relationship has also been noted by others (e.g., [104]).

We carry out experiments with the number of diagonals taken from Λ to define Λ^* to optimize our convergence rate. We find that with more diagonals the problem

converges faster, but each iteration takes longer. With fewer diagonals each iteration runs faster but more iterations are required to reach the same convergence tolerance level.

We also implement initial damping to the iterative scheme. We find that initial overcorrections (leading to negative temperature or density values within the first few iterations) may result from if too few spatial grid points are used. But if the number of spatial grid points is increased to avoid these overcorrections in the first few steps, then we pay for it in the subsequent hundreds of iterations with longer runtime per iteration. We get around this problem by applying a damping factor of 5% to the density correction for the first 5 iterations (we arrive at these values through trial and error).

4.2.3 Conclusions

We develop a nongrey atmosphere model of current Titan's troposphere to study the effect of varying methane. Our model is an improvement over the McKay nongrey models (described in detail in [106]) in the following areas: we use more grid points to resolve the spatial and spectral regions; we use the method of discrete ordinates as opposed to the two-stream approximation in [106] (which leads to better angular resolution). we put our model through rigorous testing procedures, and we implement an initial damping phase to speed up convergence and overall runtime. We also find that a Λ^* matrix equal to tridiagonal Λ to be optimal for our problem.

By solving the radiative transfer equation and subjecting the solution to radiative, hydrostatic, and local thermodynamic equilibrium constraints, we can model Titan's troposphere to a maximum deviation of 8% as compared to the data from [85] and [170].

4.2.4 Evolution of Titan

Recall that the Titan 4 code run is intended as a preliminary code run of past Titan, where we maintain the current solar radiation levels (i.e., do not change the boundary conditions) but reduce the amount of methane well below the currently accepted range of 2-10% (thus we must also reduce the amount of molecular hydrogen since methane is its source via photolysis).

The range of values in Table 4.3 are consistent with those seen in table 4.1.

Run Label	# Iterations	R.E. % Accuracy	H.E. % Accuracy
Titan 4	423	0.25	5e-8

TABLE 4.3. Titan 4: Comparison of convergence parameters.

From Table 4.4 and Figures 3.23 through 3.29, we see that the Titan 4 temperature profile is noticeably cooler than the current Titan models. The Titan 4 Rosseland mean opacity is considerably smaller than the current Titan runs: this is consistent with a decreased amount of H_2 (see discussion in section 1.5.3).

Run Label	T [K]	ρ [g/cm ³]	P [dyn/cm ²]	$\bar{\chi}_{rosseland}$ [1/cm]	$\tau_{rosseland}$ [-]
Titan 4	87	0.0053	1.37e+6	1.1e-07	0.14

TABLE 4.4. Titan 4: Comparison of surface properties.

From our results we see that a past Titan troposphere is cooler and not as optically thick as the current Titan troposphere. Our preliminary model of past Titan, Titan 4, is consistent with analytic results from another past Titan model [89]. This cooling caused by methane depletion may have been substantial enough to allow N_2 to condense onto the surface and thus collapse Titan's atmosphere (since N_2 is the main constituent of Titan's atmosphere) [89].

4.2.5 Future Directions

It would be a marked improvement to replace the estimated upper boundary flux with the actual haze layer by including the opacities for the haze, and extending the frequency range to include the optical part of the spectrum [126]. The model would then apply to the troposphere and the stratosphere.

Possible improvements for the code include adding an accelerator, such as Ng [118] [3] or bi-conjugate gradient [126], or trying out other methods for solving the radiative transfer equation [5] [57] [2]. The addition of an accelerator should decrease the number of iterations, and implementing a new radiative transfer equation solver should speed up the process per iteration, both resulting in reduced runtime.

The intent of this work is to develop a model of Titan's current troposphere that can easily be modified to model Titan's past. The model passes the test for current Titan. To model past Titan, we will need to modify the boundary conditions and the volatile inventory.

The Cassini spacecraft, launched in late 1997, is carrying an orbiter and the Huygens probe to study Saturn, its rings, magnetosphere, and satellites. Titan in particular. The mission has performed a Jupiter flyby (2000) and should reach Saturn and Titan in 2004. It is hoped that the Huygens probe, which is to descend through Titan's atmosphere via parachute, along with imaging radar experiments, will provide us with a wealth of information about Titan's atmosphere and surface properties.

4.3 Comparison of Methods

Advantages of the grey method over the nongrey model:

1. The math and physics are simpler and easier to model.
2. The grey code is about 3000 lines and took on the order of months to develop and perfect; the nongrey code is approximately 10,000 lines and took a few

years to develop and perfect.

3. The code runs much faster.
4. Given the points above, one can obtain a quick and dirty estimate of the answer to the atmosphere question.

Advantages of the nongrey method over the grey model:

1. The initial temperature approximation (e.g., from a grey approximation) is corrected to conform to the problem constraints.
2. In the grey case, it is not necessarily known which mean opacity to choose, and the results are not always self-consistent (for example, in generating an initial grey input for our nongrey model we found that if we use the Planck mean opacity, which is most appropriate for an optically thin Titan, then we end up with a grid whose surface optical depth is large; alternately if we use the Rosseland mean opacity, which is most appropriate for an optically thick atmosphere, then we end up with a grid whose surface optical depth is small).
3. This method takes into account variations in the opacity, and provides much more detailed, accurate answers.
4. The additional parameters make the model more flexible.

APPENDIX A

TIMELINES

A.1 Triton

1846: Discovered by William Lassell [115]

.....: Work progresses slowly, size and temperature uncertain [17]

1979: First infra-red spectra of Triton, indicates presence of methane (CH_4) [17]

1984: Surface consists in part of CH_4 and N_2 [17]

1989: Voyager 2 flyby provides wealth of information (radius, surface and atmosphere composition, and surface geology) [109]

A.2 Pluto

The following timeline, derived from information in [152] [93], and [9], present major discoveries regarding Pluto.

1930: Discovered by Clyde Tombaugh

1931: Pluto's orbit found to be unusually eccentric and inclined

1955: Pluto's 6.4 day rotational period determined

1965: 3:2 resonance with Neptune discovered

1973: Pluto's obliquity found to be larger than 90°

1976: Discovery of CH_4 ice on Pluto

1978: Charon (Pluto's moon) is discovered

- 1986: First reliable radii for Pluto and Charon
- 1987: Resolution of Pluto and Charon's individual spectra made possible by total occultations of Charon behind Pluto
- 1987: Discovery of H_2O ice on Pluto
- 1987: IRAS yields thermal IR data (heat profiles)
- 1988: Stellar occultation reveals Pluto's atmosphere
- 1989: Pluto and Triton are found to be similar in size, density, and surface volatile composition
- 1989: Pluto reaches perihelion
- 1992: Discovery of N_2 and CO ice on Pluto
- 1994: Discovery of CH_4 in Pluto's atmosphere
- 1995: Hubble Space Telescope images reveal polar ice caps on Pluto

A.3 Kuiper Belt

The following timeline from [166] outlines the major discoveries regarding KBOs.

- 1949: Speculation on existence of a trans-Neptunian comet belt around 36-44 AU
- 1980: Serious investigation begins, indicating this region may be a possible source of short-period comets
- 1988: The region is named "Kuiper belt"
- 1992: The first Kuiper belt object (1992 QB₁) is found
- 1998: At the time of this writing, 60 Kuiper belt objects have been discovered[71]

A.4 Titan

The following timeline, with items taken from [135], [159], and [66], outlines the major discoveries regarding Titan.

- 1655: Discovered by Christiaan Huygens
- 1908: Comas Solas detects tentative evidence of an atmosphere
- 1944: An atmosphere is definitively detected by G. Kuiper, who also identifies methane in the atmosphere via spectroscopy
- 1972: Molecular hydrogen is detected in the atmosphere by L. Trafton
- 1973-5: The following species are identified in the atmosphere: C_2H_6 , CH_3D , C_2H_4 , C_2H_2
- 1980: Titan is explored by a near encounter with Voyager I: atomic and molecular hydrogen and nitrogen. CO_2 are detected in the atmosphere
- 1983: CO is detected in Titan's atmosphere
- 1983: Observations indicate that a high-altitude haze exists in the stratosphere
- 1983: Models indicate that greenhouse effect occurs on Titan
- 1984: Models of Titan indicate that Titan's atmosphere would be depleted of methane via photolysis in $10^7 - 10^8$ years
- 1991: Models indicate that antigreenhouse effect occurs on Titan
- 1993: CH_3CN is detected
- 1997: C_4N_2 is detected
- 2004: Cassini-Huygens mission should reach Saturn/Titan

APPENDIX B

PHYSICAL CONSTANTS

c	speed of light	$2.99792456 \times 10^{10}$ cm/s
h	Planck's constant	6.63×10^{-27} dyn cm s
k	Boltzmann's constant	1.38×10^{-16} dyn cm/K
m_H	mass of hydrogen	1.66×10^{-24} g
n_L	Loschmidt's number	2.687×10^{19} particles/cm ³
R	universal gas constant	8.314×10^7 dyn cm/ g K
σ	Stefan-Boltzmann constant	5.68×10^{-5} dyn/cm s K ⁴

REFERENCES

- [1] D. A. ALLEN AND T. L. MURDOCK. *Infrared photometry of Saturn, Titan, and the rings*. Icarus, 14 (1971), pp. 1-2.
- [2] O. ATANACKOVIĆ-VUKMANOVIĆ, L. CRIVELLARI, AND E. SIMONNEAU. *A forth-and-back implicit λ -iteration*. The Astrophysical Journal, 487 (1997), pp. 735-746.
- [3] L. AUER. *Acceleration of convergence*, in Numerical Radiative Transfer, W. Kalkofen, ed., Cambridge University Press, Cambridge, 1987, pp. 101-109.
- [4] L. H. AUER. *The stellar atmospheres problem*. Journal of Quantitative Spectroscopy And Radiative Transfer, 11 (1971), pp. 573-587.
- [5] L. H. AUER AND P. F. B. J. T. BUENO. *Multidimensional radiative transfer with multilevel atoms. 1: ALI method with preconditioning of the rate equations*. Astronomy and Astrophysics, 292 (1994), pp. 599-615.
- [6] L. H. AUER AND D. MIHALAS. *Non-LTE model atmospheres: III. a complete linearization*. The Astrophysical Journal, 158 (1969), pp. 641-655.
- [7] M. BAILEY, S. CLUBE, AND W. NAPIER. *The Origin of Comets*. Pergamon Press, Oxford, 1990.
- [8] B. BÉZARD, A. MARTEN, AND G. PAUBERT. *Detection of acetonitrile on Titan*. Bulletin of the American Astronomical Society, 25 (1993), p. 1100.
- [9] R. BINZEL. *Pluto*. Scientific American, 262 (1990), pp. 50-58.
- [10] S. E. BRODIE. *Descartes' Rule of Signs*: <http://www.cut-the-knot.com/fta/ros2.html>. URL, 1999.
- [11] R. H. BROWN. *Private communication*, 1997.
- [12] C. R. CANIZARES, ed., *Exploring the Trans-Neptunian Solar System*. Space Studies Board, National Academy Press, Washington, D.C., 1998.
- [13] C. J. CANNON, *Frequency-quadrature perturbations in radiative-transfer theory*. The Astrophysical Journal, 185 (1973), pp. 621-630.
- [14] J. CHAMBERLAIN AND D. HUNTEN, *Theory of Planetary Atmospheres: an Introduction to Their Physics and Chemistry*, Academic Press, Inc., Orlando, 1987.

- [15] S. CHANDRASEKHAR, *Radiative Transfer*, Dover Publications, Inc., New York, 1960.
- [16] ———, *An Introduction to the Study of Stellar Structure*, Dover Publications, Inc., New York, 1967.
- [17] C. R. CHAPMAN AND D. P. CRUISHANK. *Prelude to exploration and the Voyager mission*, in Neptune and Triton, D. P. Cruishank, ed., University of Arizona Press, Tucson, 1995, pp. 3–14.
- [18] D. CLAYTON, *Principles of Stellar Evolution and Nucleosynthesis*, The University of Chicago Press, Chicago, 1983.
- [19] R. B. CONDON, *Private communication*, 1996–2001.
- [20] R. COURTIN, *The spectrum of Titan in the far-infrared and microwave regions*, Icarus, 51 (1982), pp. 466–475.
- [21] ———, *Pressure-induced absorption coefficients for radiative transfer calculations in Titan's atmosphere*, Icarus, 75 (1988), pp. 245–254.
- [22] ———, *Private communication*, 1997.
- [23] R. COURTIN, D. GAUTIER, AND C. P. MCKAY, *Titan's thermal emission spectrum: Reanalysis of the voyager infrared measurements*, Icarus, 114 (1995), pp. 144–162.
- [24] A. COUSTENIS AND ET AL., *Plausible condensates in Titan's stratosphere from Voyager infrared spectra*, Science, 194 (1976), pp. 835–837.
- [25] D. P. CRUISHANK, ed., *Neptune and Triton*, University of Arizona Press, Tucson, 1995.
- [26] D. P. CRUISHANK, R. H. BROWN, AND R. CLARK, *Nitrogen on Triton*, Icarus, 58 (1984), pp. 293–305.
- [27] D. P. CRUISHANK AND ET AL., *Ices on the surface of Triton*, Science, 261 (1993), pp. 742–745.
- [28] ———, *The surfaces of Pluto and Charon*, in Pluto and Charon, S. A. Stern and D. J. Tholen, eds., University of Arizona Press, Tucson, 1997, pp. 221–267.
- [29] D. P. CRUISHANK, C. B. PILCHER, AND D. MORRISON, *Pluto: Evidence for methane frost*, Science, 194 (1976), pp. 835–837.
- [30] D. P. CRUISHANK AND P. SILVAGGIO, *Triton: A satellite with an atmosphere*, The Astrophysical Journal, 233 (1979), pp. 1016–1020.

- [31] R. DESCARTES. *Geométrie*, in *The Geometry of René Descartes* (English and French), D. E. Smith and L. A. Latham. eds.. The Open Court Publishing Co., Chicago, 1925.
- [32] A. DOBROVOLSKIS, S. PEALE, AND A. HARRIS. *Dynamics of the Pluto-Charon binary*, in *Pluto and Charon*. S. A. Stern and D. J. Tholen. eds.. University of Arizona Press. Tucson, 1997. pp. 159–190.
- [33] M. DUNCAN, T. QUINN, AND S. TREMAINE. *The origin of short period comets*. *The Astrophysical Journal*. Part 2 - Letters. 328 (1988). pp. L69–L73.
- [34] R. G. EASTMAN AND P. A. PINTO. *Spectrum formation in supernovae: Numerical techniques*. *The Astrophysical Journal*. 412 (1993). pp. 731–751.
- [35] K. E. EDGEWORTH. *The origin and evolution of the Solar System*. *Monthly Notices of the Royal Astronomical Society*. 109 (1949). pp. 600–609.
- [36] J. L. ELIOT AND ET AL.. *Pluto's atmosphere*. *Icarus*. 77 (1989). pp. 148–170.
- [37] ——. *Triton's distorted atmosphere*. *Science*. 278 (1997). pp. 436–439.
- [38] J. L. ELIOT AND L. A. YOUNG. *Analysis of stellar occultation data for planetary atmospheres. I. Model fitting, with application to Pluto*. *The Astronomical Journal*. 103 (1992). pp. 991–1015.
- [39] V. R. ESHELMAN. *Pluto's atmosphere: Models based on refraction, inversion, and vapor-pressure equilibrium*. *Icarus*. 80 (1989). pp. 439–443.
- [40] V. R. ESHELMAN, G. F. LINDAL, AND G. L. TYLER. *Is Titan wet or dry?*. *Science*. 221 (1983). pp. 53–55.
- [41] G. EYINK. *Private communication*. 2001.
- [42] P. FEAUTRIER. *C. R. Acad. Sci. Paris*. 258 (1964). p. 3189.
- [43] E. FERMI. *Thermodynamics*. Dover Publications. Inc.. New York. 1956.
- [44] J. A. FERNANDEZ. *On the existence of a comet belt beyond Neptune*. *Monthly Notices of the Royal Astronomical Society*. 192 (1980). pp. 481–491.
- [45] F. FLASAR, R. E. SAMUELSON, AND B. J. CONRATH. *Titan's atmosphere: temperature and dynamics*. *Nature*. 292 (1981). pp. 693–698.
- [46] F. M. FLASAR. *Oceans on Titan?*. *Science*. 221 (1983). pp. 55–57.
- [47] ——. *The dynamic meteorology of Titan*. *Planetary and Space Science*. 46 (1998). pp. 1125–1147.

- [48] T. GEHRELS AND M. S. MATTHEWS, eds.. *Saturn*. University of Arizona Press. Tucson. 1984.
- [49] S. G. GIBBARD AND ET AL., *Titan: high-resolution speckle images from the Keck telescope*, *Icarus*. 139 (1999), pp. 189–201.
- [50] F. C. GILLETT, *Further observations of the 8-13 micron spectrum of Titan*, *The Astrophysical Journal*. 201 (1975), pp. L41–L43.
- [51] F. C. GILLETT, W. J. FORREST, AND K. M. MERRILL. *8-13 micron observations of Titan*, *The Astrophysical Journal*. 184 (1973), pp. L93–L95.
- [52] G. H. GOLUB AND C. F. V. LOAN. *Matrix Computations*. Johns Hopkins University Press. USA. 1993.
- [53] R. M. GOODY AND Y. L. YUNG. *Atmospheric Radiation: Theoretical Basis*. Oxford University Press. Inc., New York. 1989.
- [54] I. S. GRADSHTEYN AND I. M. RYZHIK. *Tables of Integrals, Series, and Products (Corrected and Enlarged Version)*. Academic Press. Inc., San Diego. 1980.
- [55] C. A. GRIFFITH. *Evidence for surface heterogeneity on Titan*, *Nature*. 364 (1993), pp. 511–514.
- [56] C. A. GRIFFITH, J. L. HALL, AND T. R. GEBALLE. *Detection of daily clouds on Titan*, *Science*, 290 (2000), pp. 509–513.
- [57] H. J. T. B. H. SOCAS-NAVARRO. *Linearization versus preconditioning: Which approach is best for solving multilevel transfer problems?*, *The Astrophysical Journal*. 490 (1997), pp. 383–392.
- [58] T. HIDAYAT AND ET AL., *Millimeter and submillimeter heterodyne observations of Titan: the vertical profile of carbon monoxide in its stratosphere*, *Icarus*. 133 (1998), pp. 109–133.
- [59] W. B. HUBBARD AND ET AL., *Occultation evidence for an atmosphere on Pluto*, *Nature*. 336 (1988), pp. 452–454.
- [60] ———. *The occultation of 28 sgr by Titan*, *Astronomy and Astrophysics*. 269 (1993), pp. 541–563.
- [61] W. B. HUBBARD, R. V. YELLE, AND J. I. LUNINE. *Nonisothermal Pluto atmosphere models*, *Icarus*, 84 (1990), pp. 1–11.
- [62] I. HUBENY AND T. LANZ. *Non-LTE line-blanketed model atmosphere of hot stars. I. Hybrid complete linearization/accelerated lambda iteration method*, *Astronomy and Astrophysics*, 262 (1992), pp. 501–514.

- [63] ——. *Accelerated complete-linearization method for calculating NLTE model stellar atmospheres*, *The Astrophysical Journal*, 439 (1995), pp. 875–904.
- [64] D. HUNTEN, *Private communication*, 1997.
- [65] D. M. HUNTEN, *The atmosphere of Titan*, *Comments on Astrophysics and Space Physics*, 4 (1972), pp. 149–154.
- [66] D. M. HUNTEN AND ET AL., *Titan*, in *Saturn*, T. Gehrels and M. S. Matthews, eds., University of Arizona Press, Tucson, 1984, pp. 671–759.
- [67] W. T. HUTZELL, C. P. MCKAY, AND O. B. TOON, *Effects of the time-varying haze production on Titan's geometric albedo*, *Icarus*, 105 (1993), pp. 162–174.
- [68] A. INGERSOLL, *Dynamics of Triton's atmosphere*, *Nature*, 344 (1990), pp. 315–317.
- [69] E. ISAACSON AND H. B. KELLER, *Analysis of Numerical Methods*, Dover Publications, Inc., New York, 1994.
- [70] W. JAFFE, J. CALDWELL, AND T. OWEN, *Radius and brightness temperature observations of Titan at centimeter wavelengths by the Very Large Array*, *The Astrophysical Journal*, 242 (1980), pp. 806–811.
- [71] D. JEWITT, *Kuiper belt page*: <http://www.ifa.hawaii.edu/faculty/jewitt/kb.html>. URL, 2001.
- [72] D. C. JEWITT AND J. LUU, *Discovery of the candidate Kuiper belt object 1992 QB₁*, *Nature*, 362 (1993), pp. 730–732.
- [73] A. K. KAPILA, *Arrhenius systems: dynamics of jump due to slow passage through criticality*, *SIAM Journal of Applied Mathematics*, 41 (1981), pp. 29–42.
- [74] B. W. KERNIGHAN AND D. M. RITCHIE, *The C Programming Language, Second Edition*, Prentice Hall, Englewood Cliffs, NJ, 1988.
- [75] B. N. KHARE AND ET AL., *Optical constants of organic tholins produced in a simulated Titanian atmosphere: from soft X-ray to microwave frequencies*, *Icarus*, 60 (1984), pp. 127–137.
- [76] V. A. KRASNOPOLSKY AND ET AL., *Temperature, N₂, and N density profiles of Triton's atmosphere: Observations and model*, *Journal of Geophysical Research*, 98 (1993), pp. 3065–3078.

- [77] E. KREYSZIG, *Advanced Engineering Mathematics*, John Wiley and Sons, New York, 1983.
- [78] G. A. KRIEGSMANN, *Thermal runaway in microwave heated ceramics: a one-dimensional model*, *Journal of Applied Physics*, 71 (1992), pp. 1960–1966.
- [79] G. P. KUIPER, *Titan: a satellite with an atmosphere*, *The Astrophysical Journal*, 100 (1944), pp. 378–383.
- [80] ———, *On the origin of the solar system*, in *Astrophysics: A Topical Symposium*, J. Hynak, ed., McGraw-Hill, New York, 1951, p. 357.
- [81] L. D. LANDAU AND E. M. LIFSHITZ, *Fluid Mechanics*, Pergamon Press, Oxford, 1983.
- [82] E. LELLOUCH AND ET AL., *Titan's atmosphere and hypothesized ocean: a re-analysis of the Voyager 1 radio-occultation and IRIS 7.7 μm data*, *Icarus*, 79 (1989), pp. 328–349.
- [83] M. T. LEMMON, E. KARKOSCHKA, AND M. TOMASKO, *Titan's rotation: surface feature observed*, *Icarus*, 103 (1993), pp. 329–332.
- [84] ———, *Titan's rotational lightcurve*, *Icarus*, 113 (1995), pp. 27–38.
- [85] G. F. LINDAL AND ET AL., *The atmosphere of Titan: an analysis of the Voyager I occultation measurements*, *Icarus*, (53), pp. 348–363.
- [86] G. W. LOCKWOOD AND ET AL., *The albedo of Titan*, *The Astrophysical Journal*, (303), pp. 511–530.
- [87] R. D. LORENZ AND ET AL., *Titan's north-south asymmetry from HST and Voyager imaging: comparison with models and ground based photometry*, *Icarus*, (127), pp. 173–189.
- [88] R. D. LORENZ AND J. I. LUNINE, *Titan's surface reviewed: the nature of bright and dark terrain*, *Planetary and Space Science*, (45), pp. 981–992.
- [89] R. D. LORENZ, C. P. MCKAY, AND J. I. LUNINE, *Photochemically driven collapse of Titan's atmosphere*, *Science*, (275), pp. 642–644.
- [90] F. J. LOW, *Planetary radiation at infrared and millimeter wavelengths*, *Lowell Observatory Bulletin*, (1965), pp. 184–187.
- [91] F. J. LOW AND G. H. RIEKE, *Infrared photometry of Titan*, *The Astrophysical Journal*, (1974), pp. L143–L145.

- [92] J. I. LUNINE. *From air pollution to extra-solar planets*. in ERCA. C. Boutron, ed., vol. 3. EDL Press, Les Ulis, France.
- [93] ———, ed., *Pluto Express: Report of Science Definition Team*. NASA, Washington, D.C., 1995.
- [94] ———, *Physics and chemistry of the surface-atmosphere systems of Titan, Triton, and Pluto*. in ERCA, C. Boutron, ed., vol. 2. Les Editions de Physique, Les Ulis, France, 1996. pp. 457–474.
- [95] ———, *Private communication*. 1996-2001.
- [96] J. I. LUNINE AND ET AL., *Sublimation and reformation of icy grains in the primitive solar nebula*. *Icarus*, 94 (1991), pp. 333–344.
- [97] J. I. LUNINE, R. D. LORENZ, AND W. K. HARTMANN, *Some speculations on Titan's past, present and future*. *Planetary and Space Science*, 46 (1998), pp. 1099–1107.
- [98] J. I. LUNINE AND M. NOLAN, *A massive early atmosphere on Triton*. *Icarus*, 100 (1992), pp. 221–234.
- [99] J. I. LUNINE, D. P. STEVENSON, AND Y. L. YUNG, *Ethane ocean on Titan*. *Science*, 222 (1983), pp. 119–120.
- [100] J. I. LUNINE, Y. K. YUNG, AND R. D. LORENZ, *On the volatile inventory of Titan from isotopic abundances in nitrogen and methane*. *Planetary and Space Science*, 47 (1999), pp. 1291–1303.
- [101] B. L. LUTZ, C. DE BERGH, AND T. OWEN, *Titan: discovery of carbon monoxide in its atmosphere*. *Science*, 220 (1983), pp. 1374–1375.
- [102] J. LUU AND D. C. JEWITT, *Color diversity among the Centaurs and Kuiper belt objects*. *The Astronomical Journal*, 112 (1996), pp. 2310–2318.
- [103] C. P. MCKAY AND ET AL., *The atmospheric temperature structure of Titan*. in *Proceedings Symposium on Titan*, ESA SP-338. European Space Agency, Noordwijk, The Netherlands, 1992, pp. 77–80.
- [104] ———, *Coupled atmosphere-ocean models of Titan's past*. *Icarus*, 102 (1993), pp. 88–98.
- [105] C. P. MCKAY, R. D. LORENZ, AND J. I. LUNINE, *Analytic solutions for the antigreenhouse effect: Titan and early Earth*, *Icarus*, 137 (1999), pp. 56–61.

- [106] C. P. MCKAY, J. B. POLLACK, AND R. COURTIN. *The thermal structure of Titan's atmosphere*. *Icarus*, 80 (1989), pp. 25–53.
- [107] ——. *The greenhouse and antigreenhouse effects on Titan*. *Science*, 253 (1991), pp. 1118–1121.
- [108] W. MCKINNON, D. SIMONELLI, AND G. SCHUBERT. *Composition, internal structure, and thermal evolution of Pluto and Charon*. in *Pluto and Charon*. S. A. Stern and D. J. Tholen, eds., University of Arizona Press, Tucson, 1997, pp. 295–343.
- [109] W. B. MCKINNON, J. I. LUNINE, AND D. BANFIELD. *Origin and evolution of Triton*. in *Neptune and Triton*. D. P. Cruikshank, ed., University of Arizona Press, Tucson, 1995, pp. 807–878.
- [110] H. J. MELOSH. *Impact Cratering: A Geologic Process*. Oxford University Press, New York, 1989.
- [111] G. MERCADO. *Private communication*, 1998–1999.
- [112] D. MIHALAS. *Stellar Atmospheres*. W. H. Freeman and Co., San Francisco, 1984.
- [113] D. MIHALAS AND B. MIHALAS. *Foundations of Radiation Hydrodynamics*. Oxford University Press, New York, 1984.
- [114] MINOR PLANET CENTER, HARVARD–SMITHSONIAN CENTER FOR ASTROPHYSICS. *List of Transneptunian Objects*: <http://cfa-www.harvard.edu/cfa/ps/lists/tnos.html>. URL, 2000–2001.
- [115] P. MOORE. *The discoveries of Neptune and Triton*. in *Neptune and Triton*. D. P. Cruikshank, ed., University of Arizona Press, Tucson, 1995, pp. 15–36.
- [116] D. MORRISON, D. P. CRUIKSHANK, AND R. E. MURPHY. *Temperatures of Titan and the Galilean satellites at 20 microns*. *The Astrophysical Journal*, 173 (1972), pp. L143–L146.
- [117] D. O. MUHLEMAN AND ET AL.. *Radar reflectivity of Titan*. *Science*, 248 (1990), pp. 975–980.
- [118] K.-C. NG. *Hypernetted chain solutions for the classical one-component plasma up to $\gamma = 7000$* . *Journal of Chemical Physics*, 61 (1974), pp. 2680–2689.
- [119] M. NOLAN AND J. I. LUNINE, *Some constraints on a greenhouse atmosphere for Triton*. *Geophysical Research Letters*, 15 (1988), pp. 1315–1318.

- [120] C. B. OLKIN AND ET AL., *The thermal structure of Triton's atmosphere: Results from the 1993 and 1995 occultations*. *Icarus*. 129 (1997), pp. 178–201.
- [121] G. L. OLSON, L. H. AUER, AND J. R. BUCHLER. *A rapidly convergent iterative solution of the non-LTE radiation transfer problem*. *Journal of Quantitative Spectroscopy And Radiative Transfer*. 35 (1986), pp. 431–442.
- [122] G. L. OLSON AND P. B. KUNASZ. *Short characteristic solution of the non-LTE line transfer problem by operator perturbation - I. The one-dimensional planar slab*. *Journal of Quantitative Spectroscopy And Radiative Transfer*. 38 (1987), pp. 325–336.
- [123] J. H. OORT. *The structure of the cloud of comets surrounding the solar system and a hypothesis concerning its origin*. *Bull. Astron. Inst. Netherlands*. 11 (1950), pp. 91–110.
- [124] T. OWEN. *The composition and origin of Titan's atmosphere*. *Planetary and Space Science*. 30 (1982), pp. 833–838.
- [125] T. C. OWEN AND ET AL.. *Surface ices and the atmospheric composition of Pluto*. *Science*. 261 (1993), pp. 745–748.
- [126] P. A. PINTO. *Private communication*. 1998-2001.
- [127] ——. *Notes on Constructing a Model Atmosphere Code (unpublished)*. 2000.
- [128] J. B. POLLACK. *Greenhouse models of the atmosphere of Titan*. *Icarus*. 19 (1973), pp. 43–58.
- [129] J. B. POLLACK AND G. CONSOLMAGNO. *Origin and evolution of the Saturn system*, in *Saturn*, T. Gehrels and M. S. Matthews, eds., University of Arizona Press, Tucson, 1984, pp. 811–866.
- [130] W. PRESS, S. TEUKLOSKY, W. VETTERLING, AND B. FLANNERY. *Numerical Recipes in C: The Art of Scientific Computing*, Cambridge University Press, New York, 1992.
- [131] K. RAGES AND J. B. POLLACK. *Vertical distribution of scattering hazes in Titan's upper atmosphere*, *Icarus*, 55 (1983), pp. 50–62.
- [132] K. RAGES, J. B. POLLACK, AND P. H. SMITH. *Size estimates of Titan's aerosols based on voyager high-phase-angle images*. *Journal of Geophysical Research*. 88 (1983), pp. 8721–8728.
- [133] N. O. RENNÓ. *Multiple equilibria in radiative-convective atmospheres*. *Tellus*. 49A (1997), pp. 423–438.

- [134] D. ROPP. *Private communication*. 1999-2001.
- [135] D. A. ROTHERY. *Satellites of the Outer Planets: Worlds in their own right*. Clarendon Press, Oxford, 1992.
- [136] C. SAGAN. *The greenhouse of Titan*. *Icarus*. 18 (1973), pp. 649-656.
- [137] C. SAGAN AND S. F. DERMOTT. *The tides in the seas of Titan*. *Nature*. 300 (1982), pp. 731-733.
- [138] C. SAGAN AND ET AL.. *Organic matter in the Saturn system*, in Saturn. T. Gehrels and M. S. Matthews, eds., University of Arizona Press, Tucson, 1984, pp. 788-807.
- [139] R. E. SAMUELSON. *A radiative equilibrium model of Titan's atmosphere*. *Icarus*. 53 (1983), pp. 364-387.
- [140] R. E. SAMUELSON AND ET AL.. *Mean molecular weight and hydrogen abundance of Titan's atmosphere*. *Nature*. 292 (1981), pp. 688-693.
- [141] ——. *CO₂ on Titan*. *Journal of Geophysical Research*. 88 (1983), pp. 8709-8715.
- [142] ——. *C₁N₂ ice in Titan's north polar stratosphere*. *Planetary and Space Science*. 45 (1997), pp. 941-948.
- [143] G. B. SCHARMER. *Solutions to radiative transfer problems using approximate lambda operators*. *The Astrophysical Journal*. 249 (1981), pp. 720-730.
- [144] ——. *Accurate solutions for the non-LTE problem using approximate Lambda operators*, in *Methods in Radiative Transfer*. W. Kalkofen, ed., Cambridge University Press, Cambridge, 1984, pp. 173-210.
- [145] W. D. SEARS. *Tidal dissipation on Titan*. *Icarus*. 113 (1995), pp. 39-56.
- [146] P. H. SMITH. *Titan's surface, revealed by HST imaging*. *Icarus*. 119 (1996), pp. 336-349.
- [147] J. STANSBERRY AND ET AL.. *Triton's surface-atmosphere energy balance*. *Icarus*. 99 (1992), pp. 242-260.
- [148] ——. *Mirages and the nature of Pluto's atmosphere*. *Icarus*. 111 (1994), pp. 503-513.
- [149] J. STANSBERRY, D. PISANO, AND R. YELLE. *The emissivity of volatile ices on Triton and Pluto*, *Planetary and Space Science*. 44 (1996), pp. 945-955.

- [150] J. STANSBERRY AND R. V. YELLE. *Emissivity and the fate of Pluto's atmosphere*. *Icarus*, 141 (1999), pp. 299–306.
- [151] S. A. STERN AND ET AL.. *Future Neptune and Triton missions*. in *Neptune and Triton*. D. P. Cruikshank, ed., University of Arizona Press, Tucson, 1995. pp. 1151–1178.
- [152] S. A. STERN, W. MCKINNON, AND J. I. LUNINE. *On the origin of Pluto, Charon, and the Pluto-Charon binary*. in *Pluto and Charon*. S. A. Stern and D. J. Tholen, eds., University of Arizona Press, Tucson, 1997. pp. 605–663.
- [153] S. A. STERN AND D. J. THOLEN, eds., *Pluto and Charon*. University of Arizona Press, Tucson, 1997.
- [154] D. J. STEVENSON. *Interior of Titan*. in *Proceedings Symposium on Titan*. ESA SP-338. European Space Agency, Noordwijk, The Netherlands, 1992. pp. 29–33.
- [155] J. STOER AND R. BULIRSH. *Introduction to Numerical Analysis*. Springer-Verlag, New York, 1983.
- [156] E. C. STONE AND E. D. MINER. *The Voyager 2 encounter with the Neptunian system*. *Science*, 246 (1989), pp. 1417–1421.
- [157] G. STRANG. *Linear Algebra and its Applications*. Harcourt Brace Jovanovich, Inc., USA, 1988.
- [158] D. F. STROBEL AND ET AL.. *On the vertical thermal structure of Pluto's atmosphere*. *Icarus*, 120 (1996), pp. 266–289.
- [159] F. W. TAYLOR AND A. COUSTENIS. *Titan in the Solar System*. *Planetary and Space Science*, 46 (1998), pp. 1085–1097.
- [160] D. J. THOLEN AND M. BUIE. *Bulk properties of Pluto and Charon*. in *Pluto and Charon*. S. A. Stern and D. J. Tholen, eds., University of Arizona Press, Tucson, 1997. pp. 193–219.
- [161] C. S. W. R. THOMPSON. *Production and condensation of organic gases in the atmosphere of Titan*. *Icarus*, 59 (1984), pp. 133–161.
- [162] T. TOKANO AND ET AL.. *Seasonal variation of Titan's atmospheric structure simulated by a general circulation model*. *Planetary and Space Science*, 47 (1999), pp. 493–520.
- [163] D. TOUBLANC AND ET AL.. *Photochemical modelling of Titan's atmospheric*. *Icarus*, 113 (1995), pp. 2–26.

- [164] L. TRAFTON. *On the possible detection of H₂ in Titan's atmosphere*. The Astrophysical Journal, 175 (1972), pp. 285–293.
- [165] ——. *Large seasonal variations in Triton's atmosphere*. Icarus, 58 (1984), pp. 312–324.
- [166] P. R. WEISSMAN AND H. F. LEVINSON. *The population of the Trans-Neptunian region: The Pluto-Charon environment*, in Pluto and Charon, S. A. Stern and D. J. Tholen, eds., University of Arizona Press, Tucson, 1997, pp. 559–604.
- [167] R. YELLE AND ET AL., *Lower atmospheric structure and surface-atmosphere interactions on Triton*, in Neptune and Triton, D. P. Cruikshank, ed., University of Arizona Press, Tucson, 1995, pp. 1031–1105.
- [168] R. V. YELLE AND J. ELLIOT. *Atmospheric structure and composition: Pluto and Charon*, in Pluto and Charon, S. A. Stern and D. J. Tholen, eds., University of Arizona Press, Tucson, 1997, pp. 347–390.
- [169] R. V. YELLE AND J. I. LUNINE. *Evidence for a molecule heavier than methane in the atmosphere of Pluto*. Nature, 339 (1989), pp. 288–290.
- [170] R. V. YELLE, D. F. STROBEL, E. LELLOUCH, AND D. GAUTIER. *Engineering models for Titan's atmosphere*, in Huygens: Science, Payload and Mission, A. Wilson, ed., ESA SP-1177, European Space Agency, Noordwijk, The Netherlands, 1997, pp. 243–256.
- [171] Y. L. YUNG, M. ALLEN, AND J. P. PINTO. *Photochemistry of the atmosphere of Titan: comparison between model and observations*. The Astrophysical Journal Supplement, 55 (1984), pp. 465–506.